STRUCTURE AND BON

Series Editor D. M. P. Mi

Volume Editors N. Kalt

113
Structure and Bonding

Series Editor:
D.M.P. Mingos

Editorial Board:

A.J. Bard · P. Day · J.A. Ibers · T.J. Meyer · H.W. Roesky
J.-P. Sauvage · F. Wudl

Structure and Bonding

Recently Published and Forthcoming Volumes

Principles and Applications of Density Functional Theory in Inorganic Chemistry II
Volume Editors:
Kaltsoyannis, N., McGrady, J.E.
Vol. 113, 2004

Principles and Applications of Density Functional Theory in Inorganic Chemistry I
Volume Editors:
Kaltsoyannis, N., McGrady, J.E.
Vol. 112, 2004

Supramolecular Assembly via Hydrogen Bonds II
Volume Editor: Mingos, D.M.P.
Vol. 111, 2004

Applications of Evolutionary Computation in Chemistry
Volume Editor: Johnston, R.L.
Vol. 110, 2004

Fullerene-Based Materials
Structures and Properties
Volume Editor: Prassides, K.
Vol. 109, 2004

Supramolecular Assembly via Hydrogen Bonds I
Volume Editor: Mingos, D.M.P.
Vol. 108, 2004

Optical Spectra and Chemical Bonding in Transition Metal Complexes
Special Volume II
dedicated to Professor Jørgensen
Volume Editor: Schönherr, T.
Vol. 107, 2004

Optical Spectra and Chemical Bonding in Inorganic Compounds
Special Volume I
dedicated to Professor Jørgensen
Volume Editor: Schönherr, T.
Vol. 106, 2004

Group 13 Chemistry III
Industrial Applications
Volume Editors:
Roesky, H.W., Atwood, D.A.
Vol. 105, 2003

Group 13 Chemistry II
Biological Aspects of Aluminum
Volume Editors:
Roesky, H.W., Atwood, D.A.
Vol. 104, 2002

Group 13 Chemistry I
Fundamental New Developments
Volume Editors:
Roesky, H.W., Atwood, D.A.
Vol. 103, 2002

High Performance Non-Oxide Ceramics II
Volume Editor: Jansen, M.
Vol. 102, 2002

High Performance Non-Oxide Ceramics I
Volume Editor: Jansen, M.
Vol. 101, 2002

π-Electron Magnetism
From Molecules to Magnetic Materials
Volume Editor: Veciana, J.
Vol. 100, 2001

Principles and Applications of Density Functional Theory in Inorganic Chemistry II

Volume Editors:
N. Kaltsoyannis · J.E. McGrady

With contributions by
M. Alfredsson · E. Canadell · E. Clot · F. Corà · R.J. Deeth
R. Dovesi · O. Eisenstein · W.C. Mackrodt · G. Mallia
D.S. Middlemiss · P. Ordejón · R. Orlando · E. Ruiz
D. Sánchez-Portal

Springer

The series *Structure and Bonding* publishes critical reviews on topics of research concerned with chemical structure and bonding. The scope of the series spans the entire Periodic Table. It focuses attention on new and developing areas of modern structural and theoretical chemistry such as nanostructures, molecular electronics, designed molecular solids, surfaces, metal clusters and supramolecular structures. Physical and spectroscopic techniques used to determine, examine and model structures fall within the purview of Structure and Bonding to the extent that the focus is on the scientific results obtained and not on specialist information concerning the techniques themselves. Issues associated with the development of bonding models and generalizations that illuminate the reactivity pathways and rates of chemical processes are also relevant.
As a rule, contributions are specially commissioned. The editors and publishers will, however, always be pleased to receive suggestions and supplementary information. Papers are accepted for *Structure and Bonding* in English.
In references *Structure and Bonding* is abbreviated *Struct Bond* and is cited as a journal.

Springer WWW home page: http://www.springeronline.com
Visit the SB content at http://www.springerlink.com/

ISSN 0081-5993
ISBN 3-540-21861-0
DOI 10.1007/b12226
Springer Berlin Heidelberg New York

Library of Congress Control Number 2004105723

This work is subject to copyright. All rights are reserved, whether the whole or part of the material is concerned, specifically the rights of translation, reprinting, reuse of illustrations, recitation, broadcasting, reproduction on microfilms or in any other ways, and storage in data banks. Duplication of this publication or parts thereof is permitted only under the provisions of the German Copyright Law of September 9, 1965, in its current version, and permission for use must always be obtained from Springer-Verlag. Violations are liable to prosecution under the German Copyright Law.

Springer is a part of Springer Science+Business Media

springeronline.com

© Springer-Verlag Berlin Heidelberg 2004
Printed in Germany

The use of registered names, trademarks, etc. in this publication does not imply, even in the absence of a specific statement, that such names are exempt from the relevant protective laws and regulations and therefore free for general use.

Cover: KünkelLopka GmbH, Heidelberg/Design & Production GmbH, Heidelberg
Typesetting: Stürtz GmbH, Würzburg
Production Editor: Angélique Gcouta, Berlin

Printed on acid-free paper 02/3020 gc – 5 4 3 2 1 0

Series Editor

Prof. D. Michael P. Mingos
Principal
St. Edmund Hall
Oxford OX1 4AR, UK
michael.mingos@st-edmund-hall.oxford.ac.uk

Volume Editors

Dr. Nikolas Kaltsoyannis
Chemistry Department
University College London
20 Gordon Street
London WC1H 0AJ, UK
uccanka@ucl.ac.uk

Dr. John E. McGrady
Department of Chemistry
Inorganic Chemistry
University of York
Heslington
York, YO 105DD, UK
jem15@york.ac.uk

Editorial Board

Prof. Allen J. Bard
Department of Chemistry and Biochemistry
University of Texas
24th Street and Speedway
Austin, Texas 78712, USA
ajbard@mail.utexas.edu

Prof. James A. Ibers
Department of Chemistry
North Western University
2145 Sheridan Road
Evanston, Illinois 60208-3113, USA
ibers@chem.nwu,edu

Prof. Herbert W. Roesky
Institute for Inorganic Chemistry
University of Göttingen
Tammannstrasse 4
37077 Göttingen, Germany
hroesky@gwdg.de

Prof. Fred Wudl
Department of Chemistry
University of California
Los Angeles, CA 90024-1569, USA
wudl@chem.ucla.edu

Prof. Peter Day, FRS
Director and Fullerian Professor
of Chemistry
The Royal Institution of Great Britain
21 Albemarle Street
London WIX 4BS, UK
pday@ri.ac.uk

Prof. Thomas J. Meyer
Associate Laboratory Director
for Strategic and Supporting Research
Los Alamos National Laboratory
PO Box 1663
Mail Stop A 127
Los Alamos, NM 87545, USA
tjmeyer@lanl.gov

Prof. Jean-Pierre Sauvage
Faculté de Chimie
Laboratoires de Chimie
Organo-Minérale
Université Louis Pasteur
4, rue Blaise Pascal
67070 Strasbourg Cedex, France
sauvage@chimie.u-strasbg.fr

Structure and Bonding is also Available Electronically

For all customers who have a standing order to Structure and Bonding, we offer the electronic version via SpringerLink free of charge. Please contact your librarian who can receive a password for free access to the full articles by registering at:

http://www.springerlink.com

If you do not have a subscription, you can still view the tables of contents of the volumes and the abstract of each article by going to the SpringerLink Homepage, clicking on "Browse by Online Libraries", then "Chemical Sciences", and finally choose Structure and Bonding.

You will find information about the

– Editorial Board
– Aims and Scope
– Instructions for Authors
– Sample Contribution

at http://www.springeronline.com using the search function.

Preface

It is difficult to overestimate the impact that density functional theory has had on computational quantum chemistry over the last two decades. Indeed, this period has seen it grow from little more than a theoreticalcuriosity to become a central tool in the computational chemist's armoury. Arguably no area of chemistry has benefited more from the meteoric rise in density functional theory than inorganic chemistry. the ability to obtainreliable results in feasible timescales on systems containing heavy elements such as the d and f transition metals has led to an enormous growth in computational inorganic chemistry. The inorganic chemical literature reflects this growth; it is almost impossible to open a modern inorganic chemistry journal without finding several papers devoted exclusively or in part to density functional theory calculations. The real importance of the rise in density functional theory in inorganic chemistry is undoubtedly the much closer synergy between theory and experiment than was previously posible.

In these volumes, world-leading researchers describe recent developments in the density functional theory and its applications in modern inorganic and bioinorganic chemistry. These articles address key issues key issues in both solidstate and molecular inorganic chemistry, such as spectroscopy, mechanisms, catalysis, bonding and magnetism. The articles in volume I are more focussed on advances in density functional methodogy, while those in Volume II deal more with applications, although this is by no means a rigid distinction. We are very grateful to all our contributors for their extensive efforts. We are very proud to present this collection of world-class science, and hope that you enjoy reading it as much as we have enjoyed putting it together.

September 2004

Nikolas Kaltsoyannis
John E. McGrady

Contents

Agostic Interactions from a Computational Perspective: One Name, many Interpretations
E. Clot · O. Eisenstein 1

Computational Bioinorganic Chemistry
R.J. Deeth 37

Theoretical Study of the Exchange Coupling in Large Polynuclear Transition Metal Complexes Using DFT Methods
E. Ruiz 71

Computing the Properties of Materials from First Principles with SIESTA
D. Sánchez-Portal · P. Ordejón · E. Canadell 103

The Performance of Hybrid Density Functionals in Solid State Chemistry
F. Corà · M. Alfredsson · G. Mallia · D.S. Middlemiss · W.C. Mackrodt
R. Dovesi · R. Orlando 171

Author Index 101–113 233

Subject Index 239

Contents of Volume 112

Principles and Applications of Density Functional Theory in Inorganic Chemistry I

Volume Editors: N. Kaltsoyannis · J.E. McGrady
ISBN 3-540-21860-2

The Calculation of NMR Parameters in Transition Metal Complexes
J. Autschbach

Excitation Energies of Metal Complexes with Time-dependent Density Functional Theory
A. Rosa · G. Ricciardi · O. Gritsenko · E.J. Baerends

Applications of Hybrid DFT/Molecular Mechanics to Homogeneous Catalysis
G. Ujaque · F. Maseras

DFT Computation of Relative Spin-State Energetics of Transition Metal Compounds
J.N. Harvey

Structure and Bonding (2004) 113:1–36
DOI 10.1007/b97940
© Springer-Verlag Berlin Heidelberg 2004

Agostic Interactions from a Computational Perspective: One Name, Many Interpretations

Eric Clot · Odile Eisenstein (✉)

Laboratoire de Structure et Dynamique des Systèmes Moléculaires et Solides (UMR 5636), cc14, Université Montpellier 2, 34095 Montpellier Cedex 05, France
odile.eisenstein@univ-montp2.fr

1 Introduction 2
1.1 Definition of the Agostic Interaction 2
1.2 Focus and Limitations of this Review. 5

2 The C-H Agostic Interaction, from Early Studies to Recent Interpretations . 5
2.1 The α-Agostic Interaction 6
2.2 The β-Agostic Interaction 9

3 The Agostic C-H Bond with a Non-Transition Metal Centre 13

4 X-H Agostic Bonds with X Different from C 14
4.1 The B-H Agostic Bond 14
4.2 The Si-H Agostic Bond 16

5 X-Y Agostic with Y Different from H 20
5.1 The C-C Agostic Interaction. 20
5.2 The Si-C Agostic Interaction 21
5.3 X-Y Agostic with Y Bearing Lone Pairs 23

6 The High Sensitivity of the C-H Agostic Interaction to the Nature of the Molecule 24
6.1 The Energetic Magnitude of the Agostic Interaction 24
6.2 The Steric Influence of the Ligands 26
6.3 The Agostic Interaction: One Weak Interaction Among Other Ones. 28

7 Conclusions 30

References 32

Abstract The agostic bond defines an intramolecular interaction where a σ bond is geometrically close to an electron deficient centre (often a transition metal). The computational studies on this energetically weak interaction are reviewed and discussed. Various types of σ bonds have been considered (C-H, C-C, Si-H, Si-C, B-H). It is suggested that a C-X bond in which X carries a lone pair should preferably not be viewed as agostic. The factors that contribute to his occurrence are discussed. In particular, the agostic interaction is very sensitive to steric effects. Explanations based on molecular orbital analysis, electron delocalization and topological analysis of the electron density are presented.

Keywords Agostic interaction · Weak interaction · Bond activation · Computational studies · DFT · QM/MM calculations · Molecular orbitals · Topological analysis · Steric effects

1 Introduction

The agostic interaction is among the key discoveries made in organometallic chemistry during the twentieth century [1, 2]. It was earlier thought that a ligand could only interact with a transition metal centre either in an ionic fashion or via a relatively strong donor-acceptor bond. We will put aside anionic (X type) ligands that, in the neutral form (e.g. Cl), have a half filled orbital for interaction with the metal (X is usually considered as X^- in the formal analysis of the metal oxidation state, however). These ligands often make rather strong bonds with the metal centre. More relevant to the present argument are neutral ligands which use their highest occupied molecular orbital (HOMO) to establish a donor-acceptor interaction with the metal centre lowest unoccupied molecular orbital (LUMO). Although the M-L bond dissociation energy does not depend in any regular way on the ligand HOMO energy, it was always understood that ligands with very low lying occupied orbitals would be unlikely to interact with a metal centre. A poor Lewis base would thus be incapable of acting as a ligand to a Lewis acidic metal centre. Hence the surprise at the announcement that a C-H bond (one of the worst Lewis bases) can interact with a metal centre. This discovery opened the coordination chemistry of metal interactions with weakly bound ligands, among which dihydrogen and alkanes are prominent [3–13]. Agostic interactions have now been seen in a large number of organometallic complexes for essentially any metal centre in the periodic table. The purpose of this chapter is to illustrate, through a description of the computational studies, that the word "agostic", commonly used for these interactions, in fact covers a wide variety of subtly different situations and the position is not as simple as was first thought.

1.1 Definition of the Agostic Interaction

The historical aspects are covered in two reviews [1, 2]. We will thus not dwell on all the experimental physical properties that are used to establish the presence of an agostic bond. The name agostic was coined by Brookhart and Green from the Greek "$\alpha\gamma o\sigma\tau o\varsigma$", which according to their papers [1, 2], may be translated as to clasp, or to draw towards. As M.L.H. Green himself stated to one of us, the term implies the idea of a "shield" behind which the metal is somewhat protected from intruders. It originally described the situation in which a C-H, B-H or Si-H bond of a ligand was coordinated to the metal centre. This implies that the pairs of atoms C *and* H, B *and* H or Si *and* H are both close to the metal. Brookhart and Green also considered that C-F, C-Cl, Au-C and even H-N could become agostic. From the early stage, the word "agostic" was used to describe different situations. Thus it seems that the metal···H-N interaction does not follow the criterion of having two

atoms both bonded to the metal [14, 15]. The M···H-N angle is usually around 180° and this situation was later considered as better described as a type of hydrogen bonding where the metal acts as a base and the H-N bond as the proton donor [16]. This is clearly the reverse of the agostic interaction where the metal seeks electron density. Even after removing the M···H-N bond from the list of agostic situations, one is left with a high variety of bonds and systems. In their fundamental papers [1, 2], Brookhart and Green view all these bonds as making a covalent bond to the metal centre, the C-H, B-H and Si-H bonds being 2e donors and the C-F or C-Cl bonds being 4e donors leading to 3c-2e or 3c-4e bonds when including the metal. Another key feature of the agostic interaction is that the X-H (X=C, B, Si) bond is part of a ligand. In other words the ligand can be viewed as a chelate strongly bonded through one end and weakly so through the X-H bond.

A large variety of agostic bonds M···H-X has been identified as summarized in Scheme 1 for X=C. Some of these are also known for X other than

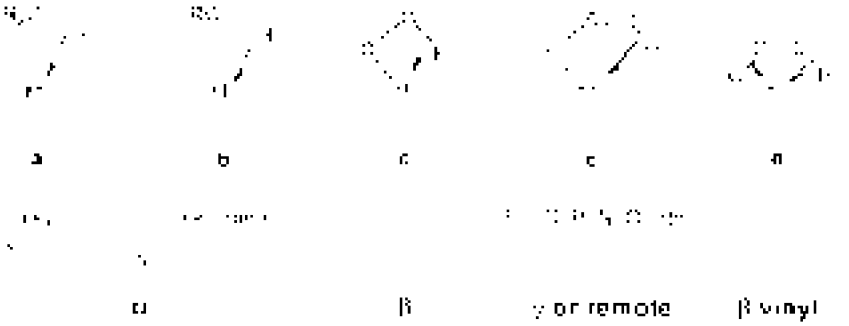

Scheme 1 The several agostic bond situations as described by Kubas [3]

C, notably Si. The half arrow shows the agostic bond [3]. The β-agostic bond is by far the most common.

The concept extremely quickly became general in the organometallic community (the original J Organomet Chem paper of 1983 [1] and the following review of 1988 [2] have a total of 1500 citations) and was soon used to describe other sorts of complexes. For instance, the intermolecular complex of an alkane with a transition metal fragment in which the alkane is bonded via one or several C-H bonds was considered sometimes as containing agostic C-H bonds. In this case again, does the word agostic describe a common geometrical situation (with a C-H in proximity of a metal centre) and/or also a bonding situation? In an alkane complex, the C-H bond is no longer part of a coordinated ligand so this is not agostic by the original definition. Kubas writes in his book: "The term *agostic* should not be used when describing external ligand binding solely through a σ bond, which is

better referred to as a *σ complex* [3]." This difference cannot be neglected since it may lead to different interactions. For example, while a C-F bond of a ligand can interact with the metal centre, there is no reported fluoroalkane complex of transition metal despite evidence for weak interactions [17, 18]. Although the distinction between *σ* complex and agostic complex is clear, we will still present some systems that qualify as *σ* complexes. The reasons are that the agostic interactions at work in species like **d** or **e** (Scheme 1) are close to those in *σ* adducts, so that the distinction is somewhat artificial.

The agostic bond was also recognized as giving crucial information on the making or breaking of the bond in the coordination sphere of the metal centre. It has been viewed as an arrested structure on the reaction path for bond cleavage. This was especially illustrated for the oxidative addition of a C-H bond by a trajectory for the reaction M+C-H to give C-M-H derived from a series of structures of agostic complexes [19]. The relation between the *β*-agostic bond and the olefin insertion into M-H or the reverse C-H *β*-elimination process is also fully apparent. Depending on the metal nature, the *β*-agostic ethyl structure or the olefin hydride complex has been observed [20–22]. For instance, the Co^{III} complex represented below has an ethyl group with a *β*-agostic interaction, whereas the corresponding Fe^{II} and Rh^{III} complexes (see below) prefer the hydrido olefin structure. This facile transformation is of key importance in the polymerization reactions.

HF studies of $Pd(PH_3)(H)(C_2H_5)$, $Pd(PH_3)(H)_2(C_2H_4)$, and of the transition state in between, show the relation between the agostic structure and the *β*-elimination reaction [23]. Replacing CH_2CH_3 by CH_2CHF_2 or Pd by Ni disfavours the agostic interaction and also raises the energy of the barrier for *β*-elimination. The shape of the LUMO of the ethyl complex shows a mixing of the metal d and C-H bonding orbitals, consistent with a donation of the *β* C-H bond into an empty metal orbital.

Hence also the interest in finding agostic bonds without H atom such as C-C and Si-C bonds. Very few examples of agostic C-C bonds are known [24–26] but many examples of agostic Si-C bond have been established especially with the early transition metals [27–31].

This is another case where we must ask if the same word truly describes the same bonding situation? From the very beginning, quite different bonding situations seem to have been included in the same concept. This was understandable in the early days when the interaction was considered from a purely structural standpoint, but subsequent theoretical studies have clearly shown that a variety of different bonding types can occur within this class of compounds.

1.2
Focus and Limitations of this Review

The existence of an M···H-C agostic interaction is mostly established by structural and spectroscopic techniques [1, 2]. For structural determinations, X-ray and neutron diffractions are both used but each technique suffers from some limitations: the hydrogen cannot be accurately located with X-ray diffraction whereas neutron diffraction studies require a large crystal as well as access to a neutron source. For these reasons, NMR measurements have been considered as the most useful probes for establishing the existence of the agostic interaction especially in the case of a C-H bond. The most characteristic feature of an M···H-C agostic interaction is the low value of $^{1}J_{C\text{-}H}$ due to the reduced bond order in the (3c-2e) system and the resultant elongated C-H bond. The theoretical calculations, which have an obvious role to play, are the focus of this chapter. Theoretical calculations can be used for determining geometries and also to discuss the nature of the interactions between atoms. The earliest studies have been carried out with the Extended Hückel Theory (EHT). After a few studies at the Hartree-Fock (HF) level, most advances have been obtained with elaborate methods. The DFT method, which includes some of the correlation energy, has been mostly used because of the size of the molecules to compute. Calculations have supported the existence of agostic interactions suggested by experimental studies, have shown their occurrence as short-lived intermediates during reactions involving bond activation, and have studied how the agostic bond influences the overall process (notably in C-H bond activation and in polymerisation reactions). Calculations have also been used to analyse the nature of the interaction. We will essentially focus on the first and last aspects (existence and nature of the interaction) but will cite some key papers for the reactivity properties. Because the agostic interaction is a weak interaction, it is very sensitive to the nature of the molecular species, and can be promoted or hindered by many factors. The computational studies have also been useful to sort out how weak interactions compete or cooperate with the agostic interaction in organometallic complexes.

2
The C-H Agostic Interaction, from Early Studies to Recent Interpretations

Ab initio HF calculations and EHT studies were successful in supporting the existence of the agostic interaction but suggested that the agostic interaction may not only be due to a C-H donor-metal acceptor interaction. The nature of the C-H agostic interaction, and more particularly the β C-H interaction, was then studied in great detail with DFT calculations and analysis of the topology of the electron density. The peculiar nature of the interaction, in comparison to the classical donor-acceptor picture, was highlighted.

2.1 The α-Agostic Interaction

The first EHT study has been carried out in the group of R. Hoffmann [32]. It concerned the α-agostic alkylidene tantalum complexes synthesized in the group of R. Schrock. These alkylidene complexes in which the metal centre is invariably unsaturated (less than 18e around the metal) display some strong distortion, characterized by a pivoting of the alkylidene group CHR to decrease the M-C-H angle (down to 78°) and to increase the M-C-R angle (up to 170°) keeping the H-C-R angle close to its normal value.

The experimental system **1** was modelled by $TaH_4CH_2^{3-}$, **2**. The EHT calculations show a preference for CH_2 to pivot in the Ta-HCH equatorial plane so that doubly occupied σ_{CH_2} orbital (HOMO of CH_2 in its singlet state) is not along the Ta-C direction. The MO analysis shows that the pivoting decreases the main bonding interaction between σ_{CH_2} and the LUMO $d_{x^2-z^2}$ of TaH_4^{3-}, **3a**, but turns on a new bonding interaction with the next higher (LUMO+1) empty metal orbital (mainly d_{xz}), **3b**. The reason why σ_{CH_2} interacts with the (LUMO+1) empty orbital at the expense of loosing some interaction with the LUMO is that d_{xz} is strongly hybridised toward the CH_2 group unlike the LUMO. Thus the overlap compensates for the difference in energy between these two empty metal orbitals and favours the distortion.

At this point, one could wonder if there is any interaction between the C-H bond and the metal centre as proposed by Brookhart and Green? The calculations show a weakening of the C-H bond associated with a decrease of the C-H overlap population. The weakening of the bond follows the decrease in the experimental $^1J_{C\text{-}H}$ value. The M···H-C interaction is possible because the molecular orbital centred on the C-H bond overlaps with d_{xz} in the distorted structure (**3c**) and this interaction transfers some electron density away from the C-H bond to the metal orbital. However, the contribution of this interaction to the overall energy stabilization is small because the energy of the C-H bonding orbital is deep and thus far from that of d_{xz}.

Several key conclusions have been established in this seminal paper. The α-agostic interaction in this alkylidene complex is built more on a change in the electronic structure of the Ta-C bond than on a Ta···H-C bonding interaction because the HOMO of CH_2, which can interact with the empty metal orbitals in the agostic structure, is carbon based and not C-H based. However, the calculations cannot give quantitative information on the relative contributions to these two interactions to the total energy stabilization associated with the agostic structure. The weakening of the C-H bond could be suggestive of a facile H transfer of H from C to Ta. This reaction does not occur experimentally and the EHT calculations rationalize this fact by a Walsh diagram, which shows that the H transfer would induce a forbidden crossing of occupied and empty molecular orbitals.

The authors also extended their study to a hypothetical CH_3 complex and showed that it would also have an acute Ta-C-H angle, signature for the α-agostic interaction. In this case, the carbon based HOMO of CH_3^- would be the key orbital to interact with the metal centre.

These studies suggest that the α-agostic complex corresponds to the best interaction between the frontier orbitals of the organic ligand and the metal fragment. This means that the metal fragment could favour or disfavour the distortion depending on the energy and shape of its unoccupied frontier orbitals. This has been illustrated by another set of EHT calculations on hexa- and tetra-coordinated Ti^{IV} complexes [33]. The surprising result is that an α-agostic interaction is observed in $Ti(dmpe)Cl_3(CH_3)$, **4**, but not in $TiCl_3(CH_3)$, **5**. In **4**, neutron diffraction studies show that the methyl group is tilted such the Ti-C-H angle is equal to 93.5° [34]. Neutron diffraction data is not available for **5** but X-ray diffraction suggested that the CH_3 group is flattened with all Ti-C-H angles equal to 101° [35]. There are two ways to do the electron counting in these complexes but none of them give a rationale for the observed structure. If one neglects the d_π/p_π interactions between Ti and Cl, complex **4** is a 12e system and **5** is a 8e complex. In this case, an agostic interaction, if driven solely by unsaturation at the transition metal centre, should have existed in **5** like in **4**. If one includes the π-donating properties of Cl, both complexes can be viewed as 18e systems and none of these complexes should be agostic.

EHT calculations and MO analysis on $TiH_5(CH_3)^{2-}$, **6**, and $TiH_3(CH_3)$, **7**, models for **4** and **5** gave an interpretation that generalizes the results found for the alkylidene complex **2**. The pivoting of CH_3, which decreases the Ti-C-H angle while keeping the H-C-H angles, was found to be energetically favourable in **6** but not in **7**. In **6**, the σ_{CH_2} orbital, HOMO of CH_3^-, interacts only with an empty orbital of TiH_5^- of cylindrical symmetry (d_{z^2} type) if the local C_3 axis of CH_3 is along the Ti-C direction as in **8a**. If the local C_3 axis of CH_3 is pivoted as in **8b**, the HOMO of CH_3^- overlaps with the empty metal orbital d_{xz}. Because d_{xz} is empty and at lower energy than d_{z^2}, the pivoting allows the HOMO of CH_3^- to interact more efficiently with the metal frag-

ment. In accord with this interpretation, the pivoting of CH_3^- in the model system $Ti(H)_2Cl_3(CH_3)^{2-}$ is found to occur in the xz plane, which contains only one Cl and not in the yz plane, which contains two Cl. The d_{xz} orbital is at lower energy than d_{yz} because of the greater destabilizing effect of the two Cl lone pairs mixing in an out-of phase manner in the later orbital. This agrees with the experimental structure.

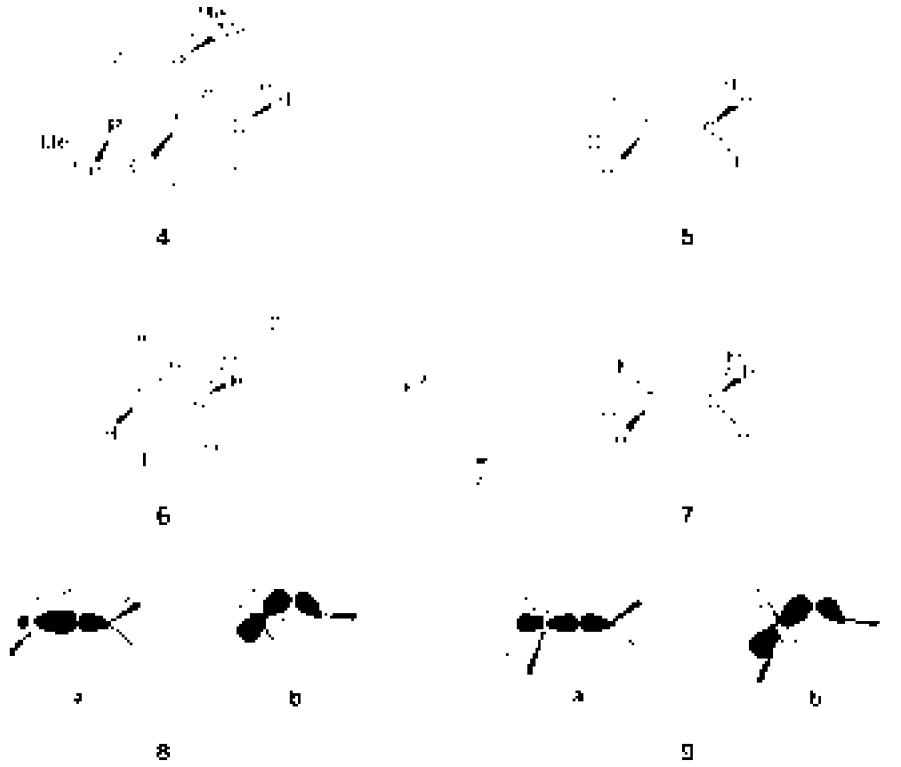

In the case of $TiH_3(CH_3)$, the HOMO of CH_3^- interacts with an orbital of *a* symmetry if the local C_3 axis of CH_3 is along the Ti-C direction (**9a**). If the CH_3 group is pivoted, the HOMO of CH_3^- interacts with one member of the *e* set of orbitals (**9b**). However, the *e* and *a* metal orbitals are at almost the same energy. Furthermore the overlap of the HOMO of CH_3^- with the *a* orbital is larger than with the *e* orbital. Therefore, the interaction of CH_3^- and the TiH_3^+ groups does not increase upon pivoting. There is no driving force for stabilizing a structure with one acute Ti-C-H angle, indicating the presence of an α-agostic interaction. In further studies, it has been proposed that the flattening of the CH_3 group is a consequence of donation of electron density associated with the C-H bonds to the empty d orbitals on the metal. The unusual positive value for $^2J_{H\text{-}H}$=11.27 Hz was interpreted by EHT calculations [36].

The messages that emerged from these studies on the α-agostic interaction are i) that electron deficient metal is a necessary but not sufficient condition, ii) a direct metal···C-H interaction is not found to be at the origin of the observed distortions of these alkylidene or alkyl complexes, iii) a reorganisation of the M-C bond associated with a stronger total interaction between the frontier orbitals of the metal and organic fragments is found to determine the pivoting of the organic group, signature for the α-agostic interaction, iv) the M···H-C interaction is not absent in these systems but appears to be a small effect. The α-agostic interaction is thus better viewed as mainly a second-order Jahn-Teller distortion of the overall complex and not only as donor-acceptor C-H···M interaction.

An ab-initio Hartree Fock (HF) geometry optimisation of $Ti(PH_3)_2X_2Y(CH_3)$ (Y coplanar with Ti-C-H) reproduces reasonably well the experimental structure of **4**, as measured by the Ti-C-H angle [37, 38]. For X=Y=Cl, Ti-C-H is calculated to be 99° to compare to the experimental value of 93.5° from neutron diffraction. Replacement of Cl by H is found to increase the Ti-C-H angle. A plot of occupied molecular orbitals shows a mixing of the metal d and C-H bonding orbital in support of an M···H-C interaction.

2.2 The β-Agostic Interaction

EHT calculations have been carried out to analyse the β-agostic interaction in $Ti(dmpe)Cl_3(C_2H_5)$, **10a** [39]. The X-ray structure shows an acute Ti-C_α-C_β angle of 85.9° and a C_α-C_β distance of 1.463 Å, shorter than the average single C-C bond of 1.54 Å [40]. This structure was redetermined at low temperature (105 K) by X-ray diffraction [41] without the problems of pronounced disorder in the structure from the earlier report. Here the Ti-C_α-C_β valence angle at 84.6° is acute, the C_α-C_β bond distance is 1.501 Å, and the Ti···C_β distance at only 2.501 Å is strikingly short, confirming the β-agostic interaction.

EHT calculations are not appropriate for a quantitative optimisation of structure and therefore no quantitative geometrical parameters should be considered. The key results from this study are that the β-agostic interaction is found to be favourable and to involve a reorganisation of the M-C bond similar to that highlighted for the methyl complex **4**. The M···H-C direct interaction seems to play a role. An opening of the angles at the metal centre is necessary for allowing H-C to approach M and this requires a significant distortion of the hexacoordinated complex away from the octahedral geometry. While such distortion is energetically unfavourable for d^6 ML_6 complex, this work shows that any distortion away from the octahedral geometry is favourable for a d^0 ML_6 complex in the presence of non-π-donor ligands (dmpe, C_2H_5). It is shown that the angular distortion around the metal

Table 1 Comparison between selected geometrical parameters of the experimental structure of $EtTi(Cl)_3(dmpe)$, **10a** [41], the HF optimized structures for $EtTi(Cl)_2H(PH_3)_2$, **10b** [42], and the DFT optimized structure for $EtTi(Cl)_3(dhpe)$, **10c** [43]. Bond distances are in Å and angle in degree

	10a	**10b**	**10c**
Ti-C_α	2.147	2.093	2.170
Ti...C_β	2.501		2.549
C_α-C_β	1.501	1.547	1.517
C_β-H_β	1.03	1.114	1.130
$TiC_\alpha C_\beta$	84.6	88.8	85.5

and the agostic interaction are strongly correlated and that both contribute to a stronger interaction between the metal and the organic ligand. In this system again, the contribution of the M···H-C interaction to the total energy stabilization, although not null, does not seem to be the leading parameter.

The optimised geometries with self-consistent field methods can be compared to the experimental structures obtained from X-ray diffraction studies (Table 1). An ab-initio HF geometry optimisation of $Ti(PH_3)_2(Cl)_2H(C_2H_5)$ (**10b**) gave metric parameters in good support of a β-agostic interaction and reasonably close to the experimental values for **10a** [42]. The geometry of $Ti(C_2H_5)(PH_3)_2(X)_2Y$ is sensitive to the nature of X and Y (Y is coplanar to Ti-C_2H_5). Electronegative groups X favour the agostic interaction, consistent with the lesser electronic density at Ti. No agostic interaction is found for X=Y=H. It should be pointed out that the influence of X and Y on the agostic interaction in the methyl and ethyl complexes is different in the EHT and ab-initio calculations. Comparing X=Y=H and X=Y=Cl, Cl favours the agostic interaction whereas the reverse applies in the EHT calculations. This comes from the fact that the electronegative Cl lowers the energy of the d orbitals, and such an effect is not present in the EHT calculations. In contrast, in an EHT calculation, Cl raises the energy of the d orbitals through d_π/p_π mixing.

The presence of a β-agostic interaction in **10a** was later confirmed by DFT calculations (BPW91) on the model complex $EtTi(Cl)_3(H_2PCH_2CH_2PH_2)$ (**10c**) [43]. The calculated geometrical parameters were in excellent agreement with the experimental structure determined by X-ray crystallography (Table 1) [41].

The HOMO of **10c**, represented schematically below, corresponds essentially to the Ti-C_α σ bond with a secondary bonding interaction between the C_β-H_β bond and the torus of the d_{z^2} orbital. This observation has led Scherer et al. to propose the description of the β C-H agostic bond as resulting from a delocalization of the *two electrons* of the HOMO on the $TiC_\alpha C_\beta$ group. Stabilization of the Ti-C_α bond appears therefore to be the major driving force in the development of the β-agostic interaction. Accordingly, the phenome-

non is best described as essentially a two-electron process involving only a *single* orbital on the metal [44].

The canting of the ethyl group is essential to achieve the stabilizing interaction between C_β-H_β and the metal centre. Hence the molecular structure of $EtTiCl_3$, **11**, determined by gas-phase electron diffraction (GED), showed no agostic interaction [41]. DFT calculations on **11** reproduced the experimental geometry and indicated that the larger Ti-C_α-C_β angle (84.6° in **10a** vs 116° in **11**) is associated with a C_β-$H_\beta \cdots$Ti antibonding interaction in the HOMO of **11**. The driving force for the β-agostic interaction in the d^0 octahedral complex **10a** is the ease of deformation of the geometry to cant the ethyl chain so as to achieve the delocalization. The d^0 tetrahedral complex **11** is shown to be more rigid, thus preventing the β-agostic interaction.

To shed more light on the nature of the β-agostic interaction, Scherer et al. have varied the nature of the metal (Ti, Zr, V, Nb) and the number of Cl ligands yielding three- and four-coordinated d^0 or d^1 complexes [43]. The β-agostic behaviour appears in practice to require that the valence shell of the metal be unsaturated with VE$\leq$16. It is most prone to occur when the metal is three-coordinated, being seldom encountered in four- and six-coordinated systems, and unknown in five-coordinated systems. It remains to be seen how far the conclusions reached by these authors regarding the nature of β-agostic bonding are applicable to α-, γ-, and other types of agostic interaction and also to late transition-metal systems.

More generally, the agostic interaction is usually described as a donor-acceptor interaction between the bonding electron of the C-H bond and a vacant site on the metal. However, sometimes it is not clear which atoms are bonded and to what extend they are bonded. This information is lacking in Lewis structures. To answer such questions, a more modern theory that enables one to extract chemical bonds from a computed wavefunction is warranted. A prime candidate theory to fulfil this purpose is the "atoms in molecule" (AIM) theory as developed by Bader [45].

Popelier and Logethetis were the first to apply the AIM theory to the study of the nature of the agostic interaction [46]. They analysed the topology of the charge density (computed at the HF, BLYP, and MP2 levels) for $CH_3TiCl_2^+$ (**12a**), $C_2H_5TiCl_2^+$ (**12b**), and $C_3H_7TiCl_2^+$ (**12c**).

12a exhibits an α-agostic interaction as illustrated by the tilting of the CH_3 group (H_α-C_α-Ti=89.9°, BLYP). However, no bond critical point (BCP) is found between H_α and Ti. The topological properties of the density of **12a** do not allow a clear and definitive picture of the α-agostic interaction to be drawn.

The β-agostic interaction in **12b** is structurally characterized by the acute Ti-C_α-C_β angle (84.9°, BLYP) and the long C_β-H_β bond distance (1.145 Å, BLYP). Topologically, there is a BCP between H_β and Ti, and *not* between Ti and the BCP of C_β-H_β. The latter would have been expected for the classical picture of the C-H bond interacting with the metal. The Ti···H_β BCP is close to the ring critical point (RCP) associated with the $TiC_\alpha C_\beta H_\beta$ fragment and its ellipticity ϵ is very large (1.173, BLYP), indicating a possible structural instability [45]. The bond path between Ti and H_β is particularly curved toward the RCP, implying that the accumulation of electron density along the bond path is shifted toward C_β. The situation is very similar for the γ-agostic interaction in **12c**.

The topology of the density exhibited by β- and γ-agostic interactions in **12b** and **12c** are in favour of a direct bonding interaction between Ti and the hydrogen atom (H_β or H_γ). However, the corresponding BCP is structurally instable and may be absent in other agostic systems. In addition, Popelier and Logethetis have shown that the topological properties of the agostic bond are different from those expected for a hydrogen bond. Consequently an agostic bond should not be confused with a conventional hydrogen bond.

The AIM theory was also used to discuss the β-agostic interaction in Et-$Ti(Cl)_3$(dmpe), **10a**, using the experimental and theoretical densities [47]. Interestingly, both the experimental and the calculated densities gave the same molecular graphs with the same number of BCP and RCP. A BCP between H_β and Ti was found (Fig. 1) and was close to the RCP. The electron densities corresponding to the Ti···H_β BCP and the RCP inside the $TiC_\alpha C_\beta H_\beta$ fragment are nearly identical. The BCP almost merge into a singularity in ρ, a phenomenon characteristic of bond fission. A further characteristic of the agostic interaction manifests itself in the gradient vector map $\nabla\rho(\mathbf{r})$ in a significant curvature of the Ti-C_α bond path (Fig. 1). The bond path is a curve joining two atoms along which the electron density is accumulated with respect to the neighbourhood, but minimal at the BCP along the path. The bond path is usually a straight line between the two atoms un-

Fig. 1 **a** Calculated gradient vector field $\nabla\rho(\mathbf{r})$. Bond critical points (CP) are denoted by *open circles* and the ring CP by *a filled circle*; nuclei on the molecular plane are denoted by a *plus sign* while the projections of the out-of-plane nuclei are denoted by a *division sign*. Inside the $TiC_\alpha C_\beta H_\beta$ four-membered ring all gradient paths originate at the (3,+1) ring CP and terminate either at the nuclei or at a (3,−1) bond CP (*dashed lines*). The gradient vectors linking the (3,−1) bond CP with the atoms constitute the bond paths (*thick lines*). **b** Bond paths in the $TiC_\alpha C_\beta H_\beta$ fragment based on experimental charge densities. **c** Experimental–$\nabla^2\rho(\mathbf{r})$ function in the $TiC_\alpha C_\beta H_\beta$ plane (negative values are marked by *broken lines*). Taken from [47]

less the electron density is influenced significantly by interactions with other atoms. In the present case, the curvature of the Ti-C_α bond path is observed for **10a**, **12b**, and **12c**. The non-linearity of the Ti-C_α bond probably offers a more robust criterion for β-agostic interaction.

Although AIM theory speaks in favour of a bonding interaction associated with an agostic interaction, the classical picture of a donating C-H bond to a vacant site on the metal is not supported. More studies are needed, particularly on late transition metal complexes, to explore further the topological properties of the agostic interaction.

3
The Agostic C-H Bond with a Non-Transition Metal Centre

The agostic bond was first seen in transition metal complexes but there is no reason that this should be limited to this class of atoms. The prerequisite for observing an agostic interaction is to have an electron deficient centre. It is not possible to give a comprehensive list and we limit ourselves to some recent references. Alkali and alkaline earth cations such as Li [48, 49], K, Ca [50] but also Al and B [51] entail C-H agostic interactions. At the limit of the transition metal series, naked Cu^+ is also an obvious excellent candidate [52, 53]. Finally one should not forget the ethyl cation **13a** and all non-classical cations where the bridged structure **13b** is probably the earliest example of an agostic interaction [54].

13a 13b

In the case of alkyl- and alkylsilyl-lithium complexes, a study of the topology of the electron density has been carried out, giving an interesting point of view on the agostic interaction [49]. An AIM analysis reveals a delocalisation of the Li-C bonding electrons within the organic ligand. It is shown that the Li···H contacts in Li-CH_2-CH_3 are a consequence of this delocalisation and that further secondary interactions, like Li···H-C interactions, play only a minor role. The interesting aspect of this approach is that the rationale extends immediately to alkylsilyl-lithium complexes. An X-ray structure of $[(2\text{-}(Me_3Si)_2CLi(C_5H_4N))_2]$ and DFT calculations of Li-CH_2-SiH_2Me show that Si-C_γ is 0.2 Å longer than C_α-Si and, that the Li-C_α-Si angle is significantly reduced. These features are shown to result from a combination of delocalisation of the Li-C_α bonding electrons along the alkyl fragment and additional secondary interactions signalled by Li···Si, Li···C_γ, and Li···H contacts. In particular, these last interactions are responsible for the *cis* conformational preference of the complex (Me toward Li). We will discuss more complexes with Si-C_γ bonds in the section on Si-C agostic interactions.

4
X-H Agostic Bonds with X Different from C

All types of X-H agostic bonds have been analysed with computational methods. However, it is not really possible to make a valid comparison between the several types of agostic bonds because of the lack of experimental data in which a given metal fragment can interact with various types of bonds. For this reason, the comparisons between the various agostic bonds, when possible, is only qualitative.

4.1
The B-H Agostic Bond

The B-H agostic bond has been reported in few large systems [2, 55] and the computational studies of B-H agostic bond with elaborate methods are therefore rather recent. In a Ru^{II} scorpionate complex, the B-H bond of the pyrazolyl borate is found to be at the empty coordination site of the metal centre [56]. The calculated Ru···B and Ru···H are found to be close to the experimental values despite the fact that the calculated complex has considerably less steric hindrance than the real system (the influence of the steric hindrance will be discussed later). These distances indicate that B and H are

both close to the metal centre (Ru-B exp=2.849 Å, calc=2.900 Å; Ru···H exp=2.07 Å, calc=1.969 Å) as also indicated by a B-H···Ru angle of 125°. It is therefore interesting to find that the calculated overlap population shows the presence of a bonding interaction only between Ru and H (Ru···B has a negative overlap population). Short distances may not always imply that a bonding interaction exists [57].

Several borane complexes have been studied by computational methods [58–60]. These complexes can be either considered as being σ adducts or as having α-agostic B-H bonds. Species like **14**, which has been found as minimum on the potential energy surface by MP2 calculations, does not correspond to an existing compound but displays some of the bonding characteristics of systems observed experimentally. The geometry of **14** is unusual: BH_3 is not planar and the complex seems to be a planar M-BH_2 unit with H bridging the M-B bond. The bonding differs substantially from that in other σ complexes. Donation from the B-H bond to M occurs, but unlike for most other σ complexes, back bonding from Os does not go into $\sigma^*_{B\text{-}H}$ but goes to a boron p_π orbital that is non-bonding with the bridging H atom. Such back donation cannot cleave the B-H bond. It would be interesting to analyse further the differences and analogies between the α-agostic CH_3 complex and this BH_3 complex.

14

The complex, **15a**, model for the titanium complex **15b**, where the ligand is a catecholborane has been calculated by MP2 calculations. As in **14**, the Ti-BO_2 moiety is planar and H bridges the Ti-B bond. The electron delocalization in the complex illustrated by **14c**, creates an unusual three centres bonding in the B-Ti-B triangle [59, 60]. In the case of much longer distance between H and the boryl group, another geometrical pattern has been recently obtained for [$(PR_3)_2$RhHCl(Boryl)] (Boryl=Bpin, Bcat). These complexes have been studied by X-ray and neutron diffraction and by DFT calculations [61]. In these complexes, a weak H···B interaction has been evidenced. The boryl group has two possible orientations depending on the exact nature of the surrounding ligands: it is either perpendicular to the plane containing Rh, H and B (and is thus similar to the previously described complexes) or it is coplanar with Rh, H and B. In the later case, it is suggest-

ed that the $\sigma^*_{BO_2}$ orbital participate to the bonding with the hydride. This later orientation is observed when steric hindrance disfavours the other one.

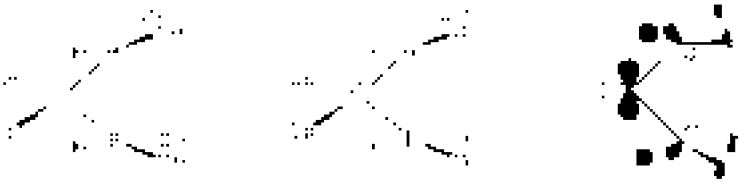

15a 15b 15c

The tendency for a σ-borane coordinated to a metal fragment to create an additional bond to B results in the formation of a coordinated dihydroborate in presence of a hydride ligand [62]. This leads naturally to the consideration of BH_4^- complexes: they are σ adducts and not agostic systems and calculations show the mode of coordination varying from η^1 to η^3 [58, 63, 64].

4.2
The Si-H Agostic Bond

Several reviews on silane organometallic chemistry have been written, both on experimental [65–67] and theoretical aspects [68]. The agostic Si-H bond has been shown in early [69–88] and late [89–96] transition metal complexes in a wide variety of situations. The Si-H bond is a better candidate for an agostic interaction than C-H because it is more polarisable and the H is more hydridic. Computational studies confirm the presence of an M···H-Si interaction in various systems. A recent review summarizes the computational studies up to 2002 [68]. It is interesting to include the σ complexes. For instance the two hexacoordinated d^6 complexes, **16** (characterized by X-ray [97]) and **17** (characterized by NMR [98]), probably have similar electronic M···Si-H interactions although no calculations have yet been carried out to test this. The difference between the two complexes could thus be mostly due to the fact that the Si-H bond is forced to remain in close vicinity to the metal in **16** because the alkene does not dissociate easily. This factor (essentially entropic) allows the experimental observation of weaker interactions.

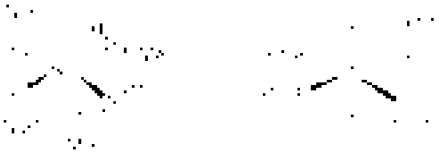

16 17

Lin showed that many complexes are consistent with the Si-H bond acting as an electron donor to the metal via $\sigma_{Si\text{-}H}$ and as an electron acceptor via $\sigma^*_{Si\text{-}H}$. The $\sigma_{Si\text{-}H}$ orbital is higher in energy than the $\sigma_{C\text{-}H}$ and the $\sigma^*_{Si\text{-}H}$ is lower in energy than the $\sigma^*_{C\text{-}H}$, so Si-H acts as a better ligand than C-H to a metal by being both a stronger Lewis base and a stronger Lewis acid. The Ru^{II} complex containing two Si-H bonds in a chelating ligand, **18**, is illustrative of the interactions at work. Computational studies have been carried out by Lin [68, 94] and Marsden, Barthelat et al. [92] independently. In this complex the two Si-H bonds would take a *trans* coordination if the complex remains octahedral. However a distortion occurs, which puts the two Si-H in a pseudo *cis* coordination, and allows optimal back donation from the occupied d orbitals into the two $\sigma^*_{Si\text{-}H}$ orbitals. It has been proven, by optimising the real system as well as a model in which the two Si-H bonds are not part of a chelating group (**19**), that the observed distortion in the experimental complex is not induced by the chelating group. Whereas, the need for optimal back bonding is clearly an important parameter, one should not neglect the fact that the two Si-H ligands, which have a weak *trans* influence do not like to be *trans* to each other. This also favours the observed distortion.

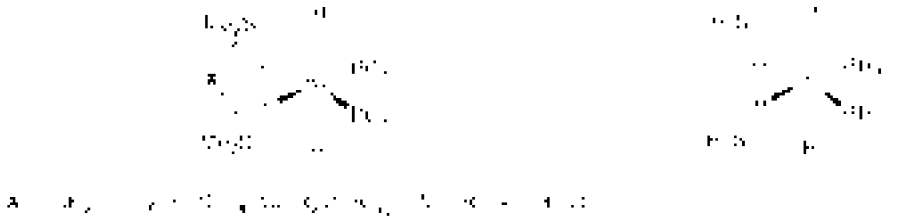

18 **19**

In cases where there is no back donation possible from the metal centre, such as in the d^0 ansa lanthanocene-$N(SiHMe_2)_2$ complex, **20**, β-agostic Si-H bonds have also been observed and calculated by DFT [72–74]. The calculations reproduce the experimental data well especially when Me groups are present on the silyl group. The nature of the La···H-Si interaction has been analysed. The attraction is found to be dominated by an electrostatic attraction. The covalent part is small and the 4f orbitals play no role in the bonding. The Si-H bonds are strongly polarized and weakened by the positively charge La centre. The interaction energy is estimated to be as high as 8 kcal mol^{-1}, which causes an unusual opening of the Si-N-Si angle. This illustrates that a Si-H bond engages in rather strong agostic interaction. The strength of the Si-H agostic interaction has even resulted in artefacts in some calculations. Thus, it proved inaccurate to use $La(N(SiH_3)_2)_3$ as a model for $La(N(SiMe_3)_2)_3$. The presence of three Si-H bonds, which do not exist in

$La(N(SiMe_3)_2)_3$ modifies the geometry of the coordination sphere at La [99]. In contrast, the calculations of the full experimental system give a geometry in very good agreement with the experimental data (see below).

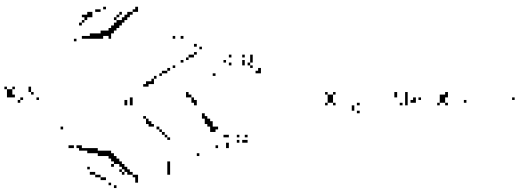

20

The propensity of the SiR_2H group to promote M···H-Si bonding is also illustrated in a study of a 14e T-shape $Pt(PH_2\text{-}C_2H_4\text{-}PH_2)(SiHR_2)^+$ complex where R=H, Me, SiH_3, Cl, OR, and NMe_2 [96]. An unusual minimum with an H bridging a Pt-silylene bond (Pt-Si-H=80°) has been found in the case of the SiH_3 group in addition to another structure, which has the traditional agostic Si-H bond (Pt-Si-H=94°). In contrast to the case of the CH_3 complex (also studied in this work) where the traditional agostic structure and the hydrido-carbene complex each correspond to minima, no hydrido-silylene complex is found as a minimum. When R is different from H, R is found to be at the bridging position in preference to H. An analysis of the electronic density by the AIM theory confirms the presence a ring critical point, not seen in the case of a C-H α-agostic interaction.

Nikonov, on one hand, and Sabo-Etienne and Chaudret on the other have shown independently the existence of an interesting secondary bonding interaction(s) named either IHI for "interligand hypervalent interaction" or Si-SHA for "silicon secondary hydrogen attraction" between the silyl group and a nearby hydride. This interaction originates from the remarkable ability of silicon to become hypervalent. The following examples are an illustration of this. In $RuH_2(H_2)L_2(SiHX_3)$ (L=PCy_3), **21**, the Si-H bond of $SiHX_3$ is significantly elongated while the distance between Si and the two hydrides is shorter than the sum of the vdW radii [93]. In this complex Si is close to six atoms, a situation which has precedents in silicon chemistry [100, 101]. The elongation of the Si-H bond can be rationalized by the donation of the Ru d orbital in $\sigma^*_{Si\text{-}H}$ but there is most probably an enhancement of the elongation due to the additional Si···H interaction with the hydride ligands. Is there an agostic interaction in this complex? Strictly speaking, $RuH_2(H_2)L_2(SiHX_3)$ is an 18e complex with a coordinated silane which according to Kubas should not qualify as an agostic complex. However, the close contacts between the nearby hydrides and Si can transfer some density to Si. This leaves the metal as electron deficient and one can thus consider that the shortest Si-H bond compensates this electron deficiency.

21

The Si···H interaction occurs in a wide variety of systems with one or two silyl groups such as **22** and **23** [79–85, 102, 103]. In the most general case, only one hydride is involved and the silicon centre is surrounded by five groups, a classical hypervalent situation for silicon [100, 101]. The presence of electron withdrawing atoms such as Cl on Si shortens the Si···H distance as shown by MP2 calculations on **22** [103] and DFT calculations on **23** [80], which agrees with the greater tendency of Si to become hypervalent in the presence of electronegative atoms.

22 23 24

It has been pointed out that the calculated Si···H distance is very sensitive to the nature of the modelling [80]. This dependence is probably associated with the relative weakness of the interaction which is thus challenging to reproduce. A related difficulty had been noticed in the case of stretched dihydrogen complex [13]. The recent characterisation of a stable hypervalent Si dihydride stabilized by the presence of K^+(18crown6) [104] and systems like $RuH_3(SiCl_2Me)(PPh_3)_3$, **24** [105], which has three non-classical Ru-H···Si interactions, further supports the proposal of IHI and Si-SHA and illustrate the generality of the Si···H attractive interaction [106]. The same interaction appears in some germyl complexes [102]. These interactions give unusual fluxional [107] and spectroscopic (notably NMR) properties to the complexes [85, 108, 109]. It has even been generalized to Si···Si interaction [110–113]. It is unclear if one should consider complex **25** as having agostic Si-H bond or not but the very unusual structure and bonding pattern deserves mention [114]. In this complex, the SiH_4 is coordinated to two metal centres and serves as both electron donor and electron acceptor towards each metal.

The unusual aspect of it is that the back-donation from one metal occurs into the Si-H bonds that act as σ-donors to the other metal.

25

In conclusion, one can look at the silyl hydride complexes in a number of ways, either as coordinated silane with a very elongated Si···H bond or as complexes of hypervalent silicon moieties with an agostic Si-H bond [109]. It should be pointed out that the ability of Si to become hypervalent in the vicinity of a transition metal fragment has some important consequence on the reactivity of silane derivative in metathesis reaction with lanthanide complexes [115].

5
X-Y Agostic with Y Different from H

5.1
The C-C Agostic Interaction

Because of the relationship between the agostic interaction and the cleavage and formation of bonds, the C-C agostic interaction is especially desired but is unfortunately very rare. In most cases where an alkyl chain is near a metal centre, a C-H agostic bond is established in preference to any other case. The CH_3 group shields the C-C bond from the metal centre resulting in a C-H bond being in general more accessible to the metal than a C-C bond. To our knowledge there are three reports of an agostic C-C bond. The first system describes an unusual electrophilic 14e titanium centre in an environment that is shielded sterically from both C-H bond and external coordinating agents, such that the metal can only make additional contacts with the accompanying C-C single bonded framework [116]. DFT calculations confirm the bonding situation between Ti and C. However further studies show the absence of a Ti···C-C contact (no bond critical point) [117]. The second system concerns a quinonoid type complex for which the X-ray structure shows well the C-C in proximity to a Rh centre [24] but no calculations have been carried out. The third system is a cyclopropyl complex $Tp^{Me2}NbCl(c\text{-}C_3H_5)(MeCCMe)$ [25, 26]. The crystal structure of this cyclopropyl complex reveals the presence of an elongated C-C bond. QM/MM(ONIOM) calculations have addressed the competition between the β C-H and α C-C agostic interactions. The α C-C agostic interaction is found to be preferred and test calculations

changing the steric bulk in the complex reveal that the preference for the α C-C agostic is of electronic origin. This is attributed to the fact that the C-C bond of the cyclopropyl group is not a normal C-C bond. Whilst the HOMO of propane has a dominant C-H bonding character, the corresponding orbital in cyclopropane is localised between the carbon centres and the orbital with dominant C-H character lies some 2 eV lower in energy. Thus although the preferred conformation places both the α C-C and β C-H bonds close to the agostic bonding position, the unusually high energy of the C-C σ orbitals in the cyclopropyl ligand dictates the preference for the C-C, rather than the C-H, agostic structure. These results suggest that a normal C-C bond may not be a good candidate for an agostic interaction. This suggests also that steric hindrance and geometrical constraint could be involved in the agostic C-C bond in the quinoid Rh complex [24], although the C-C bond is part of an *n*-alkyl chain.

5.2 The Si-C Agostic Interaction

It has been observed that the Si-C bond β to the metal centre is unusually long in early transition metal complexes and mostly in lanthanide and some uranide complexes of $CH(SiMe_3)_2$ [28, 118–120] and $N(SiMe_3)_2$ [27, 121–129]. Similar effects have also been reported in $Cr(CH(SiMe_3)_2)_3$ [130] and $In(CH(SiMe_3)_2)_3$ [131] and have been inferred in $[Mg(CH(SiMe_3)_2)_2]_\infty$ [132]. For instance, in $La(CH(SiMe_3)_2)_3$ the long Si-C bond is 1.92 Å and the short one is 1.89 Å [119]. The elongated Si-C bond is invariably that closest to the metal, the M-C-Si angle is smaller (e.g. 102°) than the usual tetrahedral angle; similarly the M-N-Si is smaller than that in an amido coordinated ligand (see, for instance, [27]). All these facts point towards an agostic Si-C bond. It is interesting that in these complexes the γ C-H bonds, whilst not so far from the metal centre, seem unaffected.

Apart from the early calculation at the HF level on a Pd complex with an alkenyl complex containing a β Si-C bond [118], the computational studies of these complexes are recent due to the large size of the species and to the presence of lanthanide metal centre. The calculations have been carried out using DFT (B3LYP) [28, 30, 31] and QM/MM(ONIOM (B3PW91/UFF)) [29, 133] approaches. All calculations well reproduce the experimental data and the results improve when a more complete model, closer to the experimental systems, is used. Since the QM/MM and DFT calculations give similar results, this shows that some of the substituents such as the Me groups not involved in the agostic interaction, play only a steric role (see more about this problem later). Studies of several models show the exclusive elongation of the bond β to the metal and closest to it regardless of the nature of the bond, i.e. Si-C, Si-H or C-C. A C-C bond would be relatively less elongated than a

Si-H or Si-C bond. Furthermore, no elongation of a γ C-H bond is noticed even for the C-H bond closest to the metal centre.

Two slightly different interpretations have been offered in the case of LnX_3 (X=$CH(SiMe_3)_2$ or $N(SiMe_3)_2$). The divergence arises from the way the bond between the lanthanide and the ligand is considered. All workers agree that the M-X bond has a large ionic component and that the covalent part is based on the high lying empty d orbitals and not on the f orbitals. All workers also agree that the non planar shape of LnX_3 is due to the participation in Ln-X bonding of the d Ln orbitals. Two sets of authors [28, 30, 31] consider that the empty d orbitals are also responsible for the Si-C agostic interaction and thus propose an interpretation following that of Brookhart and Green. The electron density of the Si-C bond is partially donated to the empty metal d orbitals. The other interpretation is based on the very large ionic character of the Ln-X bond. The calculated NBO charge is 2.3 for LnR_3 (R=alkyl), which is close to the formal charge derived from the oxidation number and the additional electron density is mostly in the d orbitals. Much larger differences between the calculated and formal charge are found in d transition metal chemistry [133]. The ionic nature of the Ln-X bond puts the two electrons of the M-X bond mostly on X. The two electrons located on the atom coordinated to the metal centre are thus delocalised through the organic ligand. This delocalisation is well known in organic chemistry and has been called "negative hyperconjugation" [134]. It occurs when electrons located in a high lying orbital are stabilized by the proper combination of σ^* orbitals of the neighbouring bonds (**26a**). This in turn lengthens the bonds involved in the delocalization. In the case of $CH(SiMe_3)_2^-$, the two electrons located on the carbanion are delocalised on all $\sigma^*_{Si\text{-}C}$ which lengthen all β Si-C bonds (**26b**). The delocalization is more efficient than in a C-C bond because $\sigma^*_{Si\text{-}C}$ is lower in energy than $\sigma^*_{C\text{-}C}$. The metal plays a role through an electrostatic interaction by lowering more the energy of orbitals located on atoms nearest to it. This makes the $\sigma^*_{Si\text{-}C}$ orbital closest to the metal, the most efficient to delocalise the electrons of the carbanion. It is thus the one to lengthen the most (**26c**). This interpretation is consistent with the lesser Si-C elongation in the case of the $N(SiMe_3)_2$ group. A more electronegative N tends to delocalise its electrons into the β Si-C bonds to a lesser extent. The presence of delocalisation has been supported by photoelectron spectroscopy [135]. The interpretation is closely related to that published at almost the same time on the alkyl-lithium complexes [49].

It is not really possible to choose between the two interpretations. They both rationalize the geometrical pattern well. The classical interpretation (electron density transferred to the metal) has the advantage of using d orbitals that are also used to rationalize the pyramidal geometry of LnX_3. It does not explain well why the γ C-H bond are so unaffected but it has the advantage of following "Occam's razor". Delocalization within the ligand is consistent with the earlier work on the α-agostic interaction. It is also consistent with the fact that the presence of a bond critical point between the

metal and the β bond has been found to be very sensitive to the nature of the complex and thus not to be the leading factor in β-agostic interaction, at least in the case of alkali (Li) [49], early transition metal [43, 44, 46, 47], and lanthanide complexes. It also accounts for the fact that there is no need of real contact between the metal and the elongated bond. This explains that the Si-C bond can be elongated even if the CH_3 groups of the trimethyl silyl group shield the σ Si-C electrons. The reality is probably a combination of the two effects.

26a 26b 26c

5.3
X-Y Agostic with Y Bearing Lone Pairs

In their initial discussion of the concept of the agostic bond, Brookhart and Green included bonds between C-X (X=halide) and a metal because they viewed them as examples of a 3c-4e C-X-M interaction. In consequence, some authors still use this terminology for C-X-M interactions. Other authors have considered that the C-X σ bond is not involved, however, and state that these species are not agostic [7]. Although further studies are needed, it is reasonable at present to say that X acts as an electron donor via its lone pair and involve less the electrons of the C-X bond (**27**) because the electrons of the X lone pair are more accessible and also at higher energy than those of the C-X bond. In this case, the C-X bond behaves like a true dihapto ligand with two *strong* bonding interactions (M-X and M-C), and a classical Lewis structure (**27**) can be written. For instance this distinction is clearly used in a paper discussing the competition between dihapto acyl and β C-H agostic interactions [136]. To argue about whether an interaction should be considered "to be or not to be" agostic could be viewed as pointless. Despite the wide diversity of agostic interactions and despite the appeal of the word, we think that it is worth limiting the term "agostic" to cases of X-Y bonds in which none of the atoms X or Y carries additional lone pairs and the X-Y σ bond is exclusively implicated in forming the new bond in question.

27

6
The High Sensitivity of the C-H Agostic Interaction to the Nature of the Molecule

The agostic interaction is a weak interaction, that can be perturbed by small changes inside the organometallic complexes or the experimental conditions. A σ bond and notably a C-H bond is a very poor Lewis base and therefore essentially any ligand acts as a stronger base than C-H and should thus displace an agostic bond. Agostic interactions are thus observed in non-coordinating solvents.

6.1
The Energetic Magnitude of the Agostic Interaction

Experimental determination of the binding energy of an agostic interaction has not been achieved and only approximate values are proposed. The reason is that one cannot observe a complex such as $W(CO)_3(PCy_3)_2$ without the agostic interaction ([3] chap. 7). An approximate binding energy of 10–15 kcal mol^{-1} is proposed based on the bond dissociation enthalpy determined by photoacoustic calorimetry for heptane binding to $W(CO)_5$ [137, 138]. Computations can also estimate in an approximate manner the energy of an agostic bond because the reference point with no agostic interaction is not precisely defined and because other parameters come into play [43, 44]. Take the β-agostic C-H interaction shown in **28a**. One could propose that **28b** has no β-agostic C-H bond. However, some interaction between M and both H_2 and H_3 cannot be excluded. Further, the alkyl chain has gone from an eclipsed conformation to the intrinsically more stable staggered conformation. The difference in energies between **28a** and **28b**, which is a composite of all these changes, is however used to evaluate the energy of the agostic interaction [43]. The agostic interaction energy ranges from very weak to usually no more than 10 kcal mol^{-1}. It is not possible to cite here the extremely large number of systems that have been calculated. We report the reader to the reviews written in 2000 for the special issue on Computational Transition Metal Chemistry in Chemical Review. The paper by Niu and Hall gives references to many works where agostic interactions have been seen (see for instance studies of olefin insertion, polymerization) [139].

We would like to highlight two pieces of work: one that addresses the role of the metal and the other one that addresses the electronic role of coordinated ligands.

A DFT study of the β-hydride and methyl migratory insertion in $CpM(PH_3)(CH_2CH_2)R^+$ (M=Co, Rh, Ir; R=H, CH_3) shows that the strength of the β-agostic interaction decreases down the cobalt triad [140]. This trend has been established by comparing the energy of the β-agostic complex with that of the α-agostic complex where the agostic interaction is weak. The β-agostic interaction is especially strong for cobalt. The M···H-C agostic bond is thus primarily established by donation of charge from the occupied $\sigma_{C\text{-}H}$ orbital to an empty d-based orbital on the metal. According to normal ligand field arguments, the destabilization increases from 3d to 5d. Thus cobalt has the most suitable acceptor orbital and the strongest β-agostic bond.

Another trend arises from the comparison of the neutral and cationic complexes $Ru(PH_3)_2(X)(H)(C_2H_5)^{q+}$ (X=Cl, q=0: X=CO, q=1). The β C-H agostic interaction is estimated to be around 7 kcal mol^{-1} in the case of the cationic complex with X=CO and 12 kcal mol^{-1} for the neutral complex with X=Cl [141]. The more elongated C-H bond in the later system is in agreement with the stronger interaction. In the agostic complex X is essentially *trans* to the agostic bond. Therefore the stronger agostic interaction in the case of X=Cl could be due to the small *trans* influence of Cl, which increases the $\sigma_{C\text{-}H}$ to Ru donation and the larger back donation M to $\sigma^*_{C\text{-}H}$ associated with the lone pairs on Cl. It is interesting that the back donation seems to play no important role in the comparison Co^{III}, Rh^{III} and Ir^{III} but rationalizes well the results for the Ru^{II} complexes.

There is probably no general rule for ranking the energy of an agostic interaction. We have just seen above how Cl acting as a poor σ-donor (weak *trans* influence) and as a π donor ligand strengthens the agostic interaction compared to CO. Opposite trends arise from the study of the compounds $Tp'Ta(CHC(CH_3)_3)(X)(X')$ (X=Cl, Br; X′=Cl, OR, NMe_2), Tp′=hydrotris (3,5-dimethylpyrazolyl)borate) [142]. $Tp'Ta(CHC(CH_3)_3)(X)(X')$ have an α H-C agostic interaction from the alkylidene C-H as proven by the low $^1J_{C\text{-}H}$ values. The strength of the α-agostic interaction depends upon the ability of the remaining ligands to function as π-donors. With weak π-donor ligands (halides), a strong α-agostic interaction is observed. Stronger π-donors disfavour the α-agostic interaction. No computational studies of these species have been carried out and the results are discussed in term of a competition between the ability of the C-H bond and the ligands to give electrons to the metal centre. The stronger the π-donor, the weaker the agostic interaction, just the opposite of what has been calculated for the $Ru(PH_3)_2$ $(X)(H)(C_2H_5)^{q+}$ complexes. The coordination sphere of the metal as well as the total charge certainly play a role in the different responses to the nature of the coordinated ligands towards agostic interaction of the two family of complexes. Also to be noticed, the early HF calculations of Morokuma on the hexacoordinated Ti^{IV} complex-

es indicates that Cl favoured the agostic interaction compared to H [23, 42]. A general rule is clearly not possible.

6.2 The Steric Influence of the Ligands

The key role of the steric factors has been established in the study of the 14e 4-coordinated d^6 $IrH_2L_2^+$ complex. The X-ray structure for L=P(^{t}Bu)$_2$(Ph) shows the presence of two remote C-H agostic interactions, one from a C-H bond of a ^{t}Bu group of each phosphine ligand. These two agostic interactions complete the octahedral coordination sphere around Ir. The P-C^1-C^2 angle of the agostic bond is 92°. It has been first established by calculation for L=PH_3 (**29**) that the saw horse geometry of $IrH_2L_2^+$ (piece of octahedron with two *cis* empty sites) is not due to the agostic interaction but is preferred for a diamagnetic tetracoordinated d^6 complex [143]. In the case of a paramagnetic electronic state, a planar structure has been found to be preferred for an isoelectronic complex [144]. Calculations have then been carried out for L=$PH_2(CH_2CH_3)$ (**30**). This model includes all the atoms of the coordination sphere of Ir and of the alkyl chain involved in the agostic interaction and models by H all other substituents. Even though the initial guess for the optimisation process is the experimental structure, in which the agostic C-H bonds are close to the metal, the optimisation process opens the Ir-P-C angle and moves CH_3 away from the metal centre. In the optimised structure, the bond angles at the phosphine are tetrahedral and the two alkyl chains are staggered in place of eclipsed. Clearly the energy to pay to diminish the P-C^1-C^2 angle and to eclipse the alkyl chain is not compensated by the binding energy of Ir···H-C, which is especially small because the agostic C-H would be trans to a hydride (strong trans influence). The full experimental complex (**31**) was then calculated at the QM/MM (B3LYP:MM3) level using IMOMM [145, 146]. In this calculation, the atoms calculated at the QM level are identical to that of the previous calculation for **30** but all substituents previously modelled by H are represented at the MM level and play exclusively a steric role. The geometry converges to a structure close to the experimental value. In particular the P-C^1-C^2 angle is 102° and the chain is eclipsed.

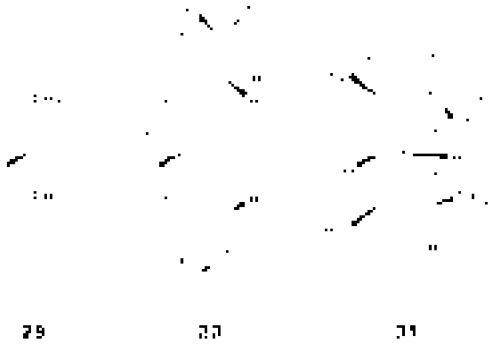

The steric hindrance of the substituents on the phosphine prevents the alkyl chain from moving away from the metal and probably even favours the eclipsed conformation. In other words the other substituents force one of the ^{t}Bu group to be in the vicinity of the metal centre. These results should be viewed in a broader context. Thorpe and Ingold have identified an influence of increasing steric bulk in R of a CR_2 group on ring formation involving this CR_2; bulky R groups, by increasing the R-C-R angle, favour the kinetics and thermodynamics of formation of rings containing the CR_2 groups, especially small rings [147]. Similarly, Shaw has elaborated a similar idea for PR_2R' ligands [148, 149]: bulky substituents R encourage ring closure [150], bridging and orthometalation when $R'=C_6H_5$ [151, 152].

The above result raises the key question: is the agostic interaction a result of the steric constraint, i.e. is the C-H bond near the metal because it is the best way to avoid the other substituents or are there some additional electronic features? A combined experimental and theoretical study has provided answers to this question. The 16e complexes $IrH_2(PR_2Ph)_3^+$, with small and large R, have been selected [153]. These complexes have one empty site *trans* to a hydride and can have a single C-H remote agostic interaction from the carbon chain of one of the phosphine ligand. When R is small (R=isopropyl), the X-ray structure shows the absence of any agostic interaction. QM/MM calculations give similar results. When R is large (R=cyclohexyl), the X-ray structure shows the presence of one agostic interaction from the cyclohexyl group. Two QM/MM calculations have been carried out. In one set of calculations, all substituents of the phosphine ligands have been represented at the MM level and only atoms directly bonded to Ir have been represented at the QM level. At such a level, the substituent position is set by the steric hindrance but there is no possible electronic interaction between C-H and the electron deficient metal centre because there is no electron density in the C-H bonds. Starting the optimisation process from the X-ray structure, the calculations give a structure that is very close to the experimental results but with a longer Ir···C distance (3.17 Å vs 2.92 Å). In the following set of calculations, the carbon backbone carrying the C-H agostic bond is introduced at the QM level. This introduces the possibility of electronic attraction between the weakly donating C-H bond and the empty Ir site. Optimisation of geometry gives essentially the experimental structure with an Ir···C distance even slightly shorter than the experimental value (2.88 Å vs 2.92 Å). This shows that the steric effects encourage the agostic interaction. It also shows that small changes (such as changing cyclohexyl to isopropyl) have remarkably large consequences on the optimal structure of the molecule because the overall structure is the result of a number of competing small interactions. Other examples of this competition will be described further in this section.

Steric factors are not mandatory for the agostic interactions as evidenced from the numerous examples deprived of any apparent steric strain. However, they can be instrumental in a number of subtle ways. As an example, in

an isopropyl tris(pyrazolyl)boratoniobium complex, the interplay between electronic and steric effects account for the rarely observed equilibrium between α- and β-agostic C-H interaction (Eq. 1) [154, 155]. The steric hindrance around the metal caused by the methyl group on the Tp group as well as by the alkyne ligand limits the conformational possibilities for the R group and increases the rotational barriers. For this reason, NMR evaluation of the difference in energy between the two types of agostic interactions was possible. The β-agostic complex has been found to be more stable in agreement with the general preference for the β-agostic bond compared to the α-agostic. However, the difference in free energy between the β- and α-agostic complexes at 193 K is only 2.2 kJ mol^{-1}. The QM/MM (IMOMM) calculations reproduce remarkably well the very small difference in energy between the two species (the computed difference in energy of 9 kJ mol^{-1} is compared to ΔH_0=7.4 to 9.7 kJ mol^{-1} depending upon the nature of the far remote substituent on the Tp^{Me2} group). Furthermore also in agreement with the experimental evidence, replacing the ^{i}Pr group by an ethyl shows only the presence of one minimum corresponding to the α-agostic complex. Whereas, the excellent agreement between experimental and calculated values is fortuitous, this illustrates the present power of the computational methods.

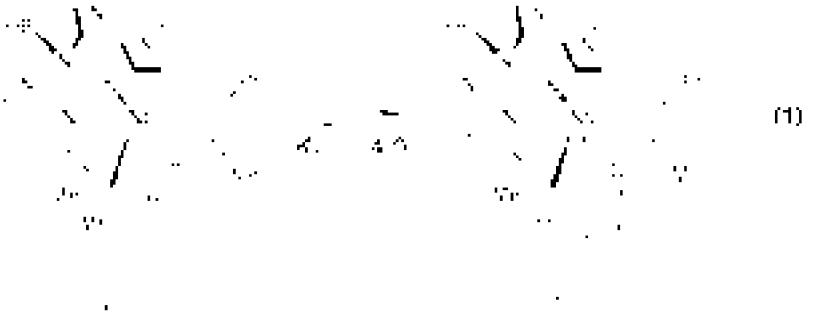

(1)

6.3
The Agostic Interaction: One Weak Interaction Among Other Ones

In the absence of severe steric hindrance among the ligands and, if electronic effects do not prevent the interaction, an agostic interaction is expected when a C-H bond can come geometrically in the vicinity of the metal empty coordination site. For these reasons, the following sets of observations have been puzzling [156]. A remote agostic Ir···H-C interaction is observed from the ^{t}Bu group in **32** (L=PPh_3) as shown by X-ray diffraction and NMR results. However when the ^{t}Bu group is replaced by an ^{i}Pr group, this interaction disappears (**33**, L=PPh_3). QM/MM (ONIOM) calculations have offered a

rational for this unexpected result. A first set of calculations at the full DFT level in which the calculated molecule differs from the experimental molecule by the replacement of L=PPh_3 by L=PH_3 reproduces well the geometrical features of **32.**

32 **33** **34**

Similar calculations done on **33** (L=PH_3) and **34** (L=PH_3) shows the presence of two minima. It also shows that the anagostic structure **33** is less stable than the agostic structure **34** by only 0.7 kcal mol^{-1} and such a discrepancy could be viewed as intrinsic to the accuracy of the calculations. However, QM/MM (ONIOM) calculations including the Ph groups of the PPh_3 ligands in the MM part reveal an unexpected result. The anagostic structure **33** (L=PPh_3) becomes more stable than the agostic species **34** (L=PPh_3) by 3.2 kcal mol^{-1}. Close examination of the geometries of the two minima reveal the presence of a efficient π-stacking between one Ph group of each phosphine and the benzoquinoleate (bq) ligand in **33** as shown in **35**, and less efficient π-stacking in the agostic structure **34** (see **36**). Furthermore the π-stacking found in **33** is identical to that which is observed in the bq-^{t}Bu complex **32**. This shows a competition between weak forces (π-stacking and agostic interaction) in this set of molecules. The best compromise in this case is not the agostic complex.

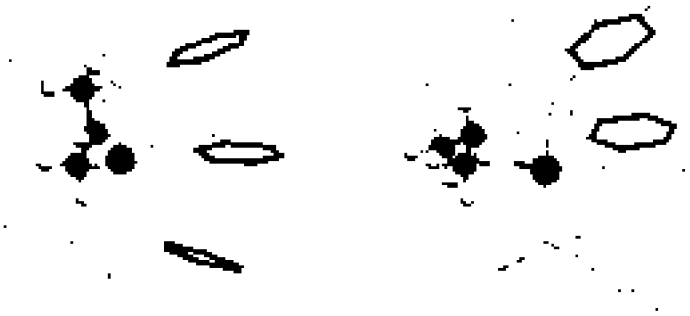

36 **35**

7 Conclusions

While there is probably rarely much ambiguity in an experimental determination of an agostic bond for a chemical system by using a combination of structural and spectroscopic information, the physical reasons for its occurrence are far from fully understood. One can at least distinguish several contributing factors.

A ligand with an agostic bond should be viewed as a dihapto ligand with a strong bond to the metal (main point of coordination) and also a weak bond, the agostic bond. With this in mind, one might expect that any factors that affect the η^1- vs η^2-character of a potentially chelating, hemilabile ligand will similarly affect a potentially agostic ligand. There are some requirements for the ligand and some for the metal fragment. The dihapto coordination of the agostic ligand requires a rather flexible ligand because geometrical distortions are needed to bring the agostic bond into the vicinity of the metal centre. Some bond angles should be able to take small values even ones far from their equilibrium values. The organic chain should be able to fold which may introduce several eclipsed-eclipsed interactions. These deformations and conformations are all energetically demanding. On the metal fragment side, the metal should have either empty coordination sites or should be able to distort at a low energy cost to accommodate the agostic bond. The ability to distort is high for certain electron counts and certain coordination numbers. For instance, the octahedral geometry is sterically unfavourable for entry of a seventh ligand but the d^0 ML_6 hexacoordinated complex naturally moves away from the octahedral structure especially in absence of strong π-donor ligands. In contrast, the tetracoordinated d^0 ML_4 complex seems to be always unfavourable for the agostic interaction.

The origin of the agostic interaction has been the object of some debate. Is the donation of the H-C bonding pair to the metal the main driving force for the agostic interaction? The case is far from being so simple. We have seen that the agostic interaction can modify the energy of the main anchoring bond of the ligand. We have discussed delocalization within the ligand. We have seen some bond formation between the metal and H with the help of the AIM analysis. Remarkably we have never mentioned the formation of a bond between the centre of the C-H bond and the metal centre but we have seen a bonding pattern involving the metal and the entire organic ligand in a cyclic bonding in the case of some β-agostic complexes, in agreement with the idea of delocalisation. This proves that there is probably through-bond and through-space bonding taking place. There are not yet enough systematic studies of all possible situations to be able to evaluate the relative importance of the two types of bonding as a function of the metal centre. In particular the delocalisation has been studied for early transition complexes where the M-X bond is very ionic, which probably enhances the delocalisa-

tion within the organic ligand. It should decrease for late transition metal complexes due to the increased covalent character of the M-X bond but no quantitative studies have been carried out in such systems. We have just been informed of further studies with AIM method for the β-agostic interaction [157].

The angular distortion is especially drastic in the α-agostic interaction. For this reason, it is more rarely found and depends very strongly on the coordination number at the metal because the agostic bond significantly modifies the main bond between the metal and the ligand carrying the agostic interaction. In fact, calculations indicate that the occurrence of the α-agostic interaction may be determine by the reorganisation of the M-C_α bond.

The delocalisation of the lone pair electrons is not very efficient in a saturated organic ligand and is limited to the bonds β to the lone pair. For this reason, the remote agostic interaction is probably mostly due to the traditional through-space interaction between the ligand and the metal.

The agostic interaction is invariably weak and although its energy cannot be accurately defined, a qualitative estimate shows that its maximum value is around 10 kcal mol^{-1} with probably very few exceptions towards higher values. The agostic interaction can thus be hampered by other conflicting interactions. We are all aware that any ligand could displace an agostic interaction and coordinate to the metal. Less obvious are some subtle interactions within the unsaturated complex such as the ligand-ligand attractive interaction. It is clear that other cases will be discovered. The agostic interaction is also favoured when the ligand is forced to stay in the vicinity of the metal centre. Steric hindrance has been found to be very efficient contributors to the agostic interaction by preventing the organic ligand to move away from the metal centre and by enforcing its folding and small bond angles in such a way that a σ bond is within reach of the empty metal coordination site. Calculations have however shown that an electronic interaction between the agostic bond and the deficient metal centre persists. After completion of this manuscript, a review on the agostic interactions in d^0 metal alkyl complexes has appeared [158]. A very recent paper combining experimental studies (structural and Database analysis) and DFT calculations shows the interesting possibility of a γ M$\cdots\eta^3$ H_2-C (in place of the usual M$\cdots\eta^2$ H-C) interaction in a Ru^{11} complex [159].

There is still much more to understand in this remarkably useful and general concept.

Acknowledgements Part of the work presented here has resulted from long-term collaborations between the authors and a number of experimental and computational chemists throughout the world, as well as from the work of previous and present co-workers. It is our pleasure to thank R.A. Andersen (Berkeley), M. Besora (UA Barcelona), R. Bosque (Barcelona), K.G. Caulton (Indiana), R.H. Crabtree (Yale), E.R. Davidson (Indiana), H. Gérard (Paris VI), Y. Jean (Paris-Sud, Ecole Polytechnique), M.F. Lappert (Sussex), A.

Lledós (UA Barcelona), F. Maseras (Tarragona), J.E. McGrady (York), M. Etienne (LCC CNRS, Toulouse), L. Perrin (Montpellier 2), L. Maron (Paul Sabatier, Toulouse), G. Ujaque (UA Barcelona).

References

1. Brookhart M, Green MLH (1983) J Organomet Chem 250:395
2. Brookhart M, Green MLH, Wong LL (1988) Prog Inorg Chem 36:1
3. Kubas GJ (2001) Metal dihydrogen and σ-bond complexes: structure, theory and reactivity. Kluwer Academic Publishers, New York
4. Kubas GJ (1988) Acc Chem Res 21:120
5. Crabtree RH (1990) Acc Chem Res 23:95
6. Crabtree RH, Hamilton DG (1988) Adv Organomet Chem 28:299
7. Crabtree RH (1993) Angew Chem Int Ed Engl 32:785
8. Jessop PG, Morris RH (1992) Coord Chem Rev 121:155
9. Heinekey DM, Oldham WJ Jr (1993) Chem Rev 93:913
10. Sabo-Etienne S, Chaudret B (1998) Coord Chem Rev 178/180:381
11. Hall C, Perutz RN (1996) Chem Rev 96:3125
12. Shilov AE, Shul'pin GB (1997) Chem Rev 97:2879
13. Maseras F, Lledós A, Clot E, Eisenstein O (2000) Chem Rev 100:601
14. Gao Y, Eisenstein O, Crabtree RH (1997) Inorg Chim Acta 254:105
15. Desideraju GR (1997) Organometallics 16:1846
16. Brammer L (2003) J Chem Soc Dalton Trans 3145
17. Bonneau R, Kelly JM (1980) J Am Chem Soc 102:1220
18. Kelly JM, Long C, Bonneau R (1983) J Phys Chem 87:3344
19. Crabtree RH, Holt EM, Lavin M, Morehouse SM (1985) Inorg Chem 24:1986
20. Green MLH, Wong LL (1987) J Chem Soc Dalton Trans 411
21. Crackness RB, Orpen AG, Spencer JL (1984) J Chem Soc Chem Commun 326
22. Werner H, Feser R (1979) Angew Chem Int Ed Engl 18:157
23. Koga N, Obara S, Kitaura K, Morokuma K (1985) J Am Chem Soc 107:7109
24. Vigalok A, Milstein D (2001) Acc Chem Res 34:798
25. Jaffart J, Etienne M, Reinhold M, McGrady JE, Maseras F (2003) Chem Commun 876
26. Jaffart J, Cole ML, Etienne M, Reinhold M, McGrady JE, Maseras F (2003) J Chem Soc Dalton Trans 4057
27. Andersen RA, Templeton DH, Zalkin A (1978) Inorg Chem 17:2317
28. Klooster WT, Brammer L, Schaverien CJ, Budzelaar PHM (1999) J Am Chem Soc 121:1381
29. Perrin L, Maron L, Eisenstein O, Lappert MF (2003) New J Chem 121
30. Clark DL, Gordon JC, Hay PJ, Martin RL, Poli R (2002) Organometallics 21:5000
31. Brady DE, Clark DL, Gordon JC, Hay PJ, Keogh DW, Poli R, Scott BL, Watkin JG (2003) Inorg Chem 42:6682
32. Goddard RJ, Hoffmann R, Jemmis ED (1985) J Am Chem Soc 102:7667
33. Eisenstein O, Jean Y (1985) J Am Chem Soc 107:1177
34. Dawoodi Z, Green MLH, Mtetwa VSB, Prout K (1982) J Chem Soc Chem Commun 1410
35. Dawoodi Z, Green MLH, Mtetwa VSB, Prout K (1982) J Chem Soc Chem Commun 802
36. Green JC, Payne MP (1987) Magn Reson Chem 25:544

37. Obara S, Koga N, Morokuma K (1984) J Organometal Chem 270:C33
38. Morokuma K, Ohta K, Koga N, Obara S, Davidson ER (1984) Farad Symp 19:49
39. Demolliens A, Jean Y, Eisenstein O (1986) Organometallics 5:1457
40. Dawoodi Z, Green MLH, Mtetwa VSB, Prout K, Schultz AJ, Williams JM, Koetzle TF (1986) J Chem Soc Dalton Trans 1629
41. Scherer W, Priermeier T, Haaland A, Volden HV, McGrady GS, Downs AJ, Boese R, Bläser D (1998) Organometallics 17:4406
42. Koga N, Obara S, Morokuma K (1984) J Am Chem Soc 106:4626
43. Haaland A, Scherer W, Ruud K, McGrady GS, Downs AJ, Swang O (1998) J Am Chem Soc 120:3762
44. McGrady GS, Downs AJ (2000) Coord Chem Rev 197:95
45. Bader RFW (1990) Atoms in molecules: a quantum theory. Clarendon Press, Oxford
46. Popelier PL, Logothetis G (1998) J Organomet Chem 555:101
47. Scherer W, Hieringer W, Spiegler M, Sirsch P, McGrady GS, Downs AJ, Haaland A, Pederson B (1998) Chem Commun 2471
48. Nakamoto M, Fukawa T, Lee VY, Sekiguchi A (2002) J Am Chem Soc 124:15160
49. Scherer W, Sirsch P, Shorokhov D, McGrady GS, Mason SA, Gardiner MG (2002) Chem Eur J 8:2324
50. Feil F, Harder S (2000) Organometallics 19:5010
51. Demachy I, Volatron F (1998) Eur J Inorg Chem 1015
52. Galiano L, Alcami M, Mó O, Yáñez M (2002) J Phys Chem A 106:9306
53. Corral F, Mó O, Yáñez M (2003) J Phys Chem A 107:1370
54. Xie Z, Bau R, Benesi A, Reed CA (1995) Organometallics 14:3933
55. Viñas C, Nuñez R, Teixidor F, Kivekäs R, Sillanpää R (1995) Organometallics 14:3952
56. Caballero A, Gomez de la Torre F, Jalon FA, Manzano BR, Rodriguez AM, Trofimenko S, Sigalas MP (2001) J Chem Soc Dalton Trans 427
57. Dunitz JD, Gavezzotti A (1999) Acc Chem Res 32:677
58. Demachy I, Esteruelas MA, Jean Y, Lledós A, Maseras F, Oro LA, Valero C, Volatron F (1996) J Am Chem Soc 118:8388
59. Lam WH, Lin Z (2000) Organometallics 19:2625
60. Hartwig JF, Muhoro CN, He X, Eisenstein O, Bosque R, Maseras F (1996) J Am Chem Soc 118:10936
61. Lam WH, Shimada S, Batsanov AS, Lin Z, Marder TB, Cowan JA, Howard JAK, Mason SA, McIntyre GJ (2003) Organometallics 22:4557
62. Montiel-Palma V, Lumbierres M, Donnadieu B, Sabo-Etienne S, Chaudret B (2002) J Am Chem Soc 124:5625
63. Esteruelas MA, Jean Y, Lledós A, Oro LA, Ruiz N, Volatron F (1994) Inorg Chem 33:3609
64. Jarid A, Lledós A, Jean Y, Volatron F (1993) Inorg Chem 32:4695
65. Corey JY, Braddock-Wilking J (1999) Chem Rev 99:175
66. Schubert (1990) Adv Organometal Chem 30:151
67. Schneider JJ (1996) Angew Chem Int Ed Engl 35:1068
68. Lin Z (2002) Chem Soc Rev 239
69. Bauer W, Schleyer PvR (1989) J Am Chem Soc 111:7191
70. Goldfuss B, Schleyer PvR, Handschub S, Hampel F, Bauer W (1997) Organometallics 16:5999
71. Braga D, Grepioni F, Biradha K, Desideraju GR (1996) J Chem Soc Dalton Trans 3925
72. Herrmann WA, Eppinger J, Spiegler M, Runte O, Anwander R (1997) Organometallics 16:1813

73. Eppinger J, Spiegler M, Hieringer W, Herrmann WA, Anwander R (2000) J Am Chem Soc 122:3080
74. Hieringer W, Eppinger J, Anwander R, Herrmann WA (2000) J Am Chem Soc 122:11983
75. Klinpel MG, Görlitzer HW, Tafilposly MT, Spiegler M, Scherer W, Anwander R (2002) J Organomet Chem 647:236
76. Ciruelo G, Cuenca T, Gómez R, Gómez-Sal P, Martín A (2001) J Chem Soc Dalton Trans 1657
77. Procopio LJ, Carroll PJ, Berry DH (1994) J Am Chem Soc 116:177
78. Nikonov GI, Kuzmina LG, Lemenovskii DA, Kotov VV (1995) J Am Chem Soc 117:10133
79. Nikonov GI, Kuzmina LG, Lemenovskii DA, Kotov VV (1996) J Am Chem Soc 118:6333
80. Nikonov GI, Mountford P, Ignatov SK, Green JC, Cooke PA, Leech MA, Kuzmina LG, Razuvaev AG, Rees NH, Blake AJ, Howard JAK, Lemenovskii DA (2001) J Chem Soc Dalton Trans 2903
81. Nikonov GI, Kuzmina LG, Vyboishchikov SF, Lemenovskii DA, Howard JAK (1999) Chem Eur J 5:2947
82. Nikonov GI, Mountford P, Green JC, Cooke PA, Leech MA, Blake AJ, Howard JAK, Lemenovskii DA (2000) Eur J Inorg Chem 1917
83. Nikonov GI, Kuzmina LG, Howard JAK (2002) J Chem Soc Dalton Trans 3037
84. Nikonov GI, Mountford P, Dubberley SR (2003) Inorg Chem 42:258
85. Dubberley SR, Ignatov SK, Rees NH, Razuvaev AG, Mountford P, Nikonov GI (2003) J Am Chem Soc 125:642
86. Ichiche M, Sekiguchi A, Takahashi M, Sakurai H (1999) Bull Chem Soc Jpn 72:1905
87. Peulecke N, Ohff A, Kosse P, Tillack A, Spannenberg A, Anke R, Baumann W, Burlakov VV, Rosenthal U (1998) Chem Eur J 4:1852
88. Rees WS Jr, Just O, Schumann H, Weiman R (1996) Angew Chem Int Ed. Engl 35:419
89. Schubert U, Schwarz M, Möller F (1994) Organometallics 13:1554
90. Luo XL, Kubas GJ, Jeffrey C, Burns CJ, Unkefer CJ (1994) J Am Chem Soc 116:10312
91. Butts MD, Bryan JC, Luo XL, Kubas GJ (1997) Inorg Chem 36:3341
92. Delpech F, Sabo-Etienne S, Daran JC, Chaudret B, Hussein K, Marsden CJ, Barthelat JC (1999) J Am Chem Soc 121:668
93. Hussein K, Marsden CJ, Barthelat JC, Rodriguez V, Conejero S, Sabo-Etienne S, Donnadieu B, Chaudret B (1999) Chem Commun 1315
94. Fan MF, Lin Z (1999) Organometallics 18:286
95. Choi SH, Feng J, Lin Z (2000) Organometallics 19:2051
96. Besora M, Maseras F, Lledós A, Eisenstein O (2002) Inorg Chem 41:7105
97. Delpech F, Sabo-Etienne S, Donnadieu B, Chaudret B (1998) Organometallics 17:4926
98. Luo XL, Crabtree RH (1989) J Am Chem Soc 111:2527
99. Maron L, Eisenstein O (2001) New J Chem 25:255
100. Corriu RJP, Guérin C, Henner B, Wang Q (1991) Organometallics 10:2297
101. Corriu RJP, Guérin C, Henner B, Wang Q (1991) Organometallics 10:3574
102. Nikonov GI, Churakov AV, Antipin MY (2003) Organometallics 22:2178
103. Fan MF, Lin Z (1998) Organometallics 17:1092
104. Bearpark M, McGrady GS, Prince PD, Steed JW (2001) J Am Chem Soc 123:736
105. Hübler K, Hübler U, Roper WR, Scherdtfeger P, Write LJ (1997) Chem Eur J 3:1608
106. Nikonov GI (2001) Angew Chem Int Ed Engl 40:3353

107. Atheaux I, Delpech F, Donnadieu B, Sabo-Etienne S, Chaudret B, Hussein K, Barthelat JC, Braun T, Duckett SB, Perutz RN (2002) Organometallics 21:5347
108. Bakhmutov VI, Howard JAK, Keen DA, Kuzmina LG, Leech MA, Nikonov GI, Voronstov EV, Wilson CC (2000) J Chem Soc Dalton Trans 1631
109. Nikonov GI (2003) Organometallics 22:1597
110. Chen W, Shimada S, Tanaka M (2002) Science 295:308
111. Crabtree RH (2002) Science 295:288
112. Aullón C, Lledós A, Alvarez S (2002) Angew Chem Int Ed Engl 41:1956
113. Scherer EC, Kinsinger CR, Kormos BL, Thompson JD, Kraner CJ (2002) Angew Chem Int Ed Engl 41:1953
114. Atheaux I, Donnadieu B, Rodriguez V, Sabo-Etienne S, Chaudret B, Hussein K, Barthelat JC (2000) J Am Chem Soc 122:5664
115. Perrin L, Maron L, Eisenstein O (2002) Inorg Chem 41:4355
116. Tomaszewski R, Hyla-Kryspin I, Mayne CL, Arif AM, Gleiter R, Ernst RD (1998) J Am Chem Soc 120:2959
117. Bader RFW, Matta CF (2001) Inorg Chem 40:5603
118. Koga N, Morokuma M (1988) J Am Chem Soc 110:108
119. Hitchcock PB, Lappert MF, Smith RG, Bartlett RA, Power PP (1988) J Chem Soc Chem Commun 1007
120. Niemeyer MZ (2002) Anorg Allg Chem 628:647
121. Tilley TD, Andersen RA, Zalkin A (1984) Inorg Chem 23:2271
122. Fjeldberg T, Andersen RA (1985) J Mol Struct 128:49
123. Fjeldberg T, Andersen RA (1985) J Mol Struct 129:93
124. Andersen RA, Beach DB, Jolly WL (1985) Inorg Chem 24:4741
125. Herrmann WA, Anwander R, Munck FC, Scherer W, Dufaud V, Huber NW, Artus GR (1994) Z Naturforsch B 49:1789
126. Rees WS, Just O, VanDerveer DS (1999) J Mater Chem 9:249
127. Eller PG, Bradley DC, Hursthouse MB, Meek DW (1977) Coord Chem Rev 24:1
128. Ghotra JS, Hursthouse MB, Welch AJ (1973) J Chem Soc Chem Commun 669
129. Westerhausen M, Hartmann M, Pfitzner A, Schwarz W (1995) Z Anorg Allg Chem 621:837
130. Barker GK, Lappert MF, Howard JAK (1978) J Chem Soc Dalton Trans 734
131. Carty AJ, Gynane MJS, Lappert MF, Miles SJ, Singh A, Taylor NJ (1980) Inorg Chem 19:3637
132. Hitchcock PB, Howard JAK, Lappert MF, Leung WP, Mason SA (1990) J Chem Soc Chem Commun 1116
133. Perrin L, Maron L, Eisenstein O (2003) Faraday Discuss 124:25
134. Roberts JD, Webb RL, McElhil EA (1950) J Am Chem Soc 72:408
135. Green JC, Payne M, Seddon EA, Andersen RA (1982) J Chem Soc Dalton Trans 887
136. Ujaque G, Maseras F, Lledós A, Contreras L, Pizzano A, Rodewald D, Sánchez L, Carmona E, Monge A, Ruiz C (1999) Organometallics 18:3294
137. Morse JM, Parker GH, Burkey TJ (1989) Organometallics 8:2471
138. Burkey TJ (1990) J Am Chem Soc 112:8329
139. Niu S, Hall MB (2000) Chem Rev 100:353
140. Han YZ, Deng LQ, Ziegler T (1997) J Am Chem Soc 119:5939
141. Gérard H, Clot E, Giessner-Prettre CK, Caulton KG, Davidson ER, Eisenstein O (2000) Organometallics 19:2291
142. Boncella JM, Cajigal ML, Abboud KA (1996) Organometallics 1905
143. Cooper AC, Streib WE, Eisenstein O, Caulton KG (1997) J Am Chem Soc 119:9069
144. Watson LA, Ozerov OV, Pink M, Caulton KG (2003) J Am Chem Soc 125:8426

145. Maseras F, Morokuma M (1995) J Comput Chem 16:1170
146. Maseras F (2000) Chem Commun 1821
147. Eliel EL, Wilen SH, Mander LN (1994) Stereochemistry of organic compounds. Wiley, New York, p 682
148. Shaw BL (1975) J Am Chem Soc 97:3856
149. Shaw BL (1980) J Organomet Chem 200:307
150. Al-Salen NA, Empsall HD, Markham R, Shaw BL, Weeks B (1979) J Chem Soc Dalton Trans 1972
151. Bottomley ARH, Crocker C, Shaw BL (1983) J Organomet Chem 250:617
152. Mason R, Textor M, Al-Salen N, Shaw BL (1976) J Chem Soc Chem Commun 292
153. Cooper AC, Clot E, Maseras F, Eisenstein O, Caulton KG (1999) J Am Chem Soc 121:97
154. Jaffart J, Mathieu R, Etienne M, McGrady JE, Eisenstein O, Maseras F (1998) Chem Commun 2011
155. Jaffart J, Etienne M, Maseras F, McGrady JE, Eisenstein O (2001) J Am Chem Soc 123:6000
156. Clot E, Eisenstein O, Dubé T, Faller JW, Crabtree RH (2002) Organometallics 21:575
157. Scherer W, Sirsch P, Shorokhov DJ, Tafipolsky M, McGrady GS, Gullo E (2003) Chem Eur J 9:6057
158. Scherer W, McGrady GS (2004) Angew Chem Int Ed 43:1782
159. Barrata W, Mealli C, Herdtweck E, Ienco A, Mason SA, Rigo P (2004) J Am Chem Soc 126:15549

Structure and Bonding (2004) 113:37–69
DOI 10.1007/b97941
© Springer-Verlag Berlin Heidelberg 2004

Computational Bioinorganic Chemistry

Robert J. Deeth (✉)

Department of Chemistry, University of Warwick, Coventry, CV4 7AL, UK
r.j.deeth@warwick.ac.uk

1 Introduction . . . 38
1.1 Density Functional Theory . . . 39
1.2 Computational Methods in Bioinorganic Chemistry . . . 41

2 Active Site Chemistry . . . 42
2.1 Active Site Models: Experimental Considerations . . . 42
2.2 Active Site Models: Computational Considerations . . . 45

3 Applications . . . 46
3.1 Plastocyanin and the 'Entatic State' . . . 46
3.2 Free Radical-Containing Enzymes . . . 49
3.2.1 Class 1 RNR . . . 50
3.2.2 Co-enzyme B_{12}-Dependent Enzymes . . . 52
3.2.3 Water Oxidation in Photosystem II . . . 53
3.2.4 Galacatose Oxidase . . . 55
3.3 Iron-Containing Enzymes . . . 56
3.3.1 Heme Peroxidases . . . 56
3.3.2 Methane Monooxygenase . . . 58
3.3.3 Nitrogenase . . . 60
3.3.4 Iron-Sulfur Clusters . . . 61

4 Other Applications . . . 63
4.1 Molybdoenzymes . . . 63
4.2 Hydrogenase . . . 64

5 Summary and Future Developments . . . 65

References . . . 66

Abstract Selected examples of density functional theory applied to modelling the active site structures and mechanisms of metalloenzymes are discussed. Factors influencing the design of suitable structural models and the theoretical strategies for computing their structures, energies and properties are presented before describing the calculations on a number of redox-active enzymes containing one or more of Cu, Co, Ni, Fe and Mo.

Keywords Transition metal · Redox enzyme · Active site · Mechanism

List of Abbreviations

Ado-CH_2·	Deoxyadenosyl radical
BDE	Bond dissociation energy
CCP	Cytochrome c peroxidase
DFT	Density functional theory

ET	Electron transfer
EXAFS	Extended X-ray absorption fine structure
FeMoco	Iron molybdenum cofactor
GO	Galactose oxidase
HAT	Hydrogen atom transfer
HF	Hartree-Fock
IMOMM	Integrated molecular orbital/molecule mechanics
LDA	Local density approximation
LSD	Local spin density
MM	Molecular mechanics
MMO	Methane monooxygenase
MO	Molecular orbital
MSXα	Multiple scattering Xα
N_2ase	Nitrogenase
QM/MM	Quantum mechanics/molecular mechanics
RNR	Ribonucleotide reductase
TM	Transition metal
TS	Transition state
WOC	Water oxidising complex
XnO	Xanthine oxidase

1 Introduction

Density functional theory (DFT) has revolutionised the quantum chemical treatment of systems containing transition metal (TM) centres [1, 2]. Although this revolution is really less than 20 years old, DFT has existed in various simplified guises for much longer—most notably for TM chemists in its Xα form [3, 4].

The Xα model is an exchange-only version of DFT and its most popular implementation employed the multiple scattering theory of plane waves with respect to the so-called "muffin tin" potential. The latter assumed each atom was surrounded by a spherical potential with a constant potential outside these spheres. Within each sphere, the Slater exchange expression was multiplied by a constant, α, which was normally chosen such that the Xα atomic energy matched its corresponding Hartree-Fock value [5]. Outside the atomic spheres, a weighted average value of α was used and, if the system carried a net charge, the whole ion was encased in a Watson sphere of equal but opposite charge.

The multiple scattering Xα (MSXα) model was successfully applied to the electronic structures of a number of TM species but the model suffered from a serious drawback. The spherical averaging of the potential leads to unrealistic geometries. For example, the MSXα predicts water to be linear. Two important developments were needed before the Xα scheme would become more useful. First, shape approximations of the molecular potential had to

be replaced by more accurate treatments [6] and second, analytical expressions for the energy gradients were needed [7].

Energy gradients allowed optimal geometries to be computed automatically. However, while the Xα method gave quite good electronic structures [8–13] it gave quite poor geometric structures, even with accurate potentials, which necessitated the rapid development of improved functionals. The simplest functional is the local density approximation (LDA), which has both exchange and correlation [14] terms constructed within the uniform electron gas model. While a good starting point, the LDA suffers from a number of problems and has largely been replaced by the plethora of extended and enhanced functionals available today.

Contemporary DFT combines both the reasonable description of the electronic structures of TM compounds with excellent geometries and has rapidly supplanted the more 'traditional' Hartree-Fock approximation. Its impact is especially marked in the field of bioinorganic chemistry and this review focuses on developments and applications of DFT to TM species of biological relevance and brings together various themes in quantum bioinorganic chemistry which have themselves been recently reviewed [15–21].

Nature employs TM ions in many diverse ways but the most significant for the present purpose is to mediate redox chemistry. Hence, the coverage will be restricted to TM systems which are associated with a change in the metal's oxidation state. This admittedly subjective choice basically precludes zinc enzymes like, for example, carbonic anhydrase, and structural proteins like the zinc fingers but is further justified here in that the theoretical treatment of zinc systems is, compared to redox-active TM species, substantially easier. We will concentrate on metalloenzymes and, in particular, on the catalytic chemistry occurring at the active site.

1.1 Density Functional Theory

Some technical aspects of DFT are covered elsewhere in these volumes and more detailed treatments can be found in the literature [2, 22–24] so only a brief resume need be repeated here. The essence of the model is the density functional theorem which states that there is a unique relationship between the ground state electron density and the total energy. Thus, in principle, if the true density, ρ, is known, the exact energy $\boldsymbol{E}=E[\rho]$ can be computed. The density ρ is a function of the electronic coordinates and $\boldsymbol{E}$ is a function of ρ—i.e. E is a functional—a function of a function.

The density functional theorem states that E exists but provides no way to derive its explicit form. In particular, there is no explicit equation for the exchange/correlation term, v_{xc}, which embodies all the difficult quantum mechanical interactions between the particles in the system. We are forced

to make approximations before reaching closed expressions which can be coded up for digital computation. The usual starting approximation is based on the uniform electron gas approximation. Assuming that the electron (and nuclear) charge density is constant throughout all space, it is possible to separate the exchange/correlation potential into explicit parts. Furthermore, each part has a more or less simple dependence on the value of the electron density. For example, the exchange potential at a point in space, v_x is proportional to $\rho^{1/3}$ at that point. In this sense, the exchange is local and contrasts with the exchange expression from, say, Hartree-Fock (HF) theory where the value of the potential at a given point involves integrating over all space. The HF exchange is non-local.

The local nature of the exchange and correlation makes them easier to compute and is essentially where the computational efficiency of DFT comes from compared to, say, HF theory. The exchange potential is particularly simple to evaluate but the expressions for correlation are more complicated and rather than use them directly, accurate calculated values of the correlation energy as a function of ρ [25] have been fitted by Vosko, Wilk and Nusair [14]. The VWN treatment of correlation is commonly available in electronic structure codes and, together with the uniform electron gas exchange forms what is commonly known as the local density approximation. For paramagnetic systems where a different treatment of up-spin vs down-spin electron density is required, the LDA has been generalised to give the local spin density (LSD) approximation [26, 27].

The LDA was extensively employed to compute the properties of extended systems but applications to molecular systems met initially with some scepticism. After all, how could a model based on a uniform electron gas possibly apply to a molecule where the electron density is far from uniform? This attitude was probably exacerbated by the (incorrect) perception that the earlier Xα approach was itself an approximation to the HF model and so could not possibly be better. Given that the single determinant HF method was known to be a poor approximation for TM organometallic species [28], the LDA was not expected to fare much better. In the event, the LDA worked surprisingly well but it tends to overbind leading to too short bond lengths and too high ionisation potentials [7]. In response to this shortcoming, a wide variety of new functionals have been proposed which generally try to take into account the inhomogeneity of the electron density.

Despite much development, the 'perfect' functional has not yet been discovered but many in common use are capable of acceptably accurate results. Perhaps the most popular current functional is not a pure DFT construct at all. In an attempt to improve the accuracy of the exchange energy, Becke mixed HF exchange with pure local density exchange and empirically fitted the resulting hybrid exchange functional to give the best agreement with experimental atomisation energies, proton affinities and ionisation potentials. In conjunction with the correlation functional of Lee, Yang and Parr, the hy-

brid functional B3LYP [29–32] has become established over the last decade or so, as the de facto standard for all manner of DFT applications. No doubt this popularity is helped by the ready availability of B3LYP in widely used program systems such as Gaussian, GAMESS, Turbomole and Jaguar but more importantly, B3LYP by and large gives good results. 'Pure' functionals are less popular but, despite their apparent shortcomings—too low reaction barriers, a tendency to favour low-spin states—there are nevertheless still plenty of applications often employing the Amsterdam Density Functional, DMol and DeMon programs.

1.2 Computational Methods in Bioinorganic Chemistry

As with other areas of TM chemistry, DFT has had an enormous impact on bioinorganic systems involving TM active sites. Most workers favour the B3LYP hybrid functional but, given the various approximations inherent in any calculation, the ultimate choice of functional and basis set is secondary to a verification and validation that the particular combination you are using is suitable for the task. For example, structural accuracy may be sacrificed if the energetics remain satisfactory. Wirstam et al. [33] have successfully employed the diimine ligand system shown in Fig. 1a as a model for the heme unit, Fig. 1b. Despite the obvious geometric structure differences, the electronic structures are sufficiently close to provide similar energetic results. This serves to re-emphasise the importance of careful validation of the computational protocols prior to embarking on extensive analyses of enzymatic processes. The validation process is usually a comparison with experimental data, often on smaller but related systems. Alternatively, if one is interested, say, in the chemistry of homolytic O-H bond cleavage to generate oxygen-centred radicals, the method can be validated against much higher levels of theory which would be impractical for the subsequent study. The most convincing computational work will employ one or both of these procedures.

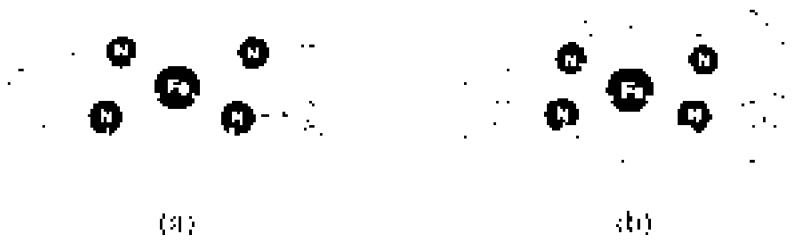

Fig. 1 **a** Cut down 'electronic' model for heme. **b** Full model for heme

2
Active Site Chemistry

Most quantum chemical modelling studies deal with active site chemistry. That is, the calculations do not really focus on how substrates and products get to and from the active site. Rather, they concentrate on the sequence of events following the arrival of substrate in the active site pocket and seek to uncover the mechanism of conversion of substrate to one or more intermediates and/or product. The obvious reason for such an approach is the assumption that the vast bulk of the protein molecule can be ignored but raises the thorny issue of whether this is a valid assumption. In practical terms, it is not possible (and arguably not desirable) to treat the entire protein quantum mechanically. Moreover, since one of the main roles of the protein is substrate selection and delivery to the active site, and since the computer modeller has explicit control over this feature, one might conclude that there is no need to consider the bulk of the protein molecule. However, the protein backbone may exert a structural influence on the active site—the entatic state [34]—while the groups around the active site produce an electrostatic field different from the in vacuo state which is the default domain of quantum chemistry. In summary, it is obviously critically important to develop a reasonable chemical model of the active site if any conclusions drawn from the calculations are to be believed.

2.1
Active Site Models: Experimental Considerations

The normal starting point for building an active site model is the single crystal X-ray structure of the relevant, or a closely related, protein or enzyme. Three types of ligating groups can be distinguished at this stage: 1) amino acid side chains, 2) cofactors such as the heme group or molybdopterin and 3) exogenous groups such as water molecules and the substrate(s). Coordination of the metal by the first two groups tends to remain largely unchanged although a side chain donor may detach and then reattach. The X-ray structure usually gives an excellent, unambiguous idea about the nature of these coordinating groups. A good example, to which we will return, is the Type I copper centre in plastocyanin (Fig. 2). The metal mediates an electron transfer process during photosynthesis and the protein has been crystallised under a variety of conditions (see, for example, [35]). Both oxidised and reduced forms have been studied and the metal remains essentially four-coordinate throughout, attached to the protein via the side chains of two histidine residues, a methionine and a cysteine.

Typically, the full amino acid is replaced by a simplified ligand which only models the metal-ligand interaction. For example, histidine is replaced by

Fig. 2 Active site structure of oxidised form of plastocyanin. The hydrogens have been removed for clarity

imidazole, cysteine by methyl thiol, tyrosine by phenol, side chains binding via carboxylate group by acetate, methionine by dimethyl sulfide and so on.

Coordination of the active site metal by water molecules and substrates is obviously much more variable and the X-ray structure may be of little assistance. In order to determine experimentally the orientation of the substrate, a crystal would need to be grown with the substrate bound. Notwithstanding the problems of obtaining X-ray quality crystals in the first place, by its very nature, the enzyme will attempt to convert the substrate to product and capturing a 'bound state' may not be possible. However, many reactions require an additional reactant—say a molecule of O_2—and thus the substrate-bound form may remain stable under anaerobic conditions. The structure of catechol dioxygenase with substrate bound has been determined in this way [36].

Although single crystal X-ray diffraction studies are considered more or less definitive depictions of the three-dimensional structure, there are significant problems both with growing crystals and with the final resolution of the data. The errors on bond lengths can be substantially larger than those for 'small molecule' systems and hydrogen atom positions can never be explicitly refined. This can lead to a certain chemical ambiguity in that the structure might suggest a metal-oxygen interaction but may not be able to distinguish between terminal metal-oxo, M=O, metal-hydroxo, M-OH or metal water, M-OH_2. Such ambiguities can usually be resolved by recourse to other experiments.

Extended X-ray absorption fine structure (EXAFS) spectroscopy is a powerful complementary technique since single crystals are not required. EXAFS gives element-specific information and has a higher resolution than single crystal diffraction albeit restricted to a range of a few Ångstroms from the

target nucleus. An illustrative example of the interplay between single crystal X-ray diffraction and EXAFS spectroscopy concerns the details of the active site of the molybdenum-containing enzyme xanthine oxidase (XnO). Single crystals of XnO were not available but the structure of the closely related enzyme, aldehyde oxidoreductase, had been solved [37]. Unfortunately, the conditions under which the crystals of the latter were grown resulted in an inactive form where the Mo=S group was replaced by a Mo=O moiety to give a five coordinate Mo(pterin)O_3. However, EXAFS data on native XnO were consistent with two sulfur atoms at about 2.34 Å, another sulfur at 2.10 Å, an oxygen at 1.75 Å and a further oxygen at 1.98 Å. These results were interpreted as being consistent with a [Mo(pterin)(S)(O)(OH_2)] or [Mo(pterin)(S)(O)(OH)]$^-$ active site. The latter was further supported by DFT calculations[38] which matched the Mo-O contact at 1.98 Å with Mo-OH rather than Mo-OH_2. The latter bond length was calculated at over 2.1 Å.

For very complicated systems, one must be cautious about over-interpreting the experimental structural data. For example, the active site of the iron molybdenum cofactor (FeMoco) in nitrogenase (N_2ase) is a large, complex iron-sulfur cluster with a Mo centre at one end (Fig. 3). An enormous amount of experimental and computational effort has been expended on this system driven, in large measure, by the structural data reported by Kim et al. in 1993 [39]. Given the enormous structural and electronic complexity of this site, a variety of proposed dinitrogen binding sites have emerged with the requisite computational support. However, in 2002, further refinement of the X-ray diffraction data apparently located an additional atom buried in the middle of the cluster [40] which calls all the previous theoretical work into question since it was based on an apparently incomplete structural model. We will return to N_2ase later.

Another issue about active site models concerns the possible roles played by groups not directly attached to the metal centre(s), and which therefore may not figure in the model built for the calculations, but which are nevertheless crucial to the activity of the enzyme. Obviously, there is a big problem if these roles are not recognised. However, in cases where, say, site directed mutagenesis experiments have revealed a critical role for some group or groups, the modeller needs to give serious consideration to how to in-

Fig. 3 Schematic representation of FeMoco cluster from nitrogenase

clude these features in his or her calculations. Several examples will be covered below.

2.2 Active Site Models: Computational Considerations

Having collected the available experimental data one tries to construct what looks like a reasonable model. Small ligands such as water or dioxygen can obviously be fully treated but many of the other ligands will have to be truncated [41]. For amino-acid side chains, there is usually an obvious choice. For example, histidine can be replaced by imidazole, methionine by dimethyl sulfide, tyrosine by phenol, cysteine by methylthiol and so on.

If additional, uncoordinated side chain groups are believed to be involved, perhaps the best solution is simply to include them from the beginning although in the absence of the entire protein, these groups need to be anchored in some way to maintain their positions relative to the complete enzyme structure. Siegbahn and co-workers have exploited this procedure to good effect on many occasions [18, 20].

More complicated cofactors such as molybdopterin and heme could, with modern powerful computers, also be modelled in their entirety. Alternatively, a physically smaller yet electronically reasonable model system can be developed like the heme replacement shown in Fig. 1.

The next vexing issue concerns how to treat the active site environment and how this might impinge on the overall charge of the model system. In gas phase calculations, the overall system charge has a large effect on molecular orbital (MO) energies. For cations, the MOs are depressed while for anions, they are elevated. This can cause substantial problems for modelling in vacuo chemical reactions which actually occur in condensed phases. For example, while a simple aquation reaction in which water replaces, say, a halide anion is a perfectly reasonable solution process, in the gas phase, the calculation may not behave properly and may not generate an X^- species irrespective of how far it is removed from the metal centre.

Another problem is for multiply charged anions which, in the gas phase, generate occupied MOs with positive energies which is physically unreasonable. In reality, such a condition should result in spontaneous ionisation but the finite extent of the basis functions does not permit an electron to escape into the ionisation continuum.

The answer to these issues is to take some account of the environment which, after all, is required for the system to be stable in the first place. The simplest computational approach is to embed the model system in a continuum dielectric with a dielectric constant chosen to simulate the environment. There has been some debate about what the effective dielectric constant for the interior of a protein should be. Based on a combination of experimental measurements and theoretical simulations [17, 42, 43] the interi-

or of a protein has a low value (2–3) while the outer aqueous solution has ϵ~80. In the absence of a full atomistic simulation of the entire protein and the solvent (where the dielectric constant used in the simulations would obviously have to be one) most authors use four as a suitable average value.

An alternative to the continuum model is to model the protein electrostatic field directly. This is normally achieved by carrying out a hybrid quantum mechanics/molecular mechanics (QM/MM) treatment in which the active site model is treated with DFT while the rest of the protein is modelled via classical molecular mechanics (MM) [44]. The MM charges then implicitly define the dielectric inside the protein. In either event, it appears that excessive charges are to be avoided. That is, the quantum mechanical part of the model system will normally not have an overall charge greater in magnitude than one.

An often critical feature of TM centres in metalloenzyme active sites is their spin states. Most biologically relevant TMs can exist in multiple oxidation states and each one can have several spin states. Iron is particularly noteworthy with both d^6 Fe^{II} and d^5 Fe^{III} each possessing three possible spin states. For mono-metal centres such as heme units, there can be the additional complication of the redox state of the porphyrin ring itself while in iron-sulfur clusters with up to four Fe centres, the possible magnetic couplings are extremely complex. Moreover, the energy differences between these various possibilities can be very small indeed which presents a significant challenge to DFT.

Finally, transition metals are heavy atoms and one should consider whether relativistic effects need to be considered [45]. In general, apart from using a relativistic effective core potential, relativity is not included for first and second-row metals but must be treated for third-row species. The relativistic effect can be broken down into three components—the Darwin correction (mass-velocity), the 'Zitterbewegung' and spin-orbit coupling. The former two are more or less straightforward to implement and capture most of the relativistic energy.

3 Applications

The aim of this section is to illustrate the main features of DFT modelling in bioinorganic systems via a number of selected examples.

3.1 Plastocyanin and the 'Entatic State'

The three-dimensional structure of plastocyanin was among the first metalloenzyme structures to be solved. Prior to this, there had been much specu-

lation as to the nature of the coordination geometry around the active site stimulated by a set of highly unusual spectroscopic properties [46].

The structure of the oxidised form showed basically a four-coordinate Cu^{II} centre bound by two histidines, a deprotonated cysteine and a methionine in a distorted tetrahedral arrangement with the $[Cu(his)_2(cys)]^+$ fragment forming a trigonal unit with an axial methionine residue weakly bound at about 2.8 Å (Fig. 2).

The active site structure of plastocyanin became an archetypal example of the 'entatic state'. The term entatic state was originally coined by Vallee and Williams [34] and brought together a number of ideas including the earlier 'rack mechanism' of Malmstrom [47].

The entatic state described the appealing proposition that the protein molecule enforces a special geometry on the metal centre designed to enhance the latter's catalytic activity. The Type I Cu centre in plastocyanin involves a redox change at the copper centre which cycles between +2 and +1 oxidation states. A typical coordination geometry for a Cu^{2+} centre is planar and this oxidation state favours N and O donors. In contrast, Cu^+ favours tetrahedral geometry and P/S donors. Since electron transport is enhanced by minimising the reorganisation energy, the optimal coordination geometry is expected to be a combination of the typical coordination requirements of both oxidation states. The actual Type I geometry is two N donors and two S donors in a distorted geometry intermediate between planar and tetrahedral and therefore appears to be perfectly designed for mediating the redox change at the copper centre. However, since the mixed donor/distorted tetrahedral structure is apparently suited to neither oxidation state, the conclusion drawn was that the protein backbone must be enforcing the structure and holding the geometry in place to facilitate the redox change, a conclusion supported by the observation that the protein structure is not significantly altered when the copper is removed. The activation energy is thereby reduced via ground state destabilisation.

This view of the entatic state of Type I copper centres held sway for two decades. However, in 1996, Ryde became interested is trying to estimate the magnitude of the entatic state energy and used DFT calculations [48]. The idea was to build reasonable models for the oxidised and reduced active sites and compare the energies of the fully relaxed structures with those constrained to be at the X-ray crystallographic coordinates. The model system was $[Cu(imidazole)_2(SMe)(SMe_2)]^{n+}$, where n=1 or 0. The unexpected result was that the DFT-optimised structure of the oxidised model system (n=1) was essentially the same as that from the experimental X-ray crystal structure and that there was little energy difference between reduced and oxidised forms. Ryde concluded that the protein does not enforce the Type I geometry. Instead, it is a natural consequence of the donors. In particular, the structure appears to be dominated by the alkyl thiolate ligand which was known to be very covalent from earlier theoretical and experimental work

from the Solomon group [49, 50]. Ryde's calculations appear to show that the role of the protein is not to enforce an unusual geometry which leads to ground state destabilisation but rather to provide a set of ligands and protection of the active site from attack. Compared to 'small molecule' copper complexes, the ligand set supplied by the protein is unusual. Alkyl thiolates are generally unstable and lead to reduction of the copper centre. Hence, the protein plays a vital role, but the calculations are not consistent with an entatic state in this instance. Ryde extended the calculations to include the whole protein [51] which, on the one hand, gave still better agreement with experimental structures and, on the other, continued to suggest the lack of an entatic state, or, as the authors put it, 'the blue copper proteins are not more strained than other metalloproteins' [51].

These conclusions are controversial. The current state of play appears to be something of a stalemate. Gray, Malstrom and Williams [35] propose that what is needed is 'a first principles calculation of a blue copper reorganisation energy that includes all inner-sphere and outer-sphere (protein and solvent) contributions'. Such a calculation is not yet possible. Moreover, there are some problems with the in vacuo theoretical models especially the axial binding in the reduced state. The X-ray structures give very much longer contacts than theory although the energetic consequences are computed to be relatively small [48]. Moreover, it is possible to modify the properties of the protein by mutating groups which are not bound to the metal and do not feature in the DFT model.

The question of the entatic state in Type I copper centres looks set to enter a new phase of controversy. Szilagyi et al. [52] have reported the 'spectroscopic calibration of DFT' which suggests a problem with calculations on copper(II) species. Experimental data on $[CuCl_4]^{2-}$ give a metal spin density of 0.62 but 'standard' DFT calculations give a much lower value, a result which appears to be independent of functional (BP86 and B3LYP were tested) or basis set. The authors conclude that the calculations overestimate the metal-ligand covalency. However, the experimental spin density can be recovered by refitting the parameters of the B3LYP functional or, in the case of the ADF program, by modifying the nuclear charge of the metal centre. In addition to getting the metal spin correct, geometries, vibrational frequencies and excited state energies are all brought into better agreement with experiment.

Using the ADF program, the present author used the same trick of modifying the Cu nuclear charge to fit the EPR g-values of the tetragonal complex $[Cu(dien)_2]^{2+}$ (dien=diethylenetriamine) [53]. In the process, the calculated d-d transition energies also came into line with experiment. Both studies begin to reveal that there may be more deep-seated problems with DFT calculations on copper systems than had been realised. They may be due to the self-interaction energy [54, 55] which might be expected to increase as the d orbitals fill towards the right side of the transition series. At the time of writing, the author was aware that the Solomon group has applied their 'retuned' B3LYP

functional to the active site models of plastocyanin used by Ryde but now the DFT optimised structures of the isolated active site models are not the same as that found experimentally in the complete protein molecule. Apparently, the protein does exert a structural entatic state influence on the metal centre.

The protein also exerts an electronic influence in that the electrostatic environment has a major effect on the reduction potential and hence the whole protein and its surrounding solvent need to be included in any calculation [56]. It is impractical to compute the entire system quantum mechanically. Instead, hybrid QM/MM methods offer the best balance between accuracy and computational efficiency.

Olsson et al. [56] advocate the frozen DFT method and have applied it to calculating the reduction potentials in plastocyanin and rusticyanin—Type I blue copper proteins which have very similar active sites but widely different reduction potentials of 375 and 680 mV respectively. The protein is divided into three regions—the copper and its immediate ligands which are treated by full DFT, an outer region where the atoms are represented by (frozen) electron densities, and finally the rest of the system where the electrostatics are represented by classical point partial charges. While this scheme gives a good description of the electrostatics and is relatively efficient, there remains the problem that a reasonable sampling of the protein conformations is necessary to get reliable free energy estimates. The authors conclude that no QM/MM method is fast enough and that we will have to rely on suitably parameterised classical schemes for the time being.

3.2
Free Radical-Containing Enzymes

Himo and Siegbahn have published a comprehensive review of quantum chemical studies of radical-containing enzymes and this section draws heavily on their work [16]. The topics involving TM active sites are listed in Table 1 although the authors also discuss metal-free systems such as glycl radicals and prostaglandin H synthase, which employ a tyrosyl radical. We will restrict ourselves to describing a few suitable examples which illustrate the main feature of quantum bioinorganic modelling.

The majority of the calculations employ the B3LYP functional which has been shown to give very satisfactory results. In many cases, the enzyme environment is described via a dielectric continuum with ϵ=4 and, with some models, certain atoms are fixed at their X-ray structure coordinates. Although the models used are quite sophisticated and have the advantage over experimental methods that short-lived species such as transition states (TSs) can be studied just as easily as longer-lived species, the authors caution that the error in calculated reaction barriers is of the order of 3–5 kcal mol^{-1}. Nevertheless, it is often possible to exploit theoretical calculations at least to dismiss energetically unreasonable mechanisms and to suggest via-

Table 1 Metalloenzyme systems discussed by Himo and Siegbahn [16]

System	Active site TMs	Remarks
Class I ribonucleotide reductase	Fe_2	Uses O_2 to generate tyrosyl radical
Coenzyme B_{12}-dependent enzymes	Co	Homolytic Co-C bond cleavage to generate Co^{II} plus radical
Water oxidation by Photosystem II	Mn and Mn_4	Mononuclear Mn complex as initial model for complete system
Galactose oxidase	Cu	Type II copper enzyme
Amine oxidase	Cu	Initial species: Cu(II)-superoxo-tyrosyl radical
Cytochrome *c* peroxidase	Fe	O-O bond cleavage with tryptophan radical
Cytochrom P450 s	Fe	Ferryl heme radical cation active oxidant
Cytochrome *c* oxidase	FeCu	O-O bond cleavage

ble alternatives. When harnessed with reproducing the available experimental data, DFT provides a very powerful tool for studying enzyme catalysis.

3.2.1 Class 1 RNR

Class 1 ribonucleotide reductase (RNR) comprises two proteins, R1 and R2, both of which have been structurally characterised. A schematic representation of the conserved residues plus the extra details of the DFT active site model in the R2 region are shown in Fig. 4 (see [16] and references therein). The latter comprises about 80 atoms. The side chain connections to the backbone were replaced by H atoms and, for those residues not anchored by direct coordination to a metal or by indirect coordination via bridging hydrogen bonded water molecules, the H atom positions (indicated by asterisks in Fig. 4) are fixed at the X-ray structure position suitably adjusted for the change from C-C to C-H bonds. This model is among the most sophisticated and complex amenable with current computational power.

The complete catalytic reaction is a complicated multi-step process necessitating a large number of calculations. Just to investigate tyrosyl radical formation and the initiation of radical transfer required nearly 100 structures to be optimised. To speed this process up, B3LYP optimisations are carried out with a relatively small basis set. When stationary points—local minima and transition states—are located, their energies are recalculated using much larger basis sets. This procedure has been proven to give reliable reaction pathways. It is more important to calculate accurate energies than to insist on highly accurate structures especially as the errors in the latter due to using small basis sets will be propagated throughout the pathway leading to substantial cancellation.

In conjunction with the available experimental data, a reasonable mechanism for most of the process has been proposed. Following O_2 binding to

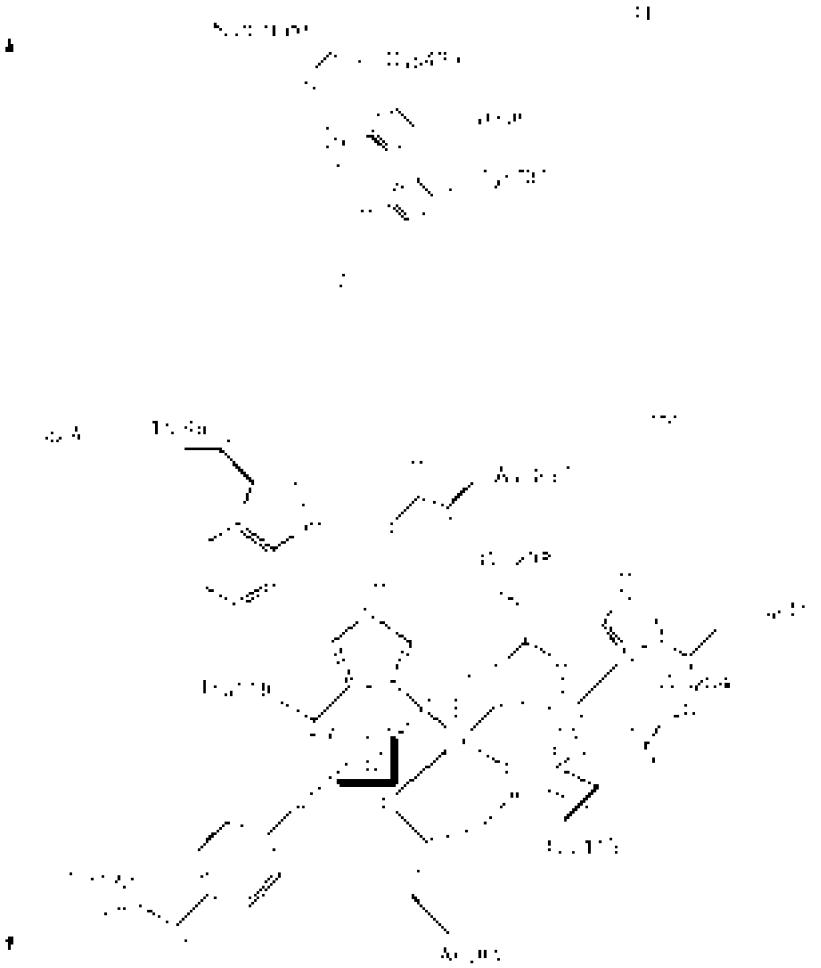

Fig. 4 Conserved residues participating in the proposed hydrogen-bonding long-range transfer chain between the substrate site in protein R1 and the tyrosyl radical in protein R2 of *E. coli* RNR. The DFT model replaced the asterisked carbon centres in R2 by H atoms fixed at the appropriate crystallographic coordinates (After Figs. 1 and 2 of [16])

the diferrous iron dimer and formation of a diferric peroxide, the O-O bond cleaves at the same time as an electron is transferred from Trp48 to generate an Fe_2(III,IV) intermediate, **X**, which has recently been studied directly by rapid-freeze-quench magnetic circular dichroism [57] which confirms a mono-oxo-bridged structure. An electron then comes in from outside to the Trp48 cation radical and a proton simultaneously binds to the iron dimer, ending up on the bridging μ-oxo group. To create the Tyr122 radical requires an electron and a proton transfer. At this point, we see the interplay

between theory and experiment in that the calculations suggest that in order to obtain a reasonable reaction barrier, an additional water molecule needs to be inserted between Tyr122 and an iron bound water (see highlighted box in Fig. 4). The rest of the reaction including that with the substrate in protein R1 is described in detail by Himo and Siegbahn [16]. In summary, a significant amount of detailed and painstaking computation coupled with all the available experimental evidence is capable of elucidating the reaction mechanism of complicated enzymatic processes.

3.2.2 Co-enzyme B_{12}-Dependent Enzymes

Co-enzyme B_{12} contains cobalt coordinated by a corrin ring and one of the few metal-carbon bonds known in biology (Fig. 5). It assists in a number of enzymatic reactions including the rearrangement reaction where a function-

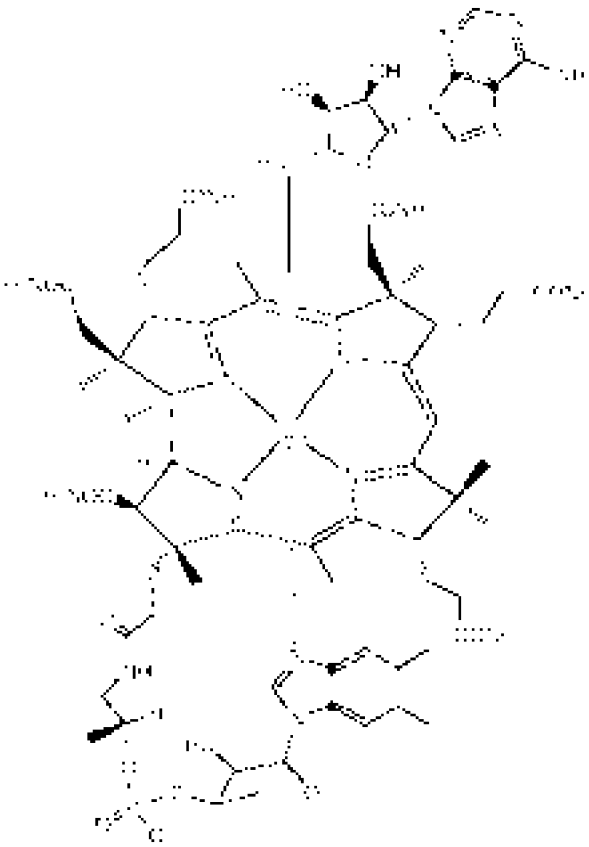

Fig. 5 Schematic representation of cobalt active site in co-enzyme B_{12}

al group X swaps places with a hydrogen on an adjacent carbon centre. The generally accepted mechanism involves initial homolytic fission of the Co-C bond to give Co(II) and a 5′-deoxyadenosyl radical (Ado-CH_2·). Naturally, the strength of the Co-C bond is crucial and recent theoretical work has been reviewed [58].

The Co-C bond energy has been measured for model systems in solution to be ~31 kcal mol^{-1} but the rate accelerations observed in enzyme catalysis suggest this value must be reduced by ~15 kcal mol^{-1}. The source of this bond weakening seems ideally suited to computational investigation. Calculations in which the *trans* Co-N distance is varied substantially (~0.5 Å) or the axial donor is replaced by a variety of other ligands do not alter the Co-C bond energy significantly. Elongation of the Co-C bond itself weakens the interaction with the Co-R bond dissociation energy (BDE) for R=*tert*-butyl about 15 kcal mol^{-1} lower than for R=methyl. However, the central issue of how the protein provides this 15 kcal mol^{-1} bond stretching energy remains unanswered. Thus, while a problem may at first sight appear amenable to calculation, there is no guarantee that theory will provide quick and easy answers. This problem continues to provide a challenge for computational chemists.

3.2.3 Water Oxidation in Photosystem II

The next illustration of how DFT can be applied to bioinorganic systems is the oxidation of water in photosystem II. Two different tyrosyl radicals have been detected with one of them, Tyr_Z, near the water oxidising complex (WOC). The WOC involves a Mn_4 cluster which mediates the evolution of one molecule of O_2 from a molecule of water for every four photons absorbed.

The oxidation and subsequent reduction of Tyr_Z are important at all stages of this process but the question of how the tyrosine is reduced has been a major issue. The two leading hypotheses are illustrated in Scheme 1. Pathway A involves a hydrogen atom transfer (HAT) but has been criticised in favour of a more conventional electron transfer (ET) process, pathway B. DFT calculations were used to try and determine which pathway is more likely. However, the detailed structure of the active site was unknown at that time. There is now a fairly low resolution structure available but in any case, trying to model the Mn_4 system would be a daunting computational task. Instead, the important feature of the reaction was identified [16] as the oxidation of Mn(III) to Mn(IV) which experimentally has an activation free energy of about 12 kcal mol^{-1}.

The mononuclear model shown in Fig. 6 was developed but the activation free energy for the HAT process was too high. One might suppose that the chemical model was at fault, being too simplistic a representation of the true

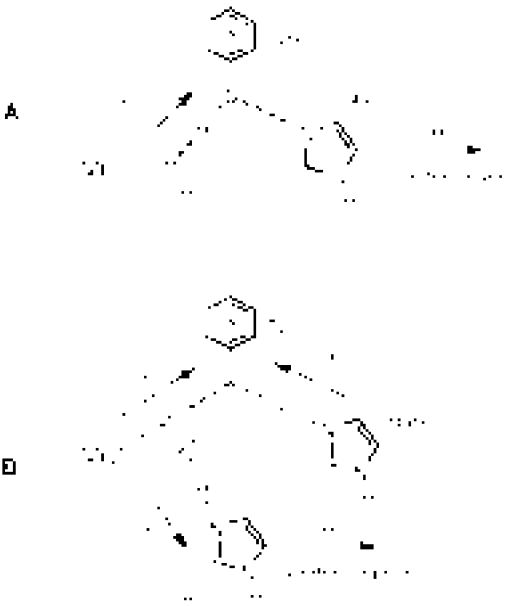

Scheme 1 Tyrosine oxidation/reduction pathways in photosystem II

active site. However, the authors were able to verify independently using a Marcus theory approach that the DFT result was internally consistent giving confidence that despite the apparent differences between the real WOC and the model system, the essential chemistry was captured correctly [16]. Further calculations for the ET pathway yielded an activation free energy of 10.6 kcal mol^{-1}, in good agreement with experiment.

There were some problems with the separate enthalpic and entropic contributions which could be attributable to tunnelling effects and the nature of the model system. However, the advantage of these calculations is that not only do they suggest the ET pathway as most likely, they also provide a good

Fig. 6 Mononuclear active-site model for PSII

starting point for extending the computational model. Transition state structures along the proposed pathways are extremely difficult to locate even for the relatively simple system shown in Fig. 6. Without a good starting point, locating a TS using a more sophisticated cluster with all four manganese centres and their attendant ligands would be very challenging indeed. Fortunately, the TS structures of the simple model are not expected to change significantly and will provide excellent guidance for further calculations.

3.2.4 Galacatose Oxidase

Galactose oxidase (GO) catalyses the two-electron oxidation of primary alcohols to aldehydes. It contains a single type II copper centre. The enzyme employs the metal and a protein radical cofactor to effect the chemistry. The crystal structure shows a square pyramidal five-coordinate copper site with the metal coordinated by two histidines, two tyrosines and a water or acetate ligand. The equatorial tyrosine, Tyr272, has an interesting crosslink to a cysteine group *ortho* to the tyrosine oxygen.

The reaction shown in Scheme 2 has been modelled with imidazoles instead of the histidines, the equatorial tyrosine with an SH substituted phenol, vinyl alcohol as the axial tyrosine and methanol as substrate. The rest of this tyrosine and the backbone link between it and His496 were treated via molecular mechanics using the IMOMM (integrated molecular orbital/molecule mechanics) approach designed by Maseras and Morokuma [59]. Con-

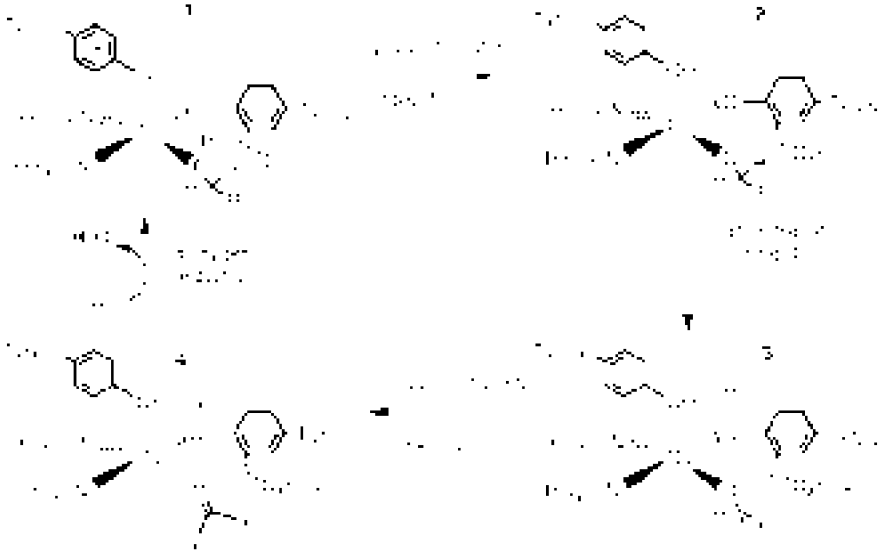

Scheme 2 Possible catalytic cycle for galactose oxidase

Fig. 7 Energetic profile (kcal mol^{-1}) for the galactose oxidase reaction scheme shown in Scheme 2 (After [16]). *Numbers in bold* refer to structures in Scheme 2. *Other numbers* refer to energies (kcal mol^{-1}) relative to the resting state structure **1**

trary to the accepted picture, the radical site prior to proton transfer (**1** in Scheme 2) is not the equatorial cysteine-substituted tyrosine. The energetics of the reaction are shown in Fig. 7 and illustrate that enzymatic processes are often multi-step and demand a serious amount of computation.

3.3 Iron-Containing Enzymes

RNR I contains a diiron centre as does methane monooxygenase (MMO). Before discussing MMO, we consider the hugely important class of systems containing iron heme units. Many of these systems also involve free radicals at some stage.

3.3.1 Heme Peroxidases

Heme-containing peroxidases use H_2O_2 generally to oxidise a variety of small aromatic substrates. Cytochrome c peroxidase (CCP) is somewhat different and has cytochrome c as its redox partner [16].

The mechanism for (most) heme peroxidases is believed to be as shown in Scheme 3. The first step involves O-O bond cleavage and the resultant formation of an oxyferryl unit and an attendant radical. In most cases, the radical is located on the porphyrin ring leading to Compound I. The electronic structure of Compound I is subtle and has itself been the subject of a num-

Scheme 3 Proposed catalytic cycle of heme peroxidases

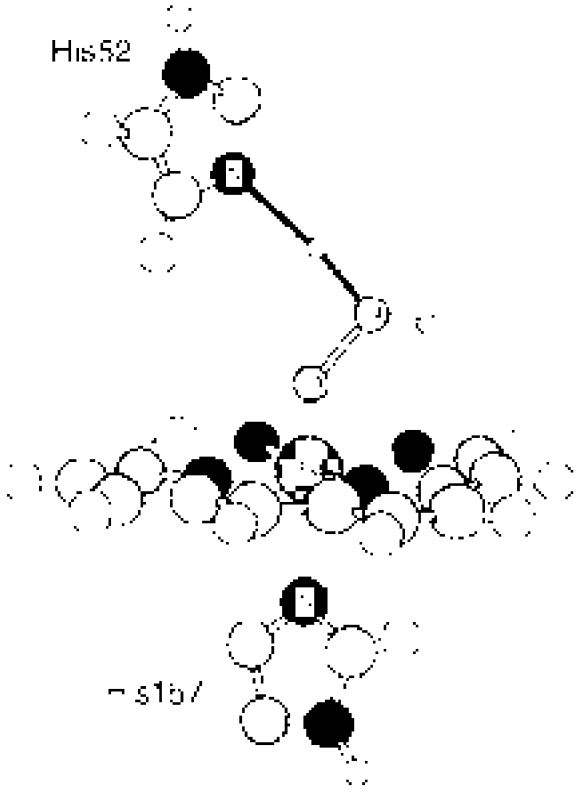

Fig. 8 Structural model used to explore the TS for O-O bond cleavage in CCP

ber of computational studies [33, 60–63]. However, for CCP, the radical is located on Trp191.

The Siegbahn group has studied both the initial O-O bond cleavage and the subsequent role of Trp191 and the details can be found elsewhere [33]. For the purposes of this review, we note that experimental site-directed mutagenesis had established an important role for His52 and was duly included in the quantum mechanical model of the O-O cleavage transition state, a representation of which is shown in Fig. 8. However, this residue is not believed to play an important role in determining the spin density distribution of the subsequent ferryl species and could safely be removed. Instead, Trp191 was added along with the intervening Asp235 which forms a bridge to the coordinated His175. The final spin distribution, based on a quartet state, placed about half a spin on a deprotonated Trp191, about half on the porphyrin ring and unit spins on both the iron and the oxo moieties which is in reasonable agreement with the experimental conclusion of a deprotonated tryptophan radical.

3.3.2 Methane Monooxygenase

MMO shares certain structural similarities with RNR I but MMO probably does not involve free radicals and so was not included above. Lovell et al. [15] have recently reviewed the current state of DFT calculations on both MMO and RNR.

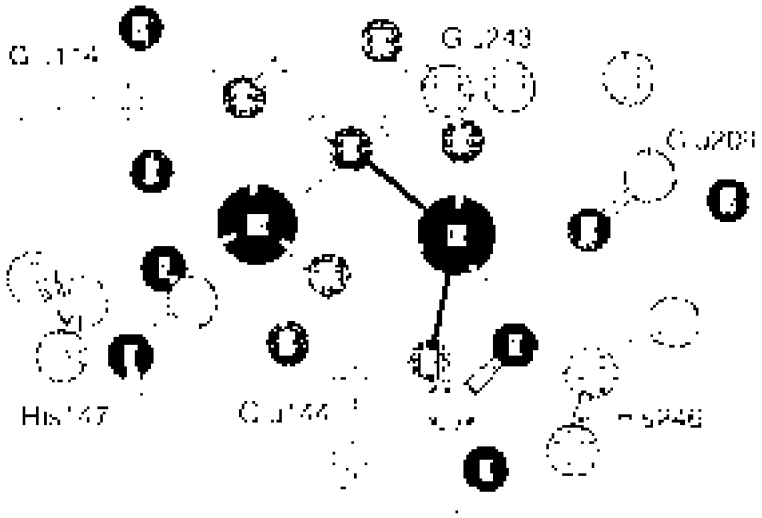

Fig. 9 X-ray crystallographic active site detail of the resting state of MMO [64]. Most side chain hydrogens have been removed for clarity

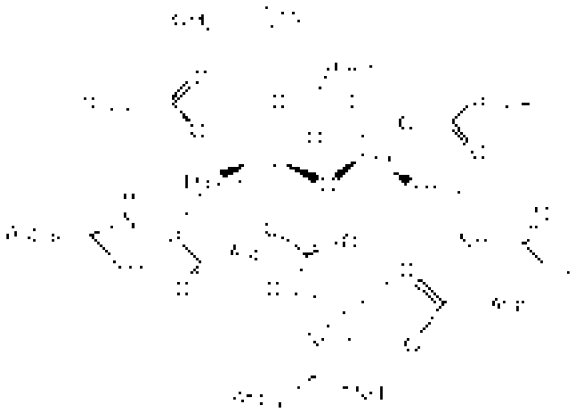

Fig. 10 Schematic view of large MMO intermediate Q model

The ability of MMO to activate the C-H bond in methane and catalytically convert it to methanol is truly remarkable and it is probably not surprising that Nature employs a fairly complex looking active site. Crystal structures of MMO active sites in various forms are now available [65–68] and provide a good starting point for theoretical modelling (Fig. 9). However, modelling the catalytic cycle is challenging partly because the active site is so complex and flexible, and partly because the crucial species, intermediate Q, has not been structurally characterised and only limited spectroscopic data are presently available, although given the Solomon group's success at isolating the comparable intermediate X in RNR [57], the latter situation may change in the near future.

Following the initial work of Siegbahn [69, 70] and Dunietz [66], Lovell et al. [15] built and geometry optimised an impressive 102 atom model (Fig. 10) of intermediate Q which incorporates a number of second- and third-shell amino acid residues [71]. Their choices were guided by their complementary studies of the protein field electrostatics which suggest those residues likely to have a large energetic effect on the active site structure.

The reliability of the computed results were gauged by comparing the calculated Fe-Fe distance to the EXAFS measurement, as well as considering the Fe coordination numbers and spin populations, the Fe exchange coupling, the spin state energy differences plus Mossbauer isomer shifts and quadrupole splittings. The latter magnetic and spectroscopic properties are particularly noteworthy in the context of this review in that they demonstrate that modern DFT can do more than compute structures and total energies. The ability to correlate experimental spectroscopic measurements with theoretical predictions promises to be an increasingly powerful tool [72]. For the moment, however, the agreement between theory and experi-

ment for intermediate Q is still patchy. The Mossbauer, X-ray absorption spectroscopy and magnetic couplings seem reasonable but the calculated Fe-Fe distance is rather too long, although the authors argue that discrepancies up to 0.2 Å between EXAFS Fe-Fe contacts and those determined subsequently via single crystal X-ray diffraction have been observed.

3.3.3 Nitrogenase

Nitrogenase (N_2ase), like MMO, is another marvel of Nature. It is capable of converting atmospheric dinitrogen to ammonia under ambient conditions, although the strong N-N bond consumes sixteen equivalents of ATP for every mole of N_2.

Prior to the solution of the X-ray crystal structure in 1993 [39], it was known that the active site of N_2ase contained a molybdenum centre and many believed this would be the site of dinitrogen activation. In fact, a whole coordination chemistry of the N_2 ligand was developed from this premise. However, for many, the actual active site was unexpected. If some of the active sites thus far have seemed complex, they all pale in comparison to that of nitrogenase. Instead of a mononuclear metal centre, the N_2ase active site resembles two cubane structures, one Fe_4S_4 and one $MoFe_3S_4$, which are connected via three bridging sulfur atoms (Fig. 3). The Mo centre is six-coordinate with the three remaining sites taken up by a bidentate homocitrate ligand and an anchor to the protein backbone via His442 while the Fe at the other end of the cluster is linked to the protein via Cys275.

This complicated but elegant active site cluster provided many more possibilities for the site of N_2 reduction such as the apparently three-coordinate iron centres. Despite being coordinatively saturated in the crystal structure, the Mo centre may still be viable in that the homocitrate may release one site for an incoming N_2. DFT calculations indicate that the homocitrate ligand of the cofactor can become monodentate on reduction, allowing N_2 to bind at Mo [73].

Many computational studies appeared purporting to shed light on the site of N_2 coordination and the mechanism of its protonation and reduction to ammonia [74–82]. However, the calculations are extremely difficult since it is hard to know what the ionisation state of the cluster is and what is its overall spin state. Even if you get these details right, there is the extra complication that the enzyme uses two more electrons than the six required for N_2 reduction, generating a molecule of H_2 for every two molecules of NH_3. However, the greater problem is that more recent refinements of the X-ray diffraction data [40] have revealed a hitherto unknown atom at the very heart of the cluster bringing into question all the previous computational work where no such atom was present. Experiment cannot distinguish the identity of this atom but both Hinnemann and Nørskov [83] and Lovell et

al. [84] propose it to be nitrogen based on DFT calculations. Some of the consequences of this so-called interstitial nitrogen have been explored [85] but there remain some puzzles. For example, Lee et al. [86] suggest that this nitrogen atom is not exchangeable which poses some intriguing issues concerning how it came to be there. Whatever the answer to that puzzle, there still seems to be a long way to go before a satisfactory computational explanation of N_2 reduction is forthcoming. N_2ase provides a salutary warning of the potential pitfalls facing the bioinorganic computational chemist.

3.3.4 Iron-Sulfur Clusters

Iron-sulfur proteins play important roles in electron transfer and catalysis in organisms ranging from simple bacteria through to higher animals. The common structural motif is iron tetrahedrally coordinated by sulfur donors with the single metal centre in rubredoxin bound by four cysteine thiolates while the 2Fe and 4Fe sites of ferredoxins have respectively two and one monodentate thiolate ligands and two or three bridging sulfido units (Fig. 11).

The relatively weak tetrahedral ligand field ensures that the Fe centres remain high spin in both the +3 and +2 oxidation states. This has an important consequence since the number of unpaired electrons, and hence spin polarisation, is high.

In a spin unrestricted treatment where the up-spin electrons are allowed to have different spatial properties to their down-spin counterparts, the extra exchange stabilisation of the majority spin (say, up-spin), means that their energies are lowered. Since in metal complexes, the spin is located

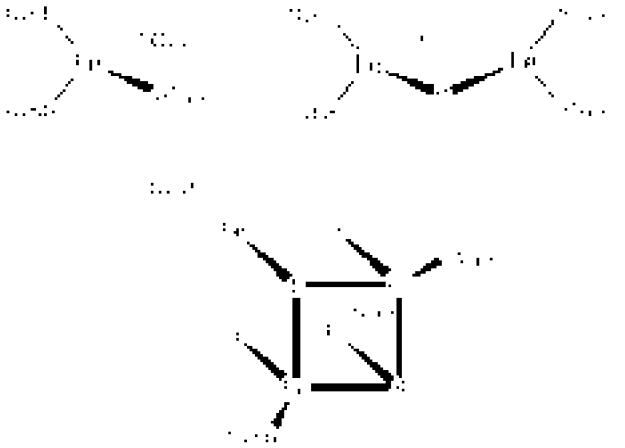

Fig. 11 Schematic representations of various iron-sulfur centres

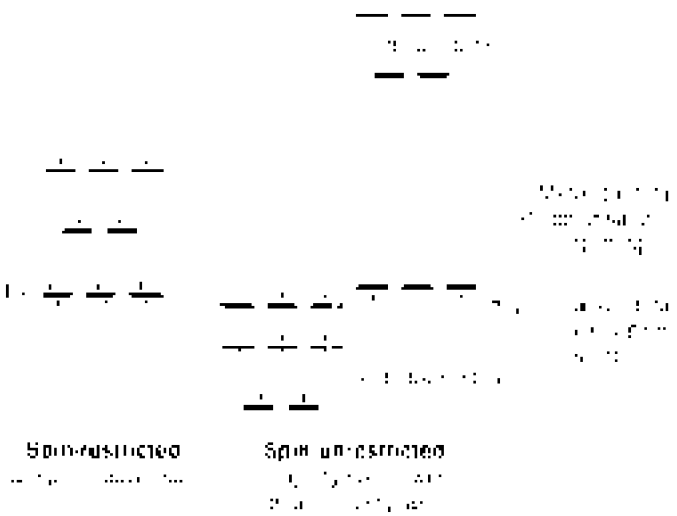

Fig. 12 The effect of spin polarisation can lead to an inversion of the normal ordering of d levels above ligand MOs

mainly in the d orbitals, the spin-polarisation splitting is particularly marked there. In contrast, since there is relatively less on the ligands, the ligand up- and down-spin pairs do not split as much. As shown in Fig. 12, if the polarisation splitting of the d orbitals is large enough, the 'normal' expectation that the d orbitals lie above the ligand σ levels is not realised and instead we have an 'inverted' energy level scheme.

In addition to inverted energy levels, for the redox-active multi-metal species, with various combinations of S=5/2 Fe^{3+} and S=2 Fe^{2+} centres, the possible magnetic spin-coupling arrangements can be very complex. In general, the ground states of these systems cannot be described by a single determinant and would require a more sophisticated multiconfiguration approach. Since DFT is normally expressed in terms of a single determinant, it is inappropriate for computing each spin state in such systems.

However, pioneering work by Case, Noodleman and co-workers has developed a modified DFT procedure which can be used to compute the correct magnetic coupling [87]. Central to this work is the notion of broken symmetry. The symmetry breaking refers to the distribution of unpaired electrons and not the geometry. For example, in the geometrically symmetrical bimetallic species such as $[M_2X_9]^{n-}$ [88, 89], where each metal has a maximum spin, S, the highest spin multiplicity corresponds to 4S+1 with each metal formally high spin, while the minimum spin multiplicity corresponds to a singlet which would normally be completely delocalised and thus correspond to formally low-spin metal centres. The broken symmetry solution allows for the possibility of a localised spin singlet where both met-

als are formally high spin but where one has all up spin density and the other all down spin density. Hence, the electronic symmetry is lower than the molecular symmetry.

The broken symmetry wavefunction is not itself a pure spin state. However, spin projection techniques allow the approximate energies and properties of the correct spin states to be calculated.

In the ground state of the 2Fe2S dimer in Fig. 11, the spin-up electrons are mainly on one side of the molecule while the spin-down electrons are on the other side—an antiparallel alignment of the spins. A 'high-spin' state can also be constructed by forcing the spins on both side to be parallel. If the two Fe sites have spin quantum numbers S_A and S_B, then the possible spin states of the coupled system have total spin S_t ranging from $|S_A - S_B|$ through $S_A + S_B$ in integer steps. If the system conforms to the Heisenberg model where the Hamiltonian is given by $H_{spin} = JS_A \times S_B$, the successive spin state energies are given by $E(S_t) - E(S_t - 1) = JS_t$. Providing the metal sites interact weakly compared to a metal-metal bond, this will be the case. Now, while the dimer has many possible spin states, it has only one broken symmetry state, Ψ_B, which is a weighted average of the pure spin states $\Psi(S_t)$. Since the Heisenberg spin ladder depends on a single parameter, J, it can be calculated from the energy difference between the high-spin and broken-symmetry states using the equation

$$E(S_{max} = S_A + S_B) - E_B(M_S = |S_A - S_B|) = 2JS_AS_B$$

The broken symmetry approach with suitable refinements has been used to good effect on iron-sulfur clusters and is reviewed by Noodleman et al. [87]. Apart from the inverted energy levels described above, they conclude that redox processes alter the magnitudes of the charges on the sulfur ligands but only change the anisotropy of the Fe charge distribution, that pairwise valence delocalisation over mixed valent pairs is effective in Fe3S4 and Fe4S4 systems rather than full delocalisation over the whole cluster, and that redox potentials are strongly influenced by Heisenberg spin coupling, valence delocalisation and solvation. The crucial role of environmental effects has also been suggested by Torres et al. [90] but they conclude that even for iron-sulfur clusters, a continuum dielectric is sufficient.

4
Other Applications

4.1
Molybdoenzymes

Most of the applications we have looked at so far involve the first transition series elements Fe, Co, Ni and Cu. However, Nature employs a number of

other metals, notably the second row metal molybdenum. Mo occurs in N_2ase although the modelling studies of the FeMoco unit have generally not considered the Mo as the reactive centre.

From a purely computational perspective, second row metal centres are rather easier to treat than their first or third row counterparts. In contrast to first-row metals, second-row metals do not generally suffer from having lots of low energy electronic states while in contrast to third-row metals, explicit relativistic effects on the valence electrons are relatively minor and are usually ignored. Secondary relativistic effects are included in the core potentials for the metal.

Molybdenum has a number of accessible oxidation states under physiological conditions and is often involved in two-electron redox processes involving oxygen atom transfer. Typically, the metal cycles between the dioxo molybdenum +6 oxidation state ($[MoO_2^{2+}]$ and the mono-oxo molybdenum +4 oxidation state ($[MoO^{2+}]$). There have been a number of studies of oxo and/or hydroxo transfer for model systems of xanthine oxidase [38, 91–95], DMSO reductase [96] and sulfite oxidase [97] but the DFT methods and protocols applied are relatively standard and have been covered elsewhere in this article.

4.2 Hydrogenase

Given the central importance of structure in applications of computer modelling in bioinorganic chemistry, it is not surprising to see an explosion of calculations soon after the publishing of reasonably accurate structural data. The hydrogenase system is a good illustrative example [98–111].

Examples of hydrogenases with an Fe-Ni and 'all-Fe' active sites are known. The single crystal X-ray diffraction studies suggested the presence of some hitherto unexpected ligands bound to the Fe centre of the bimetallic [NiFe] hydrogenase active site (Fig. 13). The data show small diatomic ligands—either CO or CN. The latter was initially a surprise since cyanide is usually associated with rather lethal biological activity. Theoreticians set out to try to correlate the spectroscopic data with various structural models but the active site is complex both geometrically and electronically with unusual coordination numbers around the metal centres and some ambiguity as to their ionisation and spin states [99–111].

While much progress has been made, the hydrogenase reaction, though superficially simple, proceeds via a complex series of steps and much work remains to be done [100].

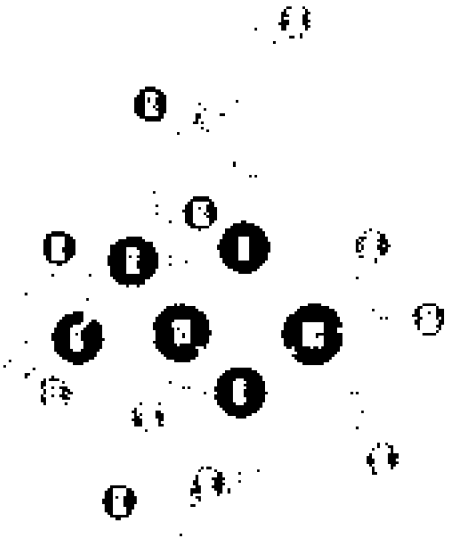

Fig. 13 Active site of NiFe hydrogenase

5 Summary and Future Developments

DFT has made a big contribution to our understanding of many of the processes in bioinorganic systems. It is difficult to get a detailed experimental mechanistic picture because spectroscopic and structural data are hard to measure while the enzymes are turning over. In contrast, theory is now sufficiently well developed and robust to be able to fill in the gaps more or less reliably. However, as we have seen on many occasions, it is critical to ensure that the quantum chemical model is a good representation of the active site and its associated chemistry. Siegbahn has shown many times how a carefully calibrated model can work very well but the recent discovery of an interstitial atom in the middle of the nitrogenase FeMoco cluster provides a salutary warning that we cannot always guarantee that the our chosen computer models are correct. The present state-of-the-art therefore is to validate the calculations as often as possible. This means comparing computed data against experimental measurements wherever possible.

Structural comparisons are, at least conceptually, amongst the most straightforward to make, but even here care must be taken. The possible (and perhaps unsuspected) roles of side chains remote from the metal active site, the chemical ambiguity of protein crystallography in that hydrogen atoms cannot be located, and the role of the protein itself all serve to complicate matters. The solution is not to rely solely on structures. An obvious example is that a viable mechanism must display reasonable energetics.

Thus, providing the quantum model gives a good description of the required chemistry, some structural shortcuts may be possible. Of course, as computers get faster, many workers are moving towards larger structural models.

As to the future, among the many exciting developments in theory is an ever increasing ability to compute accurate spectroscopic data including NMR chemical shifts and coupling constants, EPR g-values and hyperfine splittings, vibrational spectra (including intensities) and excited states [44, 72, 112]. Calculated excited state energies of TM species is arguably one of the most difficult challenges for DFT. However, there is good reason to believe that many of the current problems can be overcome and we await the coming developments with great anticipation. The ability to reproduce from first principles a wide variety of structural, energetic and spectroscopic properties can only serve to give ever greater confidence that quantum models can provide an accurate reflection of the true behaviour of the metalloenzyme active site.

References

1. Bray MR, Deeth RJ, Paget VJ (1996) Prog React Kinetics 21:169
2. Ziegler T (1995) Can J Chem 73:743
3. Johnson K (1973) Adv Quant Chem 7:143
4. Slater JC (1974) The self-consistent field for molecules and solids. McGraw-Hill, USA
5. Schwartz K (1972) Phys Rev B 5:2466
6. Delley B, Ellis DE (1982) J Chem Phys 76:1949
7. Fan LY, Ziegler T (1991) J Chem Phys 95:7401
8. Penfield KW, Gewirth AA, Solomon EI (1985) J Am Chem Soc 107:4519
9. Deeth RJ, Figgis BN, Ogden MI (1988) Chem Phys 121:115
10. Deeth RJ (1990) J Chem Soc Dalton Trans 355
11. Deeth RJ (1991) J Chem Soc Dalton Trans 1467
12. Deeth RJ (1991) J Chem Soc Dalton Trans 1895
13. Armstrong EM, Collison D, Deeth RJ, Garner CD (1995) J Chem Soc Dalton Trans 191
14. Vosko SH, Wilk L, Nusair M (1980) Can J Phys 58:1200
15. Lovell T, Himo F, Han WG, Noodleman L (2003) Coord Chem Rev 238:211
16. Himo F, Siegbahn PEM (2003) Chem Rev 103:2421
17. Blomberg MRA, Siegbahn PEM (2001) J Phys Chem B 105:9375
18. Siegbahn PEM, Blomberg MRA (2000) Chem Rev 100:421
19. Siegbahn PEM, Blomberg MRA (1999) Annu Rev Phys Chem 50:221
20. Siegbahn PEM (2003) Faraday Discuss 124:289
21. Friesner RA, Dunietz BD (2001) Accounts Chem Res 34:351
22. Velde GT, Bickelhaupt FM, Baerends EJ, Guerra CF, Van Gisbergen SJA, Snijders JG, Ziegler T (2001) J Comput. Chem 22:931
23. Baerends EJ, Gritsenko OV (1997) J Phys Chem A 101:5383
24. Kohn W, Becke AD, Parr RG (1996) J Phys Chem 100:12974
25. Ceperley D, Alder BJ (1980) Phys Rev Lett 45:4264
26. Gunnarsson O, Lundqvist BI (1976) Phys Rev B 13:4274

27. von Barth U, Hedin L (1972) Phys Rev B 4:1629
28. Veillard A (1991) Chem Rev 91:743
29. Becke AD (1988) Phys Rev A 38:3098
30. Becke AD (1993) J Chem Phys 98:1372
31. Becke AD (1993) J Chem Phys 98:5648
32. Lee CT, Yang WT, Parr RG (1988) Phys Rev B 37:785
33. Wirstam M, Blomberg MRA, Siegbahn PEM (1999) J Am Chem Soc 121:10178
34. Vallee BL, Williams RJP (1968) Proc Natl Acad Sci USA 59:498
35. Gray HB, Malmstrom BG, Williams RJP (2000) J Biol Inorg Chem 5:551
36. Solomon EI, Brunold TC, Davis MI, Kemsley JN, Lee SK, Lehnert N, Neese F, Skulan AJ, Yang YS, Zhou J (2000) Chem Rev 100:235
37. Romao MJ, Archer M, Moura I, Moura JJG, Legall J, Engh R, Schneider M, Hof P, Huber R (1995) Science 270:1170
38. Bray MR, Deeth RJ (1996) Inorg Chem 35:5720
39. Kim J, Woo D, Rees DC (1993) Biochemistry 32:7104
40. Einsle O, Tezcan FA, Andrade SLA, Schmid B, Yoshida M, Howard JB, Rees DC (2002) Science 297:1696
41. Siegbahn PEM (2001) J Comput Chem 22:1634
42. Siegbahn PEM, Blomberg MRA, Pavlov M (1998) Chem Phys Lett 292:421
43. Voges D, Karshikoff A (1998) J Chem Phys 108:2219
44. Ghosh A (2003) Curr Opin Chem Biol 7:110
45. Vanlenthe E, Snijders JG, Baerends EJ (1996) J Chem Phys 105:6505
46. Karlin KD, Tyeklar Z (1993) Bioinorganic chemistry of copper. Chapman & Hall, New York
47. Malmstrom BG (1964) In: King TE, Mason HS, Morrison M (eds) Oxidases and related redox systems. Wiley, New York, p 207
48. Ryde U, Olsson MHM, Pierloot K, Roos BO (1996) J Mol Biol 261:586
49. Gewirth AA, Solomon EI (1988) J Am Chem Soc 110:3811
50. LaCroix LB, Shadle SE, Wang YN, Averill BA, Hedman B, Hodgson KO, Solomon EI (1996) J Am Chem Soc 118:7755
51. Ryde U, Olsson MHM (2001) Int J Quantum Chem 81:335
52. Szilagyi RK, Metz M, Solomon EI (2002) J Phys Chem A 106:2994
53. Deeth RJ (2001) J Chem Soc Dalton Trans 664
54. Patchkovskii S, Autschbach J, Ziegler T (2001) J Chem Phys 115:26
55. Patchkovskii S, Ziegler T (2002) J Chem Phys 116:7806
56. Olsson MHM, Hong GY, Warshel A (2003) J Am Chem Soc 125:5025
57. Mitic N, Saleh L, Schenk G, Bollinger JM, Solomon EI (2003) J Am Chem Soc 125:11200
58. Kozlowski PM (2001) Curr Opin Chem Biol 5:736
59. Maseras F, Morokuma K (1995) J Comput Chem 16:1170
60. Deeth RJ (1999) J Am Chem Soc 121:6074
61. Harris DL, Loew GH (1998) J Am Chem Soc 120:8941
62. Kuramochi H, Noodleman L, Case DA (1997) J Am Chem Soc 119:11442
63. Antony J, Grodzicki M, Trautwein AX (1997) J Phys Chem A 101:2692
64. Elango N, Radhakrishnan R, Froland WA, Wallar BJ, Earhart CA, Lipscomb JD, Ohlendorf DH (1997) Protein Sci 6:556
65. Rosenzweig AC, Nordlund P, Takahara PM, Frederick CA, Lippard SJ (1995) Chem Biol 2:409
66. Dunietz BD, Beachy MD, Cao YX, Whittington DA, Lippard SJ, Friesner RA (2000) J Am Chem Soc 122:2828

67. Brandstetter H, Whittington DA, Lippard SJ, Frederick CA (1999) Chem Biol 6:441
68. Rosenzweig AC, Nordlund P, Takahara PM, Frederick CA, Lippard SJ (1995) Chem Biol 2:632
69. Siegbahn PEM (2001) J Biol Inorg Chem 6:27
70. Siegbahn PEM, Crabtree RH (2000) Metal-oxo and metal-peroxo species in catalytic oxidations. Struct Bonding (Berlin) 97:125
71. Lovell T, Han WG, Liu TQ, Noodleman L (2002) J Am Chem Soc 124:5890
72. Neese F (2003) Curr Opin Chem Biol 7:125
73. Durrant MC (2002) Biochemistry 41:13934
74. Dance I (1997) Chem Commun: 165
75. Dance I (1998) Chem Commun: 523
76. Siegbahn PEM, Westerberg J, Svensson M, Crabtree RH (1998) J Phys Chem B 102:1615
77. Stavrev KK, Zerner MC (1998) Int J Quantum Chem 70:1159
78. Rod TH, Hammer B, Norskov JK (1999) Phys Rev Lett 82:4054
79. Rod TH, Norskov JK (2000) J Am Chem Soc 122:12751
80. Szilagyi RK, Musaev DG, Morokuma K (2000) Theochem J Mol Struct 506:131
81. Durrant MC (2001) Inorg Chem Commun 4:60
82. Dance IG (1994) Aust J Chem 47:979
83. Hinnemann B, Norskov JK (2003) J Am Chem Soc 125:1466
84. Lovell T, Liu TQ, Case DA, Noodleman L (2003) J Am Chem Soc 125:8377
85. Dance I (2003) Chem Commun 324
86. Lee HI, Benton PMC, Laryukhin M, Igarashi RY, Dean DR, Seefeldt LC, Hoffman BM (2003) J Am Chem Soc 125:5604
87. Noodleman L, Peng CY, Case DA, Mouesca JM (1995) Coord Chem Rev 144:199
88. Stranger R, McGrady JE, Lovell T (1998) Inorg Chem 37:6795
89. McGrady JE, Stranger R, Lovell T (1998) Inorg Chem 37:3802
90. Torres RA, Lovell T, Noodleman L, Case DA (2003) J Am Chem Soc 125:1923
91. Voityuk AA, Albert K, Romao MJ, Huber R, Rosch N (1998) Inorg Chem 37:176
92. Bray MR (1997) PhD Thesis, University of Warwick
93. Bray MR, Deeth RJ (1997) J Chem Soc Dalton Trans 4005
94. Bray MR, Deeth RJ (1997) J Chem Soc Dalton Trans 1267
95. Voityuk AA, Albert K, Kostlmeier S, Nasluzov VA, Neyman KM, Hof P, Huber R, Romao MJ, Rosch N (1997) J Am Chem Soc 119:3159
96. Thapper A, Deeth RJ, Nordlander E (2002) Inorg Chem 41:6695
97. Izumi Y, Glaser T, Rose K, McMaster J, Basu P, Enemark JH, Hedman B, Hodgson KO, Solomon EI (1999) J Am Chem Soc 121:10035
98. Evans DJ, Pickett CJ (2003) Chem Soc Rev 32:268
99. Bruschi M, Fantucci P, De Gioia L (2003) Inorg Chem 42:4773
100. Stein M, Lubitz W (2002) Curr Opin Chem Biol 6:243
101. Stadler C, Lacey AL, Montet Y, Volbeda A, Fontecilla-Camps JC, Conesa JC, Fernandez VM (2002) Inorg Chem 41:4424
102. Stadler C, de Lacey AL, Hernandez B, Fernandez VM, Conesa JC (2002) Inorg Chem 41:4417
103. Liu ZP, Hu P (2002) J Am Chem Soc 124:5175
104. Fan HJ, Hall MB (2002) Abstr Pap Am Chem Soc 223:408
105. Fan HJ, Hall MB (2002) J Am Chem Soc 124:394
106. Stein M, Lubitz W (2001) Phys Chem Chem Phys 3:2668
107. Stein M, van Lenthe E, Baerends EJ, Lubitz W (2001) J Am Chem Soc 123:5839

108. Siegbahn PEM, Blomberg MRA, Pavlov MWN, Crabtree RH (2001) J Biol Inorg Chem 6:460
109. Niu S, Hall NB (2001) Inorg Chem 40:6201
110. Li SH, Hall MB (2001) Inorg Chem 40:18
111. Amara P, Volbeda A, Fontecilla-Camps JC, Field MJ (1999) J Am Chem Soc 121:4468
112. Neese F, Solomon EI (1998) Inorg Chem 37:6568

Structure and Bonding (2004) 113:71–102
DOI 10.1007/b97942
© Springer-Verlag Berlin Heidelberg 2004

Theoretical Study of the Exchange Coupling in Large Polynuclear Transition Metal Complexes Using DFT Methods

Eliseo Ruiz (✉)

Departament de Química Inorgànica, and Centre Especial
de Recerca en Química Teòrica (CeRQT), Universitat de Barcelona, Diagonal 647,
08028 Barcelona, Spain
eliseo.ruiz@qi.ub.es

1 Introduction 72
1.1 Phenomenological Hamiltonians for Polynuclear Complexes 73
1.2 Comparison of Theoretical Results with Experimental Data 74

2 Methods for Obtaining Exchange Coupling Constants in Polynuclear Systems 76
2.1 Calculation of the Exchange Coupling Constants for Test Systems. 79

3 Historical Overview of the Calculation of Exchange Interactions in Polynuclear Systems 84
3.1 Transition Metal Complexes with a Cubane Core 84
3.2 Single-Molecule Magnets 90

4 A Detailed Example: Hexanuclear Cu(II) and Ni(II) Polysiloxanolates 94

References 99

Abstract Polynuclear transition metal complexes containing paramagnetic cations have caught the attention of many chemists, since they are one of the main fields of study in molecular magnetism and they play important roles in the reactivity of active sites of systems of biological interest. Theoretical methods based on density functional theory due to the possibility of handling large systems are especially indicated for studying the electronic structure of this kind of molecules. At the same time, such methods provide good accuracy to allow the calculation of the small energy differences involved in the exchange interactions. It is worth noting that theoretical methods are especially important in the study of the exchange interactions in complexes with a large number of paramagnetic centers because they can provide a more detailed analysis of the interactions than experimental data can. This fact is due to the limitations in obtaining exchange coupling constants from experimental measurements for large size systems of this kind. The knowledge of the exchange interactions that controls the ground state of the system is crucial to the understanding of magnetic properties such as the single-molecule magnet character or the reactivity of an active site in a biological system.

Keywords Density functional calculations · Single-molecule magnets · Magnetic properties · Exchange Coupling · Polynuclear transition metal complexes

1 Introduction

The transition metal complexes have many unique and specific physical and chemical properties. For that reason, they play a crucial role in some biological systems, mainly related with the electron transfer processes due to their versatility and the easy with which they can change in the oxidation state of the transition metals. The presence of two transition metals in the same complex considerably increases the complexity of the electronic structure, giving the system completely different properties to those of the complex with only one metal. This fact allows complex metal-metal electron transfer processes and in the case of the presence of paramagnetic metallic cations, the exchange interactions between them provides a new set of magnetic behaviors in comparison with those present in mononuclear species. The gain in the complexity of such systems increases exponentially depending on the number of transition metals present in the complex. For that reason, the first steps of the research in Molecular Magnetism focused mainly on the magnetic properties of dinuclear complexes with the aim of gaining some understanding of the key structural and electronic factors that control the exchange coupling between two metal centers [1]. From the theoretical point of view many efforts have also been applied to in the study of the exchange coupling in dinuclear transition metal complexes, as is clearly reflected in the number of recent reviews in this field [2–6].

During the last decade, the aim obtaining new materials based on molecular building blocks with rationally predetermined magnetic properties has led chemists to increase the complexity of the systems studied [7–10]. In order to achieve this goal, two different strategies have been adopted. First, new magnetic properties have seen sought by extending the exchange interaction from dinuclear to chain, to two-dimensional or even to three-dimensional structures based on molecular building blocks. For instance, many oxalato- and cyano-bridged transition metal compounds are clear examples of this research resulting in a very rich chemistry and a wide variety of magnetic behaviors [11, 12]. The second procedure adopted is increasing the complexity of these building blocks by synthesizing polynuclear complexes with more than two interacting paramagnetic centers [13]. The magnetic properties of these compounds are expected to be intermediate between those of simple dinuclear complexes and those of bulk materials. However, due to the size of such complexes and the complexity of their manifold of states completely new magnetic behaviors are obtained. This review will focus on the theoretical studies of the exchange interactions in this second group of compounds, molecular entities containing more than two paramagnetic centers. Among these, the so-called Mn_{12} [14] and Fe_8 [15] compounds have attracted the interest of many researchers, especially due to magnetic bistability associated with the interplay between the quantum magnetic tun-

neling effect and the single-molecule magnet character [13]. Logically, due to the complexity of such systems, the number of publications with theoretical studies devoted to this kind of systems is relatively small, although from an experimental point of view they are actually the state-of-art research in molecular magnetism with many research groups working on them.

1.1 Phenomenological Hamiltonians for Polynuclear Complexes

The phenomenological Hamiltonian employed to describe the magnetic properties of a dinuclear complex is indicated in Eq. (1) where J is the exchange coupling constant between the two paramagnetic centers. The second and third terms are those corresponding to the zero field splitting parameters, being the axial and rhombic contributions, respectively:

$$\hat{H} = -J\hat{S}_1\hat{S}_2 + D\left(\hat{S}_z^2 - \frac{1}{3}\hat{S}^2\right) + E\left(\hat{S}_x^2 - \hat{S}_y^2\right) \tag{1}$$

where $\hat{S}$ is the total spin moment of the molecule while $\hat{S}_x$, $\hat{S}_y$ and $\hat{S}_z$ are its three components. If we turn to complexes of higher nuclearity, the Hamiltonian usually employed is considerably more complex due to the presence of several exchange pathways with different J values. The Hamiltonian for a general polynuclear complex is indicated in Eq. (2):

$$\hat{H} = -\sum_{i>j} J_{ij}\hat{S}_i\hat{S}_j + D\left(\hat{S}_z^2 - \frac{1}{3}\hat{S}^2\right) + E\left(\hat{S}_x^2 - \hat{S}_y^2\right) \tag{2}$$

where $\hat{S}_i$ and $\hat{S}_j$ are the spin operators of the different paramagnetic centers. The J_{ij} values are the coupling constants between all the paramagnetic centers of the molecule. The physical origin of the anisotropy of the system, responsible of the zero field splitting terms, is the spin-orbit coupling [16]. The non-inclusion of the spin-orbit effect in the calculation allows a direct estimation of the exchange coupling constants. Although this review is focused in the theoretical studies of the exchange coupling constant, it is worth remarking that Pederson et al. have recently presented an approach based on a perturbative method to include the spin-orbit coupling effect in DFT methods that allows the calculation of the zero field splitting parameters and we the results of such approach will be discussed later [17]. For the understanding of the magnetic properties, all the terms of Eq. (2) could be important. For example, the anisotropy energy barrier for a magnetically bistable system is $D\hat{S}_z^2$, the D value for the Mn_{12} complex is -0.5 cm^{-1} while due to the exchange interactions between the twelve manganese cations this system has $\hat{S}_z = 10$ resulting in a barrier of 50 cm^{-1}. Hence molecules with

large D and $\hat{S}_z$ are synthetic targets to obtain systems where the single-molecule magnet behavior can appear at higher temperatures [14].

1.2 Comparison of Theoretical Results with Experimental Data

The accuracy of the theoretical methods in the calculation of exchange coupling constants of polynuclear transition metal complexes will be gauged by comparing the calculated values with those obtained by fitting the experimental data. This comparison can be easily done without problems for dinuclear complexes that will allow quantifying the accuracy of different methods. However, such a comparison must be performed carefully for polynuclear complexes since experimental data are in most cases obtained from a fitting of the magnetic susceptibility data to the expression obtained using a Hamiltonian that includes several fitting parameters. One of the problems associated with this technique is the existence of several independent sets of parameters that provide fair fittings of the susceptibility curve. Another difficulty arises from some simplifying hypotheses, such as the neglect of next-nearest neighbor interactions or the assumption of identical parameters for interactions that are not equivalent by symmetry, often adopted to reduce the number of fitting parameters. An additional problem is the presence in a polynuclear complex of dominant exchange interactions that mask the influence of other small exchange constants in the magnetic susceptibility curve. In such cases these small J values are very difficult to be obtained with relatively good accuracy.

Finally, it is also important to mention that due to the large number of paramagnetic centers and exchange coupling constants, it is impossible in many cases with the available computational resources to perform an exact diagonalization of the Hamiltonian matrix required for the fitting procedure. For instance, Mn_{12} and Fe_8 complexes, with 1.0×10^8 and 1.6×10^6 states respectively, are examples of systems that cannot be fitted and some approximate methods, such as Monte Carlo simulations, must be adopted to obtain a set of exchange coupling constants [18]. Thus, the use of theoretical methods to estimate the exchange coupling constants can be foreseen as a valuable tool for the experimental chemist to rule out those sets of experimental fitted constants that are deemed unrealistic according to calculations. Likewise, alternative methods such as the Monte Carlo simulations usually require a starting set of exchange coupling constants that can be proportioned by the theoretical results. Good sources of experimental data would be inelastic neutron scattering experiments, but these are not commonly employed mainly due to the technical requirements involved [19].

It is worth discussing at this point some problems of language regarding the comparability of the calculated and experimental exchange coupling constants [20]. From the experimental point of view, the Heisenberg Hamil-

tonian is employed to estimate the energies of the states that are involved in the fitting of the magnetic susceptibility data. In the case of the theoretical methods, the eigenfunctions of the Heisenberg Hamiltonian and their energies can be straightforwardly calculated by a multiconfigurational approach. However, when using single-determinant methods, such as methods based on density functional theory or Hartree-Fock, the calculated energies are related to the diagonal matrix elements of the Heisenberg Hamiltonian and not with its eigenvalues as in the multiconfigurational methods. In this case, an alternative way to describe the system is by considering an Ising Hamiltonian as a special case of a Heisenberg Hamiltonian in which only the diagonal terms are kept. Thus, it was considered that the wavefunctions obtained with the single-determinant methods are eigenfunctions of an Ising Hamiltonian that is formulated with the same J values as the original Heisenberg Hamiltonian because their diagonal terms are identical. For that reason, the J values obtained with single-determinant methods are directly comparable to those provided by multiconfigurational methods or from experimental data. The difference between these two theoretical approaches is the kind of eigenfunctions obtained. Hence the procedure to obtain the eigenfunctions and eigenvalues of the Heisenberg Hamiltonian using the DFT methods can be summarized in two steps. The first one would consist of the calculation of the J values (in the next section it will be analyzed this point in depth). Subsequently with the calculated J values are used to perform the diagonalization of the Heisenberg matrix giving eigenfunctions and eigenvalues directly comparable to those obtained using multiconfigurational methods or from the fitting of the experimental data.

To conclude this section, it is important to keep in mind the differences in the use of an Ising Hamiltonian in theoretical and experimental work. From the theoretical point of view, the Ising Hamiltonian is usually referred when using single-determinant methods, for the reasons that were previously discussed. However, the use of the Ising Hamiltonian to fit experimental data is restricted only to cases where there is a strong anisotropy in the magnetic properties of the system [1]. Hence an anisotropic Hamiltonian, like the Ising one, must be used to fit of the experimental data. In this way the energies derived from the Ising Hamiltonian are employed like those corresponding to the states, as if they were the eigenvalues of the Heisenberg Hamiltonian. In such cases the experimental coupling constants obtained using an Ising Hamiltonian cannot be directly compared with the theoretical results using the usual approaches.

2 Methods for Obtaining Exchange Coupling Constants in Polynuclear Systems

The first example in the literature describing the procedure to calculate exchange coupling constants using DFT methods (Xα multiple-scattering) in a polynuclear complex with more than two paramagnetic centers was provided in 1982 by Aizman and Case to study Fe_4 sulfur clusters corresponding to ferredoxine protein models [21]. This paper is practically contemporaneous with those published by Noodleman et al. to establish the so-called "broken-symmetry" method widely employed to calculate the exchange interaction in dinuclear complexes [22, 23]. The procedure described with more detail and extended to other iron-sulfur clusters in two later reviews of Noodleman and Case [24, 25] consists of the calculation of two energies for the mixed valence $[Fe_4S_4(SCH_3)_4]^{2-}$ model corresponding to the high spin state with S=9 and a low spin S=0 "broken-symmetry" state considering only one J value. The difference between both energy values is 81 J/2 by considering the Hamiltonian indicated in Eq. (3). This energy was calculated from the difference between the corresponding elements of the Hamiltonian matrix to the two calculated wavefunctions:

$$\hat{H} = -\sum_{i>j} 2J\, \hat{S}_i \hat{S}_j \tag{3}$$

Despite the publication of these papers, as was indicated in the introduction, most of the later publications have focused on the calculation of dinuclear complexes employing the "broken-symmetry" approach proposed by Noodleman et al. In this approach the J value involves the calculation of the energy difference between the high-spin state and a low-spin solution that corresponds to a "broken symmetry" wavefunction in the case of symmetric homodinuclear complexes. From now on, it will be employed the expressions for the Hamiltonians indicated in Eqs. (1) and (2); Eq. (3) was kept for "historical" reasons. A general expression, (see Eq. 4) can be proposed for any dinuclear complex using the original "broken-symmetry" approach proposed by Noodleman [26]:

$$E_{BS} - E_{HS} = 2S_1 S_2 J \tag{4}$$

where S_1 and S_2 are the two local spin moments. This equation considers that the energy of the "broken-symmetry" state must be corrected by introducing a spin projection to obtain the energy of the singlet state. Recently, Polo et al. have shown that the presence of the self-interaction error in commonly used exchange functionals mimics non-dynamic pair correlation effects [27–30]. In contrast, if non-dynamic correlation effects are also introduced via the form of the wavefunction through spin projection (Eq. 4),

these effects will be also considered if the exchange functional already covers an important amount of non-dynamic correlation effects [31]. Thus, the application of spin projection techniques to DFT calculations results, probably, in the suppression (or double counting) of such non-dynamic correlation effects. Hence the following equation was proposed where the energy of the "broken-symmetry" state is not projected [32]:

$$E_{BS} - E_{HS} = (2S_1S_2 + S_2)J \tag{5}$$

where $S_2 \leq S_1$. These assumptions have been confirmed recently by performing calculations including the Perdew-Zunger correction of the self-interaction error [33]. As expected, the J values obtained including the spin projection (Eq. 4) when the self-interaction correction is included are very similar to those corresponding to the non-projected case (Eq. 5) without the self-interaction correction. Due to the huge computational resources needed to include the self-interaction correction even for small systems, the best procedure is to employ Eq. (4) for self-interaction free methods, such as Hartree-Fock and Eq. (5) for methods based on density functional theory.

Recently, this approach was extended for the theoretical estimation of the exchange coupling constants of any polynuclear complex with n different J_{ij} values through the calculation of n+1 single-determinant energies corresponding to different spin distributions [34]. Such energies, as indicated above, are related to the eigenvalues of the Ising Hamiltonian (identical to the diagonal matrix elements of the Heisenberg Hamiltonian) and it is possible to build up a system of n equations with n unknowns, the J_{ij} values. There are 2^n possible spin distributions that can be generated by flipping of the spins and the choice of n+1 distributions among them must be done in order to obtain a compatible set of linear equations. This procedure is similar to that proposed by Noodleman and Case for the iron-sulfur clusters [26], keeping in mind the difference due to the spin projection of the low spin states. An alternative, simpler approach proposed to obtain the same equations is just to analyze the changes in sign of the local spin moments between spin distributions i and j and to employ the pairwise expression of the Ising (or Heisenberg) Hamiltonians.

Since it was found that, for dinuclear complexes, the energy difference between the ferromagnetic and the antiferromagnetic spin configurations is given by Eq. (5), that approach can be extended to polynuclear compounds by just expressing the difference in energy between different spin configurations as a sum of pairwise interactions [34]. Hence for a linear trinuclear system two exchange coupling constants can be defined, J_{12} between nearest neighbors and J_{12} between next-nearest neighbors. The relative energies of the spin configurations in **1** with S=1/2 local spin moments shown are therefore given by Eqs. (6a) and (6b):

$$E_{HS} - E_{LS1} = -2J_{12} \tag{6a}$$

$$E_{HS} - E_{LS2} = -J_{12} + J_{13} \tag{6b}$$

As an example of how these expressions can be obtained, consider the HS and LS1 configurations (**1**) (Scheme 1). They differ in the two nearest-neighbor interactions (1–2 and 2–3), whereas the next nearest neighbor interaction (1–3) is identical in both cases. Hence the energy difference between these two spin configurations is given by two times the energy difference due to each interaction $(2S_1S_2+S_2)J_{12}$ (which gives $-2J_{12}$, see Eq. 6a, because $J_{12}=J_{23}$ and $S_1=S_2=S_3=1/2$). The differences between HS and LS2, on the other hand, appear in the 2–3 first neighbor interaction and in the 1–3 next-nearest-neighbor interaction, and the resulting expression is given by Eq. (6b).

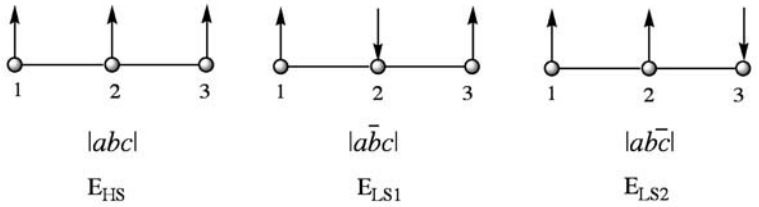

1

In the case of Hartree-Fock calculations or for self-interaction free methods in general, each interaction term has the form $2S_iS_jJ_{ij}$ and the expressions for the energy differences, obtained in a similar way, are those given in Eqs. (7):

$$E_{HS} - E_{LS1} = -J_{12} \tag{7a}$$

$$E_{HS} - E_{LS2} = -J_{12}/2 + J_{13}/2 \tag{7b}$$

The same result would be obtained if the diagonal terms of the Heisenberg Hamiltonian were taken as the energies of the spin configurations in **1**:

$$E_{HS} = -J_{12}/2 - J_{13}/4 \tag{8a}$$

$$E_{LS1} = J_{12}/2 - J_{13}/4 \tag{8b}$$

$$E_{LS2} = -J_{13}/4 \tag{8c}$$

A similar approach was employed by Pederson and Kortus to calculate the exchange coupling constants of some polynuclear complexes [35]. Instead of solving a set of equations, they have calculated the energies including the spin projection corresponding to more spin distributions that those needed to build up the system of equations as previously described, performing a fitting procedure to determine the J values. In this way, the calculated J values are more representative of a larger number of states of the sys-

tem, by eliminating some possible dependence of the obtained J values with the choice of the calculated spin distributions.

It is worth mentioning, despite the fact that they are not strictly based on DFT methods, the recent studies of Davidson and coworkers employing a semiempirical method called ZILSH derived from the ZINDO approach with the local spin formalism for the calculation of the of the $S_a \cdot S_b$ terms [36–38]. The application of such an approach to some series of polynuclear Fe(III) complexes provides reasonable J values that reproduce correctly the multiplicities of the ground states observed experimentally [39].

2.1 Calculation of the Exchange Coupling Constants for Test Systems

Systematic studies of the accuracy of theoretical methods in the calculation of the exchange coupling constants by comparison with experimental data or with high-level theoretical methods have been performed for dinuclear transition metal complexes. Probably, the test system most studied for these purposes has been the hypothetical H···He···H biradical complex using Full-CI results as [34]. Despite their simplicity the conclusions of the methods based on density functional theory deduced with this system have been corroborated subsequently for transition metal complexes. The main difference concerns the Hartree-Fock method, as it provides reasonable values for the H···He···H system; however, the lack of electronic correlation results in poor agreement for transition metal complexes [32]. The main conclusions concerning the DFT methods [40] can be summarized as: the local methods provide a large overestimation of the exchange coupling values that it is partially corrected for the inclusion of non-local GGA approximations. However, the best results are obtained when the exact exchange is included through hybrid functionals, such as B3LYP [41]. In this case, the accuracy of the results considering the controversial option of the non-projection of the low spin states is similar to that obtained with the best multiconfigurational methods [42, 43]. If the spin-projection is employed all the commonly-used functionals give, logically, an overestimation of the exchange coupling constants, for the reasons discussed previously.

Recently, a similar study was performed using multicenter structures of the H···He···H biradical system (**2–5**) to check if the conclusions obtained for dinuclear complexes can be extended to polynuclear complexes [34]. Although there is no experimental information for such hypothetical compounds, highly accurate post Hartree-Fock calculations were employed to obtain reference values for comparison.

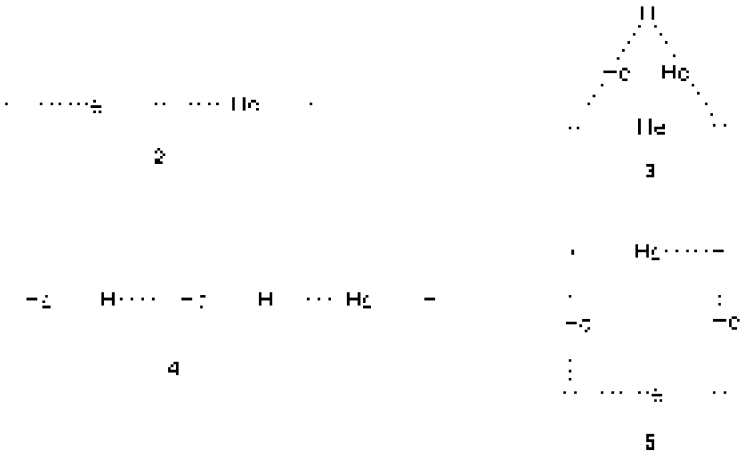

The J_{ij} values obtained for such systems using several methods are presented in Table 1. The calculated values for these four systems show the same trends found earlier for the H···He···H dinuclear model: the spin-projected Hartree-Fock method, slightly underestimates the J values, while the UBLYP method overestimates them. The UB3LYP hybrid functional provides values intermediate between those obtained in CASSCF and CASPT2 calculations [44]. The J values for next-nearest neighbor interactions obtained in CASPT2 and UB3LYP calculations are in good agreement, whilst those obtained with the CASSCF method seem to overestimate the ferromagnetic contributions, compared to the more accurate CASPT2 results. A problem

Table 1 Calculated exchange coupling constants J (cm^{-1}) for different H···He multicenter complexes represented in **2**–**5**, with H···He distances equal to 1.625 Å. The UHF values have been obtained by using spin projection while the DFT ones are non-projected [34]

Model	UHF	UB3LYP	UBLYP	CASSCF small[a]	CASPT2 small[a]	CASSCF large[b]	CASPT2 large[b]
2							
J_{12}	−453	−552	−677	−504	−586	−526	−595
J_{13}	−1.3	−4.7	−8.0	+20	−4.0	+21	−5.8
3							
J_{12}	−151	−184	−220	−174	−197	−166	−195
4							
J_{12}	−454	−554	−681	−525	−587	−546	−594
J_{23}	−488	−585	−720	−514	−629	−515	−639
J_{13}	−1.3	−4.4	−6.7	+39	−3.4	+42	−8.0
5							
J_{12}	−410	−490	−599	−444	−516	−463	−521
J_{13}	−1.2	−3.2	−0.6	+13	−8.8	+28	−5.2

[a] Active space (electrons, orbitals): **1**, (7, 5); **2**, (9, 6); **3**, (10, 7); **4**, (12, 8)
[b] Active space (electrons, orbitals): **1**, (7, 8); **2**, (9, 9); **3**, (10, 11); **4**, (12, 12)

Table 2 Exchange coupling constants J (cm^{-1}) calculated at B3LYP level for polynuclear oxalato-bridged Cu(II) complexes (see **6**) [34]

	J_{12}	J_{13}	J_{23}	J_{14}
Dinuclear Cu_2	−369			
Trinuclear	−387	−5.4		
Trinuclear Cu_2Zn	−381			
Trinuclear CuZnCu		−2.8		
Tetranuclear	−375	−5.8	−421	−0.1

that can be ascribed to the non-inclusion of dynamic correlation effects in the CASSCF calculations. For these reasons, the B3LYP functional is a good choice for the calculation of the exchange coupling constants in hypothetical benchmark systems with several paramagnetic centers. If we turn our attention to polynuclear transition metal complexes, in the same work, there is an analysis using the B3LYP functional of the exchange coupling constants in polynuclear oxalato-bridged Cu(II) complexes.

The calculated exchange coupling constants for the some polynuclear models similar to that shown in **6** are reported in Table 2 [34]. An interesting procedure to calculate exchange coupling constants in large polynuclear complexes is the substitution of some paramagnetic cations by similar diamagnetic cations, keeping only two paramagnetic cations. Thus, the new system can be treated as a dinuclear system and the exchange coupling between the two remaining paramagnetic center can be obtained directly with two energy calculations. For instance, in the oxalato-bridged trinuclear complex by replacing one of the Cu(II) ions by a diamagnetic Zn(II) cation. The resulting Cu_2Zn complexes are equivalent to a dinuclear Cu(II) complex from the magnetic point of view and it is possible to obtain the two exchange coupling constants (J_{12} and J_{13}) depending on which of the copper atoms is replaced by zinc.

From the results collected in Table 2 for oxalato-bridged Cu(II) model complexes, the conclusions were that the values of the calculated J_{12} constants are within the range of the experimental values for oxalato-bridged dinuclear complexes (−284 to −402 cm^{-1}) [45]. Likewise, the calculated J values obtained by substituting one Cu(II) cation by one Zn(II) ion are in very good agreement with those obtained directly for the trinuclear complex. Thus, the strategy of substituting paramagnetic atoms by diamagnetic

Fig. 1 Representation of the bis(μ_2-*N,N′*-propane-1,3-diyl-bis(oxamato))-bis(*N,N,N′,N′*-tetramethylethane-1,2-diamine)- bis-(selenocyanato)-tri-copper(II) dihydrate complex. The carbon, copper, oxygen, selenium, nitrogen, and hydrogen atoms are represented by *spheres of different shades of gray, from dark to bright*, respectively

ones to reduce the evaluation of coupling constants to calculations for magnetically dinuclear complexes seems highly promising and might be extended to more time demanding methods. The next-nearest neighbor (J_{13}) and next-next-nearest neighbor (J_{14}) coupling constants are much smaller than the nearest neighbor one, as expected the J_{23} value for the tetranuclear complex is slightly larger than that corresponding to the interaction involving a terminal copper ion (J_{12}) as found also for the H···He systems (see Table 1).

In the same paper [34], some non-modeled trinuclear complexes were also studied. For example, the full structure of an oxamato-bridged trinuclear Cu(II) complex, bis(μ_2-*N,N′*-propane-1,3-diyl-bis(oxamato))-bis(*N,N,N′,N′*-tetramethylethane-1,2-diamine)-bis-(selenocyanato)-tri-copper(II) dihydrate, shown in Fig. 1, including counterions and solvent molecules that are close to the molecule of the complex. The experimental data obtained from magnetic susceptibility measurements has been fitted with just one exchange coupling constant, J_{12}=−355.7 cm^{-1}.[46] The results using the UB3LYP method confirm that the interaction between the terminal Cu(II) ions is rather weak, −2.2 cm^{-1}, while the coupling constant between two adjacent Cu(II) ions is −277 cm^{-1}, thus reproducing the sign and magnitude of the experimental J value.

A heterotrinuclear Mn(III) complex with tris(dimethylglyoximato)copper(II) tetranions as bridging ligands (see Fig. 2) was also analyzed. This compound is interesting because it contains different paramagnetic centers having more than one unpaired electron in two of the paramagnetic centers. The calculated coupling constants using the B3LYP functional were −141.3 cm^{-1} for the Mn(III)Cu(II) interaction and −6.2 cm^{-1} for the Mn(III)Mn(III) one, which compare very well with the experimental values of −126.2 and −5.6 cm^{-1}, respectively [47].

Fig. 2 Representation of a heterotrinuclear Mn(III) complex with tris(dimethylglyoximato)copper(II) tetranions as bridging ligand. The carbon, copper, oxygen, manganese, nitrogen, and hydrogen atoms are represented by *spheres of different shades of gray, from dark to bright*, respectively

The presence of more than two paramagnetic centers causes the existence of next-nearest neighbor interactions. It is possible to deduce from the values presented previously that such interactions are usually small and antiferromagnetic. It is a well-known fact the strong dependence in hydroxo-bridged Cu(II) dinuclear complexes of the exchange interaction with structural parameters, such as the Cu-O-Cu angle and the out-of-plane shift of the hydrogen atoms of the bridging ligands [48, 49]. However, the analysis of the magnetostructural correlation for the next-nearest neighbor interaction in trinuclear hydroxo-bridged Cu(II) complexes show a practically constant value non-dependent of the structural parameters previously indicated, while the nearest-neighbor interaction presents practically the same magnetostructural correlations as those in the dinuclear complexes [50]. It is also worth noting that while the exchange pathway is constituted for only one oxygen atom, the next-nearest neighbor interaction is close to -60 cm^{-1}. This is considerable larger than the values previously indicated for larger bridging ligands. For that reason, as was indicated above, these interactions must be considered carefully, in many cases, during the fitting of the experimental magnetic susceptibility.

As the conclusion of this section, it is interesting to point out that a general procedure to obtain the exchange coupling constants of any polynuclear complex, including multicenter paramagnetic organic molecules, is described in the literature. Furthermore, the application of DFT methods using hybrid functionals to calculate exchange coupling constants in polynuclear complexes provides excellent results as do those described in the literature previously for dinuclear transition metal complexes.

3 Historical Overview of the Calculation of Exchange Interactions in Polynuclear Systems

3.1 Transition Metal Complexes with a Cubane Core

As was indicated previously, the first publication of a theoretical study to calculate the exchange coupling constants using DFT methods was devoted to the iron-sulfur clusters present in ferredoxine [21]. These metallo-proteins play a significant role in many electron transfer processes [51] and also in catalysis [52], e.g., in some dehydratases, in practically all types of living organisms. The analysis of the literature also indicates that considering as parameter the number of publications; it is also the most studied system in this field [24–26, 53–63]. Likewise, the redox potentials of such systems have been extensively studied to understand the electron transfer processes in which these iron-sulfur clusters are involved [59, 64, 65]. Nevertheless, these iron-sulfur clusters are particularly complex systems due to the diversity of oxidation states that they can present and the mixed valence character for the simultaneous presence of Fe(II) and Fe(III) cations. In such compounds, the electrons involved in the double exchange appear completely localized in the "broken" symmetry low-spin states whilst they are delocalized in high spin solutions. This different behavior must be considered by introducing B resonance contributions into the equations to obtain the J values. The model employed in the calculation is usually $[Fe_4S_4(SCH_3)_4]^{n-}$ where the methyl substituents replace the cysteine groups of the protein (see Fig. 3). The first results obtained for the J value of the $[Fe_4S_4(SCH_3)_4]^{2-}$ complex with the Xα-SW and Xα-LCAO methods are -376 and -454 cm^{-1}, respectively [24]. Despite the local character and the simplicity of the functional, such values are in good agreement with the experimental data of -464 cm^{-1} of a synthetic model of the protein [66]. However, the same approach overestimates

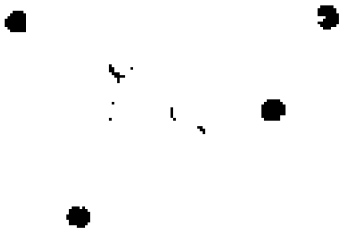

Fig. 3 Molecular model $[Fe_4S_4(SCH_3)_4]^{n-}$ of the iron-sulfur active center of ferredoxine proteins. The carbon, iron, sulfur, and hydrogen atoms are represented by *spheres of different shades of gray, from dark to bright*, respectively

Table 3 Calculated J values (cm^{-1}) for the series of iron-sulfur complexes $[Fe_4S_4(SCH_3)_4]^{n-}$ (n=0, 1, 2, 3, and 4) by using the Becke-Perdew functional and performing a structural optimization. Also the available experimental data and the multiplicity of the obtained ground state are reported [59]

n		S	J_{calc}	J_{exp}
0	4 Fe(III)	0	−907	
1	3 Fe(III)·Fe(II)	1/2	−725, −675	−797, −652
2	2 Fe(III)·2Fe(II)	0	−645	−340
3	Fe(III)·3Fe(II)	1/2	−519	
4	4 Fe(II)	0	−112	

considerably the J values for equivalent dinuclear and trinuclear complexes. The analysis of the calculated J values shows that, for this family of compounds, J(Fe(III)-Fe(III))>J(Fe(III)-Fe(II))>J(Fe(II)-Fe(II)) [26]. Recently, Torres et al. have calculated the J values for $[Fe_4S_4(SCH_3)_4]^{n-}$ (n=0, 1, 2, 3, and 4) (Table 3) using the GGA functional proposed by Becke and Perdew, confirming the trend indicated previously [59].

The molecular bistability that presents the cyclopentadienyl-capped iron-sulfur cluster $[(C_5H_5)_4Fe_4S_4]^{2+}$ has been studied by McGrady using the Becke-Perdew functional [67, 68]. These systems show two different minima, a triplet state with D_2 symmetry and a C_2-symmetric singlet state. For the same complex, even small changes, for example the kind of counterion and, consequently, the packing forces are enough to change the symmetry and the ground state of these iron-sulfur cubanes.

Czerwinski and coworkers have studied the exchange coupling constants of the $[Fe_6S_6Cl_6]^-$ cluster which is the active center in some proteins and enzymes [69, 70]. The structure can be described as two cubanes sharing one face, with the Fe(II) cation placed in the shared face (see Fig. 4) while the

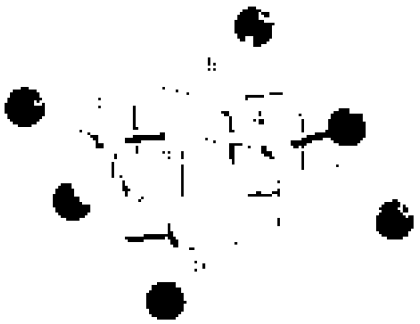

Fig. 4 View of $[Fe_6S_6Cl_6]^-$ iron-sulfur complex. The Fe(II) cation is placed in the position labeled as 6. The carbon, iron, sulfur, and hydrogen atoms are represented by *spheres of different shades of gray, from dark to bright*, respectively

other five positions are occupied by Fe(III) cations. The Hamiltonian employed to describe the interactions in this complex is the following:

$$\hat{H} = -J_1\left(\hat{S}_1 + \hat{S}_2 + \hat{S}_3 + \hat{S}_4 + \hat{S}_5\right)\hat{S}_6 - J_2\left(\hat{S}_1\hat{S}_4 + \hat{S}_1\hat{S}_5 + \hat{S}_2\hat{S}_3 + \hat{S}_2\hat{S}_5 + \hat{S}_3\hat{S}_5 + \hat{S}_4\hat{S}_5\right) - J_3\left(\hat{S}_1\hat{S}_2 + \hat{S}_3\hat{S}_4\right) - J_4\left(\hat{S}_1\hat{S}_3 + \hat{S}_2\hat{S}_4\right) \quad (9)$$

The results obtained using the BLYP functional and numerical basis sets are -22 cm^{-1} for the Fe(II)-Fe(III) interaction J_1 while the J_2, J_3, and J_4 values corresponding to the Fe(III)-Fe(III) interactions are -146, $+130$, and -81 cm^{-1}, respectively [71]. More recently, the possible ground state of the $[Fe_6S_6]^{2+}$ cluster has been analyzed using DFT calculations with the hybrid B3LYP functional. This cluster is more complex than the one previously described due to the presence of four Fe(II) cations, resulting in several possible distributions of the cations. The inclusion of the double exchange terms leads to a S=3 ground state [70].

In the field of the bioinorganic compounds, it is also worth mentioning the theoretical studies of the FeMo cofactor of the nitrogenase in the Noodleman's group [72–74]. The structure of the FeMo cofactor is closely related to the iron-sulfur clusters previously discussed, and can be described as two Fe_4S_4 and $MoFe_3S_4$ cubanes sharing an edge, where recently the presence of a light atom was discovered. Some experimental and theoretical evidence suggest that this is a nitrogen atom (see Fig. 5) [75]. Noodleman et al. have analyzed the energy of several spin distributions for the Mo(IV)·4Fe(II)·3Fe(III) and Mo(IV)·6Fe(II)·Fe(III) oxidation levels [76]. The more oxidized assignment is consistent with the ENDOR data [77] while the second one was proposed on the basis of Mössbauer measurements [78].

The first studies using DFT methods not including the central atom [72] suggest that the Mo(IV)·6Fe(II)·Fe(III) oxidation level with a spin distribu-

Fig. 5 Representation of the active site of the nitrogenase. The central part corresponds to the $MoFe_7S_9$ cluster. The carbon, molybdenum, oxygen, iron, sulfur, nitrogen, and hydrogen atoms are represented by *spheres of different shades of gray, from dark to bright*, respectively

tion shown in **7** fulfills most of the experimental data, such as redox potentials and structural parameters. This is also, theoretically, one of the more stable distributions. In this spin distribution, there is an antiferromagnetic interaction between the terminal Fe(III) cation and the other three Fe(II) ions of the Fe_4 cubane resulting in an S value of 7/2. This Fe_4 cubane is also antiferromagnetically coupled with the Fe_3 triangle that has S=2 due to the frustration, resulting in a total value of 3/2 which is in agreement with the experimental measurements. However, the inclusion of the central nitrogen atom is "non-innocent" for the electronic structure of this system. Dance has carried out an investigation [79], using a numerical basis set with the BLYP functional six different oxidation levels, to check which of them has a S=3/2 state with low energy. There are three feasible oxidation levels but only one of them, Mo(IV)·4Fe(II)·3Fe(III), shows a redox potential in agreement with the experimental data. Other authors, such as Noodleman [76] and Norskov [80], have reached the same conclusion, also using different criteria such as geometrical parameters by comparison of optimized DFT structures with the experimental crystal data. The more stable spin distribution is the one that is proposed for the other oxidation level (see **7**), with the two extra Fe(III) cations placed in the Fe_3 triangle with opposite spins corresponding to an antiferromagnetic coupling between them. This result was expected because, as was indicated previously for the iron-sulfur cluster, the J(Fe(III)-Fe(III)) value should be the strongest antiferromagnetic coupling.

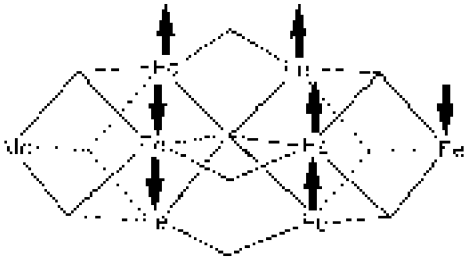

7

A theoretical study using the B3LYP functional devoted to the molecular complexes with a Cu_4O_4 core was published recently.[81] This kind of structure can be classified into three groups according to the intermetallic distance. The first contains complexes with two short and four long Cu···Cu distances, called *2+4* (see **8**). The second class presents four short and two long Cu···Cu distances, and will be labeled from here on as *4+2* (those with S_4 symmetry, **9**). Finally, for compounds in the third class all six Cu···Cu distances are similar, and they will be termed *6+0*.

Two systems were selected for such a study: a complex with a *2+4* type structure and hydroxo bridging ligands and an alkoxo-bridged complex that belongs to the *4+2* category (see Fig. 6).

The results for the *2+4* type complex indicate that the high spin state (S=2) is the ground state and the two calculated exchange coupling constants, corresponding to the intradimer (J) and interdimer coupling (J′), are +68.0 and +0.6 cm^{-1}, respectively. Experimental values are +15.1 and +0.2 cm^{-1}, respectively [82]. It is worth noting that this complex shows a relatively small experimental J value compared with other hydroxo-bridged binuclear complexes with similar Cu-O-Cu angles, even if it shows a small roof-shape distortion of the Cu_2O_2 framework which was found to enhance the ferromagnetic behavior [48, 49].

The second complex containing a Cu_4O_4 core has alkoxo-bridging ligands and adopts a 4+2 structure with approximate S_4 symmetry. The calculated J and J′ values are +44.1 and +6.2 cm^{-1}, respectively. Comparison with the experimental values, +44.9 and −16.3 cm^{-1}, indicates a discrepancy in the sign of J′ [83]. The analysis of the superexchange pathway for the J′ constant

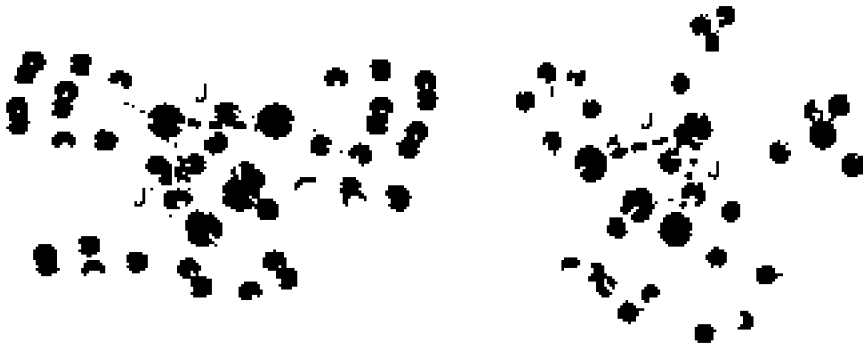

Fig. 6 Representation of two complexes with Cu_4O_4 cubane core. Attending to the proposed classification, one of them has a 2+4 type structure (*left*, see **8**) while the second one belongs to the 4+2 category (*right*, see **9**) The carbon, copper, oxygen, chlorine, nitrogen, and hydrogen atoms are represented by *spheres of different shades of gray, from dark to bright*, respectively

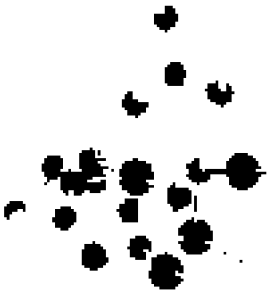

Fig. 7 Representation of a complexes containing the $[Mn(IV)Mn(III)_3O_3Cl]^{+6}$ cubane core. The Mn(IV) cation is that coordinated to the three oxygen atoms of the cubane, labeled as 4 in the exchange interactions described in the text (see Eq. 10). The carbon, manganese, oxygen, chlorine, and hydrogen atoms are represented by *spheres of different shades of gray, from dark to bright*, respectively

shows the presence of two long Cu···O distances of 2.5 Å at each side of the bridge. Equivalent binuclear complexes with long bridging Cu···O distances show rather small exchange coupling constants, of ca. ±1 cm^{-1}. An alternative procedure to calculate the coupling constants for this complex is to transform the Cu_4O_4 core in to a simple Cu(II) binuclear complex by replacing two Cu(II) centers by diamagnetic Zn(II) ones. The new hypothetical systems generated in this way are equivalent to Cu(II) binuclear complexes and allows one to calculate the two coupling constants depending on the sites occupied by the Cu(II) atoms. This approach gives values of J and J′ of +49.4 and +2.9 cm^{-1}, respectively, very close to those obtained from the calculation for the original Cu_4O_4 core.

The exchange coupling constants of a complex with a $[Mn(IV)Mn(III)_3O_3Cl]^{+6}$ cubane core (see Fig. 7) were calculated by Noodleman et al. using an LCAO X-α method [84]. Two exchange coupling constants have been employed to describe the interaction using the following Hamiltonian:

$$\hat{H} = -J_{33}\left(\hat{S}_1\hat{S}_2 + \hat{S}_1\hat{S}_3 + \hat{S}_2\hat{S}_3\right) - J_{34}\left(\hat{S}_1\hat{S}_4 + \hat{S}_2\hat{S}_4 + \hat{S}_3\hat{S}_4\right) \quad (10)$$

where J_{33} and J_{34} correspond to the Mn(III)-Mn(III) and Mn(III)-Mn(IV) interactions, respectively. The results including a perturbational GGA correction to the local results are +38.6 and −93.2 cm^{-1} for J_{33} and J_{34}, respectively, which is good agreement with the experimental values of +24.2 and −53.6 cm^{-1} [85]. The analysis of the spin populations of the S=9/2 single-determinant state reveals the predominance of a polarization mechanism in the exchange pathways for this kind of interactions.

One of the problems in polynuclear complexes with antiferromagnetic coupling, for instance in cubane structures, is the existence of frustration due to the impossibility that all the spins adopt the opposite direction in respect to their neighbors when the interactions are antiferromagnetic. This physical behavior results in a loss of the co-linearity of the spins, usually called spin canting. In order to study such effect in polynuclear transition metal complexes, Yamaguchi and coworkers have implemented a generalized spin density functional theory that allows to the spin adopt different orientations in the space [86–88]. The application of such an approach has been tested with some polynuclear complexes, such as Mn_4O_4 cubanes.

3.2 Single-Molecule Magnets

Pederson and coworkers have studied the exchange coupling constants in different polynuclear complexes, some of them presenting single-molecule magnet behavior [89]. They have employed their own computer code NRLMOL using the generalized-gradient approximation functional proposed by Perdew, Burke and Ernzerhof (PBE) [90], and Gaussian basis sets. The $K_6[V_{15}As_6O_{42}(H_2O)]\cdot 8H_2O$ compound is a polyoxometalate complex synthesized by Müller et al. showing a ground state with S=1/2 as result of the interaction of the 15 V(IV) cations [91, 92]. The structure can be described as two parallel hexagons formed by the V(IV) cations with a central triangle. The analysis of the topology reveals that there are six different exchange coupling constants (see Fig. 8). The structure was optimized using the PBE functional and thirteen spin configurations where calculated to obtain, using a fitting, the six exchange coupling constants: J=−290.3, J′=22.7, J″=−15.9, J_1=−13.8, J_2=−23.4, and J_3=−0.55 meV (1 meV=8.065 cm^{-1}) [35, 93]. It is

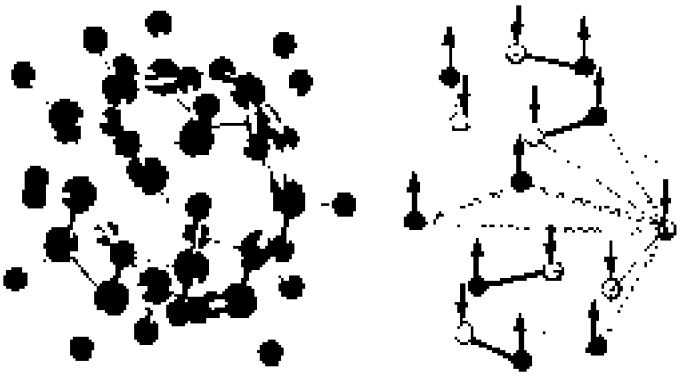

Fig. 8 Representation of the molecular structure of the V_{15} complex (*left*). The *larger spheres* correspond to the vanadium atoms. Scheme showing the interactions between the V(IV) cations corresponding to the six exchange interactions considered for the description of the magnetic properties (*right*)

worth noting the presence of a ferromagnetic coupling in this compound. The results of the diagonalization of the Heisenberg Hamiltonian matrix indicate a ground state with S=1/2 whilst the first excited state has S=3/2. This is in agreement with the experimental data, however, the calculated doublet-quadruplet gap is 10 K which is significantly larger than the experimental value of 3.7 K [94]. Likewise, there are also important differences between the calculated and experimental magnetic susceptibilities. Both discrepancies can be explained by the too large calculated J values. Boukhvalov et al. have performed a similar study of the V_{15} complex using a LDA+U method [95] obtaining the following results for U=5.0 eV, J=−139.4, J′=−5.2, J″=−20.6, J_1=−29.0, J_2=−21.0, and J_3=−0.6 meV [96]. They considered also three next-nearest-neighbor interactions with relatively small exchange coupling values with the same order of magnitude as the J_3 interaction. They analyzed the influence of the U parameter in the calculated values. The indicated value being the one that better reproduces the experimental magnetic susceptibility. The inclusion of the on-site repulsion parameter U improves the results provided by the PBE functional and results in a better agreement with the experimental magnetic susceptibility and a doublet-quadruplet gap of 4.92 K.

Recently, a new single-molecule magnet $[Mn_4O_3Cl_4(O_2CEt)_3(py)_3]_2$ was synthesized and characterized by Wernsdofer and coworkers [97]. The complex can be described as a dimer of a 3Mn(III)·Mn(IV) complex through hy-

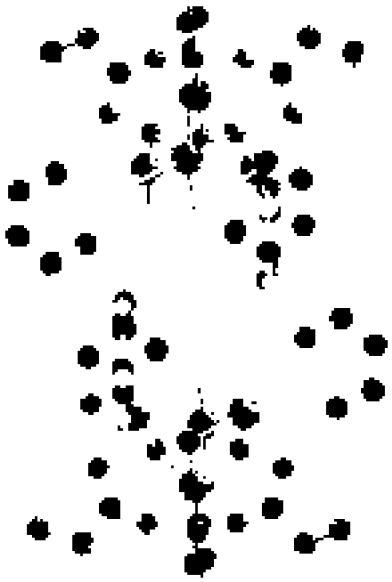

Fig. 9 View of the molecular structure corresponding to the $[Mn_4O_3Cl_4(O_2CEt)_3(py)_3]_2$ dimer complex. The carbon, manganese, oxygen, chlorine, nitrogen, and hydrogen atoms are represented by *spheres of different shades of gray, from dark to bright*, respectively

drogen bonds and Cl···Cl interactions, usually called Mn_4 dimer (see Fig. 9). Each monomer has S=9/2, due to the ferromagnetic coupling between the three Mn(III) cations, being the exchange coupling with the Mn(IV) cation through oxo bridging ligands antiferromagnetic. This compound exhibits a new and peculiar behavior, showing quantum tunneling prior to magnetic field reversal and an absence of quantum tunneling at zero field in contrast with the typical single-molecule magnets, as Fe_8 and Mn_{12} complexes. The calculated exchange interaction using the PBE functional between the two Mn4 complexes is 0.24 K using the optimized structure for the monomer and 0.27 K when the experimental structure was employed [98, 99]. These two values are slightly larger than the experimental value of 0.1 K. The study of Pederson et al. also has shown a linear dependence between the logarithm of the calculated exchange constants and the monomer-monomer relative distance.

The Mn_{12} complex is considered as the prototype of single-molecule magnet and many studies were devoted to the original compound and its derivatives (see Fig. 10) [13, 14]. The exchange coupling constant of the Mn_{12} complex has also been calculated using different approaches (see Table 4) [100–102]. In this case, some experimental values have been proposed despite the

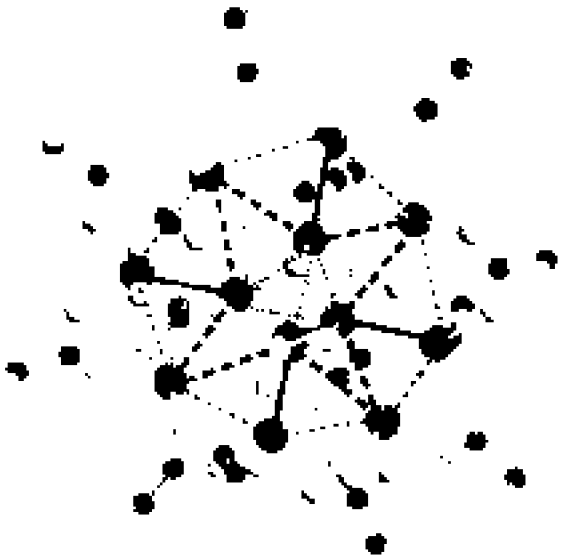

Fig. 10 Representation of the Mn_{12} complex. The four exchange interaction pathways have been indicated by different lines. The carbon, manganese, oxygen, and hydrogen atoms are represented by *spheres of different shades of gray, from dark to bright*, respectively

Table 4 Proposed parameters from experimental data and calculated values using different DFT methods of the exchange coupling constants J (K) for the Mn_{12} complex. The LDA+U results have been obtained using a U value of 8.0 eV

	Exp. 1	Exp. 2	Exp. 3	LDA+U	PBE	B3LYP
J_1	−225	−215	−119	−94	−115	−76
J_2	−90	−85	−118	−52	−84	−40
J_3	−90	−8	+8	−60	+4	+7
J_4	0	+64.5	−23	−14	−17	−9
Ref.	[14]	[103]	[104]	[101]	[102]	[100]

impossibility of performing a complete fitting of the magnetic susceptibility due to the large number of states involved. The experimental values labeled as Exp.1 correspond to the original experimental work but this set of parameters does not lead to an S=10 ground state [14]. The second set of proposed values reproduces correctly the multiplicities of the ground and first excited state and its experimental energy difference of 35 K. However, it does not lead to a satisfactory magnetization curve [103]. The third set of parameters seems to be more accurate as they reproduce correctly the essential experimental information [104]. The analysis of the DFT values indicates that only the results with the PBE functional and B3LYP functionals reproduce correctly the sign of the J_3 interaction. The theoretical methods indicate that the J_1 and J_2 interactions are the strongest antiferromagnetic coupling in agreement with the set of parameters proposed from the experimental data. As expected, due to the worse description of the exchange terms, the PBE functional leads to values that are larger than those provided by LDA+U or B3LYP functionals.

This section has been devoted to show a historical perspective of the theoretical work dedicated to studying the exchange interactions in polynuclear transition metal complexes. As indicated previously, the other important parameters that controls the magnetic properties, especially in the case of the single-molecule magnets, are those related to the magnetic anisotropy that can be quantified through the E and D zero-field splitting parameters. Despite this review being mainly dedicated to the exchange interactions, it is worth making a brief discussion about the calculation of the zero-field parameters due to the importance of the magnetic anisotropy effects. The study of such parameters for single-molecule magnets was carried out in Pederson's group by introducing the spin-orbit effect using a perturbative approach [17, 105–108]. The results using the PBE functional for some polynuclear complexes are shown in Table 5.

The agreement between the calculated zero-field splitting parameters using the PBE functional and the experimental values can be considered excellent taking into account the magnitudes involved. Only the case of the Co_4 complexes shows considerable deviations from the experimental values.

Table 5 Zero-field splitting parameters E and D (K) for some transition metal complexes calculated with the PBE functional and performing a structural optimization except for the Fe_4 complex where the experimental structure was employed

	S	D_{calc}	D_{exp}	E_{calc}	E_{exp}	Ref.
$Mn_{12}O_{12}(O_2CH)_{16}(H_2O)_4$	10	−0.56	−0.56	0	0	[17]
$[Mn_{10}O_4(2,2'\text{-biphenoxide})_4Br_{12}]^{4-}$	13	−0.06	−0.05	0	0	[110]
$[Fe_8O_2(OH)_{12}(tacn)_6]Br{\cdot}9H_2O$	10	−0.53	−0.205	0.054	0.038	[111]
$Co_4(CH_2C_5H_4\ N)_4(CH_3O)_4Cl_4$	6	−0.64	−5.6	0	0	[109]
$Fe_4(OCH_2)_6(C_4H_9ON)_6$	5	−0.56	−0.57	0.06	0.05	[89]
$Cr(N(Si(CH_3)_3)_2)_3$	3/2	−2.49	−2.66	0	0	[89]

These discrepancies are probably due to large differences between the optimized structure employed in the calculations and the experimental one [109, 112]. In conclusion, after the analysis of the presented results, it is possible to affirm that theoretical methods based on density functional methods can be employed to reproduce the experimental data and to analyze the exchange coupling constants and the zero-field splitting parameters of polynuclear transition metal as well as a predictive tool for the design of new molecular nanomagnets. In the next section, a detailed example of how theoretical methods can help in the analysis and understanding of the magnetic behavior of some hexanuclear transition metal complexes will be presented.

4
A Detailed Example: Hexanuclear Cu(II) and Ni(II) Polysiloxanolates

The hexanuclear complexes of Cu(II) and Ni(II) with polysiloxanolate ligands display different magnetic behavior [20]. The Cu(II) complex shows a ferromagnetic coupling with a ground state of S=3 [113], while in the case of the Ni(II) complex the ground state has S=0 [114]. Analysis of the crystal structures reveals a similar structure of the complex, but in the case of the nickel atom a chloride anion is placed in the center of the channel in order to complete the octahedral coordination whilst the copper atom has square pyramidal coordination (see Fig. 11).

The calculation of the exchange coupling constants of the polysiloxanolate complexes were performed using the B3LYP [41] as implemented in Gaussian98 code [115]. A basis set of triple-ζ quality [116] was employed for the copper and nickel atoms and a double-ζ quality for other atoms [117]. The only modelisation adopted was to substitute the phenyl rings of the polysiloxanolato ligands for hydrogen atoms. For the calculation of the exchange coupling constants the three spin distributions shown in **10** were calculated.

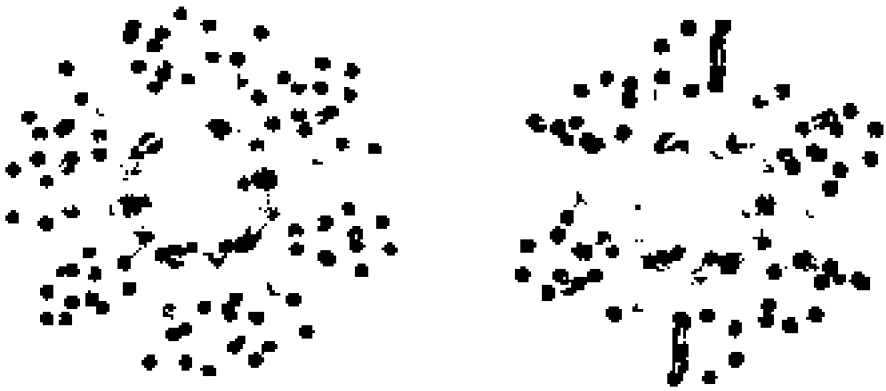

Fig. 11 View of the hexanuclear Cu(II) polysiloxanolate complex (*left*) and the corresponding Ni(II) complex with a chloride anion in the middle of the channel (*right*). The carbon, copper, nickel, oxygen, chlorine, silicon, and hydrogen atoms are represented by *spheres of different shades of gray, from dark to bright*, respectively

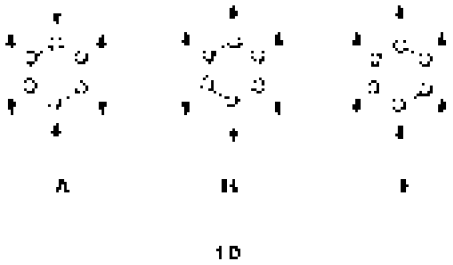

The analysis of the symmetry of the two complexes indicates that the Cu_6 complex has C_3 symmetry and C_2 the Ni_6 analogue. Many exchange coupling constants can in principle be calculated (see **11**) but these can be reduced by similarity, to facilitate the comparison with the experimental data as indicated in **12**. From the calculated energies of these spin configurations one can then extract exchange coupling constants by associating them to energy expressions obtained as explained above, assuming J (Eq. 12) for the Cu_6 complex:

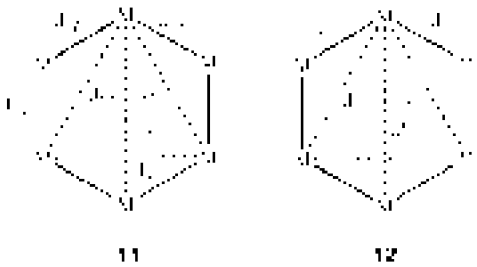

Table 6 Exchange coupling constants calculated (in cm^{-1}) for the Cu_6 complex using magnetically dinuclear compounds by means of diamagnetic Zn substitution (Cu_2Zn_4 column), and for the full hexanuclear complex using Eq. (11) [20]

	Cu_2Zn_4	Cu_6	Exp. 1	Exp. 2
J	+38 (av.)[a]	+37.9	+42	+37.5
J′	−0.3	−0.26	[b]	−0.62
J″	−1.3	-	[b]	−1.35

[a] Average of two first-neighbor interactions: J_{12}=+33 cm^{-1} and J_{13}=+43 cm^{-1}
[b] Assumed to be negligible

$$J = (E_A - E_F)/6\sigma \tag{11a}$$

$$J' = J - (E_A - E_B)/4\sigma \tag{11b}$$

or J'=0 (Eq. 12) for the Ni_6 complex:

$$J' = (E_A - E_B)/4\sigma \tag{12a}$$

$$J'' = (E_A - E_F)/3\sigma - 2J \tag{12b}$$

where σ=$2S_1S_2$+S_2 (being $S_1 \leq S_2$) because the non spin-projection option was employed due to use of the B3LYP functional (see above). The alternative approach of replacing four paramagnetic centers for diamagnetic Zn(II) cations, to obtain dinuclear complexes from the point of view of the magnetic properties, was also employed. The results for the Cu_6 and Ni_6 complexes are collected in Tables 6 and Table 7 respectively.

The coupling constants obtained for the Cu_6 complex with both approaches are consistent, giving the same description of the exchange interactions: first-neighbor interactions are ferromagnetic with J values of about +40 cm^{-1}, as expected from the Goodenough-Kanamori rules for bridging Cu-O-Cu angles of 91–92°, and are in excellent agreement with the value re-

Table 7 Exchange coupling constants calculated for the Ni_6 complex using magnetically dinuclear compounds by means of diamagnetic Zn substitution (Ni_2Zn_4Cl column), and for the full hexanuclear complex using Eq. (12), respectively, with or without the central chloride ion [20]

	Ni_6	Ni_2Zn_4Cl[a]	Ni_6Cl	Exp. 1	Exp. 2
J	+4.01	+22.8	+25.4	+18.6	+17.8
J′	+0.05	−3.3	-	−11.8[b]	−3.9
J″		−26.3	−28.1	−11.8[b]	−22.2

[a] For the Ni_2Zn_4Cl case, the values given are the averages of the analogous but non-equivalent coupling constants (J is the average of J_{12}, J_{13} and J_{24}; J′ is the average of J_{14}, J_{15}, and J_{45})
[b] J′ and J″ were assumed to be equal

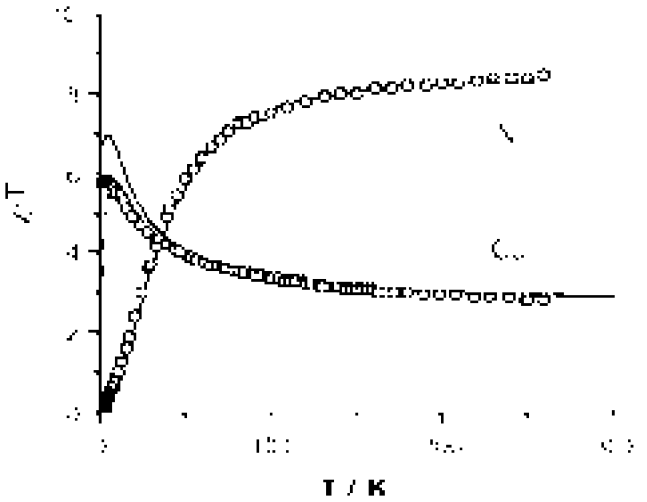

Fig. 12 Experimental (*circles*) χ·T (T) curve for the Cu_6 and Ni_6Cl complexes compared to the curves obtained with the theoretical J values

ported as the best fitting to the experimental magnetic susceptibility data. Second- and third-neighbor interactions are much weaker and just marginally antiferromagnetic, thus providing support to the hypothesis adopted for the first fitting of the experimental data, namely $J' \approx J'' \approx 0$. The temperature dependence of the magnetic behavior resulting from the theoretical J values through the full diagonalization of the Heisenberg matrix is plotted in Fig. 12 along with the previously reported experimental data, showing an excellent agreement, down to 20 K. A new fitting of the experimental data was performed guided by the calculated values yielding to coupling constants (Table 6, last column) consistent with the theoretical results obtained with three different approaches. Remarkably, the magnetic behavior of this Cu_6 complex can be explained basically through only first-neighbor interactions.

In the case of the Ni(II) complex, we will consider the calculations for the, so far hypothetical, molecule without the chloride guest, (abbreviated as Ni_6), and then it will be considered the real Ni_6Cl system. In the former case, the calculated energies for the three spin configurations considered are shown in Fig. 13 (center). It is seen that the energy ordering is the same as for the Cu_6 analogue but with smaller energy differences, and summarized by the resulting positive coupling constant between nearest neighbors.

The presence of the guest chloride in the center of the hexanuclear ring dramatically affects the energies of the spin configurations considered (Fig. 13, right), clearly indicating an antiferromagnetic behavior, as found experimentally. Such energy ordering scheme translates into the coupling

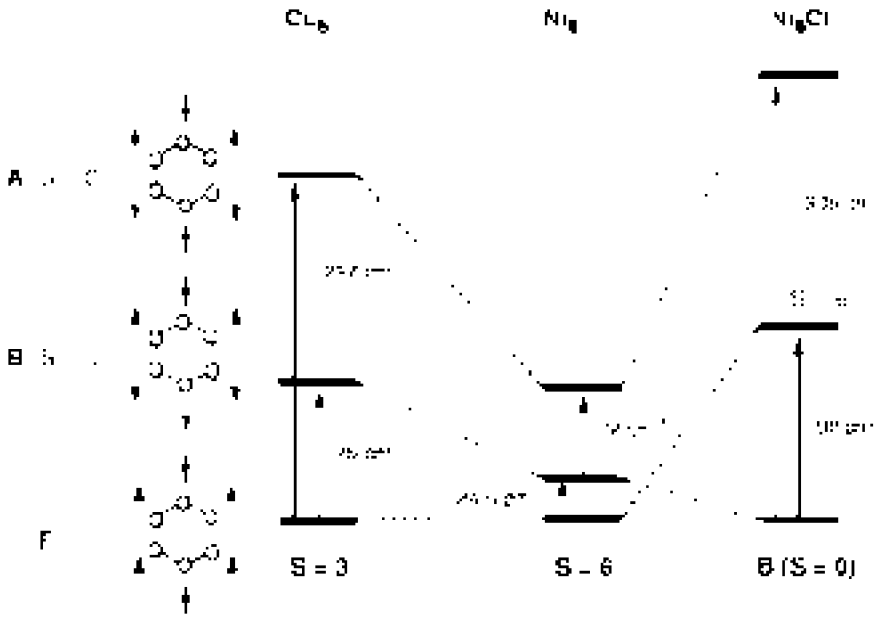

Fig. 13 Calculated energies for three different spin configurations of the hexanuclear polysiloxanolate complexes

constants of Table 7, significantly ferromagnetic between nearest-neighbors, of the same order of magnitude but antiferromagnetic for the interaction through a linear Ni-Cl-Ni bridge, and rather small for second neighbors. A better idea of how well the calculated coupling constants describe the magnetic behavior of this compound can be obtained by looking at Fig. 12, where the theoretical χ·T (T) curve together with the previously reported experimental values is shown. Therefore, in this case the approximation used in the first fitting of the temperature-dependence of the magnetic susceptibility ($J'=J''$) seems to be inappropriate. Using the calculated values as the starting point for a new fitting of the experimental data, a new set of exchange coupling constants was obtained (Table 7, last column) that are in excellent agreement with the calculated values for the Ni_2Zn_4Cl and Ni_6Cl clusters. Comparison of the results obtained for the pristine M_6 clusters with those for the Ni_6Cl compound with a chloride guest leads to the conclusion that the interaction of the Ni z^2 orbitals through the chloro-bridge determines its different behavior, as previously proposed by Cornia et al. [114].

Acknowledgements I would like to express my gratitude to Joan Cano, Antonio Rodríguez-Fortea, Santiago Alvarez, and Pere Alemany for their collaboration and many fruitful discussions in this research field.

References

1. Kahn O (1993) Molecular Magnetism. VCH, New York
2. Ruiz E, Alvarez S, Rodríguez-Fortea A, Alemany P, Pouillon Y, Massobrio C (2001) In: Miller JS, Drillon M (eds) Magnetism: molecules to materials II. Wiley-VCH, Weinheim, p 227
3. Ciofini I, Daul CA, Bencini A (2002) Rec Adv Comput Chem 1:106
4. Daul CA, Ciofini I, Bencini A (2002) In: Sen KD (ed) Reviews of modern quantum chemistry, vol 2. World Scientific, Singapore, p 1247
5. Ceulemans A, Chibotaru LF, Heylen GA, Pierloot K, Vanquickenborne LG (2000) Chem Rev 100:787
6. Ciofini I, Daul C (2003) Coord Chem Rev 238:187
7. Miller JS, Drillon M (eds) (2001) Magnetism: molecules to materials I. Models and experiments. Wiley-VCH, Weinheim
8. Miller JS, Drillon M (eds) (2001) Magnetism: molecules to materials II. Molecule-based materials. Wiley-VCH, Weinheim
9. Miller JS, Drillon M (eds) (2002) Magnetism: molecules to materials III. Nanosized magnetic materials. Wiley-VCH, Weinheim
10. Miller JS, Drillon M (eds) (2003) Magnetism: molecules to materials IV. Molecule-based materials (2). Wiley-VCH, Weinheim
11. Clement R, Decurtins S, Gruselle M, Train C (2003) Monatsh Chem 134:117
12. Marvaud V, Herrera JM, Barilero T, Tuyeras F, Garde R, Scuiller A, Decroix C, Cantuel M, Desplanches C (2003) Monatsh Chem 134:149
13. Gatteschi D, Sessoli R (2003) Angew Chem, Int Ed 42:268
14. Sessoli R, Gatteschi D, Caneschi A, Novak HA (1993) Nature (London) 365:141
15. Barra AL, Gatteschi D, Sessoli R (2000) Chem Eur J 6:1608
16. Cornia A, Gatteschi D, Sessoli R (2001) Coord Chem Rev 219/221:573
17. Pederson MR, Khanna SN (1999) Phys Rev B 60:9566
18. Benelli C, Cano J, Journeaux Y, Sessoli R, Solan GA, Winpenny REP (2001) Inorg Chem 40:188
19. Gatteschi D (2000) J Phys Chem B 104:9780
20. Ruiz E, Cano J, Alvarez S, Caneschi A, Gatteschi D (2003) J Am Chem Soc 125:6791
21. Aizman A, Case DA (1982) J Am Chem Soc 104:3269
22. Noodleman L (1981) J Chem Phys 74:5737
23. Noodleman L, Post D, Baerends EJ (1982) Chem Phys 64:159
24. Noodleman L, Case DA (1992) Adv Inorg Chem 38:423
25. Noodleman L, Peng CY, Case DA, Mouesca JM (1995) Coord Chem Rev 144:199
26. Noodleman L, Li J, Zhao X-G, Richardson WH (1997) In: Springborg M (ed) Density-functional methods in chemistry and materials science. Wiley, Chichester, p 149
27. Polo V, Grafenstein J, Kraka E, Cremer D (2003) Theor Chem Acc 109:22
28. Polo V, Grafenstein J, Kraka E, Cremer D (2002) Chem Phys Lett 352:469
29. Polo V, Kraka E, Cremer D (2002) Mol Phys 100:1771
30. Polo V, Kraka E, Cremer D (2002) Theor Chem Acc 107:291
31. Cremer D (2001) Mol Phys 99:1899
32. Ruiz E, Cano J, Alvarez S, Alemany P (1999) J Comp Chem 20:1391
33. Ruiz E, Polo V, Cano J, Alvarez S (2004) (to be published)
34. Ruiz E, Rodriguez-Fortea A, Cano J, Alvarez S, Alemany P (2003) J Comp Chem 24:982
35. Kortus J, Hellberg CS, Pederson MR (2001) Phys Rev Lett 86:3400
36. Clark AE, Davidson ER (2001) J Chem Phys 115:7382

37. Clark AE, Davidson ER (2002) J Phys Chem A 106:6890
38. Davidson ER, Clark AE (2002) Mol Phys 100:373
39. O'Brien TA, Davidson ER (2003) Int J Quant Chem 92:294
40. Koch W, Holthausen MC (2000) A chemist's guide to density functional theory. Wiley-VCH Verlag, Weinheim
41. Becke AD (1993) J Chem Phys 98:5648
42. Moreira IPR, Illas F, Calzado CJ, Sanz JF, Malrieu JP, Ben Amor N, Maynau D (1999) Phys Rev B 59:R6593
43. Caballol R, Castell O, Illas F, Moreira IPR, Malrieu JP (1997) J Phys Chem A 101:7860
44. Jensen F (1999) Introduction to computational chemistry. Wiley, Chichester
45. Cano J, Alemany P, Alvarez S, Verdaguer M, Ruiz E (1998) Chem Eur J 4:476
46. Ribas J, Diaz C, Solans X, Font-Bardia M (1997) J Chem Soc Dalton Trans 35
47. Birkelbach F, Florke U, Haupt H-J, Butzlaff C, Trautwein AX, Wieghardt K, Chaudhuri P (1998) Inorg Chem 37:2000
48. Ruiz E, Alemany P, Alvarez S, Cano J (1997) Inorg Chem 36:3683
49. Ruiz E, Alemany P, Alvarez S, Cano J (1997) J Am Chem Soc 119:1297
50. Rodríguez-Fortea A, Ruiz E, Alemany P, Alvarez S (2003) Monatsh Chem 134:307
51. Bertini I, Ciurli S, Luchinat C (1995) Struct Bonding 83:1
52. Beinert H, Kennedy MC, Stout CD (1996) Chem Rev 96:2335
53. Noodleman L, Norman JG Jr, Osborne JH, Aizman A, Case DA (1985) J Am Chem Soc 107:3418
54. Noodleman L, Case DA, Aizman A (1988) J Am Chem Soc 110:1001
55. Noodleman L, Case DA, Sontum SF (1989) J Chim Phys Phys Chim Biol 86:743
56. Noodleman L, Case DA, Baerends EJ (1991) In: Labanowski JK, Andzelm JW (eds) Density-functional methods in chemistry and materials science. Springer, Berlin Heidelberg New York, p 109
57. Noodleman L (1991) Inorg Chem 30:256
58. Noodleman L, Case DA, Mouesca JM, Lamotte B (1996) J Biol Inorg Chem 1:177
59. Torres RA, Lovell T, Noodleman L, Case DA (2003) J Am Chem Soc 125:1923
60. Fee JA, Castagnetto JM, Case DA, Noodleman L, Stout CD, Torres RA (2003) J Biol Inorg Chem 8:519
61. Mouesca J-M, Noodleman L, Case DA (1995) Int J Quant Chem Quant Biol Symp 22:95
62. Mouesca JM, Noodleman L, Case DA, Lamotte B (1995) Inorg Chem 34:4347
63. Mouesca J-M, Lamotte B (1998) Coord Chem Rev 178/180:1573
64. Mouesca J-M, Chen JL, Noodleman L, Bashford D, Case DA (1994) J Am Chem Soc 116:11898
65. Noodleman L (1988) Inorg Chem 27:3677
66. Papaefthymiou GC, Laskowski EJ, Frota-Pessoa S, Frankel RB, Holm RH (1982) Inorg Chem 21:1723
67. McGrady JE (1999) J Chem Soc Dalton Trans 1393
68. Knottenbelt SZ, McGrady JE (2003) J Am Chem Soc 125:9846
69. Matusiewicz M, Czerwinski M, Kasperczyk J, Kityk IV (1999) J Chem Phys 111:6446
70. Matusiewicz M, Czerwinski M, Kasperczyk J (2002) J Clust Chem 12:537
71. Czerwinski M (1999) Int J Quant Chem 72:39
72. Lovell T, Li J, Liu T, Case DA, Noodleman L (2001) J Am Chem Soc 123:12392
73. Lovell T, Torres RA, Han W-G, Liu T, Case DA, Noodleman L (2002) Inorg Chem 41:5744
74. Lovell T, Himo F, Han W-G, Noodleman L (2003) Coord Chem Rev 238/239:211

75. Einsle O, Teczan FA, Andrade SLA, Schmid B, Yoshida M, Howard JB, Rees DC (2002) Science 297:1696
76. Lovell T, Liu T, Case DA, Noodleman L (2003) J Am Chem Soc 125:8377
77. Lee H-I, Hales BJ, Hoffman BM (1997) J Am Chem Soc 119:11395
78. Yoo SJ, Angove HC, Papaefthymiou V, Burguess BK, Munck E (2000) J Am Chem Soc 122:4926
79. Dance I (2003) Chem Comm 324
80. Hinnemann B, Norskov JK (2003) J Am Chem Soc 125:1466
81. Ruiz E, Rodríguez-Fortea A, Alemany P, Alvarez S (2001) Polyhedron 20:1323.
82. Sletten J, Sorensen A, Julve M, Journaux Y (1990) Inorg Chem 29:5054
83. Tan XS, Fujii Y, Nukada R, Mikuriya M, Nakano Y (1999) J Chem Soc Dalton Trans: 2415
84. Schmitt EA, Noodleman L, Baerends EJ, Hendrickson DN (1992) J Am Chem Soc 114:6109
85. Hendrickson DN, Christou G, Schmitt EA, Libby E, Bashkin JS, Wang S, Tsai H-L, Vincent JB, Boyd PDW, Huffman JC, Folting K, Li Q, Streib WE (1992) J Am Chem Soc 114:2455
86. Nagao H, Nishino M, Shigeta Y, Soda T, Kitagawa Y, Onishi T, Yoshioka Y, Yamaguchi K (2000) Coord Chem Rev 198:265
87. Nagao H, Yamanaka S, Nishino M, Yoshioka Y, Yamaguchi K (1999) Chem Phys Lett 302:418
88. Yamaguchi K, Yamanaka S, Nishino M, Takano Y, Kitagawa Y, Nagao H, Yoshioka Y (1999) Theor Chem Acc 102:328
89. Kortus J, Pederson MR, Baruah T, Bernstein N, Hellberg CS (2003) Polyhedron 22:1871
90. Perdew J, Burke K, Ernzerhof M (1996) Phys Rev Lett 77:3865
91. Müller A, Döring J (1988) Angew Chem Int Ed Engl 27:1721
92. Barra A-L, Gatteschi D, Pardi L, Müller A, Döring J (1992) J Am Chem Soc 114:8509
93. Kortus J, Pederson MR, Hellberg CS, Khanna SN (2001) Eur Phys J D 16:177
94. Chiorescu I, Wernsdorfer W, Müller A, Bögge H, Barbara B (2000) Phys Rev Lett 84:3454
95. Anisimov VI, Aryasetiawan F, Lichtenstein AI (1997) J Phys Condens Matter 9:767
96. Boukhvalov DW, Kurmaev EZ, Moewes A, Zatsepin DA, Cherkashenko VM, Nemnonov SN, Finkelstein LD, Yarmoshenko YM, Neumann M, Dobrovitski VV, Katsnelson MI, Lichtenstein AI, Harmon BN, Kögerler P (2003) Phys Rev B 67:134408
97. Wernsdorfer W, Aliaga-Alcalde N, Hendrickson DN, Christou G (2002) Nature (London) 416:406
98. Park K, Pederson MR, Richardson SL, Aliaga-Alcalde N, Christou G (2003) Phys Rev B 68:020405/1
99. Park K, Pederson MR, Bernstein N (2003) Los Alamos National Laboratory, Preprint Archive, Condensed Matter: arXiv:cond-mat/0307145
100. Cano J, Ruiz E, Alvarez S (2004) (to be published)
101. Boukhvalov DW, Lichtenstein AI, Dobrovitski VV, Katsnelson MI, Harmon BN, Mazurenko VV, Anisimov VI (2002) Phys Rev B 65:184435
102. Park K, Pederson MR, Hellberg CS (2003) Los Alamos National Laboratory, Preprint Archive, Condensed Matter: arXiv:cond-mat/0307707
103. Raghu C, Rudra I, Sen D, Ramasesha S (2001) Phys Rev B 64:064419
104. Regnault N, Jolicoeur T, Sessoli R, Gatteschi D, Verdaguer M (2002) Phys Rev B 66:054409

105. Pederson MR, Porezag DV, Kortus J, Khanna SN (2000) J Appl Phys 87:5487
106. Pederson MR, Kortus J, Khanna SN (2000) Clusters and Nanostructure Interfaces (Proceedings of the International Symposium on Clusters and Nanostructure Interfaces), Richmond, VA, United States, Oct. 25–28, 1999, p 159
107. Pederson MR, Khanna SN (1999) Chem Phys Lett 307:253
108. Pederson MR, Khanna SN (1999) Phys Rev B 59: R693
109. Baruah T, Pederson MR (2002) Chem Phys Lett 360:144
110. Kortus J, Baruah T, Bernstein N, Pederson MR (2002) Phys Rev B 66:092403/1
111. Pederson MR, Kortus J, Khanna SN (2002) J Appl Phys 91:7149
112. Baruah T, Pederson MR (2003) Int J Quant Chem 93:324
113. Rentschler E, Gatteschi D, Cornia A, Fabretti AC, Barra AL, Shchegolikhina OI, Zhdanov AA (1996) Inorg Chem 35:4427
114. Cornia A, Fabretti AC, Gatteschi D, Pályi G, Rentschler E, Shchegolikhina OI, Zhdanov AA (1995) Inorg Chem 5383
115. Frisch MJ, Trucks GW, Schlegel HB, Scuseria GE, Robb MA, Cheeseman JR, Zakrzewski VG, Montgomery JA, Stratmann RE, Burant JC, Dapprich S, Millam JM, Daniels AD, Kudin KN, Strain MC, Farkas O, Tomasi J, Barone V, Cossi M, Cammi R, Mennucci B, Pomelli C, Adamo C, Clifford S, Ochterski J, Petersson GA, Ayala PY, Cui Q, Morokuma K, Malick DK, Rabuck AD, Raghavachari K, Foresman JB, Cioslowski J, Ortiz JV, Stefanov BB, Liu G, Liashenko A, Piskorz P, Komaromi I, Gomperts R, Martin RL, Fox DJ, Keith T, Al-Laham MA, Peng CY, Nanayakkara A, Gonzalez C, Challacombe M, Gill PMW, Johnson BG, Chen W, Wong MW, Andres JL, Head-Gordon M, Replogle ES, Pople JA (1998) Gaussian98 (rev a.11). Gaussian, Pittsburgh, PA
116. Schaefer A, Huber C, Ahlrichs R (1994) J Chem Phys 100:5829
117. Schaefer A, Horn H, Ahlrichs R (1992) J Chem Phys 97:2571

Structure and Bonding (2004) 113:103–170
DOI 10.1007/b97943
© Springer-Verlag Berlin Heidelberg 2004

Computing the Properties of Materials from First Principles with SIESTA

Daniel Sánchez-Portal[1] · Pablo Ordejón[2] · Enric Canadell[2] (✉)

[1] Centro Mixto CSIC-UPV/EHU and Donostia International Physics Center (DIPC), Paseo Manuel de Lardizabal 4, 20018 Donostia, Spain
sqbsapod@sc.ehu.es
[2] Institut de Ciència de Materials de Barcelona—CSIC, Campus de la UAB, 08193 Bellaterra, Barcelona, Spain
ordejon@icmab.es; canadell@icmab.es

1 Introduction: DFT and the SIESTA Method . . . 105

2 Semiconductors . . . 109
2.1 Bulk States in Crystalline Semiconductors . . . 109
2.1.1 Layered III-VI Semiconductors . . . 109
2.1.2 Ternary Semiconductors . . . 111
2.2 Defects in Crystalline Semiconductors . . . 112
2.2.1 Defects and Impurities in Silicon . . . 112
2.2.2 Defects and Impurities in Silicon Carbide . . . 114
2.2.3 Extended Defects, Lattice Instabilities and Non-Stoichiometry . . . 115
2.3 Amorphous Semiconductors . . . 116

3 Ferroelectrics . . . 117
3.1 Titanates . . . 117
3.2 H-Bonded Ferroelectrics: KDP . . . 121

4 Metallic and Magnetic Systems . . . 122
4.1 Zintl Phases . . . 122
4.2 Diluted Ferromagnetic Semiconductors: (Ga,Mn)As . . . 126
4.2.1 Role of Intrinsic Defects . . . 127
4.2.2 Transport in Digital Ferromagnetic Structures . . . 127
4.3 Clusters, Surfaces, and Interfaces . . . 128
4.3.1 Fe Systems . . . 128
4.3.2 V(001) Surface . . . 131
4.3.3 Fe/*c*-SiFe/Fe Sandwiches and Multilayers . . . 132
4.3.4 Cobalt Valence Tautomers . . . 133

5 Clathrates, Zeolites, and Minerals . . . 134
5.1 Clathrates . . . 134
5.2 Minerals and Zeolites . . . 135

6 Surfaces and Interfaces . . . 139
6.1 Clean Surfaces . . . 139
6.1.1 Liquid Si Surface . . . 139
6.1.2 Si(001) . . . 140
6.1.3 FeSi(CsCl) . . . 140
6.2 Adsorption on Metallic Surfaces . . . 141
6.2.1 Doped C_{60} Monolayers on Ag(111) . . . 141

6.2.2 H_2O on Ag(111) . . . 142
6.2.3 CO on Ni(111) . . . 143
6.2.4 Metals on Metallic Surfaces . . . 143
6.3 Adsorption on Si Surfaces . . . 144
6.3.1 Ba on Si(001) . . . 144
6.3.2 Pb on Si(111) . . . 145
6.3.3 C_{60} on Si(111) . . . 146
6.3.4 Si(557)-Au . . . 147
6.4 Surface-Tip Interactions . . . 148
6.5 Interfaces . . . 149
6.5.1 SiO_2/Si. . . . 149
6.5.2 α-Al_2O_3(0001)/Al(111) . . . 150

7 Low Dimensional Metals . . . 150
7.1 Molybdenum and Tungsten Oxides and Bronzes . . . 151
7.2 Molecular Conductors . . . 153
7.3 Other Low Dimensional Systems . . . 156

8 Nanostructured and Biological Systems . . . 157

9 Conclusions and Outlook . . . 159

References . . . 160

Abstract SIESTA was developed as an approach to compute the electronic properties and perform atomistic simulations of complex materials from first principles. Very large systems, with an unprecedented number of atoms, can be studied while keeping the computational cost at a reasonable level. The SIESTA code is freely available for the academic community (http://www.uam.es/siesta), and this has made it a widely used tool for the study of materials. It has been applied to a large variety of systems including surfaces, adsorbates, nanotubes, nanoclusters, biological molecules, amorphous semiconductors, ferroelectric films, low-dimensional metals, etc. Here we present a thorough review of the applications in materials science to date.

Keywords DFT · Localized bases · Atomic orbitals · Linear scaling · Semiconductors · Ferroelectrics · Metals · Magnetic materials · Zeolites · Minerals · Clusters · Surfaces · Interfaces · Nanomaterials · Biomolecules

List of Abbreviations

AE-LMTO	All-electron tight-binding linear muffin-tin orbitals method
AF	Antiferromagnetic
APW	Augmented plane-wave
ARPES	Angle-resolved photoemission
As_{Ga}	As occupying a Ga site in the zinc-blend GaAs structure
As_i	As interstitial in GaAs
CDW	Charge density wave
DFH	Digital ferromagnetic heterostructures
DFT	Density functional theory
DKDP	Deuterated potassium dihydrogen phosphate
DOS	Density of states

DZP	Double-ζ plus polarization basis set
E_F	Fermi energy
EXAFS	Extended X-ray absorption spectroscopy
FS	Fermi surface
GGA	Generalized gradient approximation
HOMO	Highest occupied molecular orbital
KDP	Potassium dihydrogen phosphate
KKR	Korringa, Kohn, and Rostoker method
LDA	Local density approximation
LEED	Low energy electron diffraction
LSDA	Local spin density approximation
LUMO	Lowest unoccupied molecular orbital
MD	Molecular dynamics
MMD	Magnetic multilayer device
O(N)	Order-N
PDOS	Projected density of states
PW	Plane-wave
SDW	Spin density wave
STM	Scanning tunneling microscope
SZ	Single-ζ basis set
V_{Ga}	Ga vacancy in GaAs
XANES	X-ray absorption near edge spectroscopy
XC	Exchange-correlation

1 Introduction: DFT and the SIESTA Method

During the last decades, computational simulations have emerged as a field of paramount importance in many areas of science, complementary to both experiments and traditional theory. Materials science is no exception. Among the simulation methods that are having a major impact in materials research are those that study materials from an atomistic point of view, trying to derive the macroscopic properties from the behavior at the atomic level. In this area, electronic structure based techniques are a class on their own. The electrons are ultimately responsible for the binding of the atoms that build the material, and the nature of the electronic states determines the properties and its response to the environment. The prospect of being able to solve the equations that govern the microscopic behavior of electrons and nuclei has been present since the early days of quantum mechanics as a way to understand and predict the properties of condensed matter in detail. Both the development of powerful numerical techniques (hand in hand with the advent and continuous improvement of the power of digital computers), and the derivation of approximate schemes to simplify the coupled many-body quantum-mechanical problem, has brought us to a situation in which it is possible to solve systems as complex as biological molecules like DNA [1].

Among the methodological advances that have enabled us to solve the electronic structure of complex materials, the Density Functional Theory (DFT) [2, 3] plays a starring role. It provides a framework within which the basic physics of many-electrons systems can be understood without the complexities of the many-body wave function [4]. However, and more importantly for the applications, it represents a practical way of performing computations in systems with a large number of electrons, without encountering the exponential system size dependence present in accurate wave function methods. The practical schemes for DFT rely on approximations to the exact theory, which have nevertheless been very thoroughly tested during the last decades, giving us a large body of experience on which are the properties and systems that can be accurately described. We now count on practical DFT approaches which are able to provide ground state total energies accurate to a level often comparable to that of quantum chemistry methods based on wave functions. Having access to the total energy of the ground state gives us much more information than might appear at first sight: for instance, the equilibrium geometry, the structure around defects and impurities, the activation energy of diffusion of atoms, or the atomic vibrations (to mention just a few properties) can be obtained using the knowledge of the variation of the total energy with the atomic positions. Besides, properties of the excited states (like electronic excitations, optical processes, photoinduced atomic rearrangements, etc.) are starting to be accessible to DFT techniques due to recent advances such as Time-Dependent DFT [5], although they are considerably more expensive computationally and not so widespread and commonly used as the ground state techniques.

The introduction of the so-called Car-Parrinello [6] and related methods (for a review see [7]) brought a new perspective to the field, by coupling the calculation of total energies and forces from DFT with the techniques of Molecular Dynamics (MD) [8]. These methods are allowing for realistic simulations of the atomic dynamics, thus making possible a direct understanding of chemical reactions and other atomistic processes. This has opened the door to virtual, computational experiments, in which the physical properties are simulated on a computer instead of the laboratory, leading to information and insight that can be difficult or even impossible to obtain in a real experiment.

Important effort has been devoted to the efficiency aspects of practical DFT implementations. However, their complexity, in terms of the scaling with the size of the system or the number of electrons, has remained a serious obstacle for the application to systems with very large sizes. The reason is that the computational effort required for the solution scales in general as the cube of the system size (or number of atoms being considered) [7]. This is due to the step involving the diagonalization of the electronic Hamiltonian, and the orthogonalization of the wavefunctions. Although this is a much less stringent obstacle than the exponential scaling of the most accurate

quantum chemistry methods, it still poses a practical barrier for reaching systems with more than a very few hundreds of atoms (in the most powerful parallel supercomputers). However, since the beginning of the past decade, great advances have been made towards eliminating this superlinear barrier, and to develop methods that scale only linearly with system size: the so-called Order-N, O(N) or linear-scaling methods [9, 10]. These O(N) approaches provide an approximate solution of the electronic problem, making use of the localization properties (either for the electronic states, in terms of Wannier functions, or for the density matrix), and allow to reach system sizes of a few thousands of atoms, even in (modern) personal computers.

While the implementation of (O(N)) approaches with empirical tight binding Hamiltonians [11] is rather straightforward [9], the application in the context of DFT is much more involved. One of the successful approaches is the SIESTA method, which is the subject of this paper. SIESTA (which stands for Spanish Initiative for Electronic Simulations with Thousands of Atoms) is a fully selfconsistent implementation of DFT, based on a flexible linear combination of atomic orbitals (LCAO) basis set, with essentially perfect O(N) scaling. It allows for extremely fast calculations using small basis sets, and very accurate calculations with multiple-zeta and polarized bases, depending on the accuracy required and the available computational power. Being based on localized orbitals, the method is well suited to describe systems with arbitrary dimensionality (from molecules or clusters to three-dimensional crystals), since the presence of vacuum does not involve an extra cost as in the case of plane-wave approaches. The method has been introduced in previous publications [12, 13] and thoroughly described in detail in a recent paper [14], and therefore we will only give here a brief overview of the most important aspects of the method. A previous review [15] described early applications mainly to nanoscale materials, such as nanotubes, surfaces and biomolecules.

As most of the electronic structure simulation methods, we start with the Born-Oppenheimer approximation to decouple the ionic and electronic degrees of freedom. The ions are treated classically, while the electrons are described by quantum mechanics. The electronic wavefunctions are solved in the instantaneous potential created by the ions, and are assumed to evolve adiabatically during the ionic dynamics, so as to remain on the Born-Oppenheimer surface. Beyond this, the most basic approximations of the method concern the treatment of exchange and correlation (XC) and the use of pseudopotentials. XC is treated within Kohn-Sham DFT [3]. Both the local (spin) density approximation (LDA/LSDA) [16] and the generalized gradients approximation (GGA) [17] are implemented. The pseudopotentials are standard norm-conserving [18, 19], treated in the fully non-local form proposed by Kleinman and Bylander [20].

Sparsity of the Hamiltonian and overlap matrices is a requisite for O(N) methods. To achieve sparsity, we use strictly confined basis orbitals, which go to zero beyond a certain radius from their center, as originally proposed by Sankey and Nikleski [21]. The orbitals are of the atomic type, being the product of a numerical radial function times a spherical harmonic. The angular momentum of the basis orbitals can be arbitrarily large, and for each atom there can be one or several orbitals with the same angular shape but different radial shape (multiple-ζ bases). The orbitals have a cutoff radius beyond which it is zero, this radius being in general different for each orbital. The radial shape of the orbitals, which is stored numerically, can be introduced by the user at will, so the method is not restricted to a given kind of radial functions. However, the code also provides several automatic procedures to generate basis sets. These are described in [22–24]. These works also show the quality of these basis sets, which in the case of double-ζ plus polarization (DZP) bases in general is comparable to that of plane waves (with the cutoff typically used for geometry optimizations and total energy differences calculations). Small basis sets like simple-ζ (SZ) provide semiqualitative results, in general similar to those of Car-Parrinello MD simulations with small plane wave cutoffs. In any case, it should be noted that, as in other localized basis approaches like Gaussians, the choice of the basis set is an important issue that should be given careful consideration for each particular problem (see [22–24] for details). Also, again similarly to the case of Gaussians, periodic systems require particularly chosen basis sets, which are in general more compact and shorter than the ones for molecules, since they do not need to describe the decay of the wavefunctions into vacuum.

The matrix elements of the DFT Hamiltonian between basis set orbitals are computed using a range of techniques specifically suited for strictly localized atomic orbitals, which are described in [14]. Some matrix elements can be expressed in terms of two center integrals, which are stored beforehand as a function of distance between the centers, and interpolated during the dynamics, as in the case of the overlap and the pseudopotential Kleinman-Bylander projectors. Other matrix elements are computed by direct integration on a three-dimensional real space grid. In any case, the calculation of all the non-zero matrix elements is done in O(N) operations, yielding an excellent performance even for very large systems. It should be noted that the linear scaling of the calculation of the matrix elements holds independently of the type of system being considered, and is a direct consequence of the localization of the basis sets. However, the solution of the electronic Hamiltonian in O(N) operations by means of the use of the localization properties of the Wannier functions or the density matrix, involves approximations that only remain valid for the case of systems with a gap, and therefore fail in the case of metals. In these cases, the solution of the Hamiltonian must be done using the traditional techniques which scale as the cube of the system size, whereas the calculation of the Hamiltonian still scales linearly.

Upon solution of the electronic problem, the total energy of the system is obtained, as well as the forces on the atoms and the stress tensor. This allows one to perform structural relaxations and MD simulations. Several MD techniques are implemented and available in SIESTA. Besides, a wide range of properties related to the electronic structure can be readily obtained [14]. The efficiency and the wide range of utilities indeed make SIESTA a very useful tool for the study of complex materials. In this paper, we will review applications of SIESTA to a whole variety of different materials. We will give emphasis to inorganic solids, to which most of the applications of SIESTA have been devoted. In the next section we describe applications to different aspects of semiconductors, from bulk and defect states in crystals, to amorphous semiconductors. The following section is focused on ferroelectric materials. The section after that deals with metallic and magnetic systems. Then we describe applications to minerals and other open-structure materials like zeolites and clathrates. Interfaces and surfaces (including adsorption of atomic and molecular species) are the subject of another section. After this we describe several aspects of low dimensional inorganic and organic materials. The next section deals with applications to materials at the nanoscale, like nanotubes and fullerenes, organic and biological molecules, clusters and nanoelectronic devices. Finally, we present a summary.

2
Semiconductors

2.1
Bulk States in Crystalline Semiconductors

2.1.1
Layered III-VI Semiconductors

The family of III–VI semiconductors (such as GaSe, InSe, and GaTe and their alloys) has an interest for potential applications to nonlinear optics, solar energy conversion and solid-state batteries. The materials have rather special properties due to their strongly anisotropic structure. The crystals have layers formed by anion-cation-cation-anion sheets, and while the bonds within the layer are strong (covalent and partially ionic), the layers are held together by weak, probably Van der Waals interactions. This can favor the existence of polymorphs with different stacking sequences, as observed in InSe and GaSe, but not in GaTe. The layer structure leads to strongly anisotropic electronic properties, which are still not completely understood (in contrast to those of other semiconductors). Application of hydrostatic pressure is a way to achieve a better understanding of these materials: the effect of pressure on the layers plane is very different from that be-

tween layers, leading to changes in the electronic structure that can be traced back to the structural changes, giving insight about the origin of the electronic structure features in the material. However, the availability of electronic structure calculations has shown instrumental for making this correlation. For instance, a recent work combining SIESTA calculations and experiment [25] has explored the electronic band structure of GaTe, establishing that the material is a direct gap semiconductor.

InSe is one of the III–VI semiconductors with a more interesting behavior under pressure. The effect on the electronic properties has been the subject of several studies. Segura and co-workers have provided a quite complete picture of the changes in the structural parameters (bond distances) [26] and the optical absorption [27] of InSe as a function of pressure. From the optical absorption spectra, they were able to infer the existence of three distinct electronic transitions, one direct and two indirect. However, from the experiment it was not possible to assign their origin. SIESTA calculations [27–29] have been instrumental in understanding the origin of these optical transitions. The calculations show that the direct transition takes place in the *Z* point of the Brillouin zone, where the maximum of the valence band and the minimum of the conduction band are located at P=0. The first indirect transition was proposed to originate from a change of the position of the valence band maximum with increasing pressure, from the *Z* point towards a ring around that point, within the *ZLH* plane. The absorption would correspond to transitions from this ring to the minimum of the conduction band at the *Z* point. The assignment was supported by the excellent agreement between the calculated and experimental pressure coefficients of the energy difference between the indirect *ZLH* to *Z* and the direct *Z* to *Z* transition (−20 meV/GPa and −19±5 meV/GPa, respectively). The second indirect feature was proposed to have its origin in a transition from the top of the valence band at the *Z* point to the conduction band at either the *A* [27] or *B* [28] point. Under pressure, both *A* and *B* shift down in energy, and therefore the edge of this indirect transition decreases with pressure, as observed in the experiment. Again, the pressure dependence of the difference between this transition and the direct one shows a very good agreement between the calculated (−89 meV/GPa) and experimental (−76±10 meV/GPa) results. The SIESTA calculations, however, failed to reproduce the crossover between the direct and the indirect transitions observed experimentally at about 4 GPa. Ferlat et al. [28] have shown that the reason for this failure is the well-known problems of DFT to describe the gap energies, and that a post-DFT calculation in the GW approximation was able to solve this deficiency and explain the experimental crossover.

2.1.2 Ternary Semiconductors

Because of the increased structural and chemical degrees of freedom relative to their binary analogues, ternary semiconductors exhibit a wider range of chemical and physical properties [30], which can be tuned as a function of composition to tailor the needs of particular applications. An example is that of diluted ferromagnetic semiconductors like heavily Mn-doped GaAs alloys, which show ferromagnetic ordering at relatively high temperatures, and which will be the focus of a later section.

Many applications of ternary semiconductors exploit their optical properties. As an example, $AgGaSe_2$ is a direct gap semiconductor with highly nonlinear optical properties and a wide transparency range, and is therefore useful for nonlinear optics [30]. González et al. [31] have studied experimentally the optical and structural properties at high pressures using X-ray diffraction and optical absorption techniques, extracting the volume derivatives of the energy gap and the structural parameters (anion displacement and tetragonal distortion of the unit cell). They also performed SIESTA calculations of the structure and optical gap as a function of pressure. The calculated values agree within 10% with the experimental numbers, showing the accuracy of SIESTA to describe pressure-induced effects in these materials.

Another possible application of semiconductor alloys, which so far remains a proposal at the theory level, is to high efficiency solar cells. Luque and Martí [32] showed that it is, in principle, possible to increase dramatically the efficiency of solar cells by using a material with a partially filled, intermediate band of states in the semiconductor's energy gap. This material can create an electron-hole pair by absorbing two phonons with sub-band gap energy, using this intermediate band as an intermediate state. In the quest for possible materials which display this kind of intermediate band, Wahnón et al. [33–35] have explored the formation of an intermediate band in III–V semiconductors by adding different substitutions to the binary material. In particular, they considered the case of substitutions of the transition metals Sc, Ti, V, and Cr. They only studied model phases with stoichiometric compositions (Ga_4X_3M and Ga_3X_4M, where X is As or P and M is Sc, Ti, V, or Cr), which are therefore highly ordered crystals with small unit cells, whereas one may expect that in the real alloys disorder may be present. However, they showed that some of these model compounds (in particular those in which the transition metal substitutes the As or P atoms) indeed show partially filled intermediate bands, and are therefore candidates for high efficiency solar cell materials.

2.2 Defects in Crystalline Semiconductors

2.2.1 Defects and Impurities in Silicon

Silicon is, of course, the most important materials for electronics. Despite the tremendous amount of work done both from experiment and theory, many issues still remain unresolved concerning the atomistic details of the structure and dynamics of defects and impurities in silicon. Several SIESTA studies have focused on resolving some of these open problems.

Together with vacancies, self-interstitials are the fundamental native defects in crystalline silicon. Estreicher et al. [36–38] have studied the problem of the structure and dynamics of self-interstitial clusters. After determining the most stable structures for I_n clusters (i.e., aggregates of n silicon self-interstitials), they focused on the dynamics of diffusion, by means of MD simulations. They found the surprising result that the diffusion of the I_2 and I_3 aggregates is much faster than that of a single interstitial. The diffusion of the I_2 and I_3 is so fast that it is readily observed in the MD simulations in the time scale of picoseconds, whereas no diffusion event in the single interstitial was observed. The enhanced rate of diffusion in the clusters is due to the fact that the interstitials are located around a single Si-Si bond center. The diffusion proceeds by an exchange mechanism: the cluster of interstitials pushes one of the Si host atoms, and displacing it to the next interstitial site. Then, one of the interstitial atoms takes the host position of the displaced Si, whereas the rest of the interstitials follow it, resulting in a net motion of the complex. Therefore, the presence of several interstitials in the aggregate facilitates the initial displacement of the host atom, making the exchange mechanism more likely to occur than in the simple interstitial case.

Vibrational spectroscopy is one of the most powerful experimental techniques to obtain insight about the structure of impurities in semiconductors. The availability of theoretical predictions of the vibrational modes is a key to correlate the experimental frequencies with structural models. Pruneda et al. [39, 40] have developed a method to calculate vibrational modes within SIESTA by computing the dynamical matrix using linear response theory [41]. They have computed the vibrational modes of a large number of light impurities in silicon, including interstitial hydrogen, hydrogen dimers, vacancy-hydrogen and self-interstitial-hydrogen complexes, the boron-hydrogen pair, substitutional C, and several O-related defects. They found that the method is able to predict the vibrational frequencies with a typical accuracy within about 2% from the experimental values for most of the modes, and within 5% for the most anharmonic ones, being therefore an invaluable tool for the assignment of experimental spectra.

Hydrogen is a common impurity in silicon, and often affects the electrical and optical properties of the material, mainly by passivating the energy levels associated with defects and impurities. Estreicher et al. [38, 42–45] have studied two aspects of the problem. The first one is the behavior of interstitial H_2 molecules, which, although it might seem a simple problem a priori (given the fact that the molecular nature of the impurity implies a small interaction with the host crystal), still poses a number of puzzling experimental observations [45]. Estreicher et al. [42, 43] found by means of SIESTA MD simulations, that some of the inconsistencies between previous *static* calculations and the experimental observations could be explained by the dynamic character of the molecule, which even at low temperatures moves very significantly away from the most stable position (a tetrahedral interstitial site). The second problem [44] was the structure and electronic properties of complexes of silicon self-interstitials and aggregates of hydrogen impurities (the $\{I,H_n\}$ complexes).

Besides light impurities, other heavier chemical species are common contaminants during silicon processing. An example is copper, which has a strong tendency to precipitate at oxides, lattice defects and surfaces. Estreicher et al. [46] have studied the structure of Cu impurities at intrinsic defects such as mono- and di-vacancies in silicon, and the interaction with interstitial hydrogen. They find that Cu fills the monovacancy site, with a tetrahedral coordination, but with a relatively small binding energy of 2.5 eV. At the di-vacancy, Cu takes the position near the center of the defect, becoming sixfold coordinated. Substitutional Cu becomes a trap for H interstitials, forming complexes with up to three H atoms. Another study by Estreicher and coworkers [47] focused on the vibrational features associated with Cu and Cu pairs in silicon. The heavy mass of Cu makes its vibrational modes to be below the optical phonon of the host silicon crystal, therefore making them very much less localized than those of light impurities. However, Estreicher et al. also found that, for some of the Cu impurity structures, the associated modes are pseudolocal and therefore can be observed as sidebands in the photoluminescence spectra associated with the impurity levels.

Precipitation at the oxide interface is not only a feature of undesired impurities as Cu; dopants also segregate at the Si/SiO_2 interface, becoming deactivated and therefore reducing the doping efficiency. Baierle et al. [48] studied the case of P, which was found to segregate due to three factors: (i) trapping at interfacial dangling bonds, (ii) trapping at vacancies and vacancy-oxygen complexes which abound under the interface, and (iii) formation of pairs of threefold coordinated P atoms, each one controlling the deactivation at different ranges of dopant concentration.

2.2.2 Defects and Impurities in Silicon Carbide

Over the years, silicon carbide (SiC) has established itself as the most promising candidate among wide band gap semiconductors to substitute silicon in applications involving high power and/or high frequency devices, and for operation at high temperatures or in high radiation environments. The main drawback in using SiC for device applications is the difficulty in doping the material, which in practice can only be achieved by means of ion implantation. Doping by diffusion, as is done in Si, is not possible in SiC due to the small diffusion coefficient of the main dopant species. Doping via ion implantation has the obvious problem that the crystalline lattice can be heavily damaged, and thermal annealing post-treatments are not always able to recover the crystallinity and remove the point defects created. Therefore, understanding the formation and configuration of defects and dopant impurities, and their kinetics, is of capital importance for optimizing the doping process and the thermal annealing of defects. First principles calculations are of great utility. Rurali and coworkers [49–52] and Gali et al. [53] have analyzed different aspects of dopants and intrinsic defects in SiC, by means of SIESTA calculations.

B is one of the most commonly used *p*-type dopants in SiC. Diffusion of B in SiC was found to be activated by a kick-out mechanism, in which a B substitutional impurity at a Si lattice site is displaced by a nearby Si interstitial [49]. The displaced B takes an interstitial site that can then diffuse through the crystal. Rurali et al. [49, 50] also determined the lowest energy diffusion path of the interstitial B impurity, going from a trigonal site to the next one via C and Si interstitialcies, with a barrier of 0.65 eV. B interstitials therefore diffuse easily through the SiC crystal until they recombine with an existing vacancy or they reach the surface. The difficulty observed in the experiment is therefore associated with the activation of the B interstitial, which must proceed via a Si self-interstitial, rather than the diffusion process itself. This explains the experimental observations of an enhanced diffusion rate in the presence of intrinsic defects [54].

The most stable sites for *n*-type dopants in SiC have been determined by Rurali et al. [51]. They found that N and P substitute preferentially at C and Si sites, respectively. They also studied the effect of dopant aggregation, which is likely to occur at high dopant concentrations under heavy ion implantation doses. They find that all the investigated N-dopant complexes lead to passivation (i.e., the shallow gap states transform into deep levels that cannot be ionized at room temperatures, and therefore do not lead to conducting charges in the material). In contrast, it was found that the most stable P aggregates are still active and are not self-passivated. These results explain recent observations of a higher efficiency for doping of P-implanted SiC at high doses, compared to the N-implanted material [55].

Further work on SiC with SIESTA involved studies of vacancy diffusion [52] and aggregates of C interstitials [53].

2.2.3 Extended Defects, Lattice Instabilities and Non-Stoichiometry

Extended defects are very important in semiconductors for device applications. In nitrides, the concentration of extended defects is usually larger than in other semiconductors, mainly because of the larger lattice mismatch with the substrates. The presence of stacking faults in GaN has been pointed as the origin of phenomena such as electronic confinement and spontaneous ordering of *p*-type dopants. Schmidt et al. [56] used SIESTA to study the interaction of stacking faults with Mg dopants in zinc-blende and wurtzite GaN. They found that, for both of the crystal structures, the presence of the stacking fault induce the localization of the impurity electronic level. They found that the most stable position of the substitutional Mg atom is at the stacking fault in the case of the zinc-blende structure, whereas for wurtzite it is far from the fault. Therefore, Mg substitutional impurities in GaN are expected to segregate at stacking faults in the zinc-blende structure, but not in the wurtzite case.

Extended defects leading to crystal instabilities can also develop when semiconductor crystals are subject to strong pressures (either hydrostatic or anisotropic). Chacham and Kleinman [57] performed SIESTA simulations of the behavior of carbon in the diamond structure under high shear stress. They found that the lattice is unstable under shear stresses as low as 95 GPa, leading to graphite-like layered structures. These calculations provide a possible explanation for recent experiments [58], in which vibrational signatures from graphitelike carbon were observed in a region of a diamond sample subjected to indentation by a diamond tip. Conversely, Reich et al. [59] reported the possibility of obtaining diamond from carbon nanotube samples under hydrostatic pressure, a prediction which was confirmed experimentally.

Also, deviations from stoichiometry are often frequent in oxide semiconductors. In particular, large gap transition metal oxides can be grown with significant concentrations of oxygen vacancies. Canto and coworkers [60] studied the influence of oxygen vacancies on the electronic properties of TiO_2 by means of both experiments and SIESTA calculations. They found that the presence of a significant concentration of oxygen vacancies induces the formation of a band of states below the conduction band, which leads to a decrease of the optical absorption edge. The implications of this for the application of this material for photodegradation of pollutants are very important, because the reduced band gap allow the use of visible light instead of ultraviolet radiation, making the process much more economical.

2.3 Amorphous Semiconductors

Amorphous semiconductors are an important class of materials, which are especially difficult to model due to the lack of periodicity and the complexity of the structural details at the atomistic level. However, some degree of short or even medium range order usually exists in these systems, to a degree which depends on the specific material and sometimes on the growth process and previous history. In amorphous silicon, for instance, most of the Si atoms are fourfold coordinated with a first neighbors distance very close to the one of the crystalline diamond phase, and a relatively narrow distribution in bonding angles. This permits building models which, respecting this short range order, are an approximation to the structure of the real material. These models are a basis for the calculation of physical properties like the electronic or vibrational structure.

Fedders and coworkers [61–66] have used SIESTA, among other methods, to model different aspects of the structure, properties and dynamics of amorphous silicon (a-Si) and hydrogenated amorphous silicon (a-Si:H). They have analyzed the electronic localization of states associated with dangling bonds in a-Si, showing that good agreement with electron spin resonance experiments is obtained by means of the calculated spin density, but not the wavefunctions associated with the defects. This shows that the spin moment associated with dangling bond defects is not built from a single localized one electron wavefunction, indicating that probably the quasiparticle wavefunctions are relatively different from the LDA one electron orbitals. Fedders [62] also studied the localization of the so-called tail states (states within the mobility band gap with exponentially decreasing density of states (DOS) towards the gap), finding that they are much more delocalized than previously thought. He also showed that valence band tail states are mostly associated with short bonds, whereas conduction tail states are due to stretched bonds.

Hydrogen in a-Si:H is extremely important in passivating most of the defects states in a-Si, thus cleaning the gap. This allows the doping of the material, which can not be achieved in a-Si due to the large density of defects levels, thus opening the possibility for device applications. Fedders [64] has investigated the important problem of the atomistic structure and energetics of H within the amorphous silicon matrix. He also analyzed the implications of the calculated defect and diffusion energies for the complex problem of H diffusion in a-Si:H [63, 65, 66]. Although a definite conclusion of what the exact mechanism of hydrogen diffusion is was not reached, he challenged the conventional view of diffusion through Si-Si bond centers, and proposed a mechanism based on diffusion of molecular H_2 species.

Other amorphous semiconductors have also been studied using SIESTA. In particular, Drabold and coworkers [67–69] have considered the interest-

ing problem of glassy chalcogenides. They used SIESTA to assess the quality of model networks obtained by more approximate DFT schemes [70]. In this kind of material they reached the general conclusion that, in order to produce models which compare satisfactorily with the experimental information about the structure of the network by means of standard first principles methods, it is necessary to push the limit of accuracy in the basis sets and DFT functionals. Reasonable results were only obtained when using DZP basis sets and a GGA functional for DFT. However, more approximate schemes [70] using approximate selfconsistency, small basis sets and LDA, are able to provide an excellent description. The reason for this is so far unknown, and further work in the group of Prof. Drabold is underway to understand this paradox [71].

3
Ferroelectrics

3.1
Titanates

The ferroelectric materials show a switchable macroscopic electric polarization which effectively couples external electric fields with the elastic and structural properties of these compounds. These properties have been used in many technological applications, like actuators and transducers which transform electrical signals into mechanical work [72], or non-volatile random access memories [73]. From a more fundamental point of view, the study of the phase transitions and symmetry breakings in these materials are also very interesting, and their properties are extremely sensitive to changes in temperature, strain, composition, and defects concentration [74].

In recent years much of the interest on ferroelectrics has shifted to the study of the properties and growth of very thin layers of material on metallic and semiconductor [75] substrates. This change has been driven by the steady search for faster, smaller, and more powerful microelectronic devices. This demands the miniaturization of the components while keeping their key properties. Therefore, monitoring the change of the material properties when moving from bulk samples to the ultrathin films required by the applications becomes crucial. First principles calculations are instrumental in this context. However, very efficient computational tools have to be used to deal simultaneously with the large supercells required for thin films and interfaces, and the demand of high accuracy needed to obtain reliable ferroelectric properties.

Another field of intensive research is the insulating perovskite alloys with exceptional dielectric and piezoelectric properties [74], like the so-called relaxor ferroelectric alloys PZT ($PbZr_xTi_{1-x}O_3$), PZN-PT ($Pb(Zn_{1/3}Nb_{2/3})O_3$-

$PbTiO_3$), and PMN-PT ($Pb(Mg_{1/3}Nb_{2/3})O_3$-$PbTiO_3$). Again the role of first principles calculations in the study of these materials is seriously limited by the small sizes that can be accessed with most ab initio methods. In particular, only highly ordered configurations of the alloys have been considered in most calculations performed to date [76]. The symmetries artificially imposed by these unrealistically small cells can yield to a serious underestimation of the calculated piezoelectric constants of these materials.

With these problems in mind, a series of modifications in the SIESTA code were undertaken by Sánchez-Portal et al. [77] in order to treat accurately perovskite titanates and other ferroelectric systems. The most important of them were: i) the inclusion of semicore shells and the corresponding use of several Kleinman-Bylander projectors, with different reference energies, for each angular momentum [78], and ii) the implementation of the calculation of the macroscopic polarization using the so-called Berry-phase theory of polarization [79]. With this powerful tool it is possible to calculate the change of macroscopic polarization along a continuous transformation, obtaining the effective charges [79] and piezoelectric constants [80] of a given material. Most of the previous implementations of the polarization calculation using local basis, mainly in the context of Hartree-Fock calculation [81], were based on the use of Gaussian expansion. However, the approach followed in SIESTA [77] is more suitable for numerical orbitals. Test calculations for the phonons, soft mode eigenvectors, energy and magnitude of the ferroelectric distortion, and Born effective charges of $BaTiO_3$ and $PbTiO_3$ have been carried out [77, 82]. The results are in good agreement with plane-wave (PW) and augmented plane-wave (APW) calculations from the literature, showing that SIESTA is a reliable tool for the study of perovskite oxides. The agreement is particularly good in the case of the results for the barium compound presented in [82]. In that reference the basis set was optimized following the procedure of Junquera et al. [23]. The energies of the tetragonal and rhombohedral distortion are almost indistinguishable from the APW results, with the rhombohedral phase much more stable than the tetragonal, in good agreement with the experiment. Furthermore, the phonon dispersion calculated with SIESTA is also in very good agreement with the PW results of [83], accurately reproducing all the unstable branches and the frequencies and characters of the different phonon bands along the whole Brillouin zone. The largest difference with PW calculations appears in the Born effective charges of Ti and the anomalous one of oxygen O_I (perpendicular to the BaO plane), which are systematically too large (around 6%). This seems to be related to the use of a local basis and was previously observed in a DFT study of $KNbO_3$ by Fu et al. [84], although in that case it was attributed to the use of basis sets optimized for Hartree-Fock calculations.

Once the capability of SIESTA for the study of ferroelectric oxides was demonstrated, more complex situations could be addressed. In particular,

and in the spirit of the miniaturization challenges mentioned above, one of the most important problems that the materials science community is facing nowadays is the search of an alternative material to replace silica (SiO_2) as the gate dielectric in Metal Oxide Semiconductor Field-Effect Transistors (MOSFETs). The continuous decreasing of the physical gate lengths, approaching the nanoscale size, must be accompanied by a simultaneous reduction of the gate dielectric thickness in order to preserve a high gate oxide capacitance. Unfortunately, as the size of the SiO_2 layer is reduced the leakage currents will soon become a problem. In fact, leakage current from the channel to the gate is due to tunneling and increases exponentially with the decrease of both the thickness of the gate dielectric and the height of the electrostatic barrier for the electrons through the gate stack. Thus it seems that we are rapidly approaching the minimum size attainable with the present SiO_2 based technology and, in a few years, a new gate dielectric will become necessary. The desired properties for the new dielectric are well established. Some of them are: i) higher dielectric constant than silica, ii) large band gap and band offsets to prevent tunneling, iii) stability on the Si substrate, and iv) good quality interface, with low defect concentration and, therefore, small density of midgap interface states. Because of their high dielectric constants (one order of magnitude higher than the rest of the candidates), ABO_3 (with A=Ba or Sr) perovskite oxides are considered as promising alternate materials. However, their eventual use is conditioned by the resolution of two major problems: (i) ABO_3 perovskites are thermodynamically unstable in direct contact with Si and (ii) the conduction band-offset at ABO_3/Si interface is too small to avoid the appearance of high leakage currents [85]. Recently, McKee et al. [75] have demonstrated the possibility of growing ABO_3 perovskites epitaxially on top of Si thanks to the inclusion of a AO buffer layer. With the help of the SIESTA code, Junquera et al. [86] reported structural and electronic properties (including band offsets) at the AO/$ATiO_3$ interface. They proved how the inclusion of the buffer layer not only solves the problem of the stability, but also helps to monitor the offsets in a efficient way, providing large electrostatic barriers for both holes and electrons, and avoiding the appearance of leakage currents.

Junquera and Ghosez [87] recently addressed the problem of the critical thickness for ferroelectricity using SIESTA. Experiments have detected ferroelectricity in perovskite films down to a thickness of 40 Å [88]. Recent calculations [89], using both effective Hamiltonians and first principles methods, also showed that the ferroelectric ground state was retained even for ultrathin films under the condition of vanishing internal electric field, suggesting the absence of a critical size limit. In contradiction to these results, [87] shows that a $BaTiO_3$ film between two metallic electrodes in short circuit can loose its ferroelectric properties below a thickness of about six unit cells (~24 Å). Junquera and Ghosez considered a realistic ferroelectric capacitor composed by an ultrathin $BaTiO_3$ layer between two metallic $SrRuO_3$

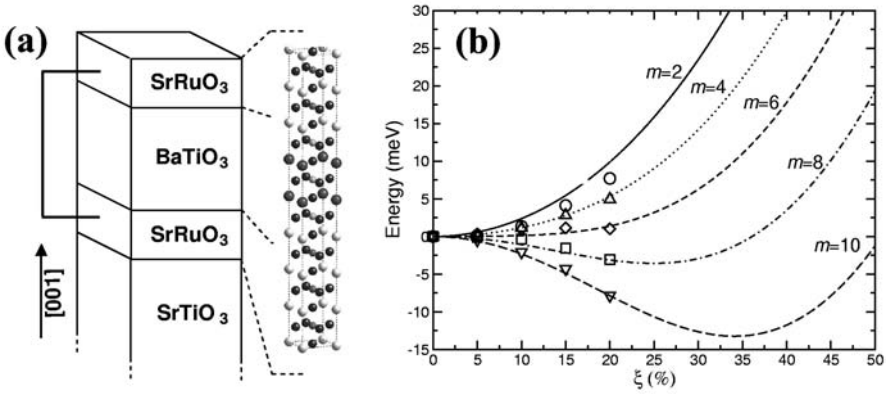

Fig. 1 **a** Schematic view of the ferroelectric capacitor considered in [87]. The epitaxy on $SrTiO_3$ is effectively taken into account by choosing the appropriate lattice parameter in the direction parallel to the interfaces. **b** Evolution of the energy as a function of the soft-mode ξ for different thickness of the ferroelectric film m. *Symbols* stand for the first principles results and *lines* present the results of a simplified electrostatic model. Reproduced with permission from [87]

electrodes. This structure was assumed to be grown on a $SrTiO_3$ substrate, and this was effectively included in the calculations by constraining the in-plane lattice constant of the whole structure to the bulk value of $SrTiO_3$. The height of the periodic supercell was chosen to minimize the strain under this constrain. The basic unit is schematically shown in Fig. 1a and corresponds to the generic formula $[SrO\text{-}(RuO_2\text{-}SrO)_n/TiO_2\text{-}(BaO\text{-}TiO_2)_m]$, where n was fixed on 5 (enough to avoid interactions between both interfaces) and m ranged from 2 to 10. Figure 1b depicts the evolution of the total energy as a function of the magnitude of the ferroelectric distortion ξ (along the bulk soft mode) relative to that of bulk $BaTiO_3$. Clearly, for films thinner than ~6 unit cells the ferroelectric distortion becomes unfavorable. This was also checked for m=2 performing full atomic relaxations starting from distorted geometries: the paraelectric structure was always recovered. In fact these are quite robust observations and can be explained solely on the basis of simple electrostatics. The polarization of the ferroelectric film leads to surface charges, σ=**P.n**, which would be screened by the neighboring metal layers. This screening charge extends into the metal over a typical distance of the screening length and, therefore, two dipoles pointing in the same direction are formed at both sides of the film. Each of these dipoles is responsible for a lineup of the electrostatic potential in the same direction; thus the only way to preserve short-circuit boundary conditions is the appearance of a depolarization electric field ϵ_d. Since the interface dipoles are roughly independent of the thickness of the ferroelectric film, ϵ_d will be larger the thinner the film. The electrostatic origin of the suppression of the ferroelectricity

can be clearly seen in Fig. 1b, where the lines present the results of a simplified model of the energy $E=U-\mathbf{P}.\epsilon_d$, where U is the internal energy under zero field for bulk and the macroscopic polarization **P** is also obtained from bulk parameters. The agreement between the model and the first principles results is excellent.

SIESTA has also been used to study the flat and stepped (001) surface of $SrTiO_3$ by Zhang and Demkov [90]. The authors first calculated the electronic and structural properties of bulk $SrTiO_3$, SrO, and TiO_2, which turned out to be in quite good agreement with previous calculations. The results for the flat surfaces are in good agreement with previous PW calculations [91], although the estimated average surface energy is somewhat higher for SIESTA (~16%). For the flat surface the SrO termination is the most stable under most chemical environments; for the stepped surface an oxygen terminated step edge is preferred under extremely oxygen-rich conditions and an Sr- or TiO-terminated step edge under oxygen-deficient conditions. However, under the majority of the chemical environments, including typical growth conditions, the termination is mixed and it is the stoichiometry that drives terrace termination.

3.2 H-Bonded Ferroelectrics: KDP

Potassium dihydrogen phosphate (KH_2PO_4, or KDP) is the prototype of the hydrogen-bonded ferroelectrics and has important applications as a nonlinear optical material [74]. The ferroelectricity in KDP is believed to be connected to proton off-center ordering in the bonds, although the exact nature of the transition still remains quite controversial, particularly the origin of the huge isotope effect (T_c increases about 107 K upon deuteration). Koval et al. [92] performed the first ab initio DFT calculation of this compound using SIESTA. The authors made a complete characterization of the structural and electronic changes accompanying the ferroelectric transition. The predicted structures of the tetragonal (paraelectric) and orthorhombic (ferroelectric) phases are in good agreement with the experimental data. In the tetragonal structure the H atoms are constrained to the center of the O-H-O. When this structure is slightly perturbed, two H atoms approach each PO_4 tetrahedron. This collective off-centering of the hydrogen atoms is accompanied by a charge redistribution. A depletion and delocalization of charge is observed in the vicinity of the oxygen atoms approached by the hydrogen, while there is an accumulation and localization of charge around the other oxygen atoms. This charge accumulation attracts the K^+ towards the PO_4, being ultimately responsible for the ferroelectric distortion. This connection between hydrogen off-centering and ferroelectricity is further supported by the fact that centered positions for K are always stable when hydrogen remains in the middle of the H bond. In [93] these authors ex-

tended their study to address quantum effects. They first estimated the ferroelectric correlation length using calculations of small KDP clusters of increasing size, embedded in a paraelectric KDP matrix. For KDP, ferroelectricity requires the correlated motion of *all* the atoms in clusters comprising at least ten hydrogen atoms. When the volume is increased to match that of deuterated KDP (DKDP), ferroelectric-like instabilities appear even when only one PO_4 cage (and the surrounding hydrogen atoms) is considered. This seems to point to a "geometric" origin of the isotope effect. In fact, since the ferroelectric mode comprises a considerable motion of heavy atoms in addition to hydrogen, at fixed lattice geometry the effect of deuteration in tunnel splittings is very small. However, the larger mass of deuterium triggers another phenomenon. Compared to the case of hydrogen, the probability of finding a deuterium atom in a centered position is smaller, with the corresponding weakening of the O-H-O bonds and subsequent expansion of the DKDP lattice. Koval et al. gathered all these elements in a simple non-linear model which successfully explains the experimental observation of a huge isotope effect [93].

4
Metallic and Magnetic Systems

4.1
Zintl Phases

The series of ideas originating from Zintl [94] and later modified and developed by others [95–98] is certainly one of the more widely used and successful conceptual schemes in solid state chemistry. These ideas lead to a rationalization in simple terms (i.e., the octet or Wade rules, for instance) of the relationship between the structure and number of electrons for many solids usually known as Zintl phases. Essentially, these ideas associate chemical stability with structural building blocks (clusters, networks, etc.) having an electronically closed shell configuration. A commonly accepted corollary is that these phases must be diamagnetic semiconductors or insulators. Even if this aspect has not been systematically scrutinized the conclusion seems to be essentially correct. With this situation in mind, an important recent development has been the preparation of several metallic and magnetic compounds of this type. Interesting problems concerning the bonding description and the rationalization of the transport properties immediately emerge and some of these materials have been recently studied on the basis of the SIESTA approach.

One of the simplest cases is that of the A_5Pn_4 (A=K, Rb, Cs; Pn=As, Sb, Bi) compounds [99]. They exhibit metallic behavior (the bismuthides even become superconducting at low temperatures) and contain tetrameric Pn_4

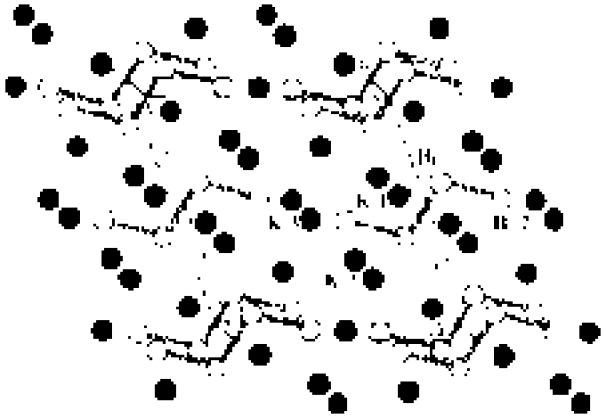

Fig. 2 Crystal structure of K_5Bi_4 where the *full* and *empty circles* refer to the K and Bi atoms, respectively. Reproduced with permission from [100]

units separated by the alkali atoms (see Fig. 2). As Gascoin and Sevov have discussed [99], a description of the tetrameric units as Pn_4^{4-} or Pn_4^{5-} are in principle equally likely. They have argued that the two descriptions should lead to different physical behaviors: temperature-dependent paramagnetism due to the spins localized in the tetrameric units in the second case but temperature-independent Pauli paramagnetism and metallic behavior in the first. Since all phases exhibit Pauli paramagnetism and metallic behavior they concluded that the first alternative was the appropriate one.

The calculated band structure and DOS for K_5Bi_4 [100] are reported in Fig. 3a,b, respectively. As shown in Fig. 3a, the Fermi level cuts two bands along the $\Gamma \rightarrow Y$ direction and one band along the $\Gamma \rightarrow Z$ direction. Since the first two bands exhibit a considerable dispersion (more that 1 eV) the system should be metallic, as reported by Gascoin and Sevov [99]. The DOS diagram of Fig. 3b shows that, as could be expected, the Bi contribution dominates in the filled energy bands. However, the important result of this figure is that the K contribution is quite large. In fact, it is almost always around one-quarter that of the Bi atoms, this ratio being quite normal for heteroatomic bonding between atoms with such electronegativity difference. Thus, there is a very considerable mixing between the Bi and K orbitals so that the covalent contribution to the bonding in this phase must be quite important.

Careful analysis of the band orbitals showed [100] that four pairs of bands have as the major components the four well known π-type levels (π_1 to π_4) of the zigzag tetrameric units (see Fig. 3a). These bands acquire dispersion mostly through the bonding mixing of the higher lying s and p orbitals of potassium (the shortest Bi$\cdots$Bi contact along *b* is 5.54 Å so that they have a practically nil influence on such dispersion). It is clear that the

Fig. 3 **a** Band structure. **b** DOS calculated for K_5Bi_4. In **a** Γ=(0, 0, 0), X=(1/2, 0, 0), Y=(0, 1/2, 0) and Z=(0, 0, 1/2) in units of the monoclinic reciprocal lattice vectors. Reproduced with permission from [100]

π_4-based bands are approximately half-filled and the π_1-, π_2- and π_3-based ones are full, as it would correspond for a formal charge of 5- for the tetrameric units. Many of the bands in Fig. 3a show quite large dispersion along the three directions of reciprocal lattice, a consequence of the strong participation of the K orbitals in these filled bands (only along *c* is there a short Bi···Bi contact of 4.388 Å, all other contacts are longer than 5.5 Å). Thus, although every one of the pairs of bands in Fig. 3a (the bands occur in pairs because there are two formula units per repeat unit of the solid) can be clearly traced back to one of the levels of a tetrameric Bi_4^{5-} unit, it would be impossible to understand the details of the electronic structure without realizing that the K atoms are far from just providing electrons to satisfy the electronic requirements of the more electronegative Bi atoms and a mostly Coulombic-type force keeping together the K_5Bi_4 network. They are indeed part of a 3D network with a large covalent bonding component. The fact that a detailed analysis of the band structure validates both this conclusion and the formal description of the tetrameric pnictide units as Pn_4^{5-} (i.e., formally assuming that the potassium atoms fully transfer the valence electron) illustrates the essential bonding ambiguity, with strong consequences for the transport properties, of these and similar systems.

$Ca_{14}MnBi_{11}$ and $Ba_{14}MnBi_{11}$ are two interesting metallic Zintl phases showing unusual magnetic behavior [101, 102]. These solids belong to a family of compounds, $A_{14}MPn_{11}$, with a crystal structure built from MPn_4 tetrahedra, Pn_3 linear units, isolated Pn atoms, and interstitial alkaline earth A atoms. For $Ca_{14}GaBi_{11}$ [103] a bonding description based on a formal electron transfer of two electrons per alkaline earth atom ($14A^{2+}$), four isolated Pn^{3-} atoms, one Pn_3^{7-} linear unit, and one $GaPn_4^{9-}$ tetrahedra is consistent with the semiconducting behavior of the system as well as with the details of the crystal structure. For the Mn phases an interesting problem arises. If the Mn atoms are formally trivalent, the bonding scheme is identical but then the metallic behavior is surprising. If the Mn atoms are divalent, the tetrahedral-based levels are one electron short so that if these levels can delocalize a metallic behavior can be expected. This is in agreement with the transport measurements but then the charge neutrality is apparently violated.

The unit cell of these phases is quite large (104 atoms) but a study of the electronic structure using the SIESTA approach has been reported [104]. A detailed analysis of the DOS, projected densities of states (PDOS) into atomic and orbital contributions and deformation density plots clearly validated the description of these phases in terms of interstitial A^{2+} cations, isolated Bi^{3-} atoms and Bi_3^{7-} linear units. These calculations also showed that there is a hole in the bonding bands which are based on levels of the $MnBi_4$ tetrahedra and exhibit a sizeable dispersion. The Mn atoms were found to be divalent and the magnetic moment quite independent of the magnetic order in the solid. Essentially the presence of the hole in the bonding levels of the tetrahedra partially compensate for the high-spin d^5 Mn moment leaving a

net spin of approximately $4\mu_B$. Of course, this moment although mostly localized in the Mn atoms is spread out to the Bi atoms of the tetrahedra so that it should be associated to the $MnBi_4$ tetrahedra. This analysis is in nice agreement with the experimental finding of the simultaneous existence of localized magnetic moments and metallic behavior. At the same time the charge balance among the different structural species suggested by the Zintl approach (i.e., A^{2+}, Bi^{3-}, $Bi_3{}^{7-}$ and $MnBi_4{}^{9-}$) seems to be perfectly valid. However, the simultaneous presence of high-spin divalent Mn atoms and a hole in the bonding levels of the tetrahedra must be recognized in order to understand the physical properties of these phases.

The origin of the different magnetic behavior of the two phases ($Ca_{14}MnBi_{11}$ is ferromagnetic with a Curie temperature of T_C=55 K whereas $Ba_{14}MnBi_{11}$ is antiferromagnetic (AF) with a Néel temperature of T_N=15 K) was also investigated [104]. The magnetic units of the crystal structure (i.e., the $MnBi_4$ tetrahedra) are part of two different but interpenetrating three-dimensional networks. It was found that a ferromagnetic coupling occurs within each network but weaker inter-networks couplings with sign and magnitude quite sensitive to the details of the crystal structure also occur and influence the final magnetic order. $Ca_{14}MnBi_{11}$ was calculated to be ferromagnetic in agreement with experimental results while for $Ba_{14}MnBi_{11}$ the ferromagnetic and AF states were found to be practically degenerate. These phases share several features of their electronic structure with that of diluted magnetic semiconductors like $Ga_{1-x}Mn_xAs$. Thus, it is quite likely that the mechanism which provides for strong ferromagnetic interactions between Mn atoms of the same network in these phases is, in fact, the same that leads to ferromagnetism in the diluted magnetic semiconductors.

4.2 Diluted Ferromagnetic Semiconductors: (Ga,Mn)As

The discovery, during the last decade, of ferromagnetic order with relatively high Curie temperatures in heavily Mn-doped GaAs and InAs [105] has attracted much attention to these materials. It opens the way for many semiconductor spin devices, like new storage media and, more interestingly, an efficient spin injection into semiconductors. The latter is a necessary step towards the possibility of quantum computation using the spin degree of freedom in solid-state devices. From a more fundamental point of view, although there is a general agreement about the carrier (hole-) mediated origin of the ferromagnetism in these materials, the detailed mechanism is still a matter of debate. Sanvito and collaborators have studied several properties of (Ga,Mn)As using SIESTA. We describe some of their results in the following.

4.2.1 Role of Intrinsic Defects

Low temperature molecular beam epitaxy is used to grow samples with high Mn concentration, avoiding the formation of MnAs clusters. Unfortunately, low temperature growth leads to the incorporation of an As excess as large a 1.5%. This excess is stored in the form of As antisites (As_{Ga}), Ga vacancies (V_{Ga}), As interstitials (As_i), or their combinations, with As_{Ga} being believed to be the most abundant of them. As a consequence, the hole concentration p is considerably reduced compared to the Mn concentration, with the subsequent decrease of the Curie temperature T_c which is supposed to be proportional to p [106]. In [107–110] Sanvito et al. studied the role of these defects in the electronic and magnetic properties of (Ga,Mn)As. As a general trend, their first principles calculations show that As excess weakens the magnetic coupling between Mn ions. However, the details depend on the kind of defect and its relative position respect to the Mn ions. Since the Mn-induced spin splitting of the impurity bands is usually quite small, their energetic position relative to the top of the valence band of GaAs is very important in order to understand the effect of defects. For example, As_{Ga} exhibits an occupied level in the middle of the gap. These electrons will occupy the holes left in the valence band by Mn doping, leading to compensation and to the weakening of ferromagnetism. As_{Ga} defects can be transformed into a metastable As_i-V_{Ga} pair upon illumination. This was already known for GaAs [111], and demonstrated for (Ga,Mn)As in [107]. Interestingly, for As_i-V_{Ga} the occupied impurity band lies much closer to the top of the valence band. As a result, the sample is left uncompensated as in the defect-free case and the ferromagnetic coupling is left almost unchanged. According to Sanvito and Hill, this could provide a route to increase T_c, although not for technological applications since the recombination of the As_i-V_{Ga} into As_{Ga} takes place at ~140 K. It is also worth mentioning the case of the isolated V_{Ga}. In this case, although hole concentration is increased, the ferromagnetic coupling is also reduced. This defect introduces holes both in the minority and majority band and, therefore, produces compensation of the spin up and down carrier density in the sample. When Mn ions are close to each other, things get even more complicated since AF double exchange interactions start to play a role. In this case Mn ions with a common As_{Ga} neighbor can align both ferromagnetic or antiferromagnetically, depending on the detailed structure and As antisite concentration [109].

4.2.2 Transport in Digital Ferromagnetic Structures

Large concentration of Mn can be obtained in the so-called digital ferromagnetic heterostructures (DFH), composed by zinc blende MnAs submonolay-

ers embedded in GaAs to form MnAs/GaAs superlattices [112]. The electronic structure of several DFHs have been studied using SIESTA by Sanvito [113], and Sanvito and Hill [114]. The self-consistent Hamiltonian and overlap matrices are then used to obtain the ballistic transport of the system using the Landauer-Buttiker formula and a Green's function technique [114]. The main conclusions of this work are: i) in the absence of intrinsic donors these systems have a half metallic band structure, with an exchange interaction much stronger than that of the random alloy with the same Mn concentration; ii) transport calculations show that the carriers at the Fermi energy are strongly confined within a few monolayers around the MnAs; and iii) the transport in the direction perpendicular to the MnAs planes is due to tunneling. Therefore DFHs can be pictured as a two-dimensional half metal in the MnAs plane, with tunneling-like conductance between MnAs planes.

4.3 Clusters, Surfaces, and Interfaces

4.3.1 Fe Systems

The use of low dimensional magnetic systems is one of the possible routes to design new magnetic storage devices with higher storage densities and miniaturization [115]. Besides this technological interest, and partially driven by it, the study of the change of the material properties with the reduction of the size and dimensionality of the samples has generated a vivid interest during the last decades. Magnetism could not be an exception in this trend, especially since the discovery that the magnetic moment of a material could be enhanced by diminishing the atomic coordination [116]. For example, certain paramagnetic materials like Rh or V seem to develop considerable magnetic moments in small aggregates. Also surfaces and clusters of ferromagnets are known to exhibit larger moments per atom than in bulk.

Izquierdo et al. [117] analyzed these trends for several iron systems using SIESTA calculations. They studied several pure iron systems: dimer, bulk bcc, (100) surface and free-standing (100)-like monolayer. They also considered a monolayer and several Fe clusters supported on Ag(100) of different *dimensionalities*: adatom, monatomic wire, rectangular patches containing four and nine atoms, and a small pyramid of thirteen atoms. Whenever it was possible, the comparison with previous calculations was very satisfactory, therefore validating SIESTA as an accurate tool for the study of complex magnetic structures. Of special interest in this regard is the observation that already a quite modest single-zeta polarized basis [118] provided a very reasonable description of all considered situations, with the obvious advantages of computational efficiency and possibilities to scale-up the size of the studied systems. The agreement with available experimental data is also good.

The results of Izquierdo et al. can be summarized saying that in all the calculated configurations the magnetic moments of the Fe atoms obey the coordination rule, i.e., the lower the coordination the larger the magnetic moment. This is not restricted to coordination with other iron atoms, it also holds for neighboring silver atoms. For example, going from the free-standing to the Ag(100) supported Fe monolayer reduces the atomic magnetic moment by ~0.30 μ_B in perfect agreement with previous all-electron calculations [119]. Another interesting observation is that SIESTA calculations tend to give somewhat larger magnetic moments as compared with all-electron results. In fact, the magnetic moments are usually in very good agreement with PW pseudopotential calculations. The origin of this small discrepancy seems then to be related to the use of pseudopotentials and not to the basis set utilized. As we will see below the differences between all-electron and pseudopotential results can be more dramatic for other systems, like the V(100) surface. The message here seems to be that special care has to be taken with the construction and testing of pseudopotentials in the case of magnetic systems [120].

One of the key advantages of SIESTA with respect to other popular methods to study large magnetic systems (like the KKR method) is that structural relaxations and calculations for distorted structures can be straightforwardly performed. This ability has been extensively used by Dieguez and collaborators [121] in their study of the structural and magnetic properties for Fe_n aggregates with n ranging from 2 to 17. This was the first ab initio study for Fe clusters containing more than seven atoms. A quite complete exploration of the energy landscape was performed by relaxing more than 200 initial configurations, and identifying the most stable isomers for each size. The authors used a quite complete triple-zeta with double-zeta polarization basis set, and local spin density approximation. In general, for $n \leq 7$ the results are in quite good agreement with previous first principles calculations. For n=8, 9, and 10, the ground-state geometries are, respectively, a bispheroid, a tricapped trigonal prism, and a bicapped square antiprism. However, not far in energy (second most stable) we can find isomers which follow an icosahedral growth pattern. In fact, the ground-state structures of n=11, 12, and 13, also follow an icosahedral packing. However, for $n>13$ nonicosahedral symmetries are instead predicted to be more stable. These structural changes (from n=13 to 14, the structural pattern also changes between n=14 and 15) are in very good agreement with the predictions by Parks et al. [122] on the basis of the observed large reactivity variations. Interestingly, the n=13 to 14 change is accompanied by an important change in the average atomic magnetic moment. The structures, binding energies, magnetic moments and nearest-neighbors distances of the low energy isomers of clusters with $14 \leq n \leq 17$ can be found in Fig. 4. In good agreement with the time-of-fly mass spectroscopy measurements [123], Dieguez et al. calculations [121] predict the Fe_{13} and Fe_{15} clusters to correspond to *magic numbers*.

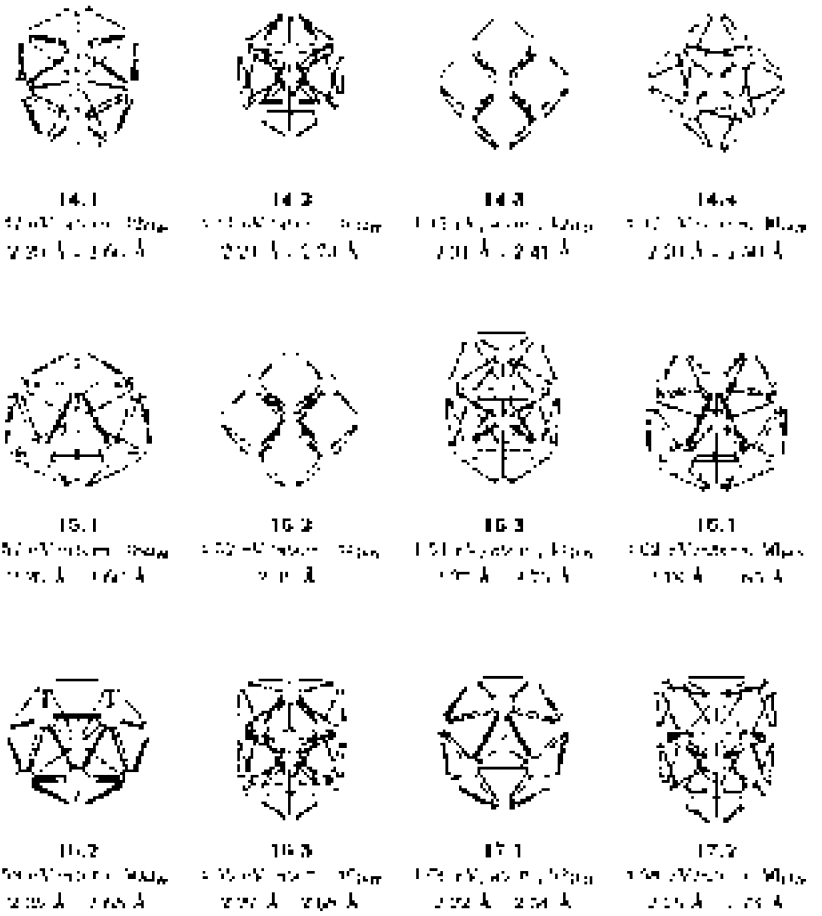

Fig. 4 Some isomers found in [121] for Fe_n ($14 \geq n \geq 17$) with their binding energies, total magnetic moments, and nearest neighbors distances. Isomer *n.m* is the *m*-th least energetic isomer with *n* atoms. Reproduced with permission from [121]

Postnikov et al. [124] performed a study of the relaxed structures and magnetic properties of larger clusters, up to Fe_{62}. In most cases only icosahedral, fcc- and bcc-derived structures were considered. For most of these aggregates this has been the first study including structural optimization. Some conclusions, roughly independent of the morphology, magnetic ordering and size, seem to emerge from this work: i) the structural relaxation is mostly confined within the 2–3 outer shells, ii) there is a strong inward relaxation of the surface layer, and iii) the magnetic moments on the surface are enhanced beyond 3 μ_B. A benchmark study of non-collinear magnetism

in Fe_3 and Fe_5 with SIESTA is included in [124], the results being in good agreement with previous calculations [125].

4.3.2 V(001) Surface

Vanadium is one of those paramagnetic metals that can exhibit magnetism under certain conditions due to its large magnetic susceptibility. In particular, there has been some controversy about the V(001) surface, where indications of possible ferromagnetism were observed [126]. Theoretical results are also inconclusive for this system. Calculations performed at the LSDA level [127] found no indication of appreciable surface induced magnetic moments. However, recent studies using GGA presented contradictory results. The all-electron results of Bihlmayer et al. only found small surface magnetic moments for very thin films [128]. However, the PWs calculations of Bryck et al. using ultrasoft pseudopotentials predicted a large magnetic moment of 1.70 μ_B [129]. To try to settle this question Robles and collaborators [130] performed a comparative study of the magnetism in the V(001) surface using the SIESTA method and an all-electron tight-binding linear muffin-tin orbital atomic-sphere approximation (AE-LMTO) method [131]. They used slabs containing 7 and 15 layers and both LSDA and GGA for the exchange-correlation potential. For bulk bcc a paramagnetic ground state is found irrespective of the calculation method and the exchange-correlation approximation used. This result is in agreement with the experiment and persists for expansions of the lattice parameter up to ~10%. In contrast, the results for the surface magnetization of V(001) are quite different for LSDA and GGA calculations. Similarly to previous calculations [127], no surface magnetization is found with both methods when using LSDA. However, GGA calculations exhibit appreciable surface moments, at least for the thinner slab: 0.66–0.25 μ_B in the case of AE-LMTO depending on the functional utilized and 1.77 μ_B for SIESTA. This is a clear indication of the well known tendency of the GGA to produce larger magnetic moments than LSDA. It also seems to indicate that pseudopotentials tend to enhance even more the surface moment. This becomes more evident by increasing the size of the slab. For the 15 layers slab case, all-electron results predict zero surface magnetic moment, while the pseudopotential ones (SIESTA) still predict a large magnetic moment of 1.70 μ_B in very good agreement with the previous PW results [129]. This points out the failure of the pseudopotential approximation to describe the magnetic properties of this surface as compared to all-electron methods, and has been confirmed with other subsequent comparative studies [132, 133]. According to Kresse et al. [132], for a good description it is not sufficient to use just non-linear core corrections—it is also essential to describe accurately the shape of the *d* wave functions in the region where the magnetization density reaches its maximum. Unfortunately, for most

generation schemes this leads to very hard pseudopontentials which are not useful in practice.

4.3.3 Fe/*c*-SiFe/Fe Sandwiches and Multilayers

Magnetic multilayer devices (MMD) can be roughly classified according to the nature of the spacer materials, which leads to very different behavior of the exchange constant between the magnetic layers J, as a function of the spacer thickness *z*. For metallic spacers the sign of J oscillates and its magnitude decays as $1/z^2$. For semiconducting spacers, however, J decays exponentially and is AF in most cases. Devices in which the spacer is a semimetallic material represent an intermediate case. The coupling is always AF, but the decay is very slow, becoming negligible at spacer thicknesses more typical of the metallic structures. One example of this behavior are the (Fe/*c*-FeSi) MMDs. The spacer here consists in iron silicide in the CsCl structure (*c*-FeSi), and can be easily formed by interdiffusion of Fe and Si slabs of appropriate thicknesses grown epitaxially. Pruneda et al. [134, 135] have recently performed an ab initio study of the magnetic and electronic properties of these structures. They considered both free standing trilayers and multilayers with the sequence $Fe_7/c\text{-}Fe_{(n-1)}Si_n/Fe_7$ with n=1–6. For fixed geometries, obtained from the experimental data, the authors compared the results obtained with a scalar relativistic all-electron AE-LMTO [131] method and those given by SIESTA. They also performed several structural relaxations with SIESTA, which were beyond the capabilities of the AE-LMTO method utilized. The structures however are quite stable and only slightly modified upon relaxation. These structural studies show that the most stable configurations are always those with the spacer layer formed by a regular *c*-FeSi structure. This is in agreement with the experimental observation, and supports the idea that these structures can be formed by interdiffusion of a thin Si film into the Fe slabs. The exchange constants obtained with SIESTA and with the AE-LMTO are similar within a 10%. They are always AF when the spacer is formed by *c*-FeSi, with a value of a few mili-rydbergs which decreases in a non-monotonic fashion, with a clear bump for n=3, and becoming negligible for $n \approx 5$–6. This behavior is almost identical for trilayers and multilayers. The authors have also considered the effects of pinholes, interface roughness and structural misconfiguration on J. The general conclusion is that structural defects and misconfigurations give rise to strong ferromagnetic couplings. Finally Pruneda et al. [134, 135] considered the limit of very thick spacers using the phenomenological theory developed by Bruno [136] in conjunction with the appropriate effective masses and band edges to provide a realistic description of the electronic structure of *c*-FeSi. With this model the authors are able to reproduce the experimental decay length of 3.6 Å, and identify the electronic bands responsible of this unusually slow decay.

4.3.4 Cobalt Valence Tautomers

Transition metal complexes with redox active ligands have been extensively studied in recent years. Some of these compounds are interesting candidates for mechanical and magnetic switching devices activated by temperature, pressure, or irradiation. In a recent paper, LaBute and collaborators [137] have studied the electronic and structural properties of cobalt based valence tautomers of generic form $Co(SQ)_2L_p$, where SQ represents a semiquinone ligand complex with formal charge −1 and spin 1/2, and L_p represents a neutral redox counterligand. When cooled in frozen organic solvents, or in molecular solid form, these molecules undergo a transition, in a narrow temperature regime, from a high spin, high volume form, to a low spin, low volume form. It has been traditionally assumed that, accompanying this transition, there is a charge transfer from Co to the SQ ligand, with an enhanced ligand field splitting arising from the bond contraction favoring the low spin Co(III). Although consistent with many experimental observations, this image was not fully supported by previous electronic structure calculations [138] and, thus, LaBute et al. [137] decided to apply SIESTA to address this problem.

In agreement with the observation, the electronic structure calculation lead to a high spin (~3/2) Co for the high temperature geometry, while a low spin (~0) Co is found for the low temperature structure. Furthermore, the low spin state cannot be stabilized for the high temperature configuration and vice versa. The authors assign this effect to the increase of the 3*d*-2*p* hybridization upon contraction, which disfavors the Hund's rule alignment of the spins. The energy difference between the two configurations is 1.3 eV for the experimental geometries, which is reduced to 0.6 eV after structural optimization. The distance between Co and the ligands change very little however, and the distinct spin states are stable during this process. Even after relaxation, this energy difference is too large compared to the experimental transition temperature. In their work, LaBute et al. argue that the high temperature phase of the valence tautomers is *mixed valent*, in the sense that the ground state is a quantum superposition of states with predominantly two well defined valences for Co. This could be at the origin of the incorrect energetics, since in order to accurately describe this state it is necessary to go beyond DFT. The authors then turn to an empirical Anderson impurity model Hamiltonian for the molecule in which local electron correlation effects are taken into account on the Co site but neglected on the *metallic* carbon rings. With this simplified model they are able to properly describe the energetics of the systems along with some unexplained feature of the X-ray absorption spectra. The DFT calculations pointed out another puzzle: the transition to the low spin states is accompanied by an increase of the Mulliken population of the *d* orbitals of Co, contrary to the expectation. A de-

tailed analysis of the projected DOS is necessary to solve this problem. As expected, it can safely be considered that one e_g electron of the metal gets transferred to the ligand SQ level. However, in the low-spin configuration there is a significant covalency between the metal-e_g and ligand-σ orbitals, so that the Co e_g states are significantly *repopulated* through their hybridization with the ligand states.

5 Clathrates, Zeolites, and Minerals

The SIESTA approach is especially designed to handle large systems so that it is not surprising that it has been quite extensively used in order to study minerals, clathrates, and zeolites. Quite often a key aspect in studying processes in these systems is the determination of the distribution of cationic species in the large cavities they exhibit. To handle this question extensive computations with methods giving reliable energy differences are needed. The SIESTA approach seems to fulfill both the precision and efficiency requirements in order to be a useful tool in this area. Here we discuss some recent applications of the SIESTA approach to this kind of materials.

5.1 Clathrates

Clathrates are materials with interesting physical properties and a large potential for technological applications. Thus, there is a need for theoretical studies which can lead to useful guidelines in the process of optimizing their physical properties. For instance, group IV X_{46} clathrates (X=Si, Ge) are cage-like materials containing X_{20}, X_{24}, and X_{28} clusters. Doped clathrates of this type have been the object of several theoretical studies using the SIESTA approach. A recent example is a study of hypothetical C_{46} clathrates and their potential use as low work function metallic systems [139]. The bare and hydrogenated (100) surfaces of the undoped and Li-doped systems were studied. In that way it was possible to suggest that under doping these materials are true metals with a low work function (i.e., significantly lower than those of alkali metals) and with a stability typical of diamond-like systems, a result opening new perspectives for the making of efficient electron emitters. A related study dealing with the tailoring of the band gap and hardness of iodine doped Si_{46} clathrates has also been reported [140]. A careful study of the structural and electronic properties of $I_8@Si_{46}$ showed that, in contrast with the situation in other doped clathrates, there is a strong hybridization between the iodine and silicon network orbitals. This fact is responsible for a large opening of the band gap. Similar results were obtained for $Xe_8@Si_{46}$, giving additional evidence for the irrelevance of ionic effects behind such

band opening. A quasi-particle calculation within the GW approximation for the last system led to a band gap of approximately 2.25 eV showing that the material is a silicon-based "green light" semiconductor. This suggests that doped clathrates may be useful materials in making silicon-based optoelectronic devices.

The discovery of superconductivity in $Na_xBa_{8-x}@Si_{46}$ and related compounds triggered a large activity on their transport properties. Interestingly, whereas $Na_xBa_{8-x}@Si_{46}$ and $Ba_8@Si_{46}$ are superconductors, $Na_8@Si_{46}$ is not. A combined experimental (inelastic neutron-scattering and extended X-ray absorption spectroscopy, EXAFS)-theoretical (SIESTA approach) study has been reported [141] in an attempt to provide some insight into the mechanism of superconductivity. Both the analysis of the calculated phonon DOS and the vibrational motion determined by inelastic neutron-scattering suggested that the coupling between the guest atom and the host through host acoustic modes was essential in governing the possible superconductivity of these materials. In fact, the combined theoretical-experimental approach clearly showed that Ba was considerably more strongly bound to the silicon cages than Na or K. A detailed analysis showed that the main parameters to be correlated with the superconductivity occurrence were the host-guest vibrational coupling inside the Si_{24} cages of the structure as well as the DOS at the Fermi level. It was also shown that a large ionic radius for the donor atoms in the Si_{24} cages of the clathrate is needed for the enhancement of the critical temperature. However this requirement is not needed for the donors in the Si_{20} cages because the coupling is already strong in that case.

5.2 Minerals and Zeolites

Structural studies of minerals are important both from mineralogical and commercial viewpoints. Some widely used commercial materials are difficult to structurally characterize fully from a purely experimental approach so that computational approaches can be extremely useful. Often quite large unit cells must be used in these studies so that empirical approaches have been extensively employed. However empirical models have well known limitations which can only be overcome through the use of first principles calculations. In addition, let us note that many minerals (and zeolites) are extensively used in catalytic processes where bonds are broken and created. Under such conditions the use of non-empirical methods is really important. Here we discuss some recent works which have used the SIESTA approach to study quite different problems (mostly structural) concerning minerals and zeolites.

Aluminum hydroxides are the hydrated precursors of transition aluminas, which are widely used as catalyst supports in refining industry. The dehydration process strongly depends on the structure of the precursor. For in-

stance, starting from the boehmite precursor, the dehydration leads to the stable α-alumina through a large variety of metastable transition aluminas. When the process is initiated from the gibbsite or bayerite precursors, three other types of transition aluminas are formed on the way to α-alumina. However the same process leads directly to α-alumina when the diaspore precursor is used. Thus, the formation and structural properties of transition aluminas are strongly dependent on the type of aluminum hydroxide precursor. The real crystal structures of some of these precursors are still not clearly known despite large effort. In particular, the hydrogen positions remain controversial in several of these layered polymorphs. Two groups have carried out theoretical studies of the different polymorphs of aluminum hydroxides using the SIESTA approach [142, 143] which have provided very valuable data concerning their structure and stability.

Digne et al. [142] carried out full structural optimizations (including cell constants, space group and atomic positions) for several aluminum hydroxide polymorphs with different degrees of hydration: gibbsite, bayerite, diaspore, boehmite and tohdite. Comparison with the more reliable structural data presently available showed that the accuracy of the theoretical approach was very good. In some cases (bayerite and gibbsite) the agreement was better than for other calculations also using the SIESTA package [143] because of an extensive optimization of the basis set used in the computations. This is an important aspect in view of future applications in this field. Trends in dehydration processes were also found to be correctly reproduced. An important result of this study was that the total energy of these systems does not seem to depend very much on the hydrogen positions. On the basis of the simulation results these authors evaluated the Gibbs enthalpy variations and could provide a consistent explanation of the thermodynamical stability as a function of temperature of aluminum hydroxide polymorphs. It was pointed out that the degree of hydration of the thermodynamically stable species decreases when the temperature increases. In addition, limiting temperatures of stability for the various polymorphs were obtained which compared well with the experimental data available.

Gale et al. analyzed in detail the gibbsite and bayerite polymorphs [143]. Although the energy difference between the two polymorphs was found to be small (6.3 kJ/mol), gibbsite was found to be more stable in agreement with the fact the it is the predominant form in nature as well as with calorimetric results suggesting that gibbsite is approximately 5 kJ/mol more stable. These authors also considered the hydroxyl stretching frequencies for both polymorphs. Experimentally, the peaks for bayerite are systematically shifted to higher wave numbers with respect to those of the gibbsite. This tendency was also found in the calculated results and correlated with the smaller volume of the unit cell of bayerite in comparison to gibbsite. Globally, the two studies make clear that the SIESTA approach can be a very useful tool in this field. As shown by Digne et al. [142], for reasonable basis sets

sizes (typically, double-ζ plus polarization functions for all atoms) the calculated results are very good when the basis set is optimized. This is important because it makes feasible theoretical studies of much larger unit cell systems which will not be possible for plane wave type methodologies. In addition, since the SIESTA approach is designed to yield improved scaling with the system size, extensive applications of the method can be anticipated in the study of minerals.

The structure and processes occurring in zeolites have also been the objects of several SIESTA type studies. Zeolites are microporous aluminosilicate minerals which are important in a large variety of industrial applications. Both their ability to act as heterogeneous acid catalysts and the shape selectivity due to the dimensions of the channels are behind many of these applications. However, zeolites have another very important use as support materials for other types of catalysts like metal particles for instance. These systems are often not quite well characterized from the structural viewpoint because of the usual lack of long range order. The complexity of the zeolite framework and the very large number of possible interactions between the metal particles and zeolites makes very difficult the task of describing the bonding and reaction mechanisms within these systems. Another important but difficult aspect in experimental zeolite studies is the location of the extra framework cations. Simulation studies are very popular in this field. Although many of these studies have used empirical potentials, first principles approaches are being also increasingly used. For the reasons outlined above, the SIESTA methodology seems very well adapted to the needs of these studies.

The more extensive use of SIESTA in this field is due to Gale and coworkers [144–146]. An illustrative example is the study of the binding of palladium atoms and dimers in the zeolite gmelinite. This material contains 12-ring channels and 8-ring apertures interconnecting the channels. In a first step, they considered gmelinite as being purely siliceous and studied the different possible ways of binding the palladium atoms. They found several different sites, the three lowest energy ones being of comparable stability and sharing an unexpected structural feature: the palladium atoms interact with both the silicon and oxygen atoms. Naively it could have been expected that the bonding with oxygen would largely dominate. However, these authors could easily explain this result by considering the nature and energy of the lowest unoccupied levels of the zeolite which are largely localized in silicon. When palladium dimers were considered it was found that the second palladium atom only interacts with the oxygen atoms. Thus the interaction is very asymmetric. The shortening of the Pd-Pd bond with respect to that in the isolated dimer was found to be due to the charge transfer from the palladium dimer highest occupied molecular orbital (HOMO), which is palladium-palladium antibonding, to the zeolite lowest unoccupied molecular orbital (LUMO). The next step in the study was the consideration of the interaction

of CO with the platinum atoms. CO is used in zeolite chemistry to probe the Brønsted and Lewis acidic sites. Essentially, it was found that when CO binds to either single palladium atoms or dimers the bonding picture is strongly modified and the interaction with the silicon atom is lost because the nature of the metal HOMO is shifted. The next step of the study was the introduction of an aluminum in the framework in place of silicon as well as a sodium cation in order to ensure charge neutrality. It was found that the presence of aluminum in the framework increases the binding strength of the palladium metal although the type of binding is not significantly changed. In contrast the binding of Co to the metal particles is reduced in the aluminosilicate regions. Thus, this study led to many useful ideas which can be used to rationalize experimental observations in this kind of materials. It also makes clear the difficulty of this kind of studies due to the large number of initial configurations one needs to consider. Of course this difficulty will increase with the size of the clusters and dynamical annealing procedures will be needed. These studies are however feasible. Since some restrictions in the basis sets will be certainly needed, as noted above for aluminum hydroxides, a key point for the success of these simulations will be a careful optimization of the basis sets.

Zeolites have been the object of other SIESTA studies. For instance, Grey et al. [145] explored the location of calcium cations in chabazite and found that the site energies converge as the aluminum content increases. The main results agreed with those of a less computing demanding approach using empirical potential functions and the Mott-Littleton approach. In fact, the problem of site ordering of cations affects not only zeolites but also many other minerals and processes. For instance, Bosenik et al. [147] have shown how the combined use of empirical and quantum mechanical approaches like SIESTA can provide an operative way to face such problems. For instance, the SIESTA code was used to obtain corrections for the chemical potentials used in the framework of an empirical approach in order to study the Mg/Al and Al/Si ordering in amphibolides. Since these calculations needed the use of unit cells with more than 300 atoms, the refinement of an accurate empirical approach was an important task. These authors also used SIESTA in order to validate the results of an empirical approach to the study of solid solutions between the garnets pyrope and grossular [147].

The combined use of a first principles method like SIESTA and either empirical approaches or experimental studies can be a very fruitful approach which has already been used by several authors. For instance, Girard et al. [146] have used SIESTA type calculations in order to validate a force field put forward to study the structure of zeolitic gallophosphates. Borowski et al. [148] used a combination of experimental and theoretical techniques in order to solve the structure of the layered silicic acid H-RUB-18. The high degree of structural disorder precluded a classical structure analysis based exclusively on diffraction data. These authors used a combination of tech-

niques (X-ray, solid state NMR and force field MD) in order to generate a plausible model. The simulation of the X-ray powder diffraction confirmed the model but disorder and pseudosymmetry yielded only a time and space averaged atomic arrangement. SIESTA calculations in triclinic symmetry finally led to a satisfactory description of the local as well as the periodic structure.

Other studies in this field for which the SIESTA approach has been used include the study of cation distributions in phyllosilicates like pyrophyllite, beidellite and several smectites and illites [149], a study of the (001) surface of galena [150] and the combined theoretical-experimental study of the structure oh the high-pressure monoclinic phase II of cristobalite [151].

6
Surfaces and Interfaces

Surfaces and interfaces play a crucial role in a large number of industrial and technological applications. This relevance can be illustrated with a few examples such as catalysis or the design and growth of coatings to avoid corrosion, thermal barriers, or microelectronic devices. Unfortunately these are hard systems to study, both experimentally and theoretically. The complex bonding patterns may lead to unexpected coordinations and structures. This, in addition to the possibility of considerable charge transfers between the adsorbed species and the substrates, or even between the surface and the corresponding bulk, reduces the applicability of semiempirical methods, which are usually fitted to the bulk properties. Self-consistent first principles electronic structure methods stand then as the ideal tool to study these systems. However, the large simulation cells usually required then become a limiting factor, and the use of computationally efficient methods becomes instrumental. Approaches like SIESTA are therefore very much needed in this context.

6.1
Clean Surfaces

6.1.1
Liquid Si Surface

At 1684 K, silicon transforms from a covalent semiconductor solid to a quite peculiar liquid metal. It is well known both from experiments and simulations that its coordination is much lower (~6–7) than that of typical liquids (~12), which is a clear indication of the persistence of directional bonding in the liquid phase. Very little is known about its surface, and the measurements are extremely difficult due to the high reactivity and melting temper-

ature. In order to get some insight into its structural properties Fabricius et al. [152, 153] performed first principles MD simulations of this surface using SIESTA. The most interesting result is the observation of a marked atomic layering of the density near the surface. This is somewhat surprising since this kind of layering is usually observed for metals with quite low melting temperature. However, the origin of the observed effect is different in the case of silicon. It is a direct consequence of the remanent directional bonding of liquid silicon which manifests in a strong anisotropy of the local coordination and translates into the creation of a well defined surface layer. The layering, however, has little effect in the electronic and dynamical properties of the surface, which rapidly converge to those of bulk liquid silicon.

6.1.2 Si(001)

Motivated by the long-standing controversy between a ground state of the Si(001) surface exhibiting symmetric or asymmetric dimers, Paz et al. [154] have performed spin-polarized density functional calculations of several reconstructions of the system ((2×1), p(2×2) and c(4×2)) using SIESTA. LSDA calculations converged to non-polarized results in very good agreement with other calculations in the literature. Calculations using GGA predict a ground state with AF order for small dimer inclinations, indicating the importance of Mott-like correlations among the dangling bonds. Lower energies, however, always correspond to higher dimer inclinations with no spin. Although DFT energies cannot be fully trusted, Paz et al. have analyzed different contributions to the energy (surface stress, hopping between neighboring dimers), which turn out to be of very similar magnitude (a few tenths of an eV per dimer) making the problem even harder. In fact, the authors argue that the observed buckling could originate in these extrinsic effects, while intrinsic (intra-dimer effects) would favor a symmetric dimer.

6.1.3 FeSi(CsCl)

Transition metal silicides and their interface with silicon have a large technological interest due to their potential application in microelectronic and optoelectronic devices. Iron silicides are particularly interesting since they can be grown on silicon substrates in a wide range of stoichiometries and structures. One example is the CsCl phase, which is unstable in the bulk, but can be successfully stabilized on Si(111) for thickness up to a few hundred Ångstroms [155] due to its small lattice mismatch (+2%) with this substrate. Low-energy electron diffraction (LEED) patterns indicate an unreconstructed 1×1 surface. Hinarejos et al. [155] tried to get more insight into the structure and termination of the surface measuring angle-resolved photoemission

(ARPES) spectra. The data was then interpreted using simplified calculations of the surface electronic structure based on a tight-binding model obtained from bulk calculations. The results seem to indicate that the Fe termination was more likely to fit the spectra. However, the problem has been recently re-examined by Junquera et al. [156] using SIESTA, and found that only the Si-terminated surface is compatible with the experimental surface band dispersion. In particular, the experimental data reveal a surface band of Λ_1 symmetry at Γ which can only be reproduced for the Si-terminated surface. The shape and energy position of this band are also in very good agreement with the experiment. Interestingly the calculations also reveal the presence of a second surface band whose energy position and dispersion seem to be quite independent of the termination. This band has always major weight on Fe atoms, even when Fe is absent from the outermost layer. This explains the insensitivity to the termination and the fact that it is not clearly resolved with photoemission. This band is probably responsible for the residual intensity detected in the s-polarized spectra. Recent scanning tunneling microscope (STM) images and LEED measurements [157] on the CsCl-structure FeSi/Si(111) film surface seem to confirm the predicted Si-termination of the samples.

6.2 Adsorption on Metallic Surfaces

6.2.1 Doped C_{60} Monolayers on Ag(111)

C_{60} fullerides exhibit several interesting phenomena related with the presence of strong correlations such as high temperature superconductivity or antiferromagnetism. The existence of non-conventional behaviors can be anticipated from the fact that both the electron-phonon and electron-electron interactions are, respectively, comparable and much larger than the narrow bandwidth predicted by standard electronic structure calculations (a few hundreds of meV). These systems are therefore close to a metal-insulator transition of the Mott-Hubbard type and the validity of the adiabatic approximation, assumed in most electronic structure calculations, can be questioned. From the experimental point of view the band derived from the molecular LUMO is usually seen as a quite broad feature, much wider that the theoretical estimates, in photoemission experiments. However, the observation of the band dispersion has proven elusive in ARPES studies until very recently. In a recent joint experimental and theoretical paper, Yang et al. [158] have reported the first photoemission measurement of the band dispersion for a K-doped C_{60} monolayer deposited on a Ag(111) substrate. The results have been compared with ab initio calculations performed with SIESTA. In those calculations the Ag substrate was modeled by a slab con-

taining six layers, and the coordinates of the three K atoms and the center of mass were relaxed. The calculated band dispersion was observed to be quite sensitive to the orientation of the molecule with respect to the substrate. This fact can be used to determine the C_{60} orientation by comparing the measured and calculated band data. The orientation determined in this way was very similar to that which minimizes the total energy. In general the shape of the calculated and observed band is in very good agreement. Surprisingly, the measured bandwidth and Fermi velocity are only renormalized by 40% and 50%, respectively, as compared with the theoretical values of 170 meV and $\sim 1.4\times10^{7}$ cm s^{-1}. This value of renormalization is within the range explainable by electron-phonon effects alone. This suggests that, contrary to the common belief, the role played by electron-electron correlations in renormalizing the bandwidth in these systems might be not substantial.

6.2.2 H_2O on Ag(111)

A reliable model for the water-metal interface, the so-called double layer, is instrumental for the accurate description of electrochemical phenomena. In spite of the large effort devoted to it there is no general consensus on a model, and the existing ones have difficulties in rationalizing all the abundant experimental information. This may not be surprising given the complexity of the problem. An intermediate step for the understanding of the electrochemical interface is the study of the adsorption of the water molecule on metallic surfaces. This is a somewhat better defined problem for theoretical methods, and a considerable corpus of experimental work exists [159]. One of the many open questions is the response of the molecule to the electric field in the interface. It is frequently assumed that the molecular orientation changes from oxygen-up to oxygen-down in response to electric fields. This behavior seems to be confirmed by the experimental evidence [159], but there were not first principles calculations supporting this idea. Recently Sanchez [160] used SIESTA to perform a series of simulations on the subject. He studied the orientation of a water molecule adsorbed on a charged Ag(111) surface as a function of the charge. Some modifications in the code were necessary to include the effects of the electric field. The method relies on the inclusion of a charged plane at the boundary of the cell parallel to the surface [161]. On the neutral substrate the molecule lies approximately parallel to the surface almost directly on top of one of the surface atoms. This geometry is explained by the character of the molecular orbitals involved in the bonding. Although all molecular orbitals are stabilized upon adsorption, the bonding interaction with the substrate is mostly mediated by the HOMO, $1B_1$. This is a π-lone pair, which maximizes its overlap with the states of the substrate for the parallel orientation. The orientation parallel to the surface and its interpretation in terms of the covalent metal-$1B_1$ has been

confirmed in a recent theoretical paper [162] on several closed-packed surfaces of transition and noble metals. The molecule is tilted as the charge of the Ag(111) surface increases, with the oxygen pointing away for negative surface charge and the oxygen pointing towards the surface for positive charge. This is solely due to the effect of the electrostatic interaction and takes place with a minor change of the height of the center of charge (~0.2 Å). The tilting of the molecule is accompanied by an increase of the binding energy, again of electrostatic origin. A linear behavior of the angle vs the surface charge density is observed in the region ±5 μC cm^{-2}. Complete orientation of the molecule in the direction of the field (i.e., perpendicular to the surface) is achieved for a critical charge density of ~15 μC cm^{-2} for both polarities. These results support the idea that the observed lowering of the inner layer capacitance at large charge densities [163] is due to the dielectric saturation of the water layers closest to the electrode.

6.2.3 CO on Ni(111)

Quiros et al. have performed an X-ray diffraction study of the absorption geometry of CO on Ni(111) under equilibrium conditions in ambient CO gas pressures ranging from 10^{-6} mbar to 1.2 bar [164]. Within this pressure range the ordered $\sqrt{7}x\sqrt{7}R19.1^{\circ}$ structure is observed. In this structure the CO molecules bind to top and bridge substrate sites with a relative population of 1:3 respectively [165]. The lattice parameter is found to change reversibly with the gas pressure by 7.6% within the range considered. These experimental observations were contrasted with first principles calculations. The SIESTA package was used to calculate the interaction potential between free-standing and absorbed CO molecules. The main conclusions of the calculations are: i) the interaction between molecules is purely repulsive in the range of distances relevant for the studied structure; ii) it is very similar for the case of supported and gas-phase molecules, being iii) quite independent of the adsorption sites; iv) the effective interaction is very well described as pairwise (the estimated three-body contributions are one order of magnitude smaller than the two-body term). At the separation characteristic of the $\sqrt{7}$ structure the repulsive forces between molecules are around 0.1 eV/Å.

6.2.4 Metals on Metallic Surfaces

The deposition of metals on different metallic substrates is not only a problem of fundamental interest but it is very relevant in electrochemistry, particularly in the field of the so-called underpotential deposition [166]. This involves the deposition of a metal monolayer at potentials more positive than the reversible Nernst deposition potential of the adsorbate. A meaning-

ful concept in the theory of underpotential deposition is the so-called underpotential shift that is defined as the difference of the chemical potential of the atom adsorbed on a foreign substrate at a given coverage θ, and the chemical potential of the same species in the bulk. At T=0 K this is just the difference between the cohesive energy of the metal in the bulk and its adsorption energy in a given substrate, the so-called excess binding energy ΔU_{ex}. In [167] Sánchez et al. have used the SIESTA code to calculate this magnitude for the (111) surface of several popular single-crystal face-centered cubic electrochemical systems (mainly noble metals), and compared the results with the available experimental information. As a general trend ΔU_{ex} can be correlated with the surface energies of both adsorbate and substrate, as was expected from very simple considerations. For a given substrate ΔU_{ex} decreases with increasing the surface energy of the adsorbed species. Conversely, for a given adsorbate ΔU_{ex} increases with the surface energy of the substrate. There are notable exceptions to these tendencies, mainly for adsorbates and substrates exhibiting a large lattice mismatch like Cu/Au(111) and Cu/Ag(111) systems. For a few systems the authors also report the values of ΔU_{ex} obtained with converged PW calculations with the fhi96md package [168]. They are in almost perfect agreement with the SIESTA calculations. The numerical values for ΔU_{ex} can be split into two contributions, one coming form exchange and correlation energy and other containing kinetic and electrostatic energy contributions. In general these two large energetic contributions behave in opposite ways with the lattice parameter and, therefore, the magnitude and sign of ΔU_{ex} comes as a delicate balance and is difficult to predict on simple grounds. The comparison with the experiment is very good is some cases like Ag/Pt(111) (0.33 eV calculated vs 0.2–0.35 eV measured). In other cases however, particularly for Cu/Pt(111), the comparison is not so favorable (0.06 eV calculated against a measured value of 0.4 eV) which seems to be related to the effect in the adsorption energies and structures of the solvent and the anions present in the solution.

6.3 Adsorption on Si Surfaces

6.3.1 Ba on Si(001)

As already mentioned, one possible way to eliminate the fundamental limitations of current field effect transistors would be to substitute the silica by other high dielectric function oxides as gate materials. Unfortunately, the growth of high-quality oxide films on silicon substrates is not a simple task, and much work is being devoted to develop appropriate methods. For example, it has been shown that the formation of thin films of alkaline-earth-met-

al silicides is an essential step in the epitaxial growth of crystalline oxides on Si(001) [169]. The quality of the growth seems to depend critically on the prior formation of a sub-monolayer of silicide. Therefore, the study of the process of adsorption and growth of these silicides is very important. Wang et al. [170] used SIESTA to simulate the first stage of the Ba deposition of Si(001). In good agreement with the STM images it was found that, at low coverages, the preferential adsorption site is located in the trough between the Si dimer rows. The bonding was found to be strongly covalent, with a small charge transfer (~0.15e) to the Ba. This is quite surprising in view of the large electronegativity difference between Ba and Si, and explains the observed core level shifts [171]. The problem of diffusion of Ba on this surface was also addressed from the analysis of the potential energy landscape for the Ba adsorption. It was found that the diffusion takes place preferentially along the direction parallel to the dimer rows (seven orders of magnitude more probable than perpendicular to the rows). Based on this observation a one-dimensional growth behavior was predicted, which seems to have been confirmed by recent STM experiments [172].

6.3.2 Pb on Si(111)

Pb/Si(111) constitutes an excellent system for the study of the metal-semiconductor interface due to the low mutual bulk solubility of both components. Consequently a number of experimental works have been devoted to this surface during the last decade, unveiling a rich phase diagram, especially at low coverage. For larger coverage, close to 1 ML (ML=monolayer), the competition between Pb-Si and Pb-Pb interactions gives rise to incommensurate phases at room temperature. However, by cooling down the system, a new ordered phase, denoted as $\sqrt{7}x\sqrt{3}$, has been observed by X-ray diffraction [173] and STM [174] among other techniques. Following this experimental work, the first electronic structure calculation of this surface has appeared very recently. In a joint experimental and theoretical paper, Brochard et al. [175] used the SIESTA code to study the structure, bonding and relative stability of several phases of Pb/Si(111). The agreement with the available experimental information was very good, including the simulated bias dependent STM images. The most stable structure predicted was unambiguously identified with the model proposed from the X-ray diffraction data [173], corresponding to a coverage of 1.2 ML. This rules out the trimer model resulting from a naive interpretation of the STM images. The ab initio calculations also confirmed the expected existence of covalent bonds between five of the Pb atoms in the surface unit cell (from a total of six) and the underlying Si atoms, thus saturating all the dangling bonds. Contrary to expectation, however, the calculations revealed that the bonding between lead

atoms has a markedly metallic character, with the valence electronic charge highly delocalized along the Pb overlayer.

6.3.3 C_{60} on Si(111)

The interaction of C_{60} molecules with silicon substrates is expected to be strong due to the presence of highly reactive dangling bonds. Indications of strong bonding have been reported by several experimental techniques. Probably one of the most striking ones is given by STM images where, contrary to the case of metallic substrates where molecules appear as fuzzy balls, on the Si(111) surface it is possible to infer the orientation of the molecules over the substrate and even to observe some of its internal features [176–178]. Two adsorption configurations are deduced from STM images: a *large* molecule with apparent height of ~0.6 nm that appears more round and fuzzy, and a *small* molecule with a height of ~0.5 nm which produces a clear internal structure and a large variety of shapes (orientations on the substrate) [176]. In order to identify the most favorable adsorption sites and structures and compare with the STM information, Sanchez-Portal et al. [179] have made an extensive study of the structure of C_{60} on the Si(111) surface using SIESTA. A 2×2 adatom surface was used as a model to simulate the terraces of the 7×7 reconstruction. In most cases the C_{60} molecule remains closely spherical, while the changes in the structure of the silicon substrate are larger, particularly the adatoms which move substantially to form extra C-Si bonds, even at the expense of breaking Si-Si bonds. In fact, the most stable adsorption models correspond to situations where one of the adatoms has broken some of its bonds with the substrate to allow for the formation of new, more stable, C-Si bonds between the fullerene and the substrate atoms. The estimated adsorption energy can be as high as 6.5 eV for this model, and the *electronic height* seems to be in good agreement with the apparent height of the small molecules in the STM experiments. Figure 5 shows two of the studied structures, corresponding to the two types of adsorption experimentally reported. Unfortunately, the agreement is somewhat poorer between the observed internal structure and the calculated plots of the local DOS of the slab calculations. Surprisingly, the comparison is more favorable when selected molecular orbitals, split from the fivefold degenerate HOMOs, are used instead [176, 177]. This is probably an indication that more sophisticated approaches than Tersoff-Hamman theory are needed to reproduce the STM images in this system.

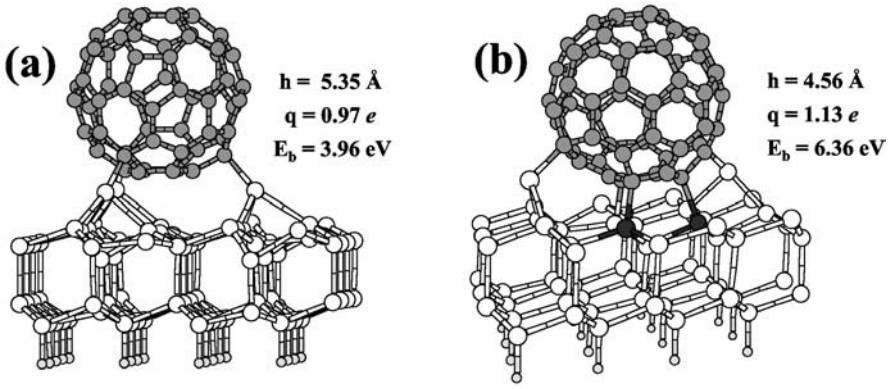

Fig. 5 Two of the configurations found for the C_{60} molecule on the Si(111) surface: **a** this structure would correspond to the *large molecules* type observed in the STM experiments; **b** this structure would correspond to experimentally more stable *small molecules* type. In the latter structure two of the adatoms have broken their bonds with the Si atoms in the surface, allowing the formation of two extra bonds (*highlighted in the figure*). Estimated binding energies, charge transfers to the fullerene, and height of the molecule center of mass over the substrate are also indicated. Reproduced with permission from [179]

6.3.4 Si(557)-Au

The Si(557)-Au reconstruction is formed after the deposition of ~0.2 ML of gold on top of a vicinal Si(111) with the misorientation chosen along the $[\bar{1}\bar{1}2]$ direction and, therefore, the steps are parallel to $[1\bar{1}0]$. This surface presents a (5×1) reconstruction, and the deposited Au atoms are supposed to form a monatomic wire on each terrace running parallel to the step edge. For this reason it has been proposed as an experimental realization of a one-dimensional metal. In fact, ARPES experiments on these systems found one band with a strong one-dimensional character (i.e., only dispersing along the steps direction) which seems to split in two bands in the proximity of the Fermi level (E_F) [180]. This was considered quite a surprising observation since, in a simple model that solely takes into account the Au chain, only one band coming from the 6*s* Au states was expected to cross E_F. The two bands were then interpreted as a signature of the one-dimensional character of the system (spin-charge separation) [180]. Sánchez-Portal et al. [181] used SIESTA to explore the electronic structure of more realistic models of this surface. The results showed that for most of the structures *two* metallic bands were obtained instead of the single 6*s* band expected. This could provide an alternative explanation for the experiments. Indeed all the bands with strong 6*s* character are located well below E_F, which can be easily understood since Au is more electronegative than Si. Instead the calculated

bands are mainly derived from Si 3*sp* lobes pointing towards the Au atoms on the surface; thus they are silicon bands. The idea that the observed features are related with band structure effects, and not with spin-charge separation, seems to be confirmed by more recent photoemission studies [182]. Sánchez-Portal and Martin [183] have identified the most favorable structure of the Si(557)-Au surface out of 15 different models. In addition to the Au chain, this structure involves a row of Si adatoms saturating some of the dangling bonds of the structure and is in very good agreement with the model proposed from recent X-ray diffraction data [184].

6.4 Surface-Tip Interactions

In a recent joint experimental and theoretical work, Forster et al. [185] have studied the dynamic scanning force microscope images of the $CaF_2(111)$ surface as a prototype of ionic substrates. The focus was made on the effects of tip and substrate relaxations in the atomic resolution of the images. The simulations were performed for pure silicon tips and ionic tips made of MgO. The results were then compared with the experimental information. For a proper treatment of the electrostatic interactions the calculations with ionic tips require a larger simulation cell and, therefore, a simplified method was used to describe the chemical forces. In the case of the silicon tips a more sophisticated description of the electronic structure is necessary, due to the expected presence of covalent interactions, and the SIESTA code was utilized. According to these authors, this would be the first ab initio simulation of this kind on an ionic substrate. As in previous studies [186] the silicon tip was modeled by a small (ten atoms) cluster with its base saturated by hydrogens, and exhibiting a single dangling bond in the apex. Both in experiments [187] and simulations [186], pure silicon tips have been shown to provide good atomic resolution on some semiconducting surfaces. The contrast in those cases is dominated by the onset of the bonding between the dangling bonds in the tip and the surface. Ionic surfaces, without clear unsaturated bonds, might lead to different results. The interaction between the silicon tip and the CaF_2 substrate is certainly weaker than in the case of a silicon substrate with dangling bonds [186]. The contrast is dominated by the high F^- sublattice (there are two inequivalent F atoms on the surface). The interaction with Ca^{2+} is much weaker and enters repulsion at larger tip heights (0.33 nm) than over F^- sites (about 0.25 nm). The interaction between the higher F^- and the tip is partially covalent, involving charge transfer from F^- into bonding states (~0.18 e for a 0.30 nm separation). The relaxations on both tip and sample are quite modest and do not seem to affect the images for this system. Two different image patterns are experimentally observed depending on the tip-surface distance. Only the long-distance pattern is recovered by the simulations with pure silicon tips. In the simulations

with ionic tips, however, both patterns are obtained as a function of the distance, and the magnitude of the contrast also seems to be in better agreement with the observation. This seems to indicate that the tips are usually highly contaminated, and is consistent with the usual experimental practice of bringing tips into contact with the surface before imaging to improve the resolution.

6.5 Interfaces

6.5.1 SiO_2/Si

As mentioned above, the constant miniaturization of the silicon-based microelectronic devices requires a reduction of the SiO_2 gate to the nanometer scale. This can only be achieved via a detailed microscopic understanding of the structure and the Si oxidation process at the SiO_2/Si interface. Some fundamental aspects of the reaction of the O_2 molecule with this interface have been revealed by recent spin-polarized total energy calculations using SIESTA [188]. The reaction results either in a peroxy linkage with a Si-Si bond in the interface (a Si-O-O-Si type of bond) for the singlet spin state, or in a perfect Si-O-Si bond plus an interstitial O atom for the triplet spin state. The singlet state, i.e., the peroxy linkage, is more stable and presents a smaller energy barrier (a calculated value of ~0.2 eV, to be compared with ~0.8 eV estimated for the triplet). However, the initial state of the reaction, i.e., the O_2 interstitial within SiO_2, is well known to have a triplet configuration, and the authors estimate a rather small probability for triplet to singlet conversion. This is in contrast with the case of the Si(001) surface, where the singlet-to-triplet conversion is a key ingredient to understand the sticking coefficient of oxygen [189]. This spin dependence of the reaction can be the key to explain the high quality of the SiO_2/Si interface, which cannot be understood from a preferential formation of the peroxy linkage.

Another interesting study of this interface has recently been published by Dabrowski et al. [190] based on DFT calculations performed with several codes, SIESTA among them. They addressed the problem of the segregation of the typical donors P and As to the SiO_2/Si(001) interface. The calculations show that the segregation is driven by the tendency of P (or As) to avoid the oxygen bonds. Donor species can then be trapped as threefold coordinated atoms and deactivated at certain defects at the interface, such as replacing a Si which has a dangling bond and is not bonded to oxygen. Donor atoms can also be trapped and deactivated at the defect-free interface by pairing. This P_2 (As_2) complex is unstable in bulk silicon but next to the interface its binding energy can be as large as 0.5 eV in the intrinsic material and even larger in the n-type material. This stabilization takes place because the oxide

can accommodate the stress caused by the deformation of the bonds around the complex and because the removal of a substrate bond (substitution of Si by P) provides a way to release part of the interfacial stress. The pairing mechanism dominates at high dopant concentration ($>10^{19}$ cm^{-3}).

6.5.2 α-Al_2O_3(0001)/Al(111)

SIESTA has been utilized to analyze the characteristics of the bonding at the interface between aluminum and alumina (Al_2O_3) [191]. The authors considered Al and O terminations of the oxide. In all cases the optimal geometry corresponds to an fcc stacking sequence, which places the metal atoms above the O hole sites of the alumina. During the relaxation process the metal atoms closest to the interface are pulled to positions usually occupied by the Al^{3+} cations for the bulk oxide. In other words, the atoms are rearranged in such a way that the oxide is always effectively terminated by an Al bilayer independently of the initial termination. The interfacial Al-O bonds are in all cases very similar to those of bulk alumina, i.e., mainly ionic with a small degree of covalency. In fact, this ionic interaction is the dominant bonding mechanism, determining the charge transfer between the Al and oxide layers. Mulliken populations and bond orders inside the oxide layer are also quite similar to those for bulk. More changes can be appreciated with the Al slab. There is a reduction of the metallic bonding (delocalized charge) in the Al near the interface as a result of its distorted atomic structure and the charge transfer to the oxide. This is compensated for by the formation of more directional, covalent-type bonds.

7 Low Dimensional Metals

Low-dimensional metals have certainly led to one of the more interesting and fruitful chapters in modern solid state science. The interest on these materials dates back to the theoretical work of Peierls [192] and Fröhlich [193] more than 40 years ago. However it was the seminal work by Wilson et al. [194] on transition metal dichalcogenides, as well as the practically simultaneous discovery of the first truly organic molecular metal, TTF-TCNQ (TTF: tetrathiafulvalene, TCNQ: tetracyanoquinodimethane) [195, 196] which launched a great effort on their study. Many of the interesting properties of these materials are related to the special topology of their Fermi surface (FS) [194, 197]. When a piece of the FS can be translated by a vector q and superimposed on another piece of the FS, this FS is said to be nested by the vector q. Metals with a nested FS are susceptible to a modulation with wave vector q of their charge or spin density, which destroys the nested part of the FS.

Metal-to-insulator or metal-to-metal transitions associated with such charge density or spin density waves (CDW or SDW) are frequently observed in low-dimensional metals although often, especially in the case of molecular metals, are in competition with other types of instabilities.

The unraveling of the interesting physics of these materials strongly depends on the availability of calculated band structures and FSs. Tight-binding extended Hückel (eH) type calculations have been remarkably successful in this area and even predictive [197]. However recent experimental studies using photoemission, magnetoresistance, and other techniques have made clear the need for first principles calculations on these materials in order to understand the fine aspects of their electronic structure. Some of these materials have been recently studied using the SIESTA approach.

7.1 Molybdenum and Tungsten Oxides and Bronzes

The discovery of nonlinear transport due to sliding of CDW in the $K_{0.3}MoO_3$ blue bronze [198] was at the origin of the renewed interest in the blue, red, and purple bronzes, Magnèli phases, monophosphate tungsten bronzes, etc. [199, 200]. Recent photoemission studies [201–204] mostly confirmed the already known tight-binding eH FSs [205, 197] of these materials but the agreement was less good for the energy bandwidths which, in general, were found to be larger by a factor of at least 2. In some cases like the blue bronzes there were noticeable disagreements in the relative dispersion of some bands. A recent SIESTA study for $K_{0.3}MoO_3$ [206] has confirmed that the Fermi level cuts two pseudo-one-dimensional bands so that the FS of this material is made of two pairs of slightly warped sheets perpendicular to the highly conducting direction (i.e., the b axis) nested by the $0.75b^*$ wave vector. These results are in agreement with the photoemission and X-ray diffuse scattering studies [204, 207]. The calculated band dispersions for the two partially filled bands are now in excellent agreement with the recently reported ARPES studies (see Fig. 6). A study of the crystal orbitals at some points of the Brillouin zone essentially confirmed the qualitative analysis based on the eH approach [197] and showed that the reason for the disagreement in the eH band dispersions (see Fig. 6) was the underestimation of the Mo d_{xz}-O p_z interactions. These first principles calculations also showed that no empty band which could be thermally populated above 180 K exists, a result which differs from the previous eH calculations [205] and which is significant for understanding the variation of the CDW wave vector with temperature.

An extensive SIESTA study of the electronic structure for all monophosphate tungsten bronzes, $(PO_2)_4(WO_3)_{2m}$, with known crystal structure (i.e., for m=4, 5, 6, 7, 8, 10, and 12) has also been carried out [208]. These materials are electronically more complex since the FS follows the so-called 'hid-

Fig. 6 Comparison of the ARPES (from [201]) and the calculated band structure (previous eH [205] and SIESTA [206]) for the blue bronze $K_{0.3}MoO_3$. Reproduced with permission from [206]

den nesting' scenario [209], i.e., the FS results from the hybridization of three different one-dimensional FS. This study, while confirming the qualitative aspects of the eH calculations, has led to a better agreement with recent ARPES studies [210, 211]. Calculation of precise FS (including interlayer interactions) and the associated Lindhard response function allowed an in-depth discussion of the origin of the structural modulations occurring in these materials. This study suggested that a FS driven instability is at the origin of the structural modulations for the low m members of the family (i.e., m=4, 5, 6, and 7) but not for the higher m members, a result which is in agreement with recent X-ray diffuse scattering studies for these solids [212, 213].

Another series of low-dimensional bronzes which have been the subject of a SIESTA study [214] are the hydrogen molybdenum bronzes, H_xMoO_3 ($0<x<2$). These phases are low-dimensional mixed conductors displaying a wide range of colors and properties [215–217]. Every one of the four stable phases—I ($x\approx0.33$), II ($x\approx1$), III ($x\approx1.66$), and IV ($x\approx2$)—exhibits a different type of superstructure. According to a recent suggestion [218, 219], the doubling of the host cell along the *c*-axis in phase II as well as the $3a\times6c$ superstructure in phase I can be seen as resulting from CDW-type instabilities of their FS. The SIESTA study showed that the topology of the FS is not the main driving force for the adoption of the superstructures but may be at the

origin of some conductivity anomalies of these phases [214]. Conjugate gradient structural optimizations and MD runs were used in a cooperative theoretical-experimental attempt to unravel the nature of the superstructures for phases II, III, and IV [220] as well as to discuss the relationship between the transport properties and structural details such as modifications of the host structure, hydrogen distribution and ordering among the two potential H+ intercalation sites (channels within the layers or van der Waals gaps between the layers).

7.2 Molecular Conductors

Molecular metals came into being with the successful marriage of the molecular donor TTF and the molecular acceptor TCNQ [195, 196]. The remarkable low-temperature behavior of this solid triggered an enormous interest on the physics of molecular conductors which soon led to the discovery of superconductivity in the molecular solid $(TMTSF)_2PF_6$ (TMTSF: tetramethyltetraselenenafulvalene) [221]. Since then molecular conductors have led to an impressive number of exciting discoveries [222]. >From the computational viewpoint their large unit cells and mixed type of bonding face the theoretician with a real challenge. However some of these solids have recently been studied using the SIESTA methodology.

The molecular superconductor β-$(BEDT\text{-}TTF)_2IBr_2$ [223] is a material subject to intense interest because of the much debated question of the origin of the slow magnetoresistance oscillations. Initially they were supposed to originate from small pockets of the FS because their behavior strongly resembles that of the Shubnikov-deHaas effect. The origin of such slow oscillations has remained as one of the more elusive features of the electronic structure of these materials until recently when Kartsovnik et al. [224] have proposed that they originate from the warping of the cylindrical FS. The calculated FS is shown in Fig. 7 [225]. It is a typical quasi-two-dimensional FS with a cylinder-like shape. The calculated transverse cross-section (Fig. 7b) is in excellent agreement with that reconstructed from the magnetoresistance data [226, 227]. The cylinder-like FS is calculated to be warped as depicted in Fig. 7c. In order to clarify the kind of warping, the region of k-space giving negative values of $\delta\epsilon/\delta c^*$ is encoded as bright color and the region of k-space giving positive values is encoded as dark color. It is clear that the striped bands are inclined with respect to the c^*-direction a feature which harmonizes with the results of the magnetoresistance reconstruction of the FS [226, 227]. This study showed without any ambiguity that the FS of β-$(BEDT\text{-}TTF)_2IBr_2$ does not contain any small closed pocket of carriers which could be at the origin of the slow oscillations. It also suggests that the dispersion along the interlayer direction is of the order of 0.8–1.7% of that in the conducting plane. The two facts together provide a firm computation-

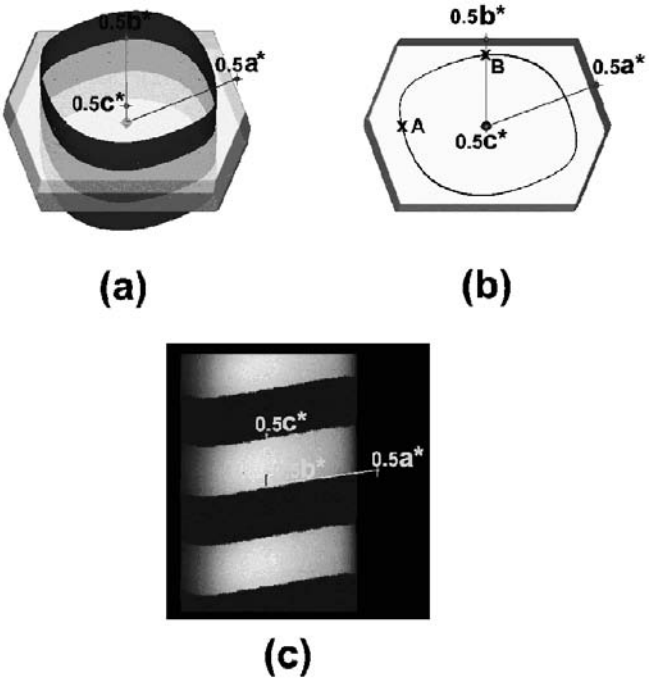

Fig. 7a–c Calculated Fermi surface for β-(BEDT-TTF)$_2$IBr$_2$: **a** three-dimensional FS; **b** FS and Brillouin zone viewed along the c^*-direction; **c** graphical representations of the FS warping (see text). Reproduced with permission from [225]

al basis to the proposal that the slow oscillations in β-(BEDT-TTF)$_2$IBr$_2$ originate from the warping of its cylindrical FS and quite clearly show the usefulness of this kind of computations in characterizing the FS of molecular conductors.

A remarkable experimental achievement in the field of molecular conductors has been the report of the first single-component neutral molecular metal, Ni(tmdt)$_2$ (tmdt: trimethylenetetrathiafulvalenedithiolate, see Fig. 8) [228]. An essential requirement for the induction of metallic behavior in molecular metals is some kind of electron transfer (either direct or electrochemically induced) leading to the partial emptying and/or filling of at least one band. Thus, these solids were thought to be always (at least) two-component systems. Theoretical work challenged this notion suggesting that for some molecular species, like metal bis(dithiolene) systems (see Fig. 8), there is the possibility of an internal electron transfer in the solid state which thus can make unnecessary the presence of the doping species [229–231].

The SIESTA calculated band structure for the Ni(tmdt)$_2$ molecular solid [232] clearly showed that the bands originating from the HOMO and LUMO (see Fig. 8) overlap (0.19 eV) leading to the metallic character. The calculat-

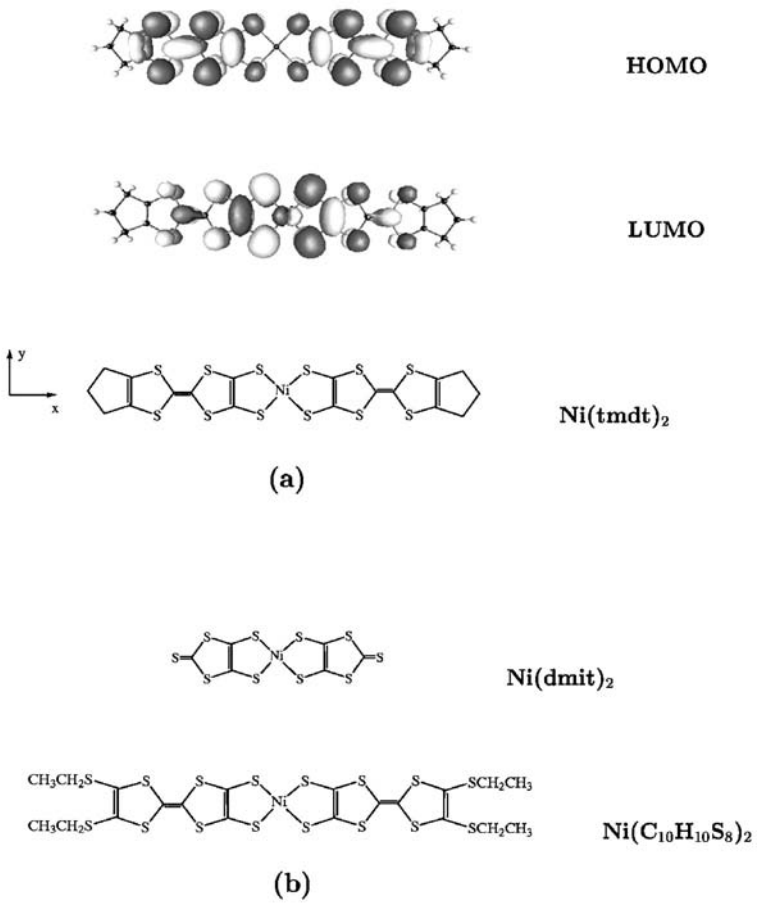

Fig. 8a,b Some relevant metal bis(dithiolene) systems used in the search for molecular conductors. Shown in **a** are isosurface plots of the HOMO and LUMO calculated for Ni[tmdt]$_2$. Reproduced with permission from [232]

ed FS clearly showed that Ni(tmdt)$_2$ must be a three-dimensional metal and that both the electron and hole pockets should lead to angle-dependent oscillations in the magnetoresistance measurements. A remarkable result of the SIESTA computations was that for the very strongly related nickel bis(dithiolene) material Ni($C_{10}H_{10}S_8$)$_2$ (see Fig. 8b) a small energy gap of 0.054 eV was found to separate the HOMO and LUMO related bands thus conferring a semiconducting character to this material. This is in excellent agreement with experimental work suggesting a small energy gap (approximately 0.10 eV as deduced from the conductivity measurements) for this material [233]. The reason for the contrasting conductivity behavior of these two materials seem to be entirely due to the differences in the crystal pack-

ing (i.e., difference in the intermolecular interactions) since the initial HOMO-LUMO gaps are calculated to be practically identical (0.36 vs 0.37 eV). The SIESTA type calculations thus seem to be very well adapted to the study of the metallic vs semiconductor behavior of these molecular solids despite well known deficiencies of DFT in dealing with band gaps for semiconductors. The reason for this success probably lies both in the molecular nature of the solids (which leads to intermolecular interactions much weaker than the intramolecular bonding ones) and to the similar nature of the HOMO and LUMO (which really are based on in-phase and out-of-phase combinations, respectively, of the same type of ligand orbital).

The characterization of the unoccupied and partially occupied states of TTF-TCNQ has recently been the object of a combined X-ray absorption near edge spectroscopy (XANES) and SIESTA study [234]. The use of synchrotron radiation allowed the determination of the partial DOS of S, N, and C because of the element selectivity of X-ray absorption and the determination of the spatial distribution of the molecular orbitals due to the polarization of the synchrotron light. The SIESTA computations were used to calculate the DOS and PDOS into the carbon, nitrogen, and sulfur of TTF, TCNQ, and TTF-TCNQ. As a consequence, an in-depth discussion of the origin of the different features of the unoccupied DOS of the three materials, TTF, TCNQ, and TTF-TCNQ, has been possible leading to the assignment of most of the experimentally obtained features to specific molecular orbitals.

7.3 Other Low Dimensional Systems

It is sometimes difficult to predict the conductivity behavior of a material solely on the basis of the crystal structure either because the unit cell is too complex or because alternative descriptions of the crystal structure suggesting different answers are possible. Sometimes it is not even clear if there is a chance for the material to exhibit low-dimensional transport properties and hence the associated peculiar physics. Band structure calculations can be of major value in these cases and indeed some studies along these lines using the SIESTA methodology have been reported. Thus, it was predicted that the complex molybdenum oxide $TeMo_5O_{16}$ would not be a metal but a semiconductor and the structural origin of the band gap was analyzed [235]. In contrast, it was suggested that the ternary nitride Ca_2GeN_2 could be a new low-dimensional metal and it was shown that the nature of the alkaline-earth atom can have a crucial influence on the conductivity behavior of this type of phases [236]. Although the crystal structure of the ternary nitride Ca_2AuN contains regular zigzag chains of Au atoms with Au-Au distances similar to those in Au metal, the analysis of the electronic structure clearly showed that both the Au and Ca atoms influence the shape of the FS and that the system should be a quasi-two-dimensional metal [237]. Sometimes, especially in the

case of molecular solids, it is difficult to predict if the conductivity will be metallic or activated because of some kind of electronic localization. First principles computational studies can be very valuable in these cases. For instance, SIESTA type calculations [238] have suggested that an AF state should be the ground state for the molecular solid $Mo_3S_7(dmit)_3$ although both the ferromagnetic and metallic states are quite close in energy so that the nature of the ground state can probably be influenced by pressure application or chemical modifications.

8
Nanostructured and Biological Systems

The last decade has witnessed the blooming of nanoscience as one of the most active areas of research. Although interdisciplinary, nanoscience bears an important materials science component, as it relies on our ability to build and characterize materials at the nanometer scale. Simulations have played a major role in this field, given the practical difficulty in the experimental control and characterization of these nanometer sized systems. Similarly, nowadays simulation tools are key in understanding biology at the molecular scale. Although the vast majority of the simulations done in biology are still done at the classical potentials level, quantum-mechanics is of course of paramount importance in may biological processes, and therefore quantum simulations are very much needed in this area. The recent advances in the ability of these techniques to describe larger and more complex systems is making possible the application of quantum simulations in biological systems. SIESTA is especially well suited for simulation in these two areas, as it is able to reach system sizes relevant for nanoscale materials and for biological systems, for which other first principles electronic structure methods are computationally too costly. In this section we will briefly mention work done along these lines.

In the field of nanoscale materials, SIESTA has probably made its largest impact in the study of carbon nanotubes. This is a field which has captivated the attention of researchers for their unusual electronic and mechanical properties. Simulation and theory have played a major role, often providing predictions that have guided the way for experimental studies. Work done with SIESTA has spanned many aspects of nanotube science: vibrational properties [239–241], electronic states [242–246] (including the effect of lattice distortions on the electronic states [247–250]), elastic and plastic properties [251–254], and interaction with other atomic and molecular species [255–259]. Boron nitride nanotubes have also received some attention [260, 261].

Fullerenes have also been the focus of several studies using SIESTA. Carbon fullerenes doped with Ni [262] and Si [263–265] have attracted some at-

tention. Tsolakidis et al. [266] developed a method to compute the optical absorption of clusters based on Time Dependent DFT, and applied it to the calculation of the optical spectrum of C_{60}. The vibrations of C_{60} on silver surfaces was studied experimentally by Pascual and coworkers, and the results were analyzed with the aid of SIESTA simulations [267]. Some aspects of fullerene growth have been studied by Hernández et al. [268]. The polymerization of fullerenes to form complexes [269] or superhard solid phases [270] has also been considered. Finally, as in the case of nanotubes, fullerenes made of boron nitride have also been proposed and studied with SIESTA by Alexandre et al. [271–273].

Besides the fullerenes and the Fe clusters described above, other atomic clusters of small and intermediate sizes have been studied using SIESTA. Examples are Ni-C [274, 275] and Ni-Al [276] clusters, bare and passivated gold nanoclusters [276–282], aluminum oxide clusters [283], and Zn and Cd nanoclusters [284].

Atomic nanowires have also been studied, especially in the case of gold, where much experimental information is available. The case of gold is especially interesting, and in particular the observation of unusually large interatomic distances in the experiments. This has concentrated the effort of several works using SIESTA [285–288]. Au wires supported on Si surfaces have also been studied [181].

One of the most promising developments in nanotechnology is the idea of building electronic devices on the molecular scale, using molecules or nanoaggregates as building blocks of electronic circuits. At this scale, electronic transport is completely dominated by quantum effects, and therefore the previous understanding of microelectronic devices is essentially useless. SIESTA has been instrumental for developing simulation tools for quantum electronic transport which can help us predict and explain the behavior of nanoscale devices for electronic applications. Brandbyge and coworkers [289–297] have developed the simulation package TranSIESTA, which, built on SIESTA, computes the current through a molecule or nanoscale contact connected between two electrodes when a finite voltage is applied on them. The method treats the electrodes as semi-infinite metallic leads, and both them and the molecule or contact are treated within the same atomistic description and detail (in contrast with previous methods in which the electrodes were treated as featureless continuous media). The method is able to obtain both the current and the shape of the voltage drop through the molecule, and provides the atomic forces exerted on the atoms by the passing current. TranSIESTA has been applied so far to predict and explain the transport properties of metallic wires, nanotubes and organic molecules. Other methods to compute transport properties have also been implemented using SIESTA to provide the electronic structure [298–302].

Finally, SIESTA has also made an impact on the study of biomolecules. Artacho et al. [1, 303–306] have contributed to establishing the currently ac-

cepted view that DNA does not behave as a metallic wire, and that, if it does conduct, some mechanism different from band conduction (like small polarons) should be responsible. Different aspects of nitrogenated bases, proteins and peptides [307–312], as well as other organic molecules like calix[4]arene [313], durene [314], and dioxin [315] have also been studied with SIESTA.

9 Conclusions and Outlook

Around seven years ago the SIESTA Project was initiated by a small group of researchers in several Spanish universities with the goal of developing a very efficient method to perform self-consistent electronic structure simulations based on DFT for complex materials. The idea was to create a method that would make possible the accurate computation of the electronic properties of systems containing up to several hundreds of atoms with modest computational capabilities, even with personal computers, that could be available for most researchers around the world. Another key concept in the project was the search of a general approach, i.e., the goal of efficiency should not be gained at the expense of the flexibility and generality of the method. The computational scheme, therefore, should not be restricted to a particular type of material or bonding configuration. It should be applicable to a wide variety of systems, especially to those situations where large scale simulations are needed and most semi-empirical or approximated methods are not reliable enough. Reconstructed and decorated surfaces, interfaces, and nanostructures are some examples of such situations. Of course, the development of a method with such characteristics extended over several years. It was necessary to address and solve many technical and fundamental problems, and new ideas were combined with techniques already used in different contexts. The results of this research were implemented in the SIESTA code, which was made available to the academic and scientific community a few years ago (http://www.uam.es/siesta). Since then, the number of research groups using the code has been steadily increasing and a considerable corpus of work has already appeared where SIESTA has shown its capabilities and potential. During these years the SIESTA development group has also benefited of several fruitful collaborations with researchers who have contributed to the code adding new features or improving its efficiency.

Here we have presented a detailed account of the status of the SIESTA Project and its impact for the materials science community. We have reviewed the applications of SIESTA for the calculation of the properties of many different materials. We have tried to include the most relevant and representative work performed with SIESTA, providing an overview of the applicability and possibilities of the method. However, given the large num-

ber of users and published research, we have probably missed some important papers, and we apologize to the authors of these works. The reviewed material covers a wide range of systems including insulators, semiconductors, and metals, which form bulk ordered and disordered phases, surfaces, interfaces, nanowires, and small atomic aggregates and nanostructures. The properties studied include electronic, magnetic, cohesive, structural, ferroelectric, dynamical, elastic, and vibrational properties. In conclusion, the present review shows that SIESTA is an effective tool for the study of complex materials and as such it is being recognized by the computational materials science community.

As a final note, we would like to mention that the development of SIESTA is certainly an ongoing task, and new capabilities are being implemented or will be in the future. Developments which are already available in a preliminary stage, and which will be included shortly in the public distribution of SIESTA, include accelerated relaxations and dynamics techniques [316, 317], hybrid quantum mechanics-molecular mechanics schemes [309–311], implementations of time dependent DFT [266, 318], electronic transport properties at the nanoscale [289], and the determination of transition states [319]. In the longer term, there are plans to implement methods based on exact and Hartree-Fock exchange (including hybrid XC functionals), GW approaches for the accurate determination of electronic excitations, and the calculations of free energies from molecular dynamics simulations.

Acknowledgements The authors want to thank E. Artacho, J.D. Gale, A. García, J. Junquera, and J.M. Soler, the members in the SIESTA Project, for years of fruitful collaboration. We are also indebted to J.M. Alonso Pruneda, E. Anglada, O. Paz, and M. Machado for their contributions to the project. DSP and PO want to thank Richard M. Martin, José L. Martins, Luís Seijo, Xavier Blase, David A. Drabold, Otto F. Sankey, Pedro M. Echenique, and Volker Heine for ideas, discussions, and support. The SIESTA project is indebted to the ESF Programme Ψ_k for continuous support. This work was partially funded by DGI-Spain (grants BFM2000-1312-C02, BFM2003-03372-C03, and MAT2001-0946), Fundación Ramón Areces, Universidad del Pais Vasco UPV/EHU (Grant 9/UPV 00206.215-13639/2001) and Generalitat de Catalunya (2001 SGR 33). DSP also acknowledges support from the Spanish Ministerio de Ciencia y Tecnología under the program "Ramón y Cajal".

References

1. Artacho E, Machado M, Sánchez-Portal D, Ordejón P, Soler JM (2003) Mol Phys 101:1587
2. Hohenberg P, Kohn W (1964) Phys Rev 136:864
3. Kohn W, Sham LJ (1965) Phys Rev 145:561
4. Kohn W (1998) Rev Mod Phys 71:1253
5. Gross EKU, Ulrich CA, Gossmann UJ (1995) In: Gross EKU, Dreizler RM (eds) Density functional theory. Plenum Press, New York; Gross EKU, Dobson JF, Petersilka M

(1996) In: Nalewajski RF (ed) Topics in current chemistry, vol 181. Springer, Berlin Heidelberg New York
6. Car R, Parrinello M (1985) Phys Rev Lett 55:2471
7. Payne MC, Teter MP, Allan DC, Arias TA, Joannopoulos JD (1992) Rev Mod Phys 64:1045
8. Allen MP, Tildesley DJ (1987) Computer simulations of liquids. Oxford University Press, Oxford
9. Ordejón P (1998) Comput Mater Sci 12:157
10. Goedecker S (1999) Rev Mod Phys 71:1085
11. Goringe CM, Bowler DR, Hernandez E (1997) Rep Prog Phys 60:1447
12. Ordejón P, Artacho E, Soler JM (1996) Phys Rev B 53:10441
13. Sánchez-Portal D, Ordejón P, Artacho E, Soler JM (1997) Int J Quantum Chem 65:453
14. Soler JM, Artacho E, Gale JD, García A, Junquera J, Ordejón P, Sánchez-Portal D (2002) J Phys Condens Matter 14:2745
15. Ordejón P (2000) Phys Stat Solidi B 217:335
16. Perdew JP, Zunger A (1981) Phys Rev B 23:5048
17. Perdew JP, Burke K, Ernzerhof M (1996) Phys Rev Lett 77:3865
18. Hamann DR, Schlüter M, Chiang C (1979) Phys Rev Lett 43:1494
19. Bachelet GB, Hamann DR, Schlüter M (1982) Phys Rev B 26:4199
20. Kleinman L, Bylander DM (1982) Phys Rev Lett 48:1425
21. Sankey O, Niklewski DJ (1989) 40:3979
22. Artacho E, Sánchez-Portal D, Ordejón P, García A, Soler JM (1999) Phys Stat Solidi B 215:809
23. Junquera J, Paz O, Sánchez-Portal D, Artacho E (2001) Phys Rev B 64:235111
24. Anglada E, Soler JM, Junquera J, Artacho E (2002) Phys Rev B 66:205101
25. Sánchez-Royo FJ, Pellicer-Porres J, Segura A, Muñoz-Sanjosé V, Tobías G, Ordejón P, Canadell E, Huttel Y (2002) Phys Rev B 65:115201
26. Pellicer-Porres J, Segura A, Muñoz V, San Miguel A (1999) Phys Rev B 60:3757
27. Manjón FJ, Errandonea D, Segura A, Muñoz V, Tobías G, Ordejón P, Canadell E (2001) Phys Rev B 63:125330
28. Ferlat G, Xu H, Timoshevskii V, Blase X (2002) Phys Rev B 66:085210
29. Segura A, Manjón FJ, Errandonea D, Pellicer-Porres J, Muñoz V, Tobías G, Ordejón P, Canadell E, San Miguel A, Sánchez-Portal D (2003) Phys Stat Sol B 235:267
30. Institute of Physics (1998) Proceedings of the 11th International Conference on Ternary and Multinary Compounds, Salford. Inst Phys Conf Ser No 152, Sect A
31. González J, Power C, Calderón E, Capet F, Muñoz A (2001) Phys Stat Sol B 223:299
32. Luque A, Martí (1997) Phys Rev Lett 78:5014
33. Wahnón P, Tablero C (2002) Phys Rev B 65:165115
34. Tablero C, García AJ, Fernández JJ, Palacios P, Wahnón P (2003) Comput Mater Sci 27:58
35. Tablero C, Wahnón P (2003) Appl Phys Lett 82:151
36. Estreicher SK, Gharaibeh M, Fedders FA, Ordejón P (2001) Phys Rev Lett 86:1247
37. Gharaibeh M, Estreicher SK, Fedders PA (2001) Physica B 308:510
38. Estreicher SK, Fedders PA, Ordejón P (2001) Physica B 308:1
39. Pruneda JM, Junquera J, Ferrer J, Ordejón P, Estreicher SK (2001) Physica B 308:147
40. Pruneda JM, Estreicher SK, Junquera J, Ferrer J, Ordejón P (2002) Phys Rev B 65:075210
41. Baroni S, de Gironcoli S, Dal Corso A, Giannozzi P (2001) Rev Mod Phys 73:515

42. Estreicher SK, McAfee JL, Fedders PA, Pruneda JM, Ordejón P (2001) Physica B 308:202
43. Estreicher SK, Wells K, Fedders PA, Ordejón P (2001) J Phys Condens Matter 13:6271
44. Gharaibeh M, Estreicher SK, Fedders PA, Ordejón P (2001) Phys Rev B 64:235211
45. Estreicher SK (2002) Acta Phys Pol A 102:513
46. Estreicher SK, West D, Ordejón P (2002) Solid State Phenom 82:341
47. Estreicher SK, West D, Goss J, Knack S, Weber J (2003) Phys Rev Lett 90:035504
48. Baierle R, Caldas MJ, Dąbrowski J, Müssig HJ, Zavodinsky V (1999) Physica B 273:260
49. Rurali R, Godignon P, Rebollo J, Ordejón P, Hernández E (2002) Appl Phys Lett 81:2989
50. Rurali R, Hernández E, Godignon P, Rebollo J, Ordejón P (2002) Mater Sci Forum 389:553
51. Rurali R, Godignon P, Rebollo J, Hernández E, Ordejón P (2003) Appl Phys Lett 82:4298
52. Rurali R, Hernández P, Godignon P, Rebollo J, Ordejón P (2003) Comput Mater Sci 27:36
53. Gali A, Deák P, Ordejón P, Don NT, Janzén E, Chokye WJ (2003) Phys Rev B 68:125201
54. Janson MS, Linnarson MK, Hallén A, Svenson BG, Nordell N, Bleichner H (2000) Appl Phys Lett 76:1434
55. Laube M, Schmid F, Pensl G, Wagner G (2002) Mater Sci Forum 389:791
56. Schmidt TM, Miwa RH, Orellana W, Chacham H (2002) Phys Rev B 65:033205
57. Chacham H, Kleinman L (2000) Phys Rev Lett 85:4904
58. Gogotsi TG, Kailer A, Nickel KG (1999) Nature 401:664
59. Reich S, Wirth R, Ordejón P, Maultzsch J, Wunder B, Müller H-J, Lathe C, Schilling F, Dettlaff-Weglikowska U, Roth S, Thomsen C (unpublished)
60. Justicia I, Ordejón P, Canto G, Mozos JL, Fraxedas J, Battiston GA, Gerbasi R, Figueras A (2002) Adv Mater 14:1399
61. Fedders PA, Drabold DA, Ordejón P, Fabricius G, Sánchez-Portal D, Artacho E, Soler JM (1999) Phys Rev B 60:10594
62. Fedders PA (2000) J Non-Cryst Solids 266:218
63. Fedders PA (2000) Phys Rev B 61:15797
64. Fedders PA (2001) Phys Rev B 64:165206
65. Fedders PA (2002) J Non-Cryst Solids 299:201
66. Fedders PA (2002) Phys Rev B 66:195308
67. Zhang X, Drabold DA (1999) Phys Rev Lett 83:5042
68. Drabold DA, Li J (2001) Curr Opin Solid State Mater Sci 5:509
69. Li J, Drabold DA (2001) Phys Rev B 64:104206
70. Demkov AA, Ortega J, Sankey OF, Grumbach M (1995) Phys Rev B 52:1618
71. Drabold DA (private communication)
72. Uchino K (1996) Piezoelectric actuators and ultrasonic motors. Kluver Academic, Boston
73. Scott JF, Paz de Araujo CA (1989) Science 246:1400
74. Lines ME, Glass AM (1977) Principles and applications of ferroelectrics and related materials. Clarendon Press, Oxford
75. Ahn CH, Tybell T, Antognazza L, Char K, Hammond RH, Beasley MR, Fischer Ø, Triscone J-M (1997) Science 276:1100; McKee RA, Walker FJ, Chisholm MF (2001) Science 293:468; McKee RA, Walker FJ, Buongiorno Nardelli M, Shelton WA, Stocks GM (2003) Science 300:1726

76. Bellaiche L, Vanderbilt D (1999) Phys Rev Lett 83:1347; Sághi-Szabó G, Cohen RE, Krakauer H (1999) Phys Rev B 59:12771; Cockayne E, Rabe KM (1998) Phys Rev B 57:R13973
77. Sánchez-Portal D, Souza I, Martin RM (2000) In: Cohen R (ed) Fundamental physics of ferroelectrics 2000. AIP Conf Proc 535:111, AIP, Melville
78. Blöchl PE (1990) Phys Rev B 41:5414
79. King-Smith RD,Vanderbilt D (1993) Phys Rev B 47:1651; Resta R (1994) Rev Mod Phys 66:899
80. Vanderbilt D (2000) J Phys Chem Solids 61:147
81. Dall'Olio S, Dovesi R, Resta R (1997) Phys Rev B 56:10105; Yaschenko E, Fu L, Resca L, Resta R (1998) Phys Rev B 58:1222
82. Ordejón P, Artacho E, Cachau R, Gale JD, García A, Junquera J, Kohanoff J, Machado M, Sánchez-Portal D, Soler JM, Weht R (2001) In: Bulatov V, Cleri F, Colombo L, Lewis L, Mosseau N (eds) Advances in materials theory and modeling-bridging over multiple-length and time scales. MRS Symposia Proceeding 677:AA9.6, Materials Research Society, Warrendale, PA
83. Ghosez P, Cockayne E, Waghmare UV, Rabe KM (1999) Phys Rev B 60:836
84. Fu L, Yaschenko E, Resca L, Resta R (1999) Solid State Commun 112:465
85. Robertson J, Chen CW (1999) Appl Phys Lett 74:1168; Chambers SA, Liang Y, Yu Z, Droopad R, Radmani J (2001) J Vac Sci Technol A 19:934
86. Junquera J, Zimmer M, Ordejón P, Ghosez P (2003) Phys Rev B 67:155327
87. Junquera J, Ghosez P (2003) Nature (London) 422:506
88. Tybell T, Ahn CH, Triscone JM(1999) Appl Phys Lett 75:856
89. Ghosez P, Rabe KM (2000) Appl Phys Lett 76:2767 (2000); Meyer B, Vanderbilt D (2001) Phys Rev B 63:205426
90. Zhang X, Demkov AA (2002) J Vac Sci Tech B 20:1664
91. Padilla J, Vanderbilt D (1998) Surf Sci 418:64; Demkov AA (2001) Phys Status Solidi B 226:56
92. Koval S, Kohanoff J, Migoni RL, Bussman-Holder A (2001) Comput Mater Sci 22:87
93. Koval S, Kohanoff J, Migoni RL, Tosatti E (2002) Phys Rev Lett 89:187602
94. Zintl E (1939) Angew Chem 52:1
95. Kauzlarich S (ed) (1996) Chemistry, structure and bonding of Zintl phases and ions. VCH Publishers, New York
96. Corbett JD (2000) Inorg Chem 39:5178
97. Corbett JD (2000) Angew Chem Int Ed 39:670
98. Nesper R (1990) Prog Sol State Chem 20:1
99. Gascoin F, Sevov S (2001) Inorg Chem 40:5177
100. Rodríguez-Fortea A, Canadell E (2003) Inorg Chem 42:2759
101. Kuromoto TY, Kauzlarich SM, Webb DJ (1992) Chem Mater 4:435
102. Siemens DP, Del Castillo J, Potter W, Webb DJ, Kuromoto TY, Kauzlarich SM (1992) Solid State Commun 84:1029
103. Gallup RF, Fong CY, Kauzlarich SM (1992) Inorg Chem 31:115
104. Sánchez-Portal D, Martin RM, Kauzlarich SM, Pickett WE (2002) Phys Rev B 65:144414
105. Ohno H, Munekata H, Penney T, von Molnar S, Chang LL (1992) Phys Rev Lett 68:2664; Ohno H, Shen A, Matsukura F, Oiwa A, Endo A, Kutsumoto S (1996) Appl Phys Lett 69:363; Ohno H (1998) Science 281:951
106. Dietl T, Ohno H, Matsujura F, Cibert J, Ferrand D (2000) Science 287:1019
107. Sanvito S, Hill NA (2002) J Magn Magn Mater 238:252
108. Sanvito S, Hill NA (2002) J Magn Magn Mater 242/245:441

109. Sanvito S, Hill NA (2001) Appl Phys Lett 78:3493
110. Sanvito S, Ordejón P, Hill NA (2001) Phys Rev B 63:165206
111. Dabrowski J, Scheffler M (1989) Phys Rev B 40:10391
112. Kawakami RK, Johnston-Halperin E, Chen LF, Hanson M, Guebels N, Speck JS, Gossard AC (2000) Appl Phys Lett 77:2379
113. Sanvito S (2003) Phys Rev B 68:054425
114. Sanvito S, Hill NA (2001) Phys Rev Lett 87:267202
115. See, for example: (1995) Phys Today 48(4), special issue devoted to magnetoelectronics
116. Bucher JP, Douglas DC, Bloomfield LA (1991) Phys Rev Lett 66:3052; Billas IML, Chatelain A, de Heer WA (1994) Science 265:1682
117. Izquierdo J, Vega A, Balbas LC, Ordejón P, Sanchez-Portal D, Junquera J, Artacho E, Soler JM (2000) Phys Rev B 61:13639; (2001) In: Barone V, Bencini A, Fantucci P (eds) Recent advances in DFT, Part III. World Scientific, Singapore, p 205
118. In [116] two basis sets were used for the SIESTA calculations. The single-zeta polarized basis contained only one *s*, five *d* orbitals and a polarization shell with three *p* basis orbitals. The double-zeta polarized basis included two different radial shapes for *s* and *d* shells, therefore two *s* and ten *d* orbitals were present along with a simple *p* shell
119. Blügel S, Drittler D, Zeller R, Dederich PH (1989) Appl Phys A Solids Surf 49:547; Stepanyuk VS, Hergert W, Rennert P, Wildberger K, Zeller R, Dederich PH (1996) Phys Rev B 54:14121
120. Indeed this has been recognized for quite some time. For example, Izquierdo et al. point out that Fe dimer is not properly described if the pseudopotential is constructed from the atomic ground state configuration, $3d^6 4s^2$. Instead they use the more appropriate $3d^7 4s^1$. It is also well known that non-linear core corrections [Louie SG, Froyen S, Cohen ML (1982) Phys Rev B 26:1738] are instrumental to recover the right magnetic momentum even in many bulk systems
121. Dieguez O, Alemany MMG, Rey C, Ordejón P, Gallego LJ (2001) Phys Rev B 63:205407
122. Parks EK, Weiller BH, Bechthold PS, Hoffman WF, Nieman GC, Pobo LG, Rilley SJ (1988) J Chem Phys 88:1622
123. Sakurai M, Watanabe K, Sumiyama K, Suzuki K (1999) J Chem Phys 111:235
124. Postnikov AV, Entel P, Soler JM (2002) Mater Res Soc Symp Proc 704:w.8.9.1–6; (2003) Eur Phys J D 25:261
125. Oda T, Pasquarello A, Car R (1998) Phys Rev Lett 233:632; Hobbs D, Kresse G, Hafner J (2000) Phys Rev B 62:11556
126. Rau C, Liu C, Schmalzbauer A, Xing G (1986) Phys Rev Lett 57:2311
127. Ohnishi S, Fu CL, Freeman AJ (1985) J Magn Magn Mater 50:161
128. Bihlmayer G, Asada T, Blugel S (2000) Phys Rev B 62:R11937
129. Bryck T, Bylander DM, Kleinman L (2000) Phys Rev B 61:R3780
130. Robles R, Izquierdo J, Vega A, Balbas LC (2001) Phys Rev B 63:172406
131. Andersen OK, Jepsen O (1984) Phys Rev Lett 53:2571
132. Batyrev IG, Cho JH, Kleinman L (2001) Phys Rev B 63:172420
133. Kresse G, Bergermayer W, Podloucky R (2002) Phys Rev B 66:146401
134. Pruneda JM, Robles R, Bouarab S, Ferrer J, Vega A (2001) Phys Rev B 65:024440
135. Robles R, Pruneda JM, Bouarab S, Ferrer J, Vega A (2001) Surf Sci 482/485:994
136. Bruno P (1995) Phys Rev B 52:411
137. LaBute MX, Kulkarni RV, Endres RG, Cox DL (2002) J Chem Phys 116:3681
138. Adams DM, Noodleman L, Hendrickson DN (1997) Inorg Chem 36:3966

139. Timoshevskii V, Connétable D, Blase X (2002) App Phys Lett 80:1385
140. Connétable D, Timoshevskii V, Artacho E, Blase X (2001) Phys Rev Lett 87:206405
141. Reny E, San-Miguel A, Guyot Y, Masenelli B, Mélinon P, Saviot L, Yamanaka S, Champagnon B, Cros C, Pouchard M, Borowski B, Dianoux JA (2002) Phys Rev B 66:014532
142. Digne M, Sautet P, Raybaud P, Toulhoat H, Artacho E (2002) J Phys Chem B 106:5155
143. Gale JD, Rohl AL, Milman V, Warren MC (2001) J Phys Chem B 105:10236
144. Durà-Vilà V, Gale JD (2001) J Phys Chem B 105:6158
145. Grey T, Gale J, Nicholson D, Artacho E, Soler J (2000) In: Unger KK et al. (eds) Stud Surf Sci Catal 128:89
146. Girard S, Gale JD, Mellot-Draznieks C, Férey G (2001) J Am Chem Soc 124:1040
147. Bosenik A, Dove MT, Myers ER, Palin EJ, Sainz-Díaz CI, Guiton BS, Warren MC, Craig MS, Redfern SAT (2001) Mineral Mag 65:193
148. Borowski M, Marler B, Gies H (2002) Z Kristallogr 217:233
149. Sainz-Díaz CI, Timón V, Botella V, Artacho E, Hernández-Laguna A (2002) Am Mineral 87:958
150. Muscat J, Gale JD (2003) Geochim Cosmochim Acta 67:799
151. Dove MT, Craig MS, Keen DA, Marshall WG, Redfern SAT, Trachenko KO, Tucker MG (2000) Mineral Mag 64:569
152. Fabricius G, Artacho E, Sanchez-Portal D, Ordejón P, Drabold DA, Soler JM (1999) Phys Rev B 60:10594
153. Soler JM, Fabricius G, Artacho E (2001) Surf Sci 482/485:1314
154. Paz O, da Silva AJR, Saenz JJ, Artacho E (2001) Surf Sci 482/485:458
155. Hinarejos JJ, Castro GR, Segovia P, Alvarez J, Michel EG, Miranda R, Rodriguez-Marco A, Sanchez-Portal D, Artacho E, Yndurain F, Yang S, Ordejón P (1997) Phys Rev B 55:16065
156. Junquera JR, Whet R, Ordejón P (2001) Surf Sci 482/485:625
157. Walter S, Bandorf R, Weiss W, Heinz K, Starke U, Strassi M, Bockstedte M, Pankratov O (2003) Phys Rev B 67:085413; Wawro A, Suto S, Czajka R, Kasuya A (2003) Phys Rev B 67:195401
158. Yang WL, Brouet L, Zhou XJ, Choi HJ, Louie SG, Cohen ML, Kellar SA, Bogdanov PV, Lanzara A, Goldoni A, Parmigiani F, Hussain Z, Shen ZX (2002) Science 300:302
159. Henderson MA(2002) Surf Sci Rep 46:1
160. Sanchez CG (2003) Surf Sci 527:1
161. Lozovi AY, Alavi A, Kohanoff J, Lynden-Bell RM (2001) J Chem Phys 115:1661
162. Michaelides A, Ranea VA, de Andres PL, King DA (2003) Phys Rev Lett 90:216102
163. Valette G (1989) J Electroanal Chem 269:601
164. Quiros C, Robach O, Isern H, Ordejón P, Ferrer S (2003) Surf Sci 522:161
165. Held G, Schuler J, Skalarek W, Steinruck HP (1998) Surf Sci 398:154
166. Leiva E (1996) Electrochim Acta 41:2185 (and references therein)
167. Sanchez CG, Leiva EPM, Kohanoff J (2001) Langmuir 17:2219
168. Bockstedte M, Kley A, Neugebauer J, Scheffler M (1997) Comput Phys Commun 107:187
169. McKee RA, Walker FJ, Chisholm MF (1998) Phys Rev Lett 81:3014
170. Wang J, Hallmark J, Marshall DS, Ooms WJ, Ordejón P, Junquera J, Sanchez-Portal D, Artacho E, Soler JM (1999) Phys Rev B 60:4968
171. Cheng CP, Hong IH, Pi TW (1998) Phys Rev B 58:4066
172. Hu X, Sarid D (private communication)
173. Kumpf C, Bunk O, Zeysing JH, Nielsen MM, Nielsen N, Johnson RL, Feidenhans'l R (2000) Surf Sci 488:L213

174. Custance O, Gomez-Rodriguez JM, Baro AM, Jure L, Mallet P, Veuillen JY (2001) Surf Sci 482/485:1399
175. Brochard S, Artacho E, Custance O, Brihuega I, Baro AM, Soler JM, Gomez-Rodriguez JM (2002) Phys Rev B 66:205403
176. Pascual JI, Gomez-Herrero J, Rogero C, Baro AM, Sanchez-Portal D, Artacho E, Ordejón P, Soler JM (2000) Chem Phys Lett 321:78
177. Pascual JI, Gomez-Herrero J, Baro AM, Sanchez-Portal D, Artacho E, Ordejón P, Soler JM (2000) Phys Rev Lett 85:2653
178. Hou JG, Jinlong Y, Haiqian W, Qunxiang L, Changgan Z, Hai L, Wang B, Chen DM, Qingshi Z (1999) Phys Rev Lett 83:3001
179. Sanchez-Portal D, Artacho E, Pascual JI, Gomez-Herrero J, Martin RM, Soler JM (2001) Surf Sci 482/485:39
180. Segovia P, Purdie D, Hengsberger M, Baer Y (1999) Nature (London) 402:504
181. Sanchez-Portal D, Gale JD, Garcia A, Martin RM (2002) Phys Rev B 65:081401
182. Losio R, Altmann KN, Kirakosian A, Lin JL, Petrovykh DY, Himpsel FJ (2001) Phys Rev Lett 86:4632
183. Sanchez-Portal D, Martin RM (2003) Surf Sci 532/535:655
184. Robinson IK, Bennet PA, Himpsel FJ (2002) Phys Rev Lett 88:096104
185. Forster AS, Barth C, Shluger AL, Nieminen RM, Reichling M (2002) Phys Rev B 66:235417
186. Perez R, Stich I, Payne M, Terakura K (1997) Phys Rev Lett 78:678
187. Lantz MA, Hug HJ, Hoffman R, van Schendel PJA, Kappenberger P, Martin S, Baratoff A, Guntherodt HJ (2001) Science 291:2580
188. Orellana W, da Silva AJR, Fazzio A (2003) Phys Rev Lett 90:016103
189. Kato K, Uda T, Terakura K(1998) Phys Rev Lett 80:2000
190. Dabrowski J, Casali RA, Mussig HJ, Baierle R, Caldas MJ, Zavodinsky V (2000) J Vac Sci Technol B 18:2160
191. Siegel DJ, Hector LG Jr, Adams JB (2002) Phys Rev B 65:085415
192. Peierls R (1959) In Quantum theory of solids. Oxford University Press, Oxford, p 108
193. Fröhlich H (1954) Proc R Soc A 223:296
194. Wilson JA, DiSalvo FJ, Mahajan S (1975) Adv Phys 24:117
195. Ferraris J, Cowan DO, Walatka VV, Perlstein JH (1973) J Am Chem Soc 95:948
196. Coleman LB, Cohen MJ, Sandman DJ, Yamagishi FG, Garito AF, Heeger AJ (1973) Solid State Commun 12:1125
197. Canadell E, Whangbo M-H (1991) Chem Rev 91:965
198. Dumas J, Schlenker C, Marcus J, Buder R (1983) Phys Rev Lett 50:757
199. Schlenker C (ed) (1989) Low-dimensional electronic properties of molybdenum bronzes and oxides. Kluwer, Dordrecht
200. Schenker C, Dumas J, Greenblatt M, van Smaalen S (eds) (1996) Physics and chemistry of low-dimensional inorganic conductors. NATO ASI Series B, Physics, vol 354, Plenum, New York
201. Gweon G-H, Allen JW, Claessen R, Clack JA, Poirier DM, Benning PJ, Olson CG, Ellis WP, Zhang YX, Schneemeyer LF, Marcus J, Schlenker C (1996) J Phys Condens Matter 8:9923
202. Grioni M, Voit J (2000) In: Stanberg H, Hughes HP (eds) Electron spectroscopies applied to low dimensional materials. Kluwer, Dordrecht, p 209
203. Smith KE, Breuer K, Greenblatt M, McCarroll W (1993) Phys Rev Lett 70:3772
204. Gweon GH, Denlinger JD, Allen JW, Claessen R, Olson CG, Höchst H, Marcus J, Schlenker C, Schneemeyer LF (2001) J Electron Spectrosc Relat Phenom 117/118:481
205. Whangbo M-H, Schneemeyer LF (1986) Inorg Chem 25:2424

206. Mozos J-L, Ordejón P, Canadell E (2002) Phys Rev B 65:233105
207. Pouget J-P, Kagoshima S, Schlenker C, Marcus J (1983) J Phys Lett 44:L113
208. Lee YJ, Nieminen RM, Ordejón P, Canadell E (unpublished)
209. Whangbo M-H, Canadell E, Foury P, Pouget J-P (1991) Science 252:96
210. Mascaraque A, Roca L, Avila J, Drouard S, Guyot H, Asensio MC (2002) Phys Rev B 66:115104
211. Roca L, Mascaraque A, Avila J, Drouard S, Guyot H, Asensio MC (2004) Phys Rev B 69:075114
212. Roussel P, Labbé P, Leligny H, Groult D, Foury-Leylekian P, Pouget JP (2000) Phys Rev B 62:176
213. Roussel P, Perez O, Labbé Ph (2001) Act Cryst B 57:603
214. Scherlis DA, Lee YJ, Rovira C, Adams S, Nieminen RM, Ordejón P, Canadell E (2004) Solid State Ionics 168:291
215. Birtill JJ, Dickens PG (1978) Mater Res Bull 13:311
216. Eda K, Sukejima A, Matsuura N, Sotani N (1998) Chem Lett 819
217. Schöllhorn R (1986) In: Setton R (ed) Chemical reactions in organic and inorganic constrained systems. Reidel, Dordrecht, p 323
218. Adams S, Ehses K-H, Spilker J (1993) Acta Crystallogr B 49:958
219. Adams S (2000) J Solid State Chem 149:75
220. Lee YJ, Braïda B, Adams ST, Nieminen RM, Ordejón P, Canadell E (unpublished)
221. Jerome D, Mazaud A, Ribault M, Bechgaard K (1980) J Phys Lett (France) 41:L–95
222. Ishiguro T, Yamaji K, Saito G (eds) (1996) Organic superconductors, 2nd edn. Springer, Berlin Heidelberg New York
223. Williams JM, Wang HH, Beno MA, Emge TJ, Sowa LM, Coppens PT, Behroozi F, Hall LN, Carlson KD, Crabtree GW (1984) Inorg Chem 23:3839
224. Kartsovnik MV, Grigoriev PD, Biberacher W, Kushch ND, Wyder P (2002) Phys Rev Lett 89:126802
225. Lee YJ, Nieminen RM, Ordejón P, Canadell E (2003) Phys Rev B 67:180505(R)
226. Kartsovnik MV, Laukhin VN, Pesotskii SI, Schegolev IF, Yakovenko VM (1991) J Phys I France 2:89
227. Wosnitza J, Goll G, Beckmann D, Wanka S, Schweitzer D, Strunz W (1996) J Phys I France 6:1597
228. Tanaka H, Okano Y, Kobayashi H, Suzuki W, Kobayashi A (2001) Science 291:285
229. Canadell E, Rachidi IE-I, Ravy S, Pouget J-P, Brossard L, Legros J-P (1989) J Phys (France) 50:2967
230. Canadell E, Ravy S, Pouget J-P, Brossard L (1990) Solid State Commun 75:633
231. Canadell E (1997) New J Chem 21:1147
232. Rovira C, Novoa JJ, Mozos J-L, Ordejón P, Canadell E (2002) Phys Rev B 65:081104(R)
233. Le Narvor N, Robertson N, Weyland T, Kilburn JD, Underhill AE, Webster N, Svenstrup N, Becher J (1996) Chem Commun 1363
234. Fraxedas J, Lee YJ, Jiménez I, Gago R, Nieminen RM, Ordejón P, Canadell E (2003) Phys Rev B 68:195115
235. Oliva JM, Ordejón P, Canadell E (2000) Phys Rev B 62:16430
236. Oliva JM, Canadell E (2002) Inorg Chem 41:4630
237. Oliva JM, Llunell M, Alemany P, Canadell E (2003) J Sol State Chem 176:375
238. Llusar R, Uriel S, Vicent C, Coronado E, Gómez-García C, Braïda B, Canadell E (unpublished)
239. Sánchez-Portal D, Artacho E, Soler JM, Rubio A, Ordejón P (1999) Phys Rev B 59:12678

240. Reich S, Thomsen C, Ordejón P (2001) Phys Rev B 64:195416
241. Thomsen C, Reich S, Ordejón P (2002) Phys Rev B 65:073403
242. Rubio A, Sánchez-Portal D, Artacho E, Ordejón P, Soler JM (1999) Phys Rev Lett 82:3520
243. Reich S, Maultzsch J, Thomsen C, Ordejón P (2002) Phys Rev B 66:035412
244. Verissimo-Alves M, Capaz RB, Koiller B, Artacho E, Chacham H (2002) Braz J Phys 32:427
245. Reich S, Thomsen C, Ordejón P (2002) Phys Rev B 65:155411
246. Machón M, Reich S, Thomsen C, Sánchez-Portal D, Ordejón P (2002) Phys Rev B 66:155410
247. Mazzoni M, Chacham H (2000) Appl Phys Lett 76:1561
248. Mazzoni M, Chacham H (2000) Phys Rev B 61:7312
249. Verissimo-Alves M, Capaz R, Koiler B, Arctacho E, Chacham H (2001) Phys Rev Lett 86:3372
250. Yoon Y-G, Mazzoni M, Choi HJ, Ihm J, Louie SG (2001) Phys Rev Lett 86:688
251. Jensen P, Gale J, Blase X (2002) Phys Rev B 66:193403
252. Reich S, Thomsen C, Ordejón P (2002) Phys Rev B 65:153407
253. Fagan SB, da Silva LB, Mota R (2993) Nanoletters 3:289
254. Reich S, Thomsen C, Ordejón P (2003) Phys Stat Sol B 235:354
255. Mazzoni M, Chacham H, Ordejón P, Sánchez-Portal D, Soler JM, Artacho E (1999) Phys Rev B 60:2208
256. Baierle RJ, Fagan SB, Mota R, da Silva AJR, Fazzio A (2001) Phys Rev B 64:085413
257. Fagan SB, Mota R, da Silva AJR, Fazzio A (2003) Phys Rev B 67:205414
258. Fagan SB, da Silva AJR, Mota R, Baierle RJ, Fazzio A (2003) Phys Rev B 67:033405
259. McIntosh GC, Tománek D, Park YW (2003) Phys Rev B 67:125419
260. Avezedo S, Mazzoni M, Chacham H, Nunes RW (2003) Appl Phys Lett 82:2323
261. Schmidt TM, Baierle RJ, Piquini P, Fazzio A (2003)) Phys Rev B 67:113407
262. Alemany MMG, Diéguez O, Rey C, Gallego LJ (2001) J Chem Phys 114:9371
263. Fu C, Weissmann M, Machado M, Ordejón P (2001) Phys Rev B 63:085411
264. Tournus F, Masenelli B, Mélinon P, Blase X, Perez A, Pellarin M, Broyer M, Flank AM, Lagarde P (2002) Phys Rev B 65:165417
265. Masenelli B, Tournus F, Mélinon P, Pérez A, Blase X (2002) J Chem Phys 117:10627
266. Tsolakidis A, Sánchez-Portal D, Martin RM (2002) Phys Rev B 66:235416
267. Pascual JI, Gómez-Herrero J, Sánchez-Portal D, Rust H-P (2002) J Chem Phys 117:9531
268. Hernández E, Ordejón P, Terrones H (2001) Phys Rev B 63:193403
269. Pellarin M, Cottancin E, Lermé J, Vialle JL, Broyer M, Tournus F, Masenelli B, Mélinon P (2002) J Chem Phys 117:3088
270. Burgos E, Halac E, Weht R, Bonadeo H, Artacho E, Ordejón P (2000) 85:2328
271. Alexandre SS, Chacham H, Nunes RW (2001) Phys Rev B 63:045402
272. Alexandre SS, Mazzoni M, Chacham H (1999) Appl Phys Lett 75:61
273. Alexandre SS, Nunes RW, Chacham H (2002) Phys Rev B 66:085406
274. Rey C, Alemany MMG, Diéguez O, Gallego LJ (2000) Phys Rev B 62:12640
275. Froudakis GE, Mühlhauser M, Andreotis AN, Menon M (2001) Phys Rev B 64:241401
276. Calleja M, Rey C, Alemany MMG, Gallego LJ, Ordejón P, Sánchez-Portal D, Artacho E, Soler JM (1999) Phys Rev B 60:2020
277. Garzón IL, Michaelian K, Beltrán MR, Posada-Amarillas A, Ordejón P, Artacho E, Sánchez-Portal D, Soler JM (1998) Phys Rev Lett 81:1600
278. Garzón IL, Michaelian K, Beltrán MR, Posada-Amarillas A, Ordejón P, Artacho E, Sánchez-Portal D, Soler JM (1999) Eur Phys J D 9:211

279. Garzón L, Rovira C, Michaelian K, Beltrán MR, Ordejón P, Junquera J, Sánchez-Portal D, Artacho E, Soler JM (2000) Phys Rev Lett 85.5250
280. Soler JM, Beltrán MR, Michaelian K, Garzón IL, Ordejón P, Sánchez-Portal D, Artacho E (2000) Phys Rev B 61:5771
281. Soler JM, Garzón IL, Joannopoulos JD (2001) Sol Stat Commun 117:621
282. Garzón IL, Reyes-Nava JA, Rodríguez-Hernáncez JI, Sigal I, Beltrán MR, Michaelian K (2002) Phys Rev B 66:073403
283. Fernández EM, Balbás LC, Borstel G, Soler JM (2003) Thin Solid Films 428:206
284. Michaelian K, Beltrán MR, Garzón IL (2002) Phys Rev B 65:041403
285. Torres JA, Tosatti E, Dal Corso A, Ercolessi F, Kohanoff JJ, Di Tolla FD, Soler JM (1999) Surf Sci 426:441
286. Sánchez-Portal D, Artacho E, Junquera J, García A, Soler JM (2001) Surf Sci 482:1261
287. Sánchez-Portal D, Artacho E, Junquera J, Ordejón P, García A, Soler JM (1999) Phys Rev Lett 83:3884
288. Novaes F, sa Silva AJR, sa Silva EZ, Fazzio A (2003) Phys Rev Lett 90:03611
289. Brandbyge M, Mozos JL, Ordejón P, Taylor J, Stokbro K (2002) Phys Rev B 65:165401
290. Brandbyge M, Stokbro K, Taylor J, Mozos J-L, Ordejón P (2003) Phys Rev B 67:193104
291. Mozos JL, Ordejón P, Brandbyge M, Taylor J, Stokbro K (2002) Nanotechnology 13:346
292. Nielsen SK, Brandbyge M, Hansen K, Stokbro K, van Ruitenbeek JM, Besenbacher F (2002) Phys Rev Lett 89:066804
293. Stokbro K, Taylor J, Brandbyge M, Mozos JL, Ordejón P (2003) Comput Mater Sci 27:151
294. Stokbro K, Taylor J, Brandbyge M (2003) J Am Chem Soc 125:3674
295. Taylor J, Brandbyge M, Stokbro K (2002) Phys Rev Lett 89:138301
296. Mozos JL, Ordejón P, Brandbyge M, Taylor J, Stokbro K (2003) Adv Quantum Chem 42:299
297. Taylor J, Brandbyge M, Stokbro K (2003) Phys Rev B 68:121101
298. Zhang X, Fonseca L, Demkov A (2002) Phys Stat Sol B 233:70
299. Tomfohr JK, Sankey OF (2002) Phys Rev B 65:245105
300. Tomfohr JK, Sankey OF (2002) Phys Stat Sol B 233:59
301. Cui XD, Primak A, Zarate X, Tomfohr J, Sankey OF, Moore AL, Moore TA, Gust D, Nagahara LA, Lindsay SM (2002) J Phys Chem B 106:8609
302. Alavi S, Larade B, Taylor J, Guo H, Seideman T (2002) Chem Phys 281:293
303. de Pablo PJ, Moreno-Herrero F, Colchero J, Gómez-Herrero J, Herrero P, Baró AM, Ordejón P, Soler JM, Artacho E (2000) Phys Rev Lett 85:4992
304. Alexandre SS, Artacho E, Soler JM, Chacham H (2003) Phys Rev Lett 91:10805
305. Garzón IL, Artacho E, Beltrán MR, García A, Junquera J, Michaelian K, Ordejón P, Rovira C, Sánchez-Portal D, Soler JM (2001) Nanotechnology 12:126
306. Vega J, Michaelian K, Garzón IL, Beltrán MR, Hernández L (1999) J Mol Struc 493:275
307. Alexandre SS, Artacho E, Soler JM, Chacham H (2003) Phys Rev Lett 91:108105
308. Fernández-Serra MV, Junquera J, Jelsch C, Lecomte C, Artacho E (2000) Solid State Commun 116:395
309. Scherlis DA, Martí MA, Ordejón P, Estrin DA (2002) Int J Quantum Chem 90:1505
310. Martí MA, Scherlis DA, Doctorovich FA, Ordejón P, Estrin DA (2003) J Biol Inorg Chem 8:595
311. Crespo A, Scherlis DA, Martí MA, Ordejon P, Roitberg AE, Estrin DA (2003) J Phys Chem B 107:13728

312. Guillot R, Muzet N, Dahaoui S, Lecomte C, Jelsch C (2001) Acta Cryst B 57:567
313. Ogden MI, Rohl AL, Gale JD (2001) Chem Commun 2001:1626
314. Plazanet M, Johnson MR, Gale JD, Yildrim T, Kearley GJ, Fernández-Díaz MT, Sánchez-Portal D, Artacho E, Soler JM, Ordejón P, García A, Trommsdorff HP (2000) Chem Phys 261:189
315. Farajian AA, Mikami M, Ordejón P, Tanabe K (2001) J Chem Phys 115:6401
316. Fernández-Serra MV, Artacho E, Soler JM (2003) Phys Rev B 67:100101
317. Anglada E, Junquera J, Soler JM (2003) Phys Rev E 68:055701
318. Blase X, Ordejón P (2004) Phys Rev B64:085111
319. El-Mellouhi F, Mousseau N, Ordejón P, Phys Rev B (in press); cond-mat/0308289

Structure and Bonding (2004) 113:171–232
DOI 10.1007/b97944
© Springer-Verlag Berlin Heidelberg 2004

The Performance of Hybrid Density Functionals in Solid State Chemistry

Furio Corà[1] (✉) · Maria Alfredsson[1] · Giuseppe Mallia[1] · Derek S. Middlemiss[2] · William C. Mackrodt[2] · Roberto Dovesi[3] · Roberto Orlando[3]

[1] Davy-Faraday Research Laboratory, The Royal Institution of Great Britain, 21 Albemarle Street, London, W1S 4BS, UK
furio@ri.ac.uk
[2] School of Chemistry, University of St. Andrews, St. Andrews, Fife, KY16 9ST, UK
[3] Dipartimento di Chimica IFM, Università di Torino, Via Giuria 5, 10125 Torino, Italy

1 Introduction . . . 172

2 Review of B3LYP Applications in the Solid-State . . . 175

3 The Use of Model Hamiltonians and Mapping of the Ab-Initio Results . . . 183
3.1 The Tight-Binding Model of Metal-Anion Interactions in Perovskites. . . . 184
3.2 The Ising Model of Magnetic Systems . . . 190
3.2.1 Temperature-Induced Magnetic Disorder . . . 192
3.3 The Kanamori Crystal Field Hamiltonian . . . 192

4 Results and Properties—Defect Free Systems. . . . 194
4.1 Computational Details and Notation . . . 194
4.2 Ferroelectric Perovskites and Polarisation Properties. . . . 196
4.2.1 Cubic Phase. . . . 196
4.2.1.1 Structural Properties. . . . 196
4.2.1.2 Electronic Properties. . . . 198
4.2.2 Pseudocubic Phase . . . 203
4.2.3 Tetragonal Phase . . . 207
4.3 Spin-Spin Interactions in Magnetic Compounds . . . 210
4.3.1 Perovskite-Structured $KMnF_3$ . . . 210
4.3.2 Rocksalt-Structured Oxides: MnO and NiO . . . 214
4.3.2.1 Electronic Structure . . . 215
4.3.2.2 Lattice Constant and Bulk Modulus . . . 220
4.3.2.3 Magnetic Effects . . . 220
4.3.2.4 d→d Excitations . . . 223
4.4 Defective Systems—Trapped Electron Hole in MgO . . . 224

5 Conclusions . . . 227

References . . . 229

Abstract We examine the performance of hybrid (HF-DFT) exchange functionals within Density Functional Theory (DFT) in describing the properties of crystalline solids. Recent applications are reviewed, and an extensive set of new results presented on transition metal compounds.

The features of the electronic density and of several calculated properties are examined as the weight of the HF (exact) exchange in the hybrid functional is increased. Clear trends emerge in the structural and electronic properties; in particular, HF exchange increases the electronic localisation. This features causes an increase in the ionicity of the materials, a systematic decrease of the lattice parameter and increase of the elastic constants and bulk moduli. When HF and standard (LDA or GGA) DFT solutions yield systematically errors with opposite sign with respect to experiment, the formulation of hybrid functionals improves the accuracy of the calculations. This is the case for band gaps, phonon spectra, magnetic coupling constants, and all properties that depend on the extent of electronic localisation at either perfect or defective lattice sites. A different weight of HF exchange is required to reproduce the experimental value of different observables; as a general rule, however, a higher fraction of HF exchange than the 20% optimised in the molecular B3LYP formulation is required in the solid state.

Keywords DFT · Hybrid functionals · Crystalline solids · Transition metal oxides · B3LYP

1 Introduction

Computer modelling can now be considered as an almost indispensable tool in solid-state and materials sciences, where it effectively complements experimental probes of matter by providing atomic-level insight in ever more complex materials and processes [1]. The increased industrial demand for 'designer solids', i.e. new materials whose electronic and structural properties are suited for specific applications, requires the availability of general and reliable ab-initio electronic structure methods that do not depend on system-specific parameters. Such techniques have seen an extraordinary development over the last decades, and are now a key component of research in solid-state chemistry, condensed matter physics and materials science, where they are increasingly employed not only to interpret existing experimental data, but also to direct new experimental efforts. With this perspective in mind, addressing the accuracy achievable with available techniques is a topic of fundamental importance. In this chapter we examine the performance of hybrid exchange functionals within density functional theory in representing the structural and electronic properties of crystalline compounds, described under periodic boundary conditions.

Historically, the field of electronic structure calculations has seen two largely independent lines of development: on the one hand molecular quantum chemists have based most work on wavefunction techniques (the Hartree Fock [2, 3] and post-HF theories [4]); on the other, condensed-matter physicists had their reference method in Density Functional Theory (DFT) [5–7]. This formal division between molecular and solid-state communities has been due to the poor transferability of the standard computational methods between the two fields: early DFT functionals underperform post-HF techniques in reproducing the known properties of small molecules

(see, e.g., the comprehensive test by Cohen and Handy [8]), while the extension of accurate post-HF methods to solid-state systems is difficult or has prohibitive computational expense. In fact, the development of wavefunction methods applicable to the study of crystalline solids is still in its scientific childhood [9].

After two decades of continuous theoretical developments and improvements, however, working formulations of the exchange and correlation functionals at the basis of DFT have been proposed that, while retaining a tractable computational cost, have adequate accuracy for most needs in both molecular and solid-state sciences. The formulation of hybrid HF/DFT functionals has been crucial in achieving this goal. Let us put this development into the context of the DFT evolution, in which we notice three key steps:

1. The first working formulation of the exchange and correlation (xc) density functional is the LDA (Local Density Approximation) [10, 11], which makes reference to the uniform electron gas (*jellium*). Despite its simplicity, the LDA provides surprisingly good results for metallic solids with delocalised electrons, i.e. those that most closely resemble the jellium model. It has, however, revealed systematic shortcomings in the description of materials with localised electrons (be these molecules or insulating solids), which lead to the underestimation of bond distances and overestimation of binding energies [12]. These shortcomings have been associated with two crucial features of the LDA: first, the local formulation of the energy expression does not account for the electronic redistribution in bonds, and hence excludes chemistry from the functional expression; and second, the non-exact cancellation of the self-energy part (self-interaction) of the Hartree term in the LDA exchange functional, which is particularly important for well localised electrons.
2. The next generation of functionals aimed at correcting the first feature, by including the so-called generalised gradient (GGA) terms in the functional formulation (following the accepted procedure, here and in the following we shall refer to the functionals by the initials of the proposing authors: B-LYP [13, 14]; HCTH [15]; PW [16, 17]; PBE [18]). The dependence of the functional on the gradient of the electronic density is performed via analytic functions, whose parameters are either fitted to experiment [13–15] or determined by some exact sum-rules [16–18]. The increased flexibility of the GGA, compared to the LDA functionals, has helped improving their performance, but does not address the self-interaction problem.
   Similar arguments apply also to the latest generation of functionals, defined as meta-GGA [19, 20], that in addition to the gradient terms also include an explicit dependence on the kinetic energy density and/or on the second derivatives of the electron density.
3. Only when an explicit orbital dependence is included in the DFT formulation can the electron self-interaction be corrected. Several directions have been followed to this aim, of which the most common are referred to as

SIC, or self-interaction corrected LDA [21, 22], and more recently the exact exchange (EXX) functionals [23], both of which include a dependence of the exchange functional on the occupied molecular or crystalline orbitals.

An alternative approach to remove the improper self-interaction term consists in making use of the HF theory, in which the self-interaction cancellation between Coulomb and exchange contributions is exact. Mixing HF and DFT formulations of the exchange forces, therefore, provides an alternative method to introduce some extent of electronic self-interaction correction and orbital dependence. One appealing feature of this choice is that it can exploit readily the progress and tools available to the quantum chemists for calculating the HF exchange.

In the class of orbital-dependent functionals, the LDA+U method [24] also deserves special mention for its importance in solid-state calculations on open-shell transition metal compounds. The LDA+U Hamiltonian contains an on-site term U, whose features reproduce in a parametric form the orbital-dependence of the HF theory.

In this chapter we are mostly concerned with the *hybrid* (HF-DFT) exchange functionals, and we shall therefore focus most of the discussion on this class of DFT functionals. The original proposition of a hybrid exchange functional is due to Becke [25, 26], who made use of the adiabatic connection formula to show how to continuously transform the HF into the DFT formulation of the exchange functional. In general terms, hybrid functionals contain one or more parameters; these include at least the fraction of HF and DFT exchange to be used, and eventually which exchange functional within DFT, whose value can be postulated (Becke's half-and-half hybrid [25]), fitted to experimental data (the original B3PW [26] or the B1LYP formulation proposed by Adamo and Barone [27]), or derived from first principles, as shown by Perdew et al. using a perturbation expansion [28].

Inclusion of the HF exchange, combined with the optimisation of the parameters included in the hybrid functionals, yielded a noticeable improvement of DFT results; it has in this way been crucial in achieving a working formulation of DFT that is accurate enough to satisfy the quantum chemistry needs for many applications. Combined with its relatively low computational cost, this development has transformed DFT into the method of choice for the ab-initio calculation of materials properties, especially for large systems of practical interest. Several critical cases remain, however, where standard one-electron Hamiltonians fail to reach sufficient accuracy to interpret and/or direct experiments. Below we shall consider some representative examples in the solid state.

2
Review of B3LYP Applications in the Solid-State

Application of the newly proposed hybrid functionals to molecular systems has been almost immediate. A crucial importance has been played by the software availability: as soon as proposed by Becke, the first hybrid functional has been coded into GAUSSIAN94 [29] (although using the LYP correlation functional instead of the PW employed by Becke), making it available to the molecular quantum chemistry community. As often happens, the solid-state community has been much slower in taking up this development, and the application of hybrid functionals to crystalline compounds (described under periodic boundary conditions (PBC)) has not been possible until the late 1990s, when they have been coded in CRYSTAL98 [30]. Five years on, several solid-state studies have been performed with hybrid functionals, providing a valuable experience on their accuracy and applicability. In this section we summarise the results of early publications in which hybrid exchange functionals have been applied under PBC to represent crystalline solids.

The properties of crystalline compounds are quite often different from those of molecular species, and the question concerning the transferability of molecular functionals to solids is therefore non-trivial. The difference is particularly evident for ionic and semi-ionic solids, in which the long-range electrostatic forces provide a strong localising field for the electronic states, that is not present in molecules. This is the type of situation in which the shortcomings of standard LDA and GGA functionals, linked to the missing electronic self-interaction, are likely to be most severe. In fact, ionic compounds of open-shell transition metal cations, such as the Mott insulators, are often referred to as *highly correlated* materials, to indicate the strong electron-electron coupling in these compounds. Complex transition metal oxides are the key components in several modern technologies: from the synthetic chemistry industry, in which oxides represent the active phase and/or support of heterogeneous catalysts [31], to electronics, where the response properties of oxides to external fields are employed to design sensors and actuators [32, 33], and where oxides are at the basis of rechargeable batteries [34], electrochromic devices [35, 36] and high-Tc superconductors, just to name a few industrially relevant applications. Understanding the performance of the different Hamiltonians available to solid-state scientists for describing these systems is therefore a topic with considerable practical, and not only academic, interest.

Before starting our discussion, two fundamental differences should be highlighted between molecular and solid systems:

1. In molecular chemistry, very accurate thermochemical and structural data exist for a selection of simple species. These data have been effectively used

in past years to define representative sets (see, e.g. Pople's G2 set [37] and Handy's set of 147 species [8]) against which to measure the results of calculations. The availability of these representative sets has enabled the *empirical* derivation of DFT functionals, which represent the current state of the art in DFT performance [8]. In contrast, the field of solid-state science has no such set available. Solids are quite often ill-defined, and contain intrinsic defects and impurities that modify their measured properties. This feature limits the direct comparison of model calculations with experimental data to few crystals that can be synthesized in (almost) defect-free form. Even in this case, the accuracy with which different experimental observables are known varies; often the most reliable experimental results on crystalline solids are not directly related to the equilibrium structure, energy and electronic density (as for molecules), but to the response of the solid to a perturbation, for instance to elastic distortions or to external electromagnetic fields. As an additional complexity, some fundamental electronic properties of solids cannot be measured directly; band gaps, for instance, can be readily calculated as edge to edge differences between specific filled and unfilled bands, but they cannot be measured directly. What experiments furnish are absorption edges and activation energies corresponding to processes that are often speculative. As another example, magnetic coupling constants can be neither measured directly nor calculated directly. Their extraction from calculations requires a mapping onto a phenomenological model of some sort, which by its very nature is inexact, while comparisons are made with indirect quantities such as disorder transition temperatures, which in turn have to be expressed in terms of the phenomenological model. Comparison to experiment in the solid state, therefore, is often indirect; the structural complexity and the cost of these calculations exceed by several orders of magnitude those of the simple molecules in the molecular sets. Even having a representative solid state set available, generating a useful ensemble of calculated properties would be beyond the reach of a systematic investigation of the type of reference [8].

2. The second difference between molecular and solid-state fields is the lack, in the latter, of a reference theoretical method. Post-HF techniques in molecular quantum chemistry can yield results with a controlled degree of accuracy. In the absence of experimental data, the results obtained with different DFT functionals could be compared against those calculated with the reference computational technique. Recent developments in wavefunction methods [9], GW techniques [38], and quantum Monte Carlo (QMC) [39] for solid-state systems aim at filling this gap, and are promising for future work, but at present they still suffer from a limited applicability.

The two differences mentioned above make a systematic quantitative testing approach for solids extremely difficult. Instead, we shall collect the published data, and present an extensive set of new results, with the aim of ex-

tracting in a qualitative way the main features of hybrid functionals in solids, as a practical guide for their efficient application.

Several papers have appeared in press in the past three years using the B3LYP functional under PBC, as embodied in CRYSTAL98 [30]. The systems studied include several compounds of main group elements [40–57], compounds containing transition metal ions in formal electronic configuration $d^{(0)}$ [58, 59], and compounds with one or more open shell transition metal ions in electronic configuration $d^{(n)}$ ($n \neq 0$) [60–64].

Studies of main group elements are the most numerous; they include the series of alkali earth oxides and hydroxides MO and $M(OH)_2$ (M=Mg, Ba, Sr) [46, 47]; α-Al_2O_3[48]; aluminophosphates[49]; ZnO [50–52]; PbS [53, 54]; H-containing defects in zeolites [55–57]; and representative H-bonded systems [45]. Both bulk [40–42] and surface [48, 50–52] materials have been investigated, including surface adsorption processes [43, 44].

In most papers referenced above, the standard molecular formulation of the B3LYP functional has been employed, and its results graded against a set of other Hamiltonians available in CRYSTAL. These usually include at least HF, LDA and one GGA functional (PW or PBE), and thus enable a critical appraisal of the B3LYP performance compared to other well established Hamiltonians in solid-state chemistry. Several observables have been examined, such as the equilibrium structure, elastic constants and bulk moduli, thermochemical data, electric field gradients, phonon spectra and vibrational frequencies, polarisation of the ferroelectric phases, magnetic coupling in open-shell transition metal oxides. We shall comment on each observable separately.

1. *Structural parameters and elastic constants*: let us start with the oxides, hydroxides [46, 47] and halides [41] of main group elements. Results are very encouraging, at least for this class of chemically well behaved systems. Despite the calculated net charges showing a clear trend, with HF being the highest (most ionic), LDA the lowest (least ionic), and B3LYP and GGA yielding intermediate values, all the systems can be well described as ionic. The main features of the electronic density and the description of bonding being qualitatively the same, only minor quantitative features differentiate the Hamiltonians. Within this relatively small variation, the structural and elastic values from the B3LYP calculations are those that best match the experimental data; results for a set of 15 cubic materials are surveyed in [41]. It is worth mentioning, however, that in a series of isostructural compounds we notice a general worsening of structural results on increasing the atomic number of the cation. This can be observed comparing results for Li, Na and K fluorides and chlorides in [41]. Similarly, in the alkali earth compounds [46, 47], the *a* cell parameters (along the densest packing direction of the solid, dominated by Coulombic interactions) from B3LYP calculations are overestimated by 0.95%, 2.90% and 3.4% in $Mg(OH)_2$, $Ca(OH)_2$

and $Sr(OH)_2$ respectively. This is a clear indication that the performance of current functional formulations, optimised in molecular studies for light atoms, degrades rapidly for heavy elements.

On comparing the different Hamiltonians we find, as a general rule, the following trend in the optimised lattice parameters: LDA<experimental<PW~B3LYP<BLYP, while the elastic constants and bulk moduli (K_0) follow the series of experimental ~BLYP<PW~B3LYP<LDA~HF. The relative value of K_0 yielded by the different DFT functionals is mostly due to the equilibrium volume V_0 (we recall that K_0 scales as $1/V_0$), while the lack of correlation in the HF solution overestimates the curvature of the potential energy surface and hence also K_0. The relative value of the HF equilibrium lattice spacing compared with the DFT ones has a less clear trend, and depends on the ionicity of the material; we shall come back to this topic later.

The situation is more complex for open-shell transition metal oxides, where different electronic states of comparable energy can exist. The relative energy of the electronic states is often reversed by small modifications in the functional; the structural properties are in this case dominated by which electronic state is predicted as stable by the different Hamiltonians. When the same electronic state is obtained (or enforced), the same trends described for the main group elements are reproduced; if different electronic states enter the solution, instead, the spread of results can be very large. In pyrite (FeS_2) [62], for instance, the optimised lattice parameter covers a range of values as large as 15% of the experimental lattice constant (LDA predicting a=5.386 and HF yielding a=6.000 Å). The internal degrees of freedom have similar differences, the S-S bond distance ranges from 2.143 Å (HF) to 2.295 Å (PBE); the B3LYP value is 2.197 Å. HF and B3LYP results are the closest to the experimental value of 2.162 Å.

2. *Surface structure* calculations performed on compounds of main group elements with different Hamiltonians show larger differences than bulk systems in the results, in particular for the relaxation of the outermost surface ions. In [48] this feature has been attributed to the change of ionicity of the surface ions (i.e. to the surface polarisability), which occurs to a different extent employing different Hamiltonians and functionals. The same trend observed in the bulk systems (ionicity increasing in the order of LDA<GGA<B3LYP<HF) occurs at the surfaces, but differences in both polarisability and the ensuing relaxation are magnified at the surfaces compared to the bulk. Surfaces represent, therefore, a more severe test for the accuracy of structural results than bulk systems; however, reliable and unambiguous experimental data on the surface structure of complex materials are extremely difficult to achieve. Even the best surface XRD results available on ZnO(0001) [50] are still affected by an error bar of ±0.05 Å in the vertical displacement of the surface oxygen ions, which is adequate at most for a qualitative comparison between the different functionals.
3. The calculated *phonon spectra* (including here also the OH stretching frequencies in hydroxides and doped zeolites) show a stronger dependence on

the Hamiltonian than the structure, not surprisingly since the second derivatives of the energy with respect to atomic displacements are very sensitive to small features of the potential energy surface (PES). The same known trends of molecular calculations [65] are recovered also in the solid-state: the HF solution overestimates the curvature of the PES and systematically overestimates frequencies (by as much as 12%), while the LDA and GGA solutions underestimate them. The hybrid functional represented by B3LYP is a suitable compromise, and is able to reproduce accurately the experimental data, to within a few wavenumbers.

4. The situation for the *band gaps* [40] is very similar to that observed for the phonons: HF and LDA (or GGA) solutions give systematically errors of opposite sign, that cancel out in the hybrid formulation (although we should recall here that the virtual bands in either HF or DFT approaches are not representative of the excited states; a time-dependent (TD-DFT) solution should be employed in this case [66, 67]). Again, open-shell transition metal compounds should be considered separately: the ability of different Hamiltonians to localise electrons on the cationic site more or less tightly leads to changes of the solution from metallic to insulating, and can modify the stable electronic configuration of the compounds. FeS_2 is predicted as metallic in LDA and PBE solutions, as a paramagnetic insulator in HF, and as a diamagnetic insulator in B3LYP. Similar variations are known in NiO [60, 61] and MnO, which are described in more detail later.
5. Calculated *thermochemical data* show a large variation depending on the choice of functional; as exemplified again by the alkaline earth oxides and hydroxides [46, 47] and by the rocksalt-structured transition metal oxides [60]. In this case, results show that the hybrid functional yields comparable results to its component GGA functional (i.e. B3LYP to BLYP; B3PW to PW). B3LYP and BLYP underestimate the experimental cohesion energy by up to 1 eV per formula unit in the systems examined; the best agreement with experiment is given by PW and PBE (and by the hybrids built on them) [60]. In contrast, HF underestimates heavily the cohesive energy due to the lack of correlation, while LDA results confirm the tendency of this functional to overbind, already known from molecular calculations. Also in the thermochemical results we notice a tendency to increase the difference between calculated and experimental results on increasing the atomic number of the cation: the B3LYP cohesive energies of $Mg(OH)_2$, $Ca(OH)_2$ and $Sr(OH)_2$ are underestimated by 0.3, 0.1 and 1.2 eV/f.u., respectively. Despite being large in absolute value, these numbers represent a relatively small fraction of the total cohesive energy, equal to 1.6, 0.4 and 5.6% in the Mg, Ca and Sr hydroxides. Errors of this order of magnitude are considered as acceptable in the solid state. When considering reaction energies, errors largely compensate; for instance, errors in the calculated hydration energy $MO+H_2O \rightarrow M(OH)_2$ are 0.0, 0.03 and 0.16 eV/f.u (or 0.0, 2.4 and 11.5% of the total hydration energy) in the Mg, Ca and Sr compounds, i.e. one order

of magnitude smaller than in the cohesive energy, although in relative terms they may represent a large fraction of the experimental data.

6. A separate discussion should be performed concerning the *properties of weak bonds*. We include in this category the interlayer interaction in the alkaline earth hydroxides [46, 47], hydrogen-bonded systems [45], and the weak adsorption of CO on MgO [43, 44]. The features of the hybrid functional in such a case are discussed exhaustively in [43, 44]; when dispersion forces have comparable energetic influence than other types of binding in the solid, none of the DFT functionals examined yields accurate structural and thermochemical predictions. In fact they should not, as dispersion forces are not accounted for in any of the available functional formulations. The B3LYP hybrid is no exception, and the calculated lattice parameters along directions dominated by intramolecular forces can be overestimated by as much as 6.5% or more. Important improvements are clearly needed in this area.
   The interaction that is commonly identified as hydrogen bond is another challenge for computational studies; depending on its strength, the H-bond varies from being dominated by covalent to electrostatic or dispersive forces [68]. The case of crystalline HCl has been investigated in [45]; its low temperature structure [69] consists of hydrogen bonded zig-zag chains of HCl molecules running along the c-axis, while inter-chain interactions along the a and b lattice vectors are of weak van der Waals nature [70]. The HCl crystal has H-bond interactions of moderate strength, and with an important electrostatic component; these are well represented by B3LYP [45]. The c lattice parameter along the direction of the H-bonded chains has the fol-lowing optimised values: c_{HF}(6.301 Å)>c_{B3LYP}(5.581 Å)>c_{exp}(5.399 Å)>c_{LDA}(4.779 Å). However, the a- and b-axes dominated by dispersion forces are poorly represented: HF and B3LYP overestimate them by more than 75%, while LDA underestimates them by up to 13%.
   Because the inter-chain binding accounts for only 4% of the binding energy of the crystal (~0.5 kJ/mol) [45], even large errors in the a- and b-axes do not affect the calculated cohesive energy. In this case, we find that LDA overestimates the lattice energy by 40 kJ/mol; HF underestimates it by 5 kJ/mol, while B3LYP gives a lattice energy of 12.66 kJ/mol, in good agreement with experiment [68]. Other properties that are only weakly dependent on the inter-chain interactions, such as the frequency of the H-Cl stretching mode (ω) and the molecular dipole moment, are also well reproduced by the B3LYP functional. The symmetric HCl stretching frequency varies as ω_{LDA}(2201 cm^{-1})<ω_{B3LYP}(2768 cm^{-1})<ω_{HF}(3138 cm^{-1}). The experimental value is ω_{exp}=2858 cm^{-1} from the Raman shift for orthorhombic HCl at high pressure (>19 Gpa) extrapolated to p=0 [71], or 2768 cm^{-1} from IR [72]. The agreement in the latter case may be fortuitous, but reflects the general agreement of B3LYP frequencies with experiment.
7. The *ferroelectric polarisation* has been calculated for the tetragonal phase of $KNbO_3$ [58] and for HCl [45]; in the case of $KNbO_3$, the macroscopic polar-

isation **P** has an important electronic component, and correlates with the degree of covalence in the Nb-O bonding [73, 74]. The polarisation has been calculated both at the experimental structures of the compounds and at their optimised geometries. In $KNbO_3$, when using the experimental structure for different Hamiltonians, **P** shows small variations, centred around the experimental value of $\mathbf{P}_{expt}$=0.37 C·m^{-2}; in particular we find $\mathbf{P}_{LDA}$=$\mathbf{P}_{PBE}$ (0.38 C·m^{-2})>$\mathbf{P}_{B3LYP}$ (0.37 C·m^{-2})>$\mathbf{P}_{HF}$ (0.33 C·m^{-2}). This trend is opposite to that discussed earlier concerning the ionicity (HF>B3LYP>GGA~LDA) and confirms the importance of the electronic contribution to **P**. The values of **P** calculated at the optimised geometries are instead $\mathbf{P}_{HF}$ (0.52 C·m^{-2})>$\mathbf{P}_{B3LYP}$ (0.51 C·m^{-2})>$\mathbf{P}_{PBE}$ (0.49 C·m^{-2})>>$\mathbf{P}_{LDA}$ (0.42 C·m^{-2})>$\mathbf{P}_{expt}$; we notice a larger dispersion of the results, indicative of optimised structures with a different extent of distortion. LDA gives in this case the best comparison with experiment, but only due to an underestimation of the distortion [75], while PBE, B3LYP and especially HF overestimate both the structural distortion and the resulting **P**. For HCl, the calculated values of **P** at the optimised structure are $\mathbf{P}_{HF}$ (0.46 C·m^{-2})<$\mathbf{P}_{B3LYP}$ (0.86 C·m^{-2})<$\mathbf{P}_{LDA}$ (1.06 C·m^{-2}), while $\mathbf{P}_{expt}$=3.6 C·m^{-2} [76]. As we observed in point 6 above, the optimised structure for HCl is affected by a large error, and this influences the calculated value of **P**. Enforcing the experimental structure, agreement with experiment is excellent; for instance $\mathbf{P}_{HF}$=3.66 C·m^{-2}. From the two comparisons above, it is clear that current electronic structure methods are able to yield an accurate ground state electronic distribution for a range of compounds, once a proper geometry is chosen. Errors in the equilibrium structure, however, are large enough to introduce an uncertainty as large as one order of magnitude for those observables that show a strong dependence on the structure.

8. In magnetic compounds (those containing open-shell transition metal ions), a useful value to grade the solution is the *magnetic coupling* (J) between neighbouring magnetic ions in the structure. The values of the coupling constants have been calculated for several compounds, including NiO [60, 61] and CoO [60], La_2CuO_4 [63], $KMnF_3$ [42]. In each case, inclusion of some HF exchange in the functional has dramatic effects on the electronic and magnetic coupling; the difference between the values of J calculated at LDA and UHF level can be as large as one order of magnitude, with LDA usually overestimating experiment by a factor of 4–5, and UHF underestimating experiment by a factor of 3. As for all the other observables in which HF and LDA (GGA) systematically yield errors of opposite sign, formulation of hybrid exchange functionals heals the shortcomings. The 20% mixing parameter of B3LYP is insufficient to lower the LDA (GGA) to the experimental value; formulations closer to Becke's 'half and half' hybrid are more accurate [61, 77–79].

Most of the works referenced above employed a standard molecular formulation of the B3LYP functional, with 20% HF exchange. Systematic inves-

tigations on the effect of changing the mixing parameter have never been performed. In fact, we are aware of only three cases in which a value of the mixing parameter different than 20% has been used (we exclude here the calculations in which pure HF exchange has been used in conjunction with a DFT correlation functional, as we do not consider it as a hybrid functional). These are the works by Bredow and Gerson on MgO, NiO and CoO [60], Moreira et al. on NiO [61], and Mackrodt et al. on VO [64]. We also need to mention here the seminal work on magnetic coupling performed by Illas and Martin, using embedded clusters methods to simulate the crystalline environment of the magnetic ions [77–79]. These works, while pointing to the need for solid-state specific formulations of the hybrid functionals, suffer from a limited applicability, as they focus on the magnetic coupling in open-shell transition metal compounds, at the expenses of other observables. In addition, the embedded cluster calculations, despite enabling the use of post-HF methods, enforce the experimental geometry of the compounds and not the equilibrium structure of each Hamiltonian/functional. The values of the coupling constants show large variations as a function of the internuclear distance (see, e.g. [80]); as we have seen in point 7 above, constraining the computational procedure to the experimental structure may therefore introduce large errors in the results when transferred to the study of new compounds, for which the experimental structure is unknown. It would be desirable to have a computational method available that is able to determine *both* structural and electronic parameters at the same time.

We consider the lack of a systematic approach to be a severe limitation of present works on hybrid functionals in the solid state. To fill this gap, we have performed a systematic investigation on the effect of changing the mixing parameter, covering the whole range from 0% to 100% in a set of compounds. The systems and properties we have chosen are the following:

- Perovskite-structured transition metal oxides AMO_3, including ferroelectric materials such as $BaTiO_3$ and $KNbO_3$. The polarisation **P** is due to a subtle combination of structural (extent of the distortion) and electronic (M-O covalence) effects.
- Magnetic perovskite and rocksalt-structured oxides and fluorides. These are highly ionic compounds, in which the calculated coupling constants J indicate the degree of localisation of the unpaired electrons on the transition metal sites, and the range of the magnetic (spin-spin) interaction.
- Open shell defects in rocksalt-structured matrices; the observables of interest are in this case the hyperfine constants, measurable experimentally by EPR, which depend both on the defect structure and on the localisation of the defect states.

The problems of interest are therefore at the same time electronic and structural. All the systems listed above share the fact that standard DFT cal-

culations, in either LDA or GGA formulations, fail to reproduce with sufficient accuracy the correct electronic ground-state and/or the structural and electronic properties of the material. We examine systematically if, and to what extent, this problem can be overcome by the use of hybrid HF-DFT exchange functionals.

We shall monitor systematically the effect of changing the percentage of HF exchange, coupled with different exchange and correlation functionals. The mixing parameter is varied between 0 and 100% in steps of 10% or 20%. The complexity and cost of solid-state calculations does not yet enable a more extensive approach. Results are presented later, and are preceded by a discussion to show how mapping of the ab initio results onto model Hamiltonians can be employed to analyse the results and relate them to experimental observations.

3
The Use of Model Hamiltonians and Mapping of the Ab-Initio Results

Ab initio calculations of the type described in the previous section, in principle, provide all the information needed to compute the time-independent properties of a system. However, the formal complexity of the calculations makes analysis of results often very difficult. In past decades, our knowledge on complex materials has been built on model Hamiltonians, which capture in a phenomenological (parametric) way the main physical/chemical interactions of the problem. Model Hamiltonians provide a reference framework to guide the interpretation of results, which focus attention on particular features of the electronic structure thereby leading to greater transparency. We propose that, instead of aiming at reproducing experimental observations, model Hamiltonians can nowadays by effectively employed to rationalise the results of ab initio calculations. This operation shall be performed, in our work described later, by mapping the ab initio solution onto that given by a model Hamiltonian. This phenomenological analysis a posteriori provides a powerful quantitative tool for rationalising the ab initio results in terms of a small set of *effective* interaction parameters with a direct physical/chemical meaning.

In particular, we have chosen to map the solution for the ferroelectric perovskites onto that provided by a Tight-Binding Hamiltonian [81–83], whose parameters are related to the strength of the interactions between nearest neighbour ions in the solid. The solution for the magnetic oxides is instead mapped onto a model spin Hamiltonian of the Ising type, that assumes that different spin orderings are differentiated only by the spin interaction between neighbouring metal ions.

3.1
The Tight-Binding Model of Metal-Anion Interactions in Perovskites

Let us consider the cubic to tetragonal ferroelectric phase transition in a ferroelectric perovskite that contains a transition metal ion in formal electronic configuration $d^{(0)}$, such as $BaTiO_3$ or $KNbO_3$. In the cubic phase, each unit cell contains one formula unit AMO_3; the transition metal ion is located at the origin; the three oxygens are along the x, y and z directions at fractional coordinates ±1/2, and the cation A in dodecahedral interstices in the sites with fractional coordinates (±1/2, ±1/2, ±1/2). The structure is shown in Fig. 1. In the tetragonal ferroelectric phase, M is displaced towards one of its six neighbour oxygens, say the one in the +z direction; this displacement is accompanied by smaller relaxations of the oxygen and A ions in the ±z direction, and by an elongation of the cell along z (the c/a ratio between the lattice parameters along z and along x (y) is ~1.01). The physics of the distortion can however be captured by a simplified *pseudocubic* phase in which only the M ion is displaced in an otherwise undistorted cubic structure.

The cubic and pseudocubic perovskite phases are relatively simple structures, for which we can derive analytically the solution given by a model Tight-Binding (TB) Hamiltonian [81–83]. The TB is the simplest quantum mechanical Hamiltonian, in which the matrix H^{eff} representative of the Hamiltonian operator is defined in the space containing the valence atomic orbitals (AO) of the component atoms. This space is divided into an active subspace, containing all the chemical interactions considered important for the solution, and the complementary inactive subspace, whose matrix elements are disregarded and which will be ignored in the chemical description of the system. The elements of the active space are assigned a parametric value.

As in molecular systems, also in solids the fundamental chemical interactions to understand are those confined to the *frontier* AOs. For a perovskite

Fig. 1 Corner-sharing arrangement of octahedra in an AMX_3 perovskite. The cation A is located in a dodecahedral interstice

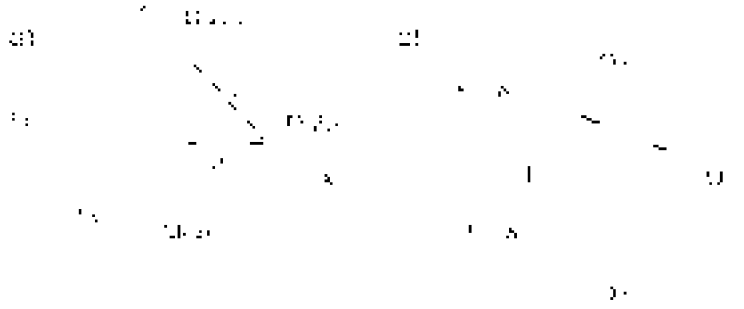

Fig. 2a,b Description of the TB parameters in: **a** a cubic perovskite; **b** a tetragonal perovskite

containing $d^{(0)}$ transition metal ions, these are the M-d(t_{2g}) and O-2p(π) AOs.

In the case of $d^{(0)}$ cubic perovskites we make reference to the effective interaction parameters shown in Fig. 2a. These are:

- The diagonal elements α; in particular α_d relative to the M-d(t_{2g}) AOs, and α_p for the O-2p(π) AOs (i.e. the 2p AOs on each oxygen, perpendicular to the M-O-M direction)
- β, the interaction element between M-d(t_{2g}) and O-2p(π) AOs on nearest neighbour ions
- γ, the interaction element between O-2p(π) AOs on next-nearest neighbour ions

We also assume that the dodecahedral ion A behaves as a perfectly ionic species in the crystal structure, whose only role is that of charge compensation, i.e. that there is no A-O covalent interaction. For alkali or alkali-earth cations the above assumption is justified.

The representative matrix H^{eff} in the above assumptions is block-diagonal in three subsets of AOs, each belonging to one of the three coordinate planes xz, yz and xy, and comprising one M-d(t_{2g}) and two O-2p(π) AOs, the same set of AOs as displayed in Fig. 2a. Let us consider one of the three degenerate sets, say the one in the xz plane.

The TB solution for the periodic system is obtained first by constructing the Bloch functions $\psi_i(k)$ relative to each AO χ_i in the basis for the representation of the TB Hamiltonian (three in our case), and then constructing the representative matrix $H^{eff}(k)$ in the basis of the Bloch functions $\psi(k)$. The solution is factorised for each point of reciprocal space, k. Following Bloch's theorem we have:

$$\psi_i(k) = \frac{1}{\sqrt{N}} \sum_{k=1}^{N} \chi_i(r) e^{i(kr)} \tag{1}$$

and

$$H^{eff}(k) = \begin{array}{c} \\ \Psi_{\mathrm{d}} \quad (k) \\ \Psi_{\mathrm{p_x}} \quad (k) \\ \Psi_{\mathrm{p_z}} \quad (k) \end{array} \begin{array}{c} \begin{array}{ccc} \Psi_{\mathrm{d}} & \Psi_{\mathrm{p_x}} & \Psi_{\mathrm{p_z}} \end{array} \\ \begin{pmatrix} H^{eff}_{\mathrm{dd}} & H^{eff}_{\mathrm{dx}} & H^{eff}_{\mathrm{dz}} \\ H^{eff}_{\mathrm{xd}} & H^{eff}_{\mathrm{xx}} & H^{eff}_{\mathrm{xz}} \\ H^{eff}_{\mathrm{zd}} & H^{eff}_{\mathrm{zx}} & H^{eff}_{\mathrm{zz}} \end{pmatrix} \end{array} \tag{2}$$

The spectrum of one electron energy levels of the system, at each k point, is now obtained by solving the secular equation

$$\left(\mathrm{H}^{eff}(k) - ES\right) = 0 \tag{3}$$

For the set of frontier AOs of a cubic perovskite, using the TB parameters and the assumptions defined above, the secular equation takes the form

$$\begin{vmatrix} \alpha_{\mathrm{d}} - e & -2i\beta s_z & -2i\beta s_x \\ -2i\beta s_x & \alpha_{\mathrm{p}} - e & 4\gamma s_x s_z \\ -2i\beta s_z & 4\gamma s_x s_z & \alpha_{\mathrm{p}} - e \end{vmatrix} = 0; \text{ where } s_x = \sin(k_x) \text{ and } s_z = \sin(k_z). \tag{4}$$

Let us examine the solution in the high-symmetry positions of reciprocal space.

1. Origin of reciprocal space Γ≡(0,0,0)
   In Γ we have s_x=s_z=0; the TB Hamiltonian is diagonal in the AO basis set, and the solutions coincide with the pure O-2p(π) and M-d(t_{2g}) ionic orbitals, of energy α_{d} and α_{p}. *No M-O covalence* is present in Γ, and the M-O interaction in the crystal structure occurs via their ionic charge only. The splitting of levels, $\Delta\alpha$=α_{d}−α_{p}, is due only to the crystal (Coulomb) field. The transition metal ion has two equidistant oxygen neighbours in each coordinate direction (x,y,z); similarly, each oxygen is exactly half way between its two nearest M ions. The bonding contributions from the two neighbours in the Bloch function $\psi(k$=0) have opposite sign (+β and −β) and cancel reciprocally: *covalence is symmetry forbidden*. The same symmetry constraint applies whenever the *local* environment of M and O ions has the same symmetry features described here.
2. Γ(0,0,0)-X(1/2,0,0) direction of reciprocal space (k in units of π/2a)
   The solution along the Γ-X direction of reciprocal space is characterised by s_z=0, but $s_x \neq 0$; the Hamiltonian matrix is block diagonal in the 2p AO of the oxygen ion along z, while the M-d and O-2p AO on the oxygen along the x direction hybridise into a combination of bonding and antibonding character. A straightforward solution of Eq. (4) in X(1/2,0,0) yields

$$\begin{cases} e_1 = \alpha_p \\ e_2 = \alpha_p - \frac{4\beta^2}{\Delta\alpha} \\ e_3 = \alpha_d + \frac{4\beta^2}{\Delta\alpha} \end{cases} . \tag{5}$$

The solution depends only on the parameters α and β and not on the oxygen-oxygen interaction γ. The crystalline orbitals in the X point of reciprocal space have M-O bonding character in the valence band, and M-O antibonding character in the conduction band. The Γ-X valence band width, i.e. the energy effectiveness of covalence, equals $4\beta^2/\Delta\alpha$. For symmetry constraints a set of levels is non k-dependent and M-O non-bonding along the whole Γ-X direction of reciprocal space; they have been called *superdegenerate* in the literature [84]. Superdegenerate levels comprise the O-2p AO that is block-diagonal in the secular equation, as described above, and all three AOs in the yz plane, whose solution is orthogonal to the k_x component of the *k* vector.

Simple algebra also shows that the admixing of M-d and O-2p in the bonding/antibonding levels is proportional to $\beta/\Delta\alpha$; the latter is therefore an effective measure of covalence in the solid.

3. X(1/2,0,0)-M(1/2,0,1/2) direction of reciprocal space

The oxygen-oxygen interaction parameter γ enters the TB solution only when two components of the *k* vector differ from zero. The energy levels in M can be obtained by solving the third order equation

$$(\alpha_d - e)(\alpha_p - e)^2 - 8\beta^2(\alpha_p - e) + 32\beta^2\gamma = 0 \tag{6}$$

Assuming first that the oxygen-oxygen interaction is negligible (γ=0), the energy levels are

$$\begin{cases} e_1 = \alpha_p \\ e_2 = \alpha_p - \frac{8\beta^2}{\Delta\alpha} \\ e_3 = \alpha_d + \frac{8\beta^2}{\Delta\alpha} \end{cases} . \tag{7}$$

i.e. one of the energy solutions of the secular equation is still *superdegenerate* and coincides with one of the unperturbed ionic O-2p energy levels. The other two solutions are again bonding and antibonding admixings of the O-2p and M-d AOs; the extent of hybridisation and the energy change due to M-O covalent interactions at M are twice as large as in the X point of reciprocal space. The O-O interaction, if different from zero, resolves the superdegeneration along the X-M direction. In particular, O-O repulsion will cause a destabilisation of the O-2p levels at the top of the valence band.

It is clear from the analysis above that the TB parameters can be attributed a straightforward physical meaning: α_p and α_d represent the energy levels in a purely ionic solution. In the crystal lattice, the values of α_p and α_d are shifted by the Madelung field, which is proportional to the net ionic charges. The value of $\Delta\alpha=\alpha_d-\alpha_p$ is therefore associated with the degree of

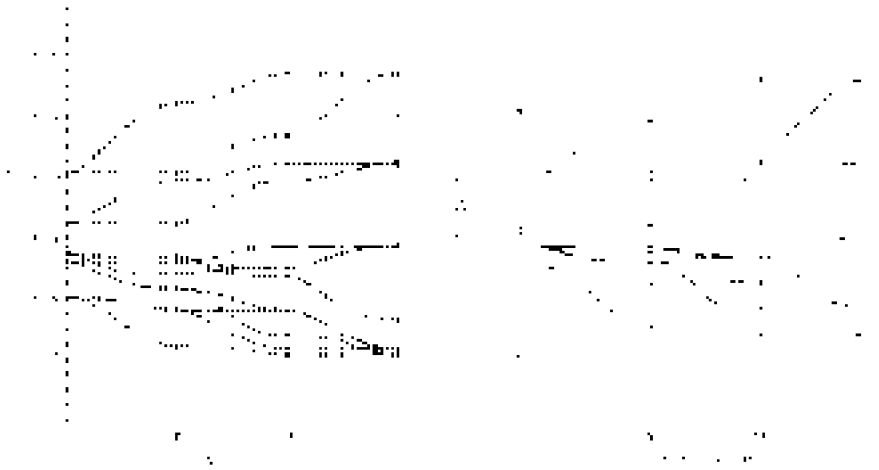

Fig. 3 Comparison of the band-structure for WO_3 calculated with a hybrid B3LYP functional with one from a TB calculation

ionicity in the solid. The energy effectiveness of covalence scales as $\beta^2/\Delta\alpha$, while the hybridisation of AOs is proportional to $\beta/\Delta\alpha$; the latter parameter represents the covalence in the solid. We also notice that covalence (proportional to $1/\Delta\alpha$) and ionicity (proportional to $\Delta\alpha$) are complementary: the greater the ionicity of the solid, the higher the splitting of energy levels due to the crystal field, and the lower the importance of covalence.

Having available a calculated band structure for a cubic perovskite, which can be achieved, for instance, by means of a periodic DFT calculation, the interactions introduced above can be easily factorised: the value of the ionicity parameter $\Delta\alpha$ can be derived from the eigenvalue spectrum at Γ; the k-dependence of the band structure along Γ-X is a function only of $\beta^2/\Delta\alpha$ and used to calculate β.

In fact, the TB solution can be made to correspond very closely to the ab initio reference; in Fig. 3 we compare the B3LYP band structure for WO_3 with that obtained with a self-consistent TB scheme [85, 86]. In addition to the parameters α–γ, the TB calculation employed for generating the band structure of Fig. 3 included crystal-field splitting terms, which however do not modify the M-O hybridisation pattern.

Let us now examine the electronic rearrangement that accompanies a displacement of M towards one of its nearest oxygens; we have chosen the oxygen in the +z direction. The TB parameters for the distorted structure are shown in Fig. 2b; we call ζ the displacement of M; $\beta(1+\delta)$ and $\beta(1-\delta)$ the M-O interaction parameters with the two oxygens along the z direction. In first approximation δ is linear in ζ [84].

The M off-centring removes the symmetry constraint described earlier for the cubic phase. The full secular equation for the three AOs in the xz plane becomes

$$\begin{vmatrix} \alpha_d - e & (-2i\beta s_z + 2\beta\delta c_z)e^{-ik_z\xi a} & 2i\beta s_x e^{-ik_z\xi a} \\ (-2i\beta s_x + 2\beta\delta c_z)e^{-ik_z\xi a} & \alpha_p - e & 4\gamma s_x s_z \\ -2i\beta s_z e^{-ik_z\xi a} & 4\gamma s_x s_z & \alpha_p - e \end{vmatrix} = 0 \qquad (8)$$

In particular, at Γ(0,0,0) Eq. (8) reduces to

$$\begin{vmatrix} \alpha_d - e & 2\beta\delta & 0 \\ 2\beta\delta & \alpha_p - e & 0 \\ 0 & 0 & \alpha_p - e \end{vmatrix} = 0 \qquad (9)$$

The TB Hamiltonian at Γ contains off-diagonal terms in the block of M-d and O_z-2p AOs, which can be expressed as

$$H^{eff} = \begin{vmatrix} \alpha_d & 2\beta\delta \\ 2\beta\delta & \alpha_p \end{vmatrix} = \begin{vmatrix} \alpha_d & 0 \\ 0 & \alpha_p \end{vmatrix} + 2\beta\delta \begin{vmatrix} 0 & 1 \\ 1 & 0 \end{vmatrix} = H_0 + \lambda H' \qquad (10)$$

where $\lambda=2\beta\delta$, and H_0 is the Hamiltonian for the cubic phase. The energy solutions are

$$\begin{cases} e_1 = \alpha_p \\ e_2 = \alpha_p - \frac{4\beta^2\delta^2}{\Delta\alpha} \\ e_3 = \alpha_d + \frac{4\beta^2\delta^2}{\Delta\alpha} \end{cases} . \qquad (11)$$

In the distorted phase, covalence between M and its closest oxygen along the direction of displacement z is no longer symmetry forbidden. The superdegenerate (M-O non-bonding) M-d and O-2p levels of the cubic phase hybridise now into an M-O bonding level in the valence band and M-O antibonding state in the conduction band. The electronic modification in the tetragonal distortion involves therefore the formation of a new M-O bond.

As clear from Eq. (10), in a first-order perturbative treatment, the energy effectiveness of the new covalent M-O bond is proportional to λ^2 (it equals $4\beta^2\delta^2/\Delta\alpha$), while the covalent mixing of M-d and O-2p states is proportional to $2\beta\delta/\Delta\alpha$. The extra splitting of the superdegenerate levels due to M-O covalence (Eq. 11) is retained along the whole Γ-X direction of reciprocal space.

The energy effectiveness of the new M-O bond formed upon the M off-centring is proportional to $\beta^2/\Delta\alpha$, i.e. to the same parameter defining the band dispersion in the solution of the cubic phase; it is also proportional to δ^2 and to the extent of the distortion. The one electron energy for a perovskite containing $d^{(0)}$ ions, in which the M-O bonding level in the valence band is filled and the M-O antibonding level in the conduction band is empty, will be stabilised in this ferroelectric distortion. The M-O short-range re-

pulsion will however limit the maximum M off-centring that is energetically stable.

It is also important to notice that the rehybridisation of the frontier π levels causes a displacement of electronic charge from the O_z-2p towards the M-d AOs, in the opposite direction with respect to the displacement of nuclear charge from which it originates. This electronic contribution to the polarisation scales as $\beta\delta/\Delta\alpha$ (the additional weight of the M-d AO in the occupied eigenstates of the distorted phase); it is this electronic polarisability that causes the large values of effective (Born) charges measured experimentally for ferroelectric perovskites [87].

3.2 The Ising Model of Magnetic Systems

In the case of magnetic crystals, i.e. of compounds in which one or more of the constituent ions carry a spin polarisation, one fundamental question concerns the relative stability of different spin patterns in the lattice. A ferromagnetic (FM) ordering, in which all the magnetic ions have the same spin polarisation, is of particular technological interest, as a thin film built up from an FM material would operate as a spin valve in microelectronics. In practice, the FM order will compete with other long-range arrangements, such as antiferromagnetic ones (AFM), in which the ionic spins along one or more crystallographic directions have alternate sign.

In ionic transition metal compounds, the spin population is highly localised on the cationic sites. In such a case, a commonly made assumption, when comparing different spin alignments, is that the metal-anion (M-X) bonding is the same in each magnetic phase, and that the solution is differentiated *only* by the spin-spin interaction, i.e. that we can write

$$E = E_0 + E_M \tag{12}$$

where E_0 is the reference energy of an hypothetic phase in which the spin-spin interaction is excluded, and E_M is the spin-spin interaction characterising the magnetic phase M.

In turn E_M can be expressed as a sum of pairwise interactions between nearest neighbour magnetic ions i and j in the structure, whose strength is proportional to a coupling constant J_{ij}

$$E_M = \frac{1}{2}\sum_{i \neq j} J_{ij} S_{z,i} S_{z,j} \tag{13}$$

where $S_{z,i}$ is the z component of total spin.

The value of the coupling constant J_{ij} decays rapidly on increasing the distance between ions i and j in the lattice, which leaves only the terms be-

tween nearest neighbour (nn) and next-nearest neighbour (nnn) ions in the summation of Eq. (13).

The mechanism by which the two spins interact in the lattice is referred to as *direct exchange* when the two magnetic ions do not share a common ligand (the anion X) in the lattice, and *superexchange* when there is one linear (or close to linear) M_i-X-M_j bridge in the crystal. We refer to the coupling constants in the two cases as J_d for direct exchange, and J_{se} for superexchange. The value of the coupling constants can be shown to relate directly to measurable quantities such as the disorder transition temperature, or Néel temperature (T_N) of the solid.

In a computational study, the values of J_d and J_{se} can be obtained by mapping the total energies of different long-range ordered magnetic arrangements onto an Ising spin Hamiltonian of the form

$$\hat{H}_{Ising} = \hat{H}_0 - \frac{J_d}{2}\sum_{ij}^{nn} S_{z,i}S_{z,j} + \frac{J_{se}}{2}\sum_{ij}^{nnn} S_{z,i}S_{z,j} \tag{14}$$

Let us consider a rocksalt-structured oxide as an example, and examine the ferro- (FM) and two antiferromagnetic (AFM) alignments. The type-I AFM structure (AF_1) consists of ferromagnetic (100) planes of alternating spin along the [100] axis, while the type-II (AF_2) structure consists of ferromagnetic (111) planes of alternating spin in the [111] direction. The Miller indices and crystal directions noted above are for the conventional crystallographic cell.

The corresponding mapping equations take the form

$$E_M = E_0 - \frac{J_d S_z^2}{2}[N_{nn}(\uparrow\uparrow) - N_{nn}(\uparrow\downarrow)] + \frac{J_{se}S_z^2}{2}[N_{nnn}(\uparrow\uparrow) - N_{nnn}(\uparrow\downarrow)] \tag{15}$$

where N_{nn} and N_{nnn} are the numbers of nn and nnn parallel ($\uparrow\uparrow$) and antiparallel spins ($\uparrow\downarrow$) in the M alignment. For the three phases examined we have

$$\begin{aligned} E_{FM} &= E_0 + S_z^2[-6J_d + 3J_{se}] \\ E_{AF1} &= E_0 + S_z^2[2J_d + 3J_{se}] \\ E_{AF2} &= E_0 + S_z^2[-3J_{se}] \end{aligned} \tag{16}$$

The coupling constants are then given by

$$\begin{aligned} J_d &= \frac{1}{8S_z^2}[E_{AF_1} - E_{FM}] \\ J_{se} &= J_d + \frac{1}{6S_z^2}[E_{FM} - E_{AF_2}] \end{aligned} \tag{17}$$

in which the energies of the magnetic states are per formula unit.

3.2.1
Temperature-Induced Magnetic Disorder

Let us now consider the AF_2 ground state of the late rocksalt structured transition metal oxides. Within a mean field (MF) approximation for H_{Ising}, a statistical treatment of the magnetic ordering indicates that the mean magnetisation, $<\sigma>$, of the cation lattice as a function of temperature (T) for the AF_2 phase is given by

$$<\sigma>_{AF_2} = \tanh\left(\frac{3S_z^2 J_{se}}{k_B T}\right) \tag{18}$$

The Néel temperature (T_N) is defined as the temperature at which the mean magnetisation is completely suppressed by the thermal disorder, i.e. $<\sigma>=0$, which leads to

$$T_N^{AF_2}(MF) = 3S_z^2 J_{se}/k_B \tag{19}$$

An approximate allowance for the effect of fluctuations can be made in the usual way by reducing T_N(MF) by a factor of 3/4 [88], giving

$$T_N^{AF_2} \approx 2.25 S_z^2 J_{se}/k_B \tag{20}$$

Via Eqs. (17) and (20), T_N can be related to the total energies of the FM, AF_1 and AF_2 spin alignments, and hence can be calculated as a function of the hybridisation parameter.

3.3
The Kanamori Crystal Field Hamiltonian

The energy of electronic excitations is usually expressed employing the notation of atomic spectroscopy. In the case of a $d^{(n)}$ ($n \neq 0,10$) transition metal ion in a crystalline matrix, *local* d→d transitions can be employed to measure its allowed energy levels, and the crystal field acting on the metal site.

Just as the magnetic state energies can be mapped onto an Ising spin Hamiltonian, so may the energies of various crystal field split states be mapped onto the Kanamori Hamiltonian [89]. For an isolated metal site in which bonding and magnetic interactions are neglected, this takes the form

$$\hat{H}_{CF} = \hat{H}^0_{CF} + \frac{1}{2}\sum_{\bar{\gamma}}\sum_{\bar{\sigma}} C(1,2) a^{\dagger}_{\gamma_1\sigma_1} a^{\dagger}_{\gamma_2\sigma_2} a_{\gamma'_2\sigma'_2} a_{\gamma'_1\sigma'_1} \tag{21}$$

in which $\bar{\gamma} = \gamma_1\gamma_2\gamma'_1\gamma'_2$ are four AOs of the metal site, and $\bar{\sigma} = \sigma_1\sigma_2\sigma'_1\sigma'_2$ the corresponding spins. The integrals of the two-electron interactions are

$$C(1,2) = \left\langle \gamma_1\sigma_1, \gamma_2\sigma_2 \left| \frac{e^2}{\mathbf{r}_1 - \mathbf{r}_2} \right| \gamma'_1\sigma'_1, \gamma'_2\sigma'_2 \right\rangle \tag{22}$$

where γ and γ' label the orbitals of the d-manifold, and σ and σ' the electron spin. The single-particle creation and annihilation operators follow the usual notation. Three distinct types of interaction can be identified:

- The intraband Coulomb terms $U = \langle \gamma\sigma, \gamma\sigma' \| \gamma\sigma, \gamma\sigma' \rangle$ with $\sigma \neq \sigma'$
- The interband Coulomb terms $U' = \langle \gamma\sigma, \gamma'\sigma' \| \gamma\sigma, \gamma'\sigma' \rangle$ with $\gamma \neq \gamma'$
- The interband exchange terms $J = \langle \gamma\sigma, \gamma'\sigma \| \gamma'\sigma, \gamma\sigma \rangle$ with $\gamma \neq \gamma'$.

In atomic spectroscopy these terms are expressed as a function of the Racah A, B and C parameters [90], yielding U=A+4B+3C. U′ and J, however, are orbital dependent; for a d transition metal ion in an octahedral crystal field they are shown in the table below

γ	γ'	U′	J
t_{2g}	t_{2g}	A−2B+C	3B+C
e_g	e_g	A−4B+C	4B+C
xy	x^2-y^2	A+4B+C	C
xy	z^2	A−4B+C	4B+C
yz, xz	x^2-y^2	A−2B+C	3B+C
yz, xz	z^2	A+2B+C	B+C

The Racah A parameter is not involved in the determination of the energies of d→d excitations, and the C parameter enters only in excitations forbidden by the spin selection rule.

For the octahedrally coordinated Ni^{2+} ion in NiO, the level ordering (using U' and J averaged over all orbitals in the manifold) is

$$e_g(\alpha) \leftarrow 2J - \Delta_{CF} \rightarrow t_{2g}(\alpha) \leftarrow 2J \rightarrow t_{2g}(\beta) \leftarrow U' - J + \Delta_{CF} \rightarrow e_g(\beta)$$

All orbitals up to and including $t_{2g}(\beta)$ are occupied. Spin-allowed excitations must therefore be from the $t_{2g}(\beta)$ to the $e_g(\beta)$ orbitals. Mapping the ground and spin-allowed d→d excited states onto H_{CF} yields

$$E_g = E^0_{CF} + 28A - 50B + 21C$$
$$E_{xy \rightarrow x^2-y^2} = E^0_{CF} + 28A - 50B + 21C + \Delta_{CF}$$
$$E_{xy \rightarrow z^2} = E^0_{CF} + 28A - 38B + 21C + \Delta_{CF}$$
$$E_{xz,yz \rightarrow z^2,x^2-y^2} = E^0_{CF} + 28A - 47B + 21C + 2\Delta_{CF}$$

where Δ_{CF} is the e_g−t_{2g} crystal field splitting. The excitation energies derived from first principles calculations may then be equated to the differences between the states above, and in this way the Racah B parameter and crystal field splitting are obtained.

4
Results and Properties—Defect Free Systems

4.1
Computational Details and Notation

Results reported in the following sections have been obtained via periodic HF and DFT calculations employing the Crystal code, in its CRYSTAL98 [30] and CRYSTAL2003 [91] versions. The basis set is composed of localised atomic orbitals, expressed in a series of Gaussian type functions. All the basis sets employed are available via the online library of the code [92] and can be obtained on request from the authors. They are the best available basis sets for crystalline calculations for each element investigated, and correspond to a triple valence plus polarisation quality for most ions. All the elements are treated at the all-electron level, except for the heavy elements for which we used effective core pseudopotentials (small core for Ba and Mo, large core for W and Re). Open shell systems have been treated by a spin-unrestricted procedure; defects and excitation energies are calculated in the periodic model using a supercell expansion of the primitive unit cell.

The implementation of DFT in the CRYSTAL code requires the specification of either an auxiliary basis of Gaussian type functions for fitting the exchange-correlation potential, or of a grid to evaluate the potential numerically. In the magnetic materials we have employed the former option, using the following even-tempered bases of Gaussian-type functions: for O, 14 s-type functions with exponents in the range 0.07–4000.0, and one p-type, one d-type and one f-type function, each with exponent 0.5; for Mn and Ni, 13 s-type functions with exponents in the range 0.1–4000.0, three p-type function with exponents in the range 0.3–0.9, one f-type function with exponent 0.8 and three g-type functions with exponents in the range 0.45–3.3.

The numerical integration route has instead been employed for the ferroelectric perovskites and for the defects in MgO; the grid consisted of atom-centred contributions with 80 radial points covering a range of 4.0 ionic radii, and a very dense angular grid with at least 590 points. This tight tolerance has been necessary to ensure convergence in the calculated energy to well within 10^{-6} Hartree, as required for evaluating the energetic contribution of small structural distortions.

A Monkhorst-Pack shrinking factor of 8 (12 in case the solution converged to a metallic state) and truncation thresholds of 10^{-7}, 10^{-7}, 10^{-7}, 10^{-7} and 10^{-14} for the Coulomb and exchange series [93] ensured convergence of the total energies to within 0.1 meV, while SCF convergence thresholds were set to 10^{-7} Hartree or smaller for both eigenvalues and total energies. These tolerances ensure high numerical accuracy in the calculations [93, 94].

In addition to determining the TB parameters, as described above, we also performed standard Mulliken population analyses of the crystalline or-

bitals, to extract net atomic charges, magnetic moments and individual orbital occupations.

Different formulations of the hybrid functionals have been used in the calculations. Here we introduce the notation employed in the following sections. In the Hartree-Fock and Kohn-Sham (DFT) theories, the one-electron Hamiltonian takes the form

$$h_{HF} = T + V_N(R) + J + X_e = h_0 + X_e$$
$$h_{KS} = h_0 + X_i(\rho) + C_j(\rho) \tag{23}$$

The symbols refer to kinetic energy (T), external (nuclear) potential (V_N), electron-electron Coulomb (J) and HF (exact) exchange (X_e) operators; exchange (X_i) and correlation (C_j) functionals. For a generic *hybrid* functional, the one electron Hamiltonian is defined as

$$h_{hyb}(\alpha,\beta) = h_0 + \alpha X_e + (1-\alpha)X_i(\rho) + \beta C_j(\rho) \tag{24}$$

α and β are arbitrary mixing parameters that can be chosen in such a way as to optimise the correspondence of the calculated properties to one or more experimental observables. In this notation, $h_{HF}=h_{hyb}(1,0)$; $h_{KS}=h_{hyb}(0,1)$. We also define as correlated (U)HF limit the case of $h_{hyb}(1,1)$. A proper hybrid functional is achieved when $0<\alpha<1$, and $\beta\leq 1$.

We have examined the properties of $h_{hyb}(\alpha,1)$ within the full range $0\leq\alpha\leq 1$, based on different exchange and correlation functionals, $X_i(\rho)$ and $C_j(\rho)$. In principle, there are no restrictions on which formulation of $X_i(\rho)$ and $C_j(\rho)$ should be used, and an interesting strategy, first proposed by Becke [26], is to combine different exchange and correlation functionals in a single formulation. Thus, his 'B3LYP'combination is based on

$$X_i(\rho) = X_{LSDA}(\rho) + 0.9\Delta X_{B3}(\rho); C_j(\rho) = 0.81C_{LYP}(\rho) + 0.19C_{VWN}(\rho)$$

Clearly, the possible number of combinations of X_i and C_j is large, and, for the most part, an exhaustive examination is impracticable. In this chapter we have confined our attention to a limited set of combinations, namely BLYP [13, 14], PW [16, 17], and B3LYP [26]. The shorthand notation F_α-XC will indicate an hybrid functional with a fraction α of HF exchange, used in conjunction with the XC exchange and correlation functionals. So, for instance $F_{0.6}$-PW and $F_{0.3}$-B3LYP will correspond to

$$F_{0.6} - PW = h_0 + 0.6X_e + 0.4X_{PW} + C_{PW}$$
$$F_{0.3} - B3LYP = h_0 + 0.3X_e + 0.7(X_{LDSA} + 0.9\Delta X_{B3}) + (0.81C_{LYP} + 0.19C_{VWN})$$

We finally refer to a F-XC *scheme* or *series* to indicate a series of calculations with the hybrid F_α-XC functional, in which α spans the entire range $0\leq\alpha\leq 1$.

4.2 Ferroelectric Perovskites and Polarisation Properties

A recent review of published ab initio calculations on ferroelectric perovskites can be found in [87]. Here we shall employ this well understood class of materials to highlight how varying the formulation of the hybrid functional modifies the features of the calculated electronic density, and how this affects other structural and electronic properties. All the calculations described in this section have been performed within the F-BLYP scheme.

4.2.1 Cubic Phase

We start the description of ferroelectric perovskites by commenting on the results obtained for the cubic phase. We have examined a set of 13 different compositions AMO_3, all of which have been optimised using a set of 10 Hamiltonians. These include the hybrid F-BLYP series, in which the mixing parameter α is varied from 0.0 to 1.0 in steps of 0.2, and standard Hamiltonians used as reference. The latter are HF, LDA, PW, and B3LYP in its molecular formulation.

The cubic perovskite phase is an ideal polymorph, that we employ in this section only to describe the trends in the calculated properties with hybrid functionals on changing the mixing parameter. Comparison with experiment will be performed later. Here we shall consider separately the structural and electronic properties of the materials.

4.2.1.1 Structural Properties

For each combination of chemical composition and Hamiltonian, we have run a series of calculations with different values of the lattice parameter a. Fitting of the calculated energy curve as a function of the volume with the Birch-Murnaghan equation of state [95, 96] yields the equilibrium lattice parameter a_0 and bulk modulus K_0 reported in Table 1. The variation of a_0 for a selection of materials is shown in Fig. 4. We observe clear trends: a_0 increases systematically on increasing the mixing parameter α within the F-BLYP series, and has a variation of approximately 3% in the series $0 \leq \alpha \leq 1$. The change $\partial a_0/\partial \alpha$ is steeper for low values of α, and less pronounced for $\alpha \rightarrow 1$. The bulk modulus K_0, instead, increases with increasing α, with a change for most materials of ~80% between α=0 and α=1, but as large as 150% in MoO_3. The change $\partial K_0/\partial \alpha$ is larger for $\alpha \rightarrow 1$, and smaller for $\alpha \rightarrow 0$. Increasing the percentage of HF exchange in the functional, therefore, makes the structure more compact and harder, and we may expect this feature to influence the behaviour of the material towards structural distortions.

Table 1 Equilibrium lattice parameter a_0 (Å), and bulk modulus K_0 (GPa), for a selection of cubic perovskites, as a function of the hybridisation parameter α in the hybrid F-BLYP scheme

Compos.		LDA	PW	BLYP	B3LYP	α=0.2	α=0.4	α=0.6	α=0.8	α=1.0	HF
MgO	a_0	4.161	4.244	4.274	4.229	4.234	4.198	4.164	4.133	4.103	4.194
	K_0	181.7	161.3	151.7	166.3	165.2	177.9	190.1	202.7	214.7	182.9
$CaTiO_3$	a_0	3.817	3.884	3.921	3.885	3.890	3.863	3.840	3.820	3.802	3.870
	K_0	213.8	187.2	175.8	194.6	193.0	208.9	223.2	236.5	248.5	218.0
$SrTiO_3$	a_0	3.888	3.960	4.001	3.959	3.965	3.935	3.909	3.887	3.867	3.937
	K_0	207.7	176.8	163.3	185.0	183.2	201.1	217.2	232.0	245.6	212.3
$BaTiO_3$	a_0	3.953	4.024	4.072	4.033	4.039	4.011	3.987	3.966	3.947	4.020
	K_0	204.7	177.8	162.5	181.6	179.8	195.4	209.7	222.9	235.0	203.9
$CaZrO_3$	a_0	4.084	4.149	4.186	4.155	4.160	4.137	4.117	4.098	4.081	4.150
	K_0	187.8	167.4	157.9	170.1	168.9	178.9	188.1	196.7	205.0	181.4
$SrZrO_3$	a_0	4.133	4.203	4.244	4.208	4.214	4.187	4.164	4.143	4.124	4.197
	K_0	179.4	157.3	147.5	161.4	160.1	171.7	182.0	191.9	201.1	176.1
$BaZrO_3$	a_0	4.167	4.235	4.282	4.249	4.255	4.232	4.212	4.193	4.175	4.250
	K_0	189.3	166.0	154.6	166.9	165.5	175.4	184.8	193.5	201.7	176.5
$NaNbO_3$	a_0	3.960	4.018	4.051	4.008	4.013	3.980	3.951	3.927	3.905	3.962
	K_0	203.7	178.0	168.3	188.2	186.6	205.4	222.9	238.7	235.1	226.7
$KNbO_3$	a_0	3.996	4.063	4.103	4.057	4.063	4.028	3.998	3.972	3.949	4.013
	K_0	197.4	172.1	158.9	182.5	181.0	200.5	218.8	235.6	251.0	221.5
$KTaO_3$	a_0	3.938	3.992	4.018	3.978	3.982	3.951	3.923	3.900	3.881	3.941
	K_0	144.7	146.4	155.4	156.6	156.8	164.8	176.0	187.7	208.5	189.8
MoO_3	a_0	3.806	3.853	3.880	3.833	3.838	3.798	3.766	3.743	3.740	3.767
	K_0	230.3	195.0	195.7	220.9	219.3	248.0	290.8	342.0	490	396
WO_3	a_0	3.777	3.807	3.814	3.779	3.782	3.740	3.703	3.673	3.650	3.696
	K_0	184.8	183.5	257.0	186.1	186.6	194.9	207.8	225.3	250.7	274.3
ReO_3	a_0	3.725	3.770	3.806	3.740	3.745	3.690	3.645	3.609	3.579	3.626
	K_0	172.6	167.4	164.1	172.4	172.2	193.2	217.5	249.3	275.2	259.6

Fig. 4 Variation of the calculated equilibrium lattice parameter of cubic perovskites with the mixing parameter in the F-BLYP series. *Open symbols* refer to standard formulations of the Hamiltonian, as indicated

4.2.1.2 Electronic Properties

We analyse how the electronic properties of perovskite-structured materials change as a function of the mixing parameter α by making use of the model TB Hamiltonian, as detailed earlier. In particular, we examine the calculated band-structure of the materials along the Γ-X direction of reciprocal space, from which we can evaluate the effective parameters $\Delta\alpha$ and β.

The band structure of cubic $KNbO_3$ along the Γ-X direction, calculated using the ten Hamiltonians described above, is reported in Fig. 5. We notice

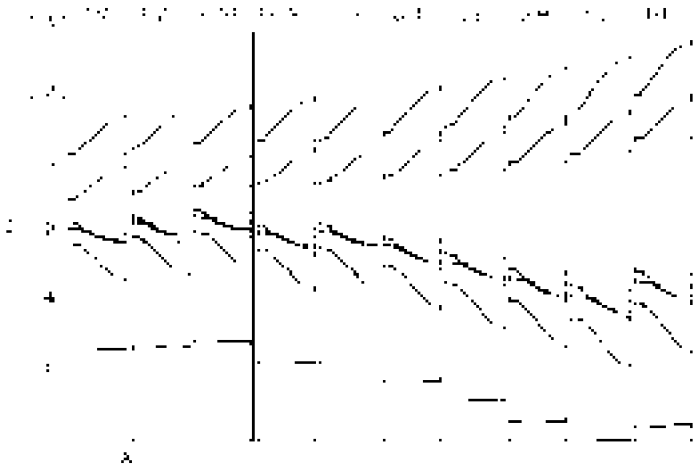

Fig. 5 Calculated band structure for cubic $KNbO_3$ along the Γ-X direction of reciprocal space, as a function of the Hamiltonian. The values 0.2–1.0 indicate the mixing parameter α in the F-BLYP scheme

that the *shape* of the bands is very similar in each case, which is a strong indication that the Nb-O bonding is qualitatively similar. There are, however, important quantitative differences; the most clearly noticeable is the amplitude of the band gap ($\Delta\alpha$ in the TB notation), that increases on increasing the amount of HF exchange in the hybrid functional. Band-widths also change; as we have seen above, this feature is an indication of how effective the Nb-O covalent interactions are in the solid.

For each material reported in Table 1, and for each Hamiltonian, we have calculated the band structure in the equilibrium geometry; for $KNbO_3$ we have also repeated the calculation at a common structure with a=4.03 Å for all the Hamiltonians. Following the description given earlier, from the ab initio band structure we have calculated the following TB parameters:

- $\Delta\alpha$ as the direct band gap in Γ
- $\beta^2/\Delta\alpha$ from the dispersion of the valence band π M-O bonding level along the Γ-X segment
- β and $\beta/\Delta\alpha$ as combination of the two parameters above

The values of the TB parameters that reproduce the ab initio band structure are reported in Table 2 for a subset of materials; the others show the same behaviour. The variation of $\Delta\alpha$ and $\beta/\Delta\alpha$ as a function of the mixing parameter of the hybrid functional is also depicted in Fig. 6. Trends are again very clear: on increasing the fraction of HF exchange, the band gap $\Delta\alpha$ increases (the change is higher at the HF end of the series); this feature makes the material more ionic. The parameter $\beta/\Delta\alpha$, that is the TB definition of covalence in the materials, decreases systematically on moving from the pure DFT to the HF end of the series.

To confirm the above results, in Fig. 7 we show a series of difference electron density plots $\Delta(\rho)=\rho(H_i)-\rho(HF)$, taking the HF solution as reference. The plots refer to $KNbO_3$ at the common lattice parameter of a=4.03 Å, and

Fig. 6 Value of the TB parameters $\Delta\alpha$ (*open symbols*) and $\beta/\Delta\alpha$ (*filled symbols*) that reproduce the ab initio band structure in the F-BLYP series, as a function of the mixing parameter α

Table 2 Value of the TB parameters that reproduce the ab-initio band structure in the hybrid F-BLYP series

Compos.	Param.	LDA	PW	BLYP	B3LYP	α=0.2	α=0.4	α=0.6	α=0.8	α=1.0	HF
$SrTiO_3$	$\Delta\alpha$	0.0975	0.0977	0.0961	0.1576	0.1574	0.2272	0.3038	0.3858	0.4734	0.4690
	$\beta^2/\Delta\alpha$	0.0200	0.0179	0.0168	0.0195	0.0194	0.0213	0.0229	0.0242	0.0252	0.0235
	β	0.0442	0.0419	0.0402	0.0554	0.0552	0.0696	0.0835	0.0966	0.1092	0.1051
	$\beta/\Delta\alpha$	0.4531	0.4286	0.4184	0.3518	0.3507	0.3065	0.2749	0.2504	0.2306	0.2241
$BaTiO_3$	$\Delta\alpha$	0.0795	0.0821	0.0814	0.1396	0.1396	0.2055	0.2783	0.3564	0.4386	0.4383
	$\beta^2/\Delta\alpha$	0.0167	0.0153	0.0144	0.0166	0.0165	0.0181	0.0193	0.0202	0.0207	0.0198
	β	0.0365	0.0355	0.0343	0.0481	0.0480	0.0610	0.0732	0.0847	0.0953	0.0931
	$\beta/\Delta\alpha$	0.4585	0.4320	0.4210	0.3446	0.3436	0.2968	0.2632	0.2378	0.2174	0.2124
$KNbO_3$	$\Delta\alpha$	0.0683	0.0704	0.0720	0.1210	0.1212	0.1783	0.2419	0.3112	0.3854	0.3879
a=4.03	$\beta^2/\Delta\alpha$	0.0192	0.0188	0.0185	0.0205	0.0204	0.0219	0.0230	0.0238	0.0243	0.0243
	β	0.0362	0.0364	0.0365	0.0498	0.0498	0.0625	0.0745	0.0860	0.0968	0.0970
	$\beta/\Delta\alpha$	0.5303	0.5167	0.5069	0.4111	0.4105	0.3503	0.3081	0.2763	0.2512	0.2502
$KNbO_3$	$\Delta\alpha$	0.0698	0.0692	0.0690	0.1193	0.1192	0.1784	0.2445	0.3175	0.3949	0.3894
	$\beta^2/\Delta\alpha$	0.0200	0.0181	0.0171	0.0199	0.0198	0.0219	0.0237	0.0252	0.0262	0.0248
	β	0.0371	0.0354	0.0343	0.0488	0.0486	0.0625	0.0761	0.0894	0.1017	0.0982
	$\beta/\Delta\alpha$	0.5383	0.5117	0.4974	0.4087	0.4076	0.3505	0.3114	0.2817	0.2575	0.2521
MoO_3	$\Delta\alpha$	0.0317	0.0314	0.0316	0.0664	0.0663	0.1126	0.1690	0.2315	0.3026	0.2994
	$\beta^2/\Delta\alpha$	0.0256	0.0239	0.0229	0.0273	0.0272	0.0306	0.0330	0.0343	0.0354	0.0350
	β	0.0285	0.0274	0.0269	0.0426	0.0424	0.0587	0.0747	0.0892	0.1035	0.1023
	$\beta/\Delta\alpha$	0.8988	0.8726	0.8509	0.6417	0.6403	0.5215	0.4420	0.3851	0.3420	0.3417

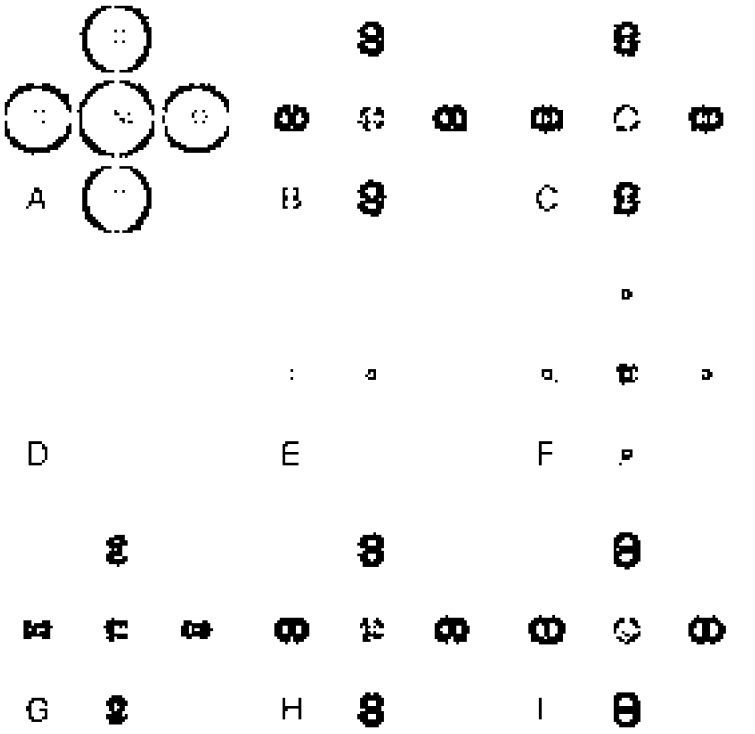

Fig. 7A–I Electron density plots for cubic $KNbO_3$: **A** total electron density for the HF solution; **B to I** difference electron density (H_i–H_{HF}) using the HF solution as reference. Plot B is for PW, C for LDA, D–I for the hybrid F-BLYP scheme with α=1.0 (D), 0.8 (E), 0.6 (F), 0.4 (G), 0.2 (H), 0.0 (I)

are drawn in a plane containing Nb in the centre, and four of its six nearest neighbour oxygens. In a purely ionic description (as for the solution at the Γ point of reciprocal space), all the valence electrons would be located in O-2p levels, with empty Nb-4d levels. The more electrons populate the Nb-4d states, the more the solution is covalent. Figure 7 confirms the trend of $\beta/\Delta\alpha$ described earlier: on decreasing the fraction of HF exchange in the hybrid functional, the Nb-4d population increases, and is maximum for the pure DFT (no HF exchange) solution. Within the same fraction of HF exchange, variations due to a different correlation or type of DFT exchange functional are much smaller; results for B3LYP and $F_{0.2}$-BLYP, $F_{1.0}$-BLYP and HF are indistinguishable; among the pure DFT functionals examined, the difference between LDA, PW and BLYP ($\equiv F_0$-BLYP) are much smaller than those caused by a change in the fraction of HF exchange.

The trends in the structural properties described earlier can be rationalised in terms of the electronic structure: the higher electronic polarisabil-

ity for low values of the mixing parameter contributes to decreasing the bulk modulus, while the increased ionicity obtained on increasing the mixing parameter makes the materials harder.

Results reported in Table 2 and Fig. 6 can also be effectively employed to compare the behaviour of perovskite materials with different composition. Independently of the Hamiltonian employed in the calculations, we notice that on increasing the formal charge of the octahedral ion M, the band gap $\Delta\alpha$ decreases, while the covalence parameter $\beta/\Delta\alpha$ increases. The highest electronic polarisability is given by the $M^{6+}O_3$ oxides (MoO_3), followed by $A^+M^{5+}O_3$ ($KNbO_3$), while $A^{2+}M^{4+}O_3$ ($BaTiO_3$) is more ionic and has the lowest electronic polarisability. It is also of interest to notice that $BaTiO_3$ and $SrTiO_3$ show small differences, due to the different equilibrium lattice spacing and hence Ti-O distance, but results are indicative that the Ti-O interaction has the same qualitative and quantitative features in both materials. A more complete comparison of different perovskites, although limited to the HF solution, can be found in [73]. The similar behaviour of Ti in different $ATiO_3$ perovskites is confirmed by calculations of its effective (Born) charge Z^*_{Ti}, which embodies the electronic rearrangement upon structural distortions; Z^*_{Ti} shows only minor variations in Ca, Sr, Ba and Pb-containing perovskites [97].

Different degrees of ionicity can modify the value of the calculated equilibrium lattice parameter. In a very ionic solid, such as MgO (added in Table 1 for comparison) or $BaTiO_3$ and $SrTiO_3$ in the perovskite-structured compounds, the calculated net charges with different Hamiltonians are very similar; within this class of compounds, the LDA lattice parameter is the smallest, and HF the largest [98]. In partially covalent materials, instead, the different Hamiltonians yield noticeably different net charges, which modify the Madelung field in the solid. In this situation, the highly ionic HF solution generates a much higher Madelung field, which is an important contribution to the bonding in the solid, and contracts the equilibrium structure. The HF lattice parameter a_0 for the most covalent transition metal oxides reported in Table 1 is always smaller than the LDA value of a_0. In Fig. 8 we

Fig. 8 Relative value of the optimised lattice parameter a_0 for different cubic perovskites with respect to the HF solution, within the F-BLYP scheme

report the difference $\Delta a_0 = a_0\ (H_i) - a_0(HF)$: on increasing the covalence of the solution, the relative value of the DFT equilibrium lattice parameter compared to the HF is shifted to higher values. We have in fact $\Delta a_0(MoO_3) > \Delta a_0\ (KNbO_3) > \Delta a_0(Ba,SrTiO_3)$. This feature of transition metal oxides, therefore, challenges a commonly accepted belief, relating to the overestimation of the lattice parameter with HF calculations, which is based on earlier studies of main group elements [98].

4.2.2 Pseudocubic Phase

We now examine results concerning ferroelectric-like (FE) distortions in a pseudocubic perovskite phase, in which the oxygen sublattice is kept fixed in its undistorted cubic coordinates, and only the transition metal ion M displaced within its octahedron. The pseudocubic is another idealised phase, for which no direct comparison with experiment can be made, but it enables us to compare different functionals in describing structural distortions. For each combination of composition and Hamiltonian reported in Table 3, we examined an FE distortion, in which the M ion is displaced along the [001] direction. Each phase is based on the equilibrium lattice parameter for the cubic phase (Table 1). This idealised distortion makes reference to the tetragonal phase of FE materials such as $BaTiO_3$ and $KNbO_3$ [99].

In Table 3 we report the equilibrium displacement Δ_M of M from its cubic position, and the energy associated with the distortion, E_0.

We first compare the results yielded by different Hamiltonians. The distortion profile of Nb along the FE [001] direction in $KNbO_3$, calculated with all ten Hamiltonians under investigation, is shown in Fig. 9. In each case, we

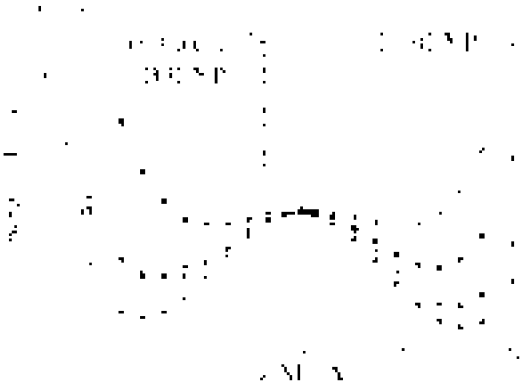

Fig. 9 Energy profile for a pseudocubic FE [001] distortion of Nb in $KNbO_3$. The *right side* of the diagram (z>0) reports results for the F-BLYP series; the *left side* (z<0) the results for standard DFT functionals and for HF

Table 3 Equilibrium displacement Δ_M (Å) of the M ion in its octahedron in pseudocubic [001] FE distortion, and energy gain E (Hartree per formula unit) for different Hamiltonians. α reports the mixing parameter in the hybrid F-BLYP functionals

Compos.		LDA	PW	BLYP	B3LYP	α=0.2	α=0.4	α=0.6	α=0.8	α=1.0	HF
$SrTiO_3$	Δ_M	0	0.0002	0.0001	0.0023	0.0081	0	0	0	0	0
	E	0	6E−11	3E−11	1.5E−7	1.5E−6	0	0	0	0	0
$BaTiO_3$	Δ_M	0	0.0007	0.0312	0.0411	0.0453	0	0.0055	0.0054	0	0.0005
	E	0	2E−8	2.3E−6	5.9E−6	7.2E−6	0	1.2E−6	2.2E−6	0	2E−8
$SrZrO_3$	Δ_M	0	0	0.00112	0	0	0	0	0	0	0
	E	0	0	1.6E−7	0	0	0	0	0	0	0
$KNbO_3$	Δ_M	0.084	0.135	0.137	0.150	0.143	0.145	0.115	0.127	0.087	0.142
	E	2.05E−4	1.30E−3	9.7E−4	1.60E−3	2.00E−3	1.75E−3	1.18E−3	8.65E−4	2.24E−4	1.03E−3

find that the distortion is characterised by a double-well profile, as expected since $KNbO_3$ is a prototypical FE material. The extent of the Nb displacement, and the associated energy gain, however, differ by one order of magnitude among the Hamiltonians.

Earlier we described the electronic rearrangement that accompanies the FE distortion using the model TB Hamiltonian: the Nb off-centring is accompanied by the formation of a Nb-O bond that was symmetry-forbidden in the cubic phase. The energy effectiveness of this bond scales as $\beta^2/\Delta\alpha$; on purely electronic grounds, therefore, expect a trend similar to that shown in Fig. 6 for the cubic phase. However, the bond distance between Nb and one oxygen becomes shorter during the distortion, giving rise to short-range repulsion that opposes the Nb off-centring. The equilibrium value of the Nb displacement is a compromise between the gain in one-electron energy, and the loss due to short-range repulsion.

The LDA Hamiltonian, despite having the largest value of $\beta/\Delta\alpha$ (i.e. highest Nb-O covalence) among the Hamiltonians examined, yields the smallest distortion, indicative of a very high short-range repulsion in the equilibrium structure of the cubic phase (the small LDA lattice parameter is consistent with this finding). As a result, the ability of the LDA functional to yield structural distortions is underestimated, compared to all the other Hamiltonians. In absolute terms, this feature is already known from the literature [75]: at the calculated lattice parameter for the cubic phase, LDA is unable to predict a stable FE phase for $BaTiO_3$.

In the F_α-BLYP series, the distortion shows a maximum around a value of the mixing parameter α=0.2, and decreases on both sides; $F_{0.2}$-BLYP and B3LYP are the functionals that give maximum values of Δ_M and E_0. Surprisingly, given the different features of the M-O bonding, HF, PW and BLYP calculations yield an almost identical energy profile. We observed a similar trend in $BaTiO_3$ and $SrTiO_3$, although the energy gained in the distortion is much smaller in the titanates, consistently with the larger band gap and lower $\beta/\Delta\alpha$ parameter compared to $KNbO_3$.

To investigate further the distortion, in Fig. 10 we report the maximum distortion energy E_0 for the pseudocubic FE [001] distortion of $BaTiO_3$ and $KNbO_3$, within the F-BLYP series. In both cases, the curves display two distinct maxima, the first for mixing parameter α=0.2, and the second at higher values of α, indicative of two different mechanisms operating in the distortion. To explain this result we make use of Figs. 6 ($\beta/\Delta\alpha$), 7 ($\Delta\rho$) and 8 (Δa_0). The equilibrium position, as we have already stated, is achieved as a compromise between short-range repulsion and energy gain due to covalence. The trend in $\beta/\Delta\alpha$ shown in Fig. 6 indicates that the "covalent driving force" is highest at the pure DFT end of the hybrid series, and decreases on increasing the component of HF exchange. At the same time, by increasing the ionicity of the material, inclusion of HF exchange in the hybrid functional depopulates the M-d AOs (see Fig. 7), reducing the effective size of the M

Fig. 10 Distortion energy (Ha/f.u.) for the pseudocubic FE [001] distortion of $BaTiO_3$ and $KNbO_3$ (the value for $BaTiO_3$ has been multiplied by 100 to fit the same energy scale) as a function of the mixing parameter in the F-BLYP series

ion. This contraction effect reduces the M-O short-range repulsion, allowing a larger displacement of M in its octahedron, and hence also causing an increase of the energy gain E_0. At low values of the mixing parameter the decreased repulsion prevails, and the values of Δ_M and E_0 increase on passing from α=0 to α=0.2. On further increasing the mixing parameter, a third structural component comes into play: the equilibrium lattice parameter a_0 shrinks on increasing α, reducing the M-O spacing. Since a_0 is due to A-O and O-O contacts, as well as M-O, the contraction of a_0 is largely complementary to the depopulation of the M-d AOs. When the octahedral "cage" formed by the six nearest neighbour oxygens around M contracts, it leaves less space available for the M off-centring. With the decrease in M-O covalence, the new M-O bond ceases to be the driving force for the distortion, leaving place to a "rattling" mechanism, in which a highly ionic but smaller M ion is smaller than the octahedral cage in which it is located. This second mechanism prevails at the HF-end of the F-BLYP hybrid functionals. This behaviour suggests that on varying the mixing parameter α, the relative sizes of A, M and O ions of the perovskite structure changes, giving rise to the double-maximum profile displayed in Fig. 10. The behaviour reported in Fig. 8 (Δa_0) confirms this finding: the relative size depends systematically on the ionicity of each ion, and can vary both in sign and modulus. Further work, including the binary component oxides AO and MO_2 in which the A-O and M-O bond distances are individually optimised, is however necessary to quantify the importance of covalence, ionic size of M and lattice parameter in determining the complex distortion profile of Fig. 10.

4.2.3 Tetragonal Phase

In the previous sections we have used two idealised phases of FE perovskites to describe the main electronic and structural features of the solution yielded by different hybrid functionals. We now examine a fully distorted tetragonal phase, which enables us to compare the calculated results with experimental data.

The tetragonal perovskite phase is the stable polymorph of $BaTiO_3$ and $KNbO_3$, in a temperature range between the cubic and orthorhombic modifications (393K>T>278 K in $BaTiO_3$ [100], 708K>T>498 K in $KNbO_3$ [101]).

In our calculations we have performed a full geometry optimisation of the tetragonal phase. The structural parameters are the a and c lattice vectors, and the z coordinate of each symmetry unique ion (M, A, one axial (O_1) and one equatorial (O_2) oxygen) in the unit cell. The lattice parameters have been re-defined to give the unit cell volume $V=a^2\,c$, and the ratio c/a; we further relate the volume to that optimised for the cubic phase, $\upsilon=V/V_0$. Given the increased computational cost of this study, only $BaTiO_3$ and $KNbO_3$ have been investigated in the tetragonal phase. For both materials, and for each of the ten Hamiltonians examined, we have performed a series of geometry optimisations of the internal coordinates at different values of the structural parameters υ and c/a. These span the range of $0.95<\upsilon<1.15$, and $0.99<c/a<1.09$. For each value of υ, the equilibrium energy for the different c/a ratios examined has been fitted with a parabolic function (in each case, the residuals are 10^{-10} Ha or smaller) to yield the equilibrium energy at the value of υ examined. The points of the curve $E(\upsilon)$ thus collected have then been used in a Birch-Murnaghan equation of state to calculate the volume υ_0 corresponding to the global minimum; we do not report the value of the bulk modulus K_0 for the distorted phase, as we have not collected enough volumes to ensure a low numerical noise for this observable. A single energy point calculation has been performed for the equilibrium tetragonal structure to generate the corresponding electronic density.

In Table 4 we report the structural parameters that define the equilibrium tetragonal structure for each Hamiltonian examined. In addition, we report the value of the spontaneous polarisation **P** calculated at both equilibrium and experimental structures of the two phases. Comparison with experiment [100, 102–104] enables us to identify the functional that best describes the fully distorted phase. As described in the previous sections, accurate results are achieved in the calculations only when the electronic, structural and distortional properties of the material are reproduced simultaneously by the Hamiltonian under investigation. We have shown earlier that each of these observables varies appreciably as a function of the mixing parameter in the hybrid F-BLYP series. The tetragonal phases of $BaTiO_3$ and $KNbO_3$ provide

Table 4 Equilibrium structure for the tetragonal phase of $BaTiO_3$ and $KNbO_3$ for different Hamiltonians. α represents the mixing parameter in the hybrid F_α-BLYP functionals. V is the equilibrium volume ($Å^3$), υ_0 the ratio between optimised volume of tetragonal and cubic phases, Z the fractional coordinates, **P** the macroscopic polarisation (Cm^{-2}) calculated at the experimental and optimised geometries

	LDA	PW	BLYP	B3LYP	α=0.2	α=0.4	α=0.6	α=0.8	α=1.0	HF	Expt
$BaTiO_3$											
V	61.70	65.86	69.12	67.38	67.80	64.54	62.97	62.89	61.52	66.25	64.98
υ_0	0.999	1.011	1.024	1.027	1.030	1.000	0.994	1.008	1.005	1.020	
c/a	0.998	1.023	1.051	1.053	1.032	1.033	1.013	1.013	1.004	1.032	1.011
Z_{Ba}	−0.498	−0.490	−0.480	−0.481	−0.485	−0.474	−0.491	−0.493	−0.498	−0.489	0.500
Z_{Ti}	0.004	0.026	0.037	0.037	0.033	0.029	0.023	0.019	0.008	0.029	0.022
Z_{O1}	0.498	0.481	0.469	0.468	0.470	0.474	0.485	0.485	0.496	0.473	0.486
Z_{O2}	−0.001	−0.006	−0.008	−0.008	−0.008	−0.008	−0.002	−0.003	−0.001	−0.005	−0.010
$\mathbf{P}_{expt}$	0.3173	0.3179	0.3180	0.3108	0.3106	0.3020	0.2926	0.2830	0.2739	0.2729	0.27
$\mathbf{P}_{opt}$	0.0426	0.3159	0.4449	0.4467	0.4098	0.3603	0.2504	0.2113	0.0741	0.3199	0.27
$KNbO_3$											
V	64.05	68.98	73.06	68.10	70.68	67.66	68.32	64.11	62.97	68.79	64.91
υ_0	1.004	1.028	1.058	1.020	1.054	1.035	1.069	1.023	1.022	1.064	
c/a	1.020	1.054	1.089	1.040	1.095	1.062	1.078	1.034	1.035	1.089	1.017
Z_K	−0.484	−0.475	−0.464	−0.475	−0.464	−0.471	−0.468	−0.481	−0.483	−0.466	0.500
Z_{Nb}	0.029	0.039	0.045	0.040	0.046	0.042	0.040	0.035	0.034	0.048	0.023
Z_{O1}	0.489	0.473	0.461	0.476	0.459	0.468	0.455	0.476	0.477	0.457	0.483
Z_{O2}	−0.014	−0.016	−0.018	−0.014	−0.020	−0.017	−0.025	−0.015	−0.014	−0.016	−0.019
$\mathbf{P}_{expt}$	0.3855	0.3874	0.3856	0.3795	0.3793	0.3711	0.3619	0.3521	0.3423	0.3415	0.37
$\mathbf{P}_{opt}$	0.4029	0.4396	0.3457	0.4604	0.3487	0.4224	0.3765	0.4866	0.4625	0.3832	0.37

Fig. 11 Variation of the macroscopic polarisation $\mathbf{P}(Cm^{-2})$ in the optimised tetragonal phase of $BaTiO_3$, as a function of the mixing parameter α in the hybrid F-BLYP series

therefore a complete test for the ability of hybrid functionals to describe $d^{(0)}$ transition metal oxides.

The variation of the calculated value of $\mathbf{P_{opt}}$ for $BaTiO_3$, as a function of the mixing parameter in the hybrid F-BLYP series, is shown in Fig. 11. We observe a steady decrease of **P** as the HF-exchange component in the hybrid functional is increased, in agreement with the degree of Ti-O covalence in each solution. This result confirms that the polarisation of the ferroelectric phase is dominated by the electronic polarisability, as described earlier. Correspondence with experimental results is achieved for a value of α~0.55.

The FE distortion in the fully optimised tetragonal phase of $BaTiO_3$ is further described in Fig. 12. The distortion is characterised by a shortening of the Ti-O_1 bond length and a change of the c/a ratio from the cubic value of

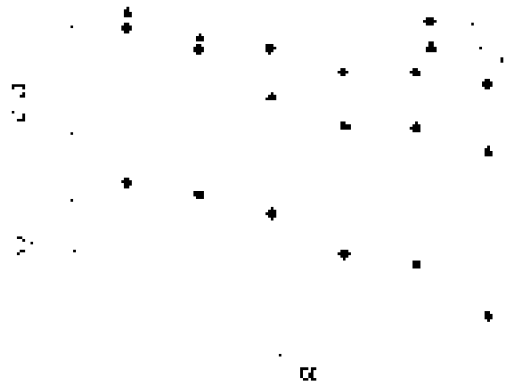

Fig. 12 Variation of the c/a ratio, of the ratio between optimised and experimental volume (V/V_{exp}) and of the parameter ΔZ (in fractional coordinates) in the optimised tetragonal phase of $BaTiO_3$, as a function of the mixing parameter α in the F-BLYP scheme

1. We characterise the shortening of the Ti-O_1 bond by plotting the sum (ΔZ) of the displacement of Ti along +z (towards O_1), and of O_1 along the −z direction of the tetragonal unit cell (towards Ti), in fractional coordinates. We see that on increasing α in the hybrid functional, the extent of the distortion decreases: in the F-BLYP series, ΔZ varies from 0.068 to 0.012; the c/a ratio from 1.051 for α=0 to 1.004 for α=1. For α~0.5/0.6 there is a close correspondence of both structural (c/a and ΔZ) and electronic (**P**) parameters between calculated and experimental values. Similar trends occur in $KNbO_3$, although in this case the polarisation appears to be overestimated across the whole F-BLYP series when compared to the experimental result. Results obtained here for $KNbO_3$ differ from those of reference [58]; we have employed an all-electron basis set, as opposed to the effective core pseudopotential of [58], which yields larger values of the equilibrium volume, and hence smaller values of **P**.

It is also of interest to observe that in the fully optimised tetragonal phase, the double maximum profile in the distortion energy as a function of the mixing parameter α, described for the pseudocubic phase, is no longer present. Removing the structural constraint of the cubic phase, the equilibrium structure is allowed to adapt to the relative ionic sizes, and its features are characterised only by the relative covalence in the Ti-O bonding (the $\beta/\Delta\alpha$ TB parameter shown in Fig. 6). The double minimum profile of Fig. 10 is therefore introduced in the constrained optimisation corresponding to the pseudocubic phase.

4.3 Spin-Spin Interactions in Magnetic Compounds

4.3.1 Perovskite-Structured $KMnF_3$

As a first example of a magnetic compound, we describe the calculated properties of $KMnF_3$. This material shares the same perovskite structure described above for the ferroelectric oxides, but contains in the octahedral sites an open-shell $Mn^{2+}(d^5)$ ion. The structure has cubic symmetry, with a=4.19 Å [105].

The observable of interest, in this case, is the relative spin orientation on neighbouring Mn ions, which will be investigated using a model Ising Hamiltonian, as described earlier.

Three magnetic phases have been studied, shown in Fig. 13: these are the ferromagnetic phase (FM), where all the Mn ions have the same spin (say α), and two antiferromagnetic (AFM) phases. In the first, formed by alternating (111) planes with opposite spin, each α-spin Mn ion is surrounded by six nearest neighbour Mn ions with β-spin; in the second, formed by

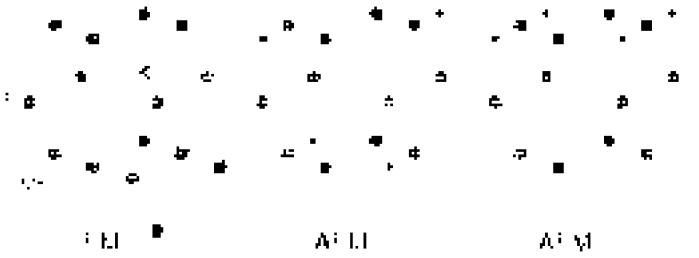

Fig. 13 Magnetic phases of $KMnF_3$. *Black and white small spheres* represent spin up and down Mn ions; *the dashed lines* in the AFM structure connect Mn ions with the same spin in (111) planes

(001) planes with opposite spin, each α-spin Mn ion has four nearest neighbour Mn ions with α-spin and two with β-spin.

All the Hamiltonians describe Mn^{2+} as a high spin d^5 ion with S_z=5/2. The calculated band-structure in the F-BLYP series is shown in Fig. 14; comparison with the band-structure of $KNbO_3$ (Fig. 5) shows that the bandwidths are much smaller in $KMnF_3$, indicative of the stronger ionic character in the latter compound. A summary of the equilibrium lattice parameters corresponding to a set of ten different Hamiltonians (the same employed for the ferroelectric perovskites, with the exception of PBE replacing PW) is reported in Table 5, together with a description of net charges (q) and magnetic moments (μ) of the constituent ions in the equilibrium geometry. The same trends in ionicity described for the cubic perovskites are found here

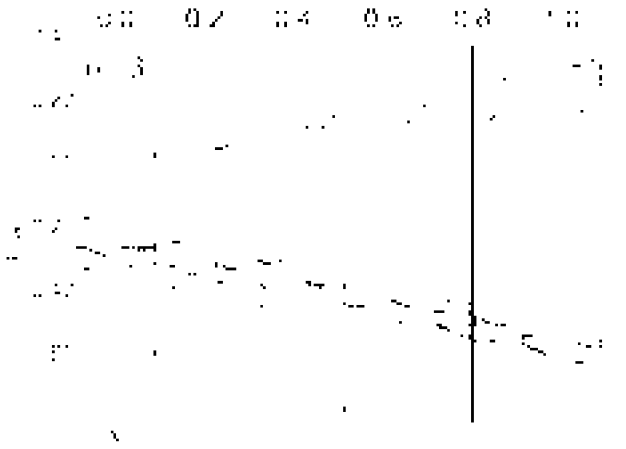

Fig. 14 Band structure for FM-$KMnF_3$ along the Γ-X direction of reciprocal space, as a function of the mixing parameter α in the F-BLYP scheme. Bands for the majority and minority spins are shown separately

Table 5 Structural, electronic and geometric parameters of $KMnF_3$ at the equilibrium geometry for different Hamiltonians. α reports the mixing parameter in the hybrid F-BLYP functionals. a_0 is the lattice parameter (Å), ΔE (mHa) the energy difference between AFM and FM phases at the experimental and optimised (a_0) lattice parameters, J (Kelvin) the corresponding coupling constant. For each ion, q and μ are net charge and spin moment (|e|)

	LDA	PBE	BLYP	B3LYP	α=0.2	α=0.4	α=0.6	α=0.8	α=1.0	HF	Expt
a_0	4.13	4.28	4.31	4.27	4.28	4.25	4.22	4.18	4.15	4.28	4.19
Δa_0(%)	−1.42	+2.12	+2.86	+1.98	+2.15	+1.43	+0.72	−0.24	−0.95	+2.21	
$\Delta E(a_{exp})$	7.992	6.438	7.732	3.491	3.605	2.339	1.753	1.374	1.086	0.594	1.75
$J_{se}(a_{exp})$	33.64	27.10	32.56	14.70	15.18	9.85	7.38	5.78	4.57	2.50	7.30–7.40
$\Delta E(a_0)$	10.099	5.268	5.855	2.878	2.930	1.971	1.619	1.502	1.222	0.403	1.75
$J_{se}(a_0)$	42.52	22.18	24.65	12.12	12.34	8.30	6.82	6.33	5.14	1.70	7.30–7.40
$J(a_0)/J_{(exp)}$	5.7	3.0	3.3	1.6	1.7	1.1	0.9	0.9	0.7	0.2	
FM											
Mn:q	1.54	1.62	1.62	1.67	1.67	1.70	1.72	1.74	1.75	1.80	
μ	4.75	4.80	4.79	4.85	4.84	4.88	4.89	4.91	4.92	4.95	
F:q	−0.84	−0.87	−0.87	−0.88	−0.88	−0.89	−0.90	−0.91	−0.91	−0.93	
μ	0.08	0.07	0.07	0.05	0.05	0.04	0.04	0.03	0.03	0.02	
K:q	0.98	0.98	0.97	0.98	0.98	0.98	0.99	0.99	0.99	0.99	
μ	0.00	0.00	0.00	0.00	0.00	0.00	0.00	0.00	0.00	0.00	
AFM											
Mn:q	1.51	1.61	1.61	1.66	1.66	1.70	1.72	1.73	1.75	1.80	
μ	4.66	4.75	4.73	4.83	4.82	4.86	4.89	4.90	4.91	4.95	
F:q	−0.83	−0.86	−0.86	−0.88	−0.88	−0.89	−0.90	−0.91	−0.91	−0.93	
K:q	0.98	0.98	0.97	0.98	0.98	0.98	0.99	0.99	0.99	0.99	

for $KMnF_3$, with net charges and magnetic moments increasing on increasing the HF-exchange component in the F-BLYP series. Furthermore, the equilibrium lattice parameter a_0 shows the same behaviour as the most ionic oxidic compounds examined earlier: HF yields the largest value, LDA the smallest, while a_0 decreases along the F-BLYP series.

Net charges are very close to the formal values, and the spin moments show that the five unpaired electrons are almost fully localised on Mn, for each of the Hamiltonians examined. A small polarisation is observed, however, on the F ions of the FM phase, which is responsible for the superexchange interaction along the Mn-F-Mn path [106]. For symmetry reasons, the spin polarisation on F is null in the AFM phase; the Mn-F bonding in the FM and AFM phases is otherwise identical.

The bonding features described above satisfy the conditions of applicability of the Ising model Hamiltonian described above. In the perovskite lattice, direct exchange between next-nearest neighbour Mn ions is negligible, given the long bond distance of ~6 Å; only the superexchange constant J_{se} enters the Ising Hamiltonian. The energy difference (per formula unit) between AFM and FM phases is given by $\Delta E = E_{AFM} - E_{FM} = 6 J_{se} S_z^2$, where $S_z = 5/2$, is the spin moment of the Mn^{2+} ion.

In Table 5 we report the energy difference between FM and AFM phases (ΔE), the calculated value of J_{se} at the experimental and calculated equilibrium lattice parameter, and the ratio J_{calc}/J_{exp} between calculated and experimental values of the coupling constant. All the pure DFT calculations overestimate J_{se}, up to a factor of 5.7 for the LSDA solution; on the other hand, pure UHF calculations underestimate J_{se} by a factor of 5.0. Values in the F-BLYP series interpolate the HF and BLYP extremes, and are therefore closer to the experimental value than either UHF or pure DFT results.

Another piece of information that is available from experiment is the dependence of J_{se} on the Mn-Mn distance [80]; this behaviour has been analysed under the hypothesis that the monovalent cation has no influence on the magnetic structure (supported by our results of Table 5), and by replacing K with larger Rb and Tl ions which modify the lattice parameter of the solid. In the computational model, we simply modify the lattice parameter a of $KMnF_3$. Results are shown in Fig. 15. In each calculated $J(a)$ curve, the cross marks the equilibrium lattice parameter a_0 for the Hamiltonian under investigation. The bold circle marks the experimental values of J_{se} and a_0. Via Fig. 15 we can therefore explore which formulation of the hybrid DFT functional is able to reproduce simultaneously and with highest accuracy the experimental values of lattice parameter and magnetic interaction. Our results indicate that, in $KMnF_3$, a fraction of HF exchange around 70% is required in the hybrid F-BLYP series to satisfy the above requirement. Modifying the mixing parameter may improve the accuracy in one of the two observables, but only at the expenses of the other.

Fig. 15 Energy difference (mHa/f.u.) between FM and AFM phases of $KMnF_3$, as a function of the Mn-Mn distance d(Å). In each curve, corresponding to a different functional, the *crosses* mark the equilibrium lattice parameter a_0; the *bold circle* marks the experimental values of J and a_0

4.3.2 Rocksalt-Structured Oxides: MnO and NiO

We shall now examine the performance of hybrid exchange functionals in describing the electronic, structural and magnetic properties of two rocksalt-structured transition metal monoxides, namely MnO and NiO. At variance with the work described in the previous sections, modification of the hybrid functionals within a selected F-XC series has been accomplished here by smaller steps of the mixing coefficient α (of 10%, or sometimes even 5%); even small modifications in the Hamiltonian can cause a change of the ground electronic state, which has dramatic effects on the calculated properties. We need therefore to characterise the boundaries in the behaviour

much more accurately than in the cases of ferroelectric perovskites and $KMnF_3$ described earlier.

4.3.2.1 Electronic Structure

The paradigm magnetic oxide NiO was for many years thought to be a Mott-Hubbard insulator [107], in that metal derived states compose the valence and conduction band edges, separated by a gap of ~4 eV (optical absorption) [108]. LDA calculations [109] support this view of the insulating state, but in the AF_2 magnetic alignment find a gap of less than 0.15 eV, which is much smaller than the experimental value. GGA functionals [110] increase the width of the gap to ~1 eV and preserve the Mott-Hubbard character, while the self-interaction correction method drastically improves many of the computed properties [111]. More recent photoemission experiments on NiO [112] have definitively shown that the insulating character is of the charge-transfer type, in that the valence band edge is composed of oxygen states and the conduction band edge by metal states. All previous calculations are in disagreement with this finding, but UHF calculations [113] yield a highly ionic Ni($3d^8$), charge transfer ground state. The work discussed here is by no means the first to apply hybrid functionals to NiO, for Bredow and Gerson [60] and Moreira et al. [61] have employed a variety of schemes which generally show systematic improvement in the agreement with experimental data. To our current knowledge, there is no comparable hybrid functional study of MnO, although previous DFT calculations have found an energy gap ~1.4 eV in both LDA and GGA methods [114, 115].

In Table 6 we report the calculated electronic structures of NiO in the ferromagnetic (FM) and antiferromagnetic (AF_2) spin alignments, based on the F-PW scheme, at a fixed lattice constant of 4.2 Å, which is close to the measured low temperature value of 4.1705 Å [116]. Results as a function of the mixing parameter α show the same qualitative trend discussed for $KMnF_3$. Within the hybrid F-PW scheme, the AF_2 spin alignment is predicted to be a largely ionic, d^8 charge-transfer insulator from the correlated UHF limit (α=1.0) down to α=0.3. Within this range the Fermi energy, e_F, varies from −9.52 eV to −5.02 eV, the local spin moment from 1.92 μ_B to 1.76 μ_B, the filled-to-unfilled energy gap from 14.2 eV to 6.4 eV and the weight of O(p) states at e_F from 92% to 71%. Between 30% and 20% exact exchange there is a change in the nature of the gap states, for at 20% exact exchange the weight of O(p) states at e_F is 41%, indicating an essentially Mott-Hubbard system, but the change in the ionic charge is less than 0.5% and that of the local moment less than 4%. The change from charge transfer to Mott-Hubbard is not abrupt, but rather a continuous evolution in which the filled Ni-3d bands are shifted at higher energy on decreasing the percentage of HF

Table 6 Variation of lattice constant a_0(Å), bulk modulus K_0(GPa), ionic charge q(*e*), spin moments $\mu(\mu_B)$ in NiO, with both composition of the hybrid functional and magnetic state

	AF_2				FM			
α	a_0	K_0	q	μ_{Ni}, μ_O	a_0	K_0	q	μ_{Ni}, μ_O
UHF	4.2589	209.34	1.878	1.924, 0	4.2629	210.01	1.880	1.930, 0.070
1.0	4.1658	249.18	1.860	1.907, 0	4.1710	250.07	1.864	1.915, 0.085
0.9	4.1732	245.17	1.850	1.897, 0	4.1787	246.09	1.854	1.907, 0.093
0.8	4.1804	241.16	1.837	1.886, 0	4.1865	241.66	1.843	1.897, 0.103
0.7	4.1871	237.46	1.822	1.871, 0	4.1935	238.12	1.829	1.884, 0.116
0.6	4.1942	231.80	1.804	1.852, 0	4.2009	234.18	1.813	1.869, 0.131
0.5	4.2015	225.16	1.780	1.827, 0	4.2103	229.11	1.791	1.847, 0.153
0.4	4.2072	220.31	1.750	1.793, 0	4.2192	223.47	1.764	1.819, 0.181
0.3	4.2120	218.14	1.711	1.747, 0	4.2274	218.47	1.730	1.783, 0.217
0.2	4.2158	212.53	1.662	1.681, 0	4.2350	212.82	1.687	1.735, 0.265
0.1	4.2234	201.39	1.600	1.581, 0	4.2458	204.22	1.635	1.677, 0.323
0.0	4.2238	197.41	1.519	1.344, 0	4.2563	157.26	1.510	1.185, 0.236
Expt	4.1705[a]	145–190[b]	-	1.64–1.90[c]				

[a] [116]
[b] [117–118]
[c] [119–121]

exchange in the hybrid functional. Between 20% and 30% HF exchange, the energy of the Ni-3d band becomes higher than that of the O-2p.

For comparison, the B3LYP functional with 20% exact exchange leads to ionic charges and local moments which are within 0.5% of the $F_{0.2}$-PW values, but the O(p) weight at e_F is lower at 30%, and the energy gap smaller by 0.1 eV. In either scheme, for intermediate amounts of exact exchange, the distinction between the overly simplistic Mott-Hubbard and charge-transfer insulator classifications is unclear, since the valence band edge shows evidence of Ni-O hybridisation. As the amount of exact exchange is reduced further, the ionicity and local moment are decreased, though the system remains insulating at the DFT limit (α=0) where the weight of O(p) states at e_F is <10%, the local moment 1.36μ_B and the energy gap 0.8 eV.

There is essentially no change in the electronic structure of the FM spin alignment, which also undergoes a charge-transfer to Mott-Hubbard transition between 30% and 20% exact exchange. The principal difference is that for the FM alignment there is a relative shift of the majority and minority spin bands of 0.5/1.0 eV, which at the DFT limit leads to a filled to unfilled gap of ~0.3 eV for both the majority and minority spin bands, but a *net* gap which is close to zero. The close similarity between the FM and AF_2 electronic structures (except at the DFT limit) is the basis for our use of the computationally less expensive FM alignment in the study of d→d electronic transitions. It is of interest to note that the calculated moments for the AF_2 alignment compare with experimental values of 1.90 μ_B to 1.64 μ_B [119, 120],

which are reproduced at high values of α, whereas the measured strong adsorption edge, ~4 eV [108], if it can be equated with the energy gap, would seem to favour a much lower weight (α~30%).

The moments and charges emerging from F-BLYP calculations are essentially identical to those obtained above with F-PW (the difference is at most 0.02*e*). In agreement with the perovskite-structured compounds, the net charges indicate a steady increase in covalence as we move towards pure DFT exchange, with a net decrease of ~0.35*e* from the essentially ionic UHF ground state across the range. The difference between the Ni spin moments

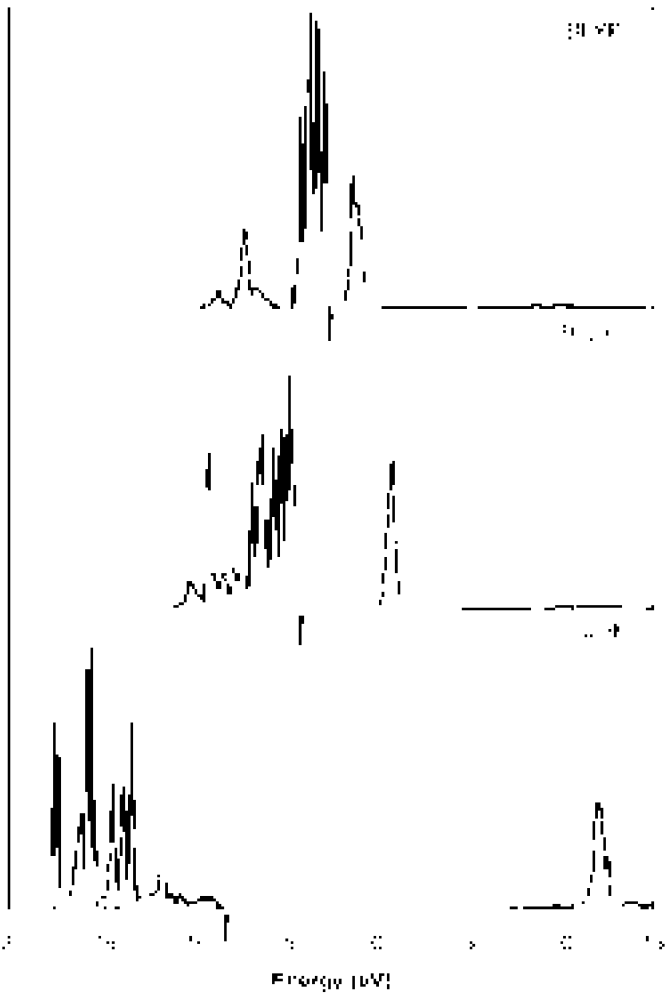

Fig. 16 Projected densities of states, N(E), as a function of energy for AF_2 NiO. *Light line*: oxygen; *dark line*: Ni

in the AF_2 and FM alignments becomes notable at low amounts of exact exchange, which indicates the increasing rôle that the Ni(3d) orbitals play in bonding as the proportion of exact exchange decreases. The band gaps for the AF_1, AF_2 and FM states are always in the order of $\Delta E_g(AF_2) > \Delta E_g(AF_1) > \Delta E_g(FM)$, and vary almost linearly across the F-BLYP series; the B3LYP values are 4.255, 2.574 and 2.411 eV respectively, where the AF_2 value is close to the ~4 eV derived experimentally (in absorption) by Powell and Spicer. At the DFT extreme, both the AF_1 and FM states metallise, whereas the AF_2 state remains insulating with a gap ΔE_g=0.709 eV, in good agreement with previous GGA values. Figure 16 shows the atom projected densities of states (PDOS) in NiO for the UHF, B3LYP and BLYP Hamiltonians.

For comparison, we have calculated the electronic structure of MnO within the F-B3LYP scheme, and at the equilibrium lattice constant corresponding to each functional (Fig. 17). Results are in Table 7. The evolution of the electronic structure with the degree of hybridisation (α) is similar to that described above for NiO. There is a sharp decrease in the energy gap as the weight of exact exchange is decreased, but the AF_2 alignment remains insulating at the DFT limit, with a gap of 1.4 eV. Figure 18 shows that the energy gap in the AF_1 and FM alignments decreases similarly throughout the hybridisation range down to the DFT limit where the AF_1 gap is close to zero, but the FM alignment is conducting. The atom projected densities of states (not shown here) are very similar to those obtained for NiO; the cross-over from oxygen to metal dominance at the Fermi energy again occurs between 30 and 20% exact exchange, but the caveat regarding the usefulness of such

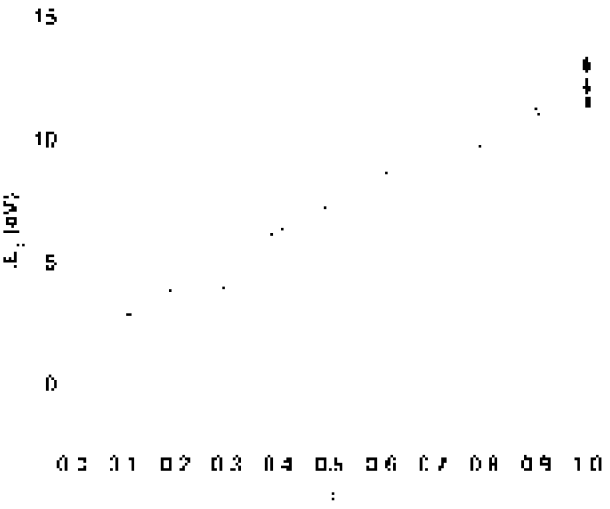

Fig. 17 AF_2 (*empty circles*), AF_1 (*empty triangles*) and FM (*empty squares*) band gaps in MnO as a function of α

Table 7 Variation of lattice constant a_0(Å), bulk modulus K_0(GPa), rhombohedral distortion angle $\Delta\gamma$(°), charge q(*e*), and spin moments $\mu(\mu_B)$, in MnO with both composition of the hybrid functional and magnetic state

	AF_2					FM			
α	a_0	K_0	$\Delta\gamma$	q	μ_{Mn}, μ_O	a_0	K_0	q	μ_{Mn}, μ_O
1.0	4.4190	193.97	+0.1870[a]	1.837	4.878, −0.001	4.4252	195.38	1.835	4.888, 0.112
0.9	4.4273	190.65	+0.2098	1.827	4.871, −0.001	4.4342	192.19	1.825	4.882, 0.118
0.8	4.4355	188.58	+0.2361	1.815	4.863, −0.001	4.4435	190.59	1.814	4.875, 0.125
0.7	4.4430	183.58	+0.2675	1.802	4.853, −0.001	4.4522	185.05	1.801	4.866, 0.134
0.6	4.4509	183.18	+0.2619	1.787	4.840, −0.001	4.4612	185.20	1.787	4.856, 0.144
0.5	4.4575	180.48	+0.3088	1.770	4.824, −0.002	4.4696	183.27	1.771	4.843, 0.157
0.4	4.4635	178.17	+0.3652	1.749	4.802, −0.002	4.4779	182.97	1.752	4.826, 0.174
0.3	4.4693	175.27	+0.4864	1.724	4.774, −0.002	4.4872	180.34	1.730	4.806, 0.194
0.2	4.4738	172.16	+0.6006	1.694	4.734, −0.002	4.4952	179.93	1.704	4.780, 0.220
0.1	4.4771	167.65	+0.7752	1.656	4.674, −0.002	4.5081	176.39	1.672	4.747, 0.253
0.0	4.4742	160.57	+1.1040	1.604	4.567, −0.003	4.4890	140.38	1.602	4.547, 0.250
Exp	4.445[b]	144–162[c]	+0.62[d]		4.58–4.79, 0[e]				

[a] UHF value is +0.1477
[b] [122]
[c] [122–126]
[d] [127]
[e] [119, 121]

simple classifications also applies here. The B3LYP band gaps for the AF_2, AF_1 and FM states are 3.953, 2.855 and 2.052 eV respectively. Again, the B3LYP AF_2 band gap is close to the experimental value ~3.6 eV [128]. Our B3LYP results for MnO and NiO confirm one of the results of a previous study by Muscat, Wander and Harrison [40], namely that the B3LYP functional can potentially act as a useful tool for the prediction of band gaps in transition metal compounds (and in a variety of other materials [40]).

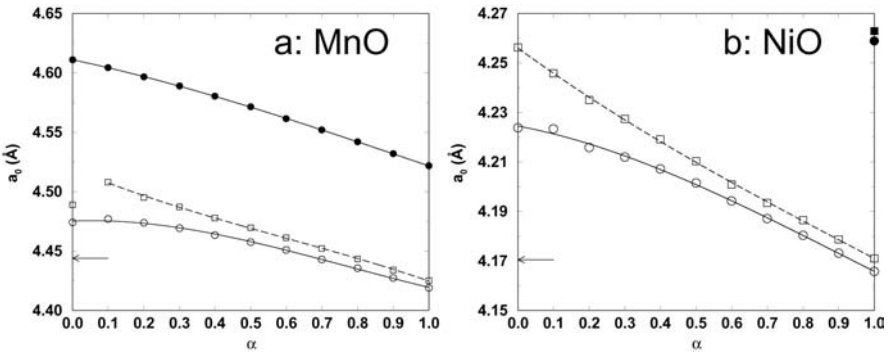

Fig. 18a,b AF_2 (*empty circles*) and FM (*empty squares*) optimised lattice constants, a_0, as a function of α in: **a** MnO; **b** NiO. *Filled symbols* in MnO are for a hybrid exchange without LYP correlation; in NiO for uncorrelated UHF. *Arrows* mark the experimental values

4.3.2.2 Lattice Constant and Bulk Modulus

Both MnO and NiO have AF_2 arrangements at low temperature. Figure 18 shows the variation of a_0 as a function of the hybridisation parameter, α, within the F-BLYP scheme; for the F-BLYP scheme there is a close match to the experimental value at α~0.7. The FM lattice constant follows the AF_2 values from the UHF limit down to α~0.4, but then diverges from the latter, at least up to α~0.1, followed by a sharp fall at the DFT limit with the onset of a conducting state. A similar pattern is found for NiO, although here the fall in a_0 at the DFT limit is absent, despite the metallic FM state. The measured low temperature lattice constants of MnO and NiO suggest an 'optimum' value of α for the lattice constant in the region of 0.7 and 0.9 respectively, certainly well above the value of 0.2 that yields a band gap in close agreement with experiment.

The calculated bulk modulus of MnO and NiO in the FM and AF_2 spin alignments as a function of exact exchange are reported in Tables 6 and 7. Differences between the FM and AF_2 alignment show that there is a small spin-lattice effect, which increases as the weight of exact exchange is reduced, with a sharp fall in the FM value at the DFT limit resulting from the onset on conductivity. The difference between bulk moduli of the magnetic states is less pronounced in NiO than in MnO. The variation in the experimental determination of K_0, of over 11%, makes quantitative estimates somewhat difficult.

4.3.2.3 Magnetic Effects

Table 8 shows the calculated values of J_d and J_{se} for MnO within the F-BLYP series, obtained from the mapping equations given earlier, together with the experimental values derived from the magnon spectra. Also included is the Bloch parameter, $-\partial(\ln J)/\partial(\ln V)$, which characterises the dependence of the interaction upon pressure and has, for a range of materials, been shown to have a value close to 10/3. Two points are evident from the table: first, the sensitivity of the coupling constants to the weight of exact exchange: both J_d and J_{se} show at least a sixfold increase from 100% exact exchange to the DFT limit, and, in the case of J_d, a change in sign from positive to negative between α=0.7 and α=0.8. The latter is not altogether surprising, for ferromagnetic nn spins (J_d>0) are stabilised by strong (more exact) exchange, whereas antiferromagnetic nn spins, which embody the elements of d-d bonding, are stabilised by strong correlation. The second, and perhaps more problematic point, is that the percentages of exact exchange for which the calculated coupling matches experiment differ for J_d and J_{se}. For direct coupling the optimum weight is between 10% and 20%, whereas for superexchange it is between 40% and 60%. To assess the influence of correlation we have derived values of J_d, J_{se} and the Bloch parameter without the inclusion

Table 8 Calculated direct J_d(K) and super-exchange J_{se}(K) coupling constants, fluctuation-corrected mean field Neel temperature, $T_N{}^{mf}$(K) and Bloch constant in MnO

	Becke–HF Hybrid+LYP				Becke–HF Hybrid			
α	J_d	J_{se}	$T_N{}^{mf}$	Bloch	J_d	J_{se}	$T_N{}^{mf}$	Bloch
1.0	1.639	6.327	88.97	3.846	−0.032	2.062	29.00	5.317
0.9	0.968	6.852	96.36	3.735	−0.463	2.185	30.72	5.376
0.8	0.204	7.338	103.19	3.735	−0.867	2.379	33.45	5.420
0.7	−0.624	8.155	114.67	3.722	−1.324	2.750	38.67	5.544
0.6	−1.570	9.093	127.87	3.678	−1.877	2.910	40.92	5.395
0.5	−2.656	10.512	147.82	3.674	−2.386	3.458	48.63	5.331
0.4	−4.286	12.108	170.26	3.706	−2.707	4.541	63.86	5.236
0.3	−5.890	15.176	213.41	3.490	−4.036	5.271	74.12	5.008
0.2	−8.966	19.558	275.03	3.403	−5.005	7.316	102.87	4.634
0.1	−13.085	25.913	364.40	3.286	−6.538	10.887	153.09	4.219
0.0	−15.917	37.903	533.00	1.341	−9.700	17.338	243.82	3.419
Expt	−10[a], −8.9, −8.5	+11[a], +10.3, +9.6	116	≈10/3				

[a] [129–131]

of LYP correlation. As Table 8 shows, correlation increases J_{se} roughly by a factor of 2 with somewhat less influence on J_d. In NiO, whose values are reported in Table 9, the optimum weight for J_d is between 40% and 50%, and for J_{se} between 20% and 30%. It would appear that, within the F-BLYP scheme, there is no single choice of α that describes all components of

Table 9 Variation of direct J_d(K) and super-exchange J_{se}(K) coupling constants, fluctuation-corrected mean field Neel temperature, $T_N{}^{mf}$(K) with composition of the hybrid functional in NiO

α	J_d	J_{se}	$T_N{}^{mf}$
UHF	8.601	39.556	89.00
1.0	9.366	56.918	128.07
0.9	9.912	63.298	142.42
0.8	10.736	70.674	159.02
0.7	11.691	80.339	180.76
0.6	13.881	95.065	213.90
0.5	15.879	114.719	258.12
0.4	18.804	141.972	319.44
0.3	22.668	186.187	418.92
0.2	28.542	248.948	560.13
0.1	36.392	353.586	795.57
0.0	85.175	670.744	1509.17
Exp	<+16.2[a]	+229.8 +197.28[a]	525

[a] [132, 133]

magnetism correctly within even one material. The Fock-35% proposed by Moreira et al. for NiO [60] seems to be a compromise of the optimal value for the J_d and J_{se} requirements.

Turning now to the disorder transition, we have estimated the Néel temperature, T_N, from the calculated values of J_d and J_{se}, using eq. 20. For the AF_2 spin alignment, T_N depends only on J_{se}, so that if the statistical approximation outlined earlier is sound, the optimum weight of exact exchange to match the measured T_N for MnO should coincide with that for J_{se} derived from the magnon spectrum. Table 8 shows that this is indeed the case, for the optimum weighting to match the experimental T_N of 116 K, is ~70%. The consistency of the magnon spectrum and the disorder transition lends credence to the use of the Ising Hamiltonian, at least in this case.

Below the Néel temperature, both AF_2 MnO and NiO undergo a rhombohedral contraction as a result of the interaction between adjacent antiferromagnetically-aligned {111} cation planes of ferromagnetically-aligned spins. The magnitude of this distortion is defined in terms of the change ($\Delta\gamma$) in the cell angle, and for MnO it has been measured at 8 K by neutron scattering [127]. Pask et al. [115] argued that the direct nn interaction is the predominant interaction that drives the rhombohedral distortion. If this argument is correct, then the optimum weight of exact exchange to match the experimental distortion should coincide with that to match J_d, assuming comparable values of the restoring c_{44} elastic constant across the F-BLYP series. The calculated c_{44} elastic constant ranges from 147GPa for UHF to 114GPa for B3LYP [61], showing a small change compared to that in J_d. Figure 19

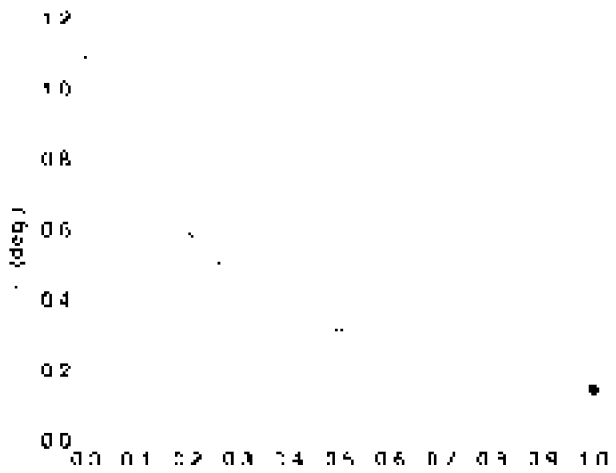

Fig. 19 Rhombohedral distortion angle, $\Delta\gamma$, as a function of α in MnO. *Filled symbol* is for UHF. An *arrow* marks the experimental value

shows the calculated value of $\Delta\gamma$ for MnO as a function of hybridisation within the F-B3LYP scheme. At high values of α, $\Delta\gamma$ is too small, roughly by a factor of two, whereas as the DFT limit is approached $\Delta\gamma$ is much too large. The optimum weight based on the measured distortion of 0.62° is approximately 20%, which is close to that which matches the calculated J_d to that derived from the magnon spectra. Pask et al., in their study find LDA and GGA optimised distortions of 1.68 and 1.69° respectively.

4.3.2.4 d→d Excitations

Crystal field excitations are a fundamental property of the rocksalt-structured transition metal oxides, and their measurement and calculation reveal important aspects of the physics of these systems. In strongly ionic solids d→d excitations are highly local in the manner of Frenkel excitons and always Laporte forbidden ($\Delta l=0$), so that they are generally weak. In the case of NiO both one- and two-electron spin allowed excitations [134] have been observed below the strong absorption edge which is now widely accepted as due to O(p)→Ni(d) charge transfer excitations [135]. From a theoretical point of view, it is clear that d→d excitation energies cannot be estimated from the ground state eigenvalue spectrum (density of states) in view of the strong renormalisation that accompanies orbital re-ordering. On the other hand, they are obtained straightforwardly from direct calculations, i.e. from the differences in total energy between the ground and variationally minimised excited states. For a high spin d^8 metal as Ni^{2+}, all one-electron excitations are of the type $d^2_{t2g} \rightarrow d^1_{eg}$ and all two-electron excitations of the type $d^2_{t2g}\, d'^2_{t2g} \rightarrow d^1_{eg}\, d'^1_{eg}$. Thus the leading order correlation contributions to the excitation energies are the differences in correlation energy between d^2_{t2g} and d^2_{eg} for the one-electron excitation and between $d^2_{t2g}\, d'^2_{t2g}$ and $d^2_{2g}\, d'^2_{2g}$ for the two-electron excitations, which cannot amount to more than a few tenths of an eV.

This has indeed been found to be the case for both the bulk and (001) surface of NiO, for which (uncorrelated) UHF calculations are in agreement with the observed spectra to within this accuracy [137]. It is of interest, therefore, to see whether hybrid calculations can improve on this, particularly in view of the putative agreement between B3LYP and experimental band gaps of varying provenance, discussed earlier.

Table 10 lists the calculated energies for the one-electron $d_{xy} \rightarrow d_{x^2-y^2}$ and $d_{xy} \rightarrow d_{z^2}$ and two-electron $d_{xz}d_{yz} \rightarrow d_{z^2}d_{x^2-y^2}$ excitations in an eight formula unit supercell of FM NiO (using a=4.2 Å) as a function of the hybridisation parameter in the F-BLYP series. Within this scheme, 20% exact exchange appears to be the stability limit for all three excited states, and the ground state is metallic in the DFT limit. The lower energy $t_{2g}\rightarrow e_g$ excitation increases from 0.82 eV at the limit of exact exchange to 0.94 eV at 20% exact exchange,

Table 10 Calculated energies of one- and two-particle excitations in NiO; crystal field splitting Δ_{CF}(eV), Racah B parameter (eV), and analytically predicted value for the two-particle excitation

α	$\Delta E[xy \rightarrow x^2-y^2]=\Delta_{CF}$	$\Delta E[xy \rightarrow z^2]$	$\Delta E[xz,yz \rightarrow z^2,x^2-y^2]$	B	$3B+2\Delta CF$
UHF	0.8129	2.6100	2.0697	0.1498	2.0751
1.0	0.8167	2.5775	2.0567	0.1467	2.0736
0.9	0.8216	2.5465	2.0645	0.1437	2.0744
0.8	0.8395	2.5197	2.0918	0.1400	2.0991
0.7	0.8458	2.4843	2.1028	0.1365	2.1012
0.6	0.8567	2.4471	2.1261	0.1325	2.1110
0.5	0.8668	2.4006	2.1483	0.1278	2.1171
0.4	0.8967	2.3574	2.2159	0.1217	2.1586
0.3	0.8988	2.2667	2.2101	0.1140	2.1396
0.2	0.9441	2.2080	2.2958	0.1053	2.2042
Expt	1.05–1.16[a]	2.75–3.00[a]	1.79–1.95[a]	0.1277[b]	

[a] [134]
[b] [136]

which compares with experimental values in the range 1.05 eV–1.16 eV [134]; for the higher energy excitation, the energy decreases from 2.58 eV to 2.21 eV over the same range of hybridisation, compared with experimental values in the range 2.75 eV–3 eV [134]. For the two-electron excitation, the energy increases from 2.06 eV to 2.30 eV, compared with an experimental range of 1.74 eV–1.95 eV [134]. Mapping of the energies onto the Kanamori Hamiltonian (see above) results in $\Delta E_{xy \rightarrow x^2-y^2} = \Delta_{CF}, \Delta E_{xy \rightarrow z^2} = 12B + \Delta_{CF}$ and $\Delta E_{xz,yz \rightarrow z^2,x^2-y^2} = 3B + 2\Delta_{CF}$. We extract the Racah B parameter from the two single-particle excitations, and use the derived value to calculate the energy of the two-particle excitation, as a check on the consistency of the mapping; as can be seen in Table 10, the agreement is excellent. The free ion value for B is most closely matched by a weight of ~50%, but this is purely due to the difference between excitation energies; a better match with their absolute placement is obtained by uncorrelated UHF calculations. We may further conclude that density functional theory is unable to capture the small but subtle correlation corrections involved in d→d excitations, at least not in NiO.

4.4 Defective Systems—Trapped Electron Hole in MgO

Earlier we highlighted how DFT shows systematic shortcomings when describing open-shell transition metal oxides, which may lead to the calculations predicting a wrong electronic ground state for these materials. The DFT shortcomings are associated with the highly localised nature of the d electrons, which requires an orbital-dependent DFT functional to be correctly accounted for. At least, to a certain extent, the solution is improved by us-

ing hybrid exchange functionals. In this section, we examine a new type of open-shell system, namely a trapped electron hole in MgO.

Trapped electron holes in MgO represent a typical electronic defect in a main group oxide, formed upon irradiation [138, 139] or aliovalent doping. They are experimentally well-characterised electronic defects in a host matrix, MgO, in which DFT is known to perform well. They represent therefore a suitable test to benchmark the ability of pure and hybrid DFT functionals in describing unpaired electrons in crystalline solids.

When one Mg^{2+} ion in MgO is replaced by a Li^{+} dopant, one electron hole h^{+} is generated as a charge-balancing defect. Extremely accurate EPR and ENDOR results are available concerning the coupling between the unpaired electron (in the same orbital hosting the electron hole) and the Li nuclear spin (I_z=3/2) [138, 140, 141], that allow us to characterise the electronic structure of the defect very accurately. In particular, experimental data [142] are compatible with a model where the hole is localised on one of the oxygen ions that are nearest neighbour of the Li dopant. We label this ion as O_1, while we identify the other oxygen ions nearest neighbour of Li as O_2 (the oxygen opposite to O_1) and O_{eq} (the four oxygens perpendicular to the O_1-Li-O_2 direction, see Fig. 20).

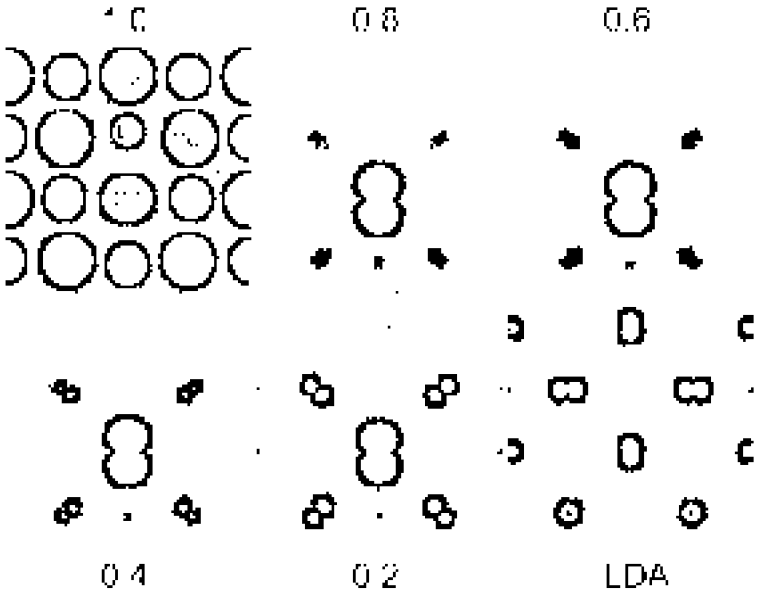

Fig. 20 Electron and spin density maps for the MgO:$[Li]^0$ defect within the F-BLYP series. The total density is shown for α=1.0; the spin density for the other mixing parameters. BLYP has been replaced by the LDA solution

Table 11 Equilibrium bond distances R(Å), charges q(*e*) and spin moments $\mu(\mu_B)$ for the MgO:$[Li]^0$ defect; calculated and experimental hyperfine isotropic (a), anisotropic (b) and nuclear quadrupole (P) constants (MHz)

	LDA	PW	B3LYP	α=0.2	α=0.4	α=0.6	α=0.8	α=1.0	HF	Expt[a]
R(Li-O_1)	2.124	2.464	2.284	2.306	2.283	2.270	2.250	2.239	2.284	
R(Li-O_2)	2.122	1.948	1.973	1.969	1.914	1.890	1.874	1.858	1.900	
Li:q	0.969	0.972	0.972	0.971	0.974	0.976	0.978	0.979	0.982	
μ	0	0	0.001	0.001	0	0	0	0	0	
O_1:q	−1.692	−1.600	−1.255	−1.252	−1.053	−1.003	−0.984	−0.974	−0.979	
μ	0.074	0.181	0.636	0.638	0.876	0.935	0.958	0.969	0.983	
O_2:q	−1.693	−1.769	−1.800	−1.800	−1.822	−1.837	−1.850	−1.861	−1.880	
μ	0.073	0.029	0.003	0.003	0.001	0	0	0	0	
O_{eq}:q	−1.684	−1.688	−1.751	−1.751	−1.790	−1.812	−1.828	−1.842	−1.859	
μ	0.081	0.095	0.042	0.042	0.015	0.008	0.005	0.004	0.003	
a	−3.140	−2.074	−6.368	−6.209	−3.143	−0.629	1.008	1.720	0.122	−4.539
b	−0.078	0.003	1.747	1.687	2.691	2.995	3.199	3.305	3.180	2.313
P	0.001	0.008	−0.007	−0.007	−0.012	−0.014	−0.016	−0.017	−0.015	−0.014

[a] Expt from [140]

The Li/Mg defect has been simulated in our work with a 32-atom supercell, in which one Mg^{2+} ion has been replaced by one Li^+. For each Hamiltonian, the lattice parameter employed is the equilibrium one for undoped MgO (see Table 1). In the calculations on the Li/Mg defect, the lattice parameter has been kept fixed, while the fractional coordinates of each ion of the supercell have been relaxed to find the minimum energy geometry.

The equilibrium structure of the defect is summarised in Table 11, together with an analysis of charge and spin density. Spin density maps are reported in Fig. 20; they clearly show that different Hamiltonians yield a very different degree of hole localisation. This feature is quantified by the spin moment (μ)of O_1 in Table 11, which ranges from 0.98 (UHF) to 0.07 (LDA). The same shortcomings of pure DFT functionals in describing localised electrons in open-shell transition metal ions (above) are therefore found also here in Li/MgO. Several attempts to converge the LSDA and GGA self-consistent cycles to a localised solution always yielded the same delocalised hole state. As for the transition metal oxides, inclusion of HF exchange in the functional formulation has a dramatic effect on results: when the fraction of HF exchange is increased, the hole becomes more and more localised on the O_1 ion.

The different degree of hole localisation has important consequences on the structural relaxation: the more h^+ is localised on O_1, the more its Coulomb interaction with Li decreases, leading to a relaxation of Li away from O_1. Since we have used the equilibrium lattice parameter for each formulation of the functional, the absolute value of M-O and Li-O distances is irrelevant; we report instead the difference ΔR_{12} between the Li-O_1 and Li-O_2 dis-

tances, which measures the strength of the association of Li with O_2. We notice a clear correlation between ΔR_{12} and the hole localisation on O_1.

The electronic structure of the Li/MgO defect centre has been investigated experimentally via EPR techniques; to compare the calculated results with experiment, we have therefore evaluated the isotropic (a) and anisotropic (b) hyperfine coupling constants, and the nuclear quadrupolar coupling constant (P), also available from experimental EPR spectra. Results are reported in Table 11. Pure DFT results differ from the experimental data for a in magnitude, and for b and P also in sign. Admixing of HF exchange in the hybrid functional improves the correspondence of results with experiment; the best match is achieved for α~0.3, while increasing the exact exchange component further has the effect of over-correcting the DFT shortcomings, and results in a prediction for a with the wrong sign at the HF end of the hybrid F-BLYP series. From a computational point of view, it is of interest to notice that the Li/MgO defect had been examined with HF, B3LYP and LDA Hamiltonians in [42]. In that case, structural relaxation was limited to the Li and O_1 ions, while here we performed a full optimisation of the 32-ion supercell. This different structural constraint leads to qualitatively different results. While the extent of hole localisation on the different oxygens is essentially the same in the two studies, relaxation of the O_2 and equatorial oxygens (allowed here but not in [42]) modifies the symmetry of the hole state and the Li-O_1 bond-distance, and causes a large variation of the hyperfine EPR constants. This comparison highlights one critical component of modelling studies: when the calculated observable is very sensitive to small structural relaxations, the computational model must be flexible enough to not impose structural constraints on the solution. A partial relaxation, or the imposition of a higher symmetry, may lead to qualitatively and quantitatively wrong results.

5 Conclusions

In this chapter we have extensively presented the properties of hybrid exchange functionals in describing crystalline solids, with a particular emphasis on transition metal compounds. This work extends greatly the applications of hybrid functionals to crystalline solids available in the literature, in that a systematic investigation of the whole hybridisation range has been performed consistently for a set of compounds.

The features of the calculated electronic density have been examined as the weight of HF (exact) exchange in the hybrid functional is increased. Clear trends emerged in the structural and electronic properties; the most important is that inclusion of HF exchange increases the degree of electronic localisation in the solution. This feature causes a systematic increase in the

ionicity of the materials, a systematic decrease of the lattice parameter and increase of the elastic constants and bulk moduli.

Whenever HF and standard (LDA/GGA) DFT functionals yield systematically errors with opposite sign with respect to experiment, the formulation of hybrid functionals improves the accuracy of the calculations. This is the case for band gaps, phonon spectra, magnetic coupling constants, and all properties that depend on the extent of electronic localisation at either perfect or defective lattice sites. This feature is particularly important at lattice defects that break the translational symmetry of the crystal; in this case, non orbital-dependent DFT functionals appear unable to localise the defect states, even in simple matrices as MgO.

For other properties that do not show systematic errors in HF, LDA or GGA solutions, however, formulation of hybrid functionals does not always improve results. Most notably, this is the case for the structure; our results on transition metal oxides challenge in this case a traditional piece of information derived for main group elements, namely that the HF solution overestimates the experimental bond-distances. For semicovalent materials, the higher ionic charges in the HF solution generate a higher Madelung field that contracts the lattice parameter. Trends in the bond-distances and lattice parameters have been shown to depend on the degree of ionicity in the material.

A stringent requirement for the functional is provided by open shell transition metal compounds; in the cases investigated in this chapter, high weights of HF exchange always ensured convergence of the solution to the correct ground electronic state, which instead is not always the case for a low HF component (<20%).

The best percentage of HF exchange to be included in the functional differs according to a combination of system and property under investigation. As a general rule, however, the optimum weight of HF exchange for a solid-state specific hybrid functional is higher than the 20% optimised in the B3LYP formulation for molecular species, and much closer to Becke's half-and-half hybrid with 50% HF exchange. We associate this requirement to the Madelung field, which creates a strong localising potential in the crystal, that is not present in molecules. Under this condition, the shortcomings of LDA and GGA functionals associated with the lack of electronic self-interaction are more severe.

We have finally shown that the use of experimental geometries and/or constrained optimisations can lead to fictitious results, especially for those observables that are strongly dependent on the interatomic distances, such as the magnetic coupling constants J in magnetic oxides and the EPR parameters of open-shell defects. Whenever possible, theoretical predictions should be achieved without imposing structural constraints on the solution.

Acknowledgements We would like to thank the CRYSTAL group, in both Torino and Daresbury, for valuable discussions throughout the years; in particular we thank Carla Roetti, Vic Saunders and Nic Harrison; we would also like to thank Mike Finnis and Tony Paxton for making available their Tight-Binding code. FC acknowledges EPSRC for an advanced research fellowship.

References

1. Catlow CRA (1997) (ed) Computer modelling in inorganic crystallography. Academic Press, London
2. Fock V (1930) Z Phys 61:126
3. Slater JC (1930) Phys Rev 35:210
4. Szabo A, Ostlund NS (1989) Modern quantum chemistry. McGraw-Hill, New York
5. Hohenberg P, Kohn W (1964) Phys Rev B 136:864
6. Kohn W, Sham L (1965) Phys Rev A 140:1133
7. Dreizler RM, Gross EKU (1990) Density functional theory. Springer, Berlin Heidelberg New York
8. Cohen AJ, Handy NC (2000) Chem Phys Lett 316:160
9. Fulde P (2002) Adv Phys 51:909
10. Dirac PAM (1930) Proc Cambridge Phil Soc 26:376
11. Vosko SH, Wilk L, Nusair M (1980) Can J Phys 58:1200
12. Jones RO, Gunnarsson O (1985) Phys Rev Lett 55:107
13. Becke AD (1988) Phys Rev A 38:3098
14. Lee C, Yang W, Parr RG (1988) Phys Rev B 37:785
15. Hamprecht FA, Cohen AJ, Tozer DJ, Handy NC (1998) J Chem Phys 109:6264
16. Perdew JP (1986) Phys Rev B 33:8800
17. Perdew JP, Wang Y (1992) Phys Rev B 45:13244
18. Perdew JP, Burke K, Ernzerhof M (1996) Phys Rev Lett 77:3865
19. Perdew JP, Kurth S, Zupan A, Blaha P (1999) Phys Rev Lett 82:2544
20. Van Voorhis T, Scuseria GE (1998) J Chem Phys 109:400
21. Perdew JP, Zunger A (1981) Phys Rev B 23:5048
22. Jones RO, Gunnarsson O (1989) Rev Mod Phys 61:689
23. Krieger JB, Li Y, Iafrate GJ (1992) Phys Rev A 45:101
24. Anisimov VI, Zaanen J, Andersen OK (1991) Phys Rev B 44:943
25. Becke AD (1993) J Chem Phys 98:1372
26. Becke AD (1993) J Chem Phys 98:5648
27. Adamo C, Barone V (1997) Chem Phys Lett 274:242
28. Perdew JP, Ernzerhof M, Burke K (1996) J Chem Phys 105:9982
29. Frisch MJ, Trucks GW, Schelgel HB, Gill PMW, Johnson BG, Robb MA, Cheeseman JR, Keith TA, Pettersson GA, Montgomery JA, Raghavachari K, Al-Laham MA, Zakrevski VG, Ortiz JV, Foresman JB, Cioslowski J, Stefanov BB, Nanayakkara A, Challacombe M, Peng CY, Ayala PY, Chen W, Wong MW, Andres JL, Replogle ES, Gomperts R, Martin RL, Fox DJ, Binkley JS, Defrees DJ, Baker J, Stewart JJP, Head-Gordon M, Gonzalez C, Pople JA (1995) Gaussian94 (Revision A.I), Gaussian Inc, Pittsburgh PA
30. Saunders VR, Dovesi R, Roetti C, Causà M, Harrison NM, Orlando R, Zicovich-Wilson CM (1998) CRYSTAL98 User's manual. University of Torino, Torino

31. Kung HH (1989) Transition metal oxides: surface chemistry and catalysis. Studies in Surface Science and Catalysis, vol 45. Elsevier, Amsterdam
32. Newnham RE (1997) MRS Bull XXII(5):20
33. Busch-Vishniac IJ (1998) Phys Today July 1998:28
34. Owen JR (1997) Chem Soc Rev 26:147
35. Green M (1996) Chem Ind 17:641
36. Mortimer RJ (1997) Chem Soc Rev 26:147
37. Curtiss LA, Raghavachari K, Redfern PC, Pople JA (1997) J Chem Phys 106:1063
38. Hedin L (1965) Phys Rev 136:A796; Hybertsen MS, Louie SG (1985) Phys Rev Lett 55:1418
39. Foulkes WMC, Mitas L, Needs RJ, Rajagopal G (2001) Rev Mod Phys 73:33
40. Muscat J, Wander A, Harrison NM (2001) Chem Phys Lett 342:397
41. Wilson N, Muscat J (2002) Molec Simul 28:903
42. Mallia G, Orlando R, Llunell M, Dovesi R (2003) In: Catlow CRA, Kotomin EA (eds) Computational materials science. NATO Science Series III, vol 187, IOS Press, Amsterdam, pp 102–121
43. Damin A, Dovesi R, Zecchina A, Ugliengo P (2001) Surf Sci 479:253
44. Ugliengo P, Damin A (2002) Chem Phys Lett 366:683
45. Alfredsson M (1999) Thesis, Acta Universitatis Upsaliensis. Uppsala, Sweden
46. Baranek P, Lichanot A, Orlando R, Dovesi R (2001) Chem Phys Lett 240:362
47. Mérawa M, Civalleri B, Ugliengo P, Noël Y, Lichanot A (2003) J Chem Phys 119:1045
48. Gomes JRB, Moreira I de PR, Reinhardt P, Wander A, Searle BG, Harrison NM, Illas F (2001) Chem Phys Lett 341:412
49. Corà F, Catlow CRA (2001) J Phys Chem 105:10278
50. Wander A, Schedin F, Steadman P, Norris A, McGrath R, Turner TS, Thornton G, Harrison NM (2001) Phys Rev Lett 86:3811
51. Wander A, Harrison NM (2000) Surf Sci 457:L342
52. Wander A, Harrison NM (2000) Surf Sci 468:L851
53. Muscat J, Gale JD (2003) Geochim Cosmochim Acta 67:799
54. Muscat J, Klauber C (2001) Surf Sci 491:226
55. Ugliengo P, Civalleri B, Zicovich-Wilson CM, Dovesi R (2000) Chem Phys Lett 318:247
56. Ugliengo P, Civalleri B, Dovesi R, Zicovich-Wilson CM (1999) Phys Chem Chem Phys 1:545
57. Pascale F, Ugliengo P, Civalleri B, D'Arco P, Dovesi R (2002) J Chem Phys 117:5337
58. Baranek P, Dovesi R (2002) Ferroelectrics 268:155
59. Heifets E, Eglitis RI, Kotomin EA, Maier J, Borstel G (2001) Phys Rev B 64:235417
60. Bredow T, Gerson AR (2000) Phys Rev B 61:5194
61. Moreira I de PR, Illas F, Martin RL (2002) Phys Rev B 65:155102
62. Muscat J, Hung A, Russo S, Yarovsky I (2002) Phys Rev B 65:054107
63. Perry JK, Tahir-Kheli J, Goddard WA (2001) Phys Rev B 63:144510
64. Mackrodt WC, Middlemiss DS, Owens TG (2004) Phys Rev B 69:115119
65. Scott AP, Radom L (1996) J Phys Chem 100:16502
66. Runge E, Gross EKU (1984) Phys Rev Lett 52:997
67. Marques MA, Castro A, Rubio A (2001) J Chem Phys 115:3006
68. Gilli G, Gilli P (2000) J Mol Struct 552:1
69. Sandor E, Farrow RFO (1967) Nature 14:171
70. Bushbeck K-C (ed) (1968) Gmelins handbuch der anorganischen chemie; Chlor 6(1):90–92, 8th edn. Verlage Chemie, GMBH, Weinhem/Bergst, Germany
71. Aoki K, Katoh E, Yamawaki H, Sakashita M, Fujihisa H (1999) Physica B 265:83

72. Vinogradov SN, Linnell RH (1971) Hydrogen bonding. van Nostrand Reinhold Company, New York, p 55
73. Corà F, Catlow CRA (1999) Faraday Discuss 114:421
74. Corà F, Catlow CRA (2000) In: Bortsel G (ed) Defects and surface-induced effects in advanced perovskites. Kluwer Academic Publishers, The Netherlands, p 175
75. Cohen RE (1992) Nature 358:136
76. Abrahams SC, Keve ET (1971) Ferroelectrics 2:129
77. Martin RL, Illas F (1997) Phys Rev Lett 79:1539
78. Illas F, Martin RL (1998) J Chem Phys 108:2519
79. de Graaf C, Illas F, Broer R, Nieuwpoort WC (1997) J Chem Phys 106:3287
80. de Jongh LJ, Block R (1975) Physica 79B:568
81. Hoffmann R (1963) J Chem Phys 39:1397
82. Hoffmann R, Lipscomb WN (1962) J Chem Phys 36:2179; 37:2872
83. Burdett KJ (1995) Chemical bonding in solids. Oxford University Press, New York
84. Wheeler RA, Whangbo M-H, Hughbanks T, Hoffman R, Burdett JK, Albright TA (1986) J Am Chem Soc 108:2222
85. Finnis MW, Paxton AT, Methfessel M, von Schilfgaarde M (1998) Phys Rev Lett 81:5149
86. Fabris S, Paxton AT, Finnis MW (2000) Phys Rev B 61:6617
87. Resta R (2003) Modell Simul Mater Sci Eng 11:R69
88. Ashcroft N, Mermin N (1976) Solid state physics. WB Saunders and Co., Philadelphia
89. Kanamori J (1959) J Phys Chem Solids 10:87
90. Griffith JS (1964) The theory of transition metal ions. Cambridge University Press, Cambridge
91. Saunders VR, Dovesi R, Roetti C, Orlando R, Zicovich-Wilson CM, Harrison NM, Doll K, Civalleri B, Bush I, D'Arco P, Llunell M (2003) CRYSTAL2003 User's manual, University of Torino, Torino
92. www.crystal.unito.it/Basis_Sets/ptable.html
93. Pisani C, Dovesi R, Roetti C (1988) Hartree Fock ab initio treatment of crystalline systems, vol 48. Lecture notes in chemistry. Springer, Berlin Heidelberg New York
94. Pisani C (ed) (1996) Quantum mechanical ab initio calculation of the properties of crystalline materials, vol 67. Lecture notes in chemistry. Springer, Berlin Heidelberg New York
95. Birch F (1978) J Geophys Res 83:1257
96. Murnaghan FD (1944) Proc Nat Acad Sciences 30:244
97. Zhong W, King-Smith RD, Vanderbild D (1994) Phys Rev Lett 72:3618
98. Dovesi R, Roetti C, Freyria Fava C, Aprà E, Saunders VR, Harrison NM (1992) Phyl Trans R Soc A341:203
99. Lines ME, Glass AM (1977) Principles and applications of ferroelectrics and related materials. Clarendon Press, Oxford
100. Kwei GH, Lawson AC, Billinge SJL, Cheong S-W (1993) J Phys Chem 97:2368
101. Frenkel AI, Wang FM, Kelly S, Ingalls R, Haskel D, Stern EA (1997) Phys Rev B 56:10869
102. Wieder HH (1955) Phys Rev 99:1161
103. Hewat AW (1973) J Phys C 6:1074
104. Kleemann W, Schäfer FJ, Fontana MD (1984) Phys Rev B 30:1148
105. Madelung O (1982) Landolt-Börnstein New Series. Springer, Berlin Heidelberg New York
106. Dovesi R, Freyria Fava F, Roetti C, Saunders VR (1997) Faraday Discuss 106:173

107. Brandow BH (1977) Adv Phys 26:651
108. Powell RJ, Spicer WE (1970) Phys Rev B 2:2182
109. Terakura K, Oguchi T, Williams AR, Kluber J (1984) Phys Rev B 30:4734
110. Leung TC, Chan CT, Harmon BN (1991) Phys Rev B 44:2923
111. Szotek Z, Temmerman WM, Winter H (1993) Phys Rev B 47:4029
112. Zaanen J, Sawatzky GA, Allen JW (1985) Phys Rev Lett 55:418
113. Towler MD, Allan NL, Harrison NM, Saunders VR, Mackrodt WC, Aprà E (1994) Phys Rev B 50:5041
114. Fang Z, Solovyev IV, Sawada H, Terakura K (1999) Phys Rev B 59:762
115. Pask JE, Singh DJ, Mazin II, Hellberg CS, Kortus J (2001) Phys Rev B 64:024403
116. Bartel LC, Morosin B (1971) Phys Rev B 3:1039
117. Notis R, Spriggs RM, Hahn WC (1973) J Appl Phys 44:4165
118. DuPleiss PDV, Van Tonder SJ, Alberts L (1971) J Phys C 4:1983
119. Fender BEF, Jacobson AJ, Wedgewood FA (1968) J Chem Phys 48:990
120. Alperin HA (1962) J Phys Soc Jpn Suppl B 17:12
121. Cheetham AK, Hope DAO (1983) Phys Rev B 27:6964
122. Kondo K, Yagi T, Syono Y, Noguchi Y, Atou T, Kikegawa T, Shimomura O (2000) J App Phys 87:4153
123. Clendenen RL, Drickamer HG (1966) J Chem Phys 44:4223
124. Jeanloz R, Rudy A (1987) J Geophys Res 92:11433
125. Webb SL, Jackson I, FitzGerald JD (1988) Phys Earth Planet Int 52:117
126. Noguchi Y, Kusaba K, Fukuokaand K, Syono Y (1996) Geophys Res Lett 23:1469
127. Shaked H, Faber J Jr, Hitterman RL (1988) Phys Rev B 38:11901
128. Cox PA (1995) Transition metal oxides. Clarendon Press, Oxford
129. Lines ME, Jones ED (1965) Phys Rev 139:A1313
130. Kohgi M, Ishikawa Y, Endoh Y (1972) Solid State Commun 11:391
131. Pepy G (1974) J Phys Chem Solids 35:433
132. Hutchings MT, Samuelsen EJ (1972) Phys Rev B 6:3447
133. Shanker R, Singh RA (1973) Phys Rev B 7:5000
134. Hufner S, Steiner P, Reinert F, Schmitt H, Sandl P (1992) Z Phys B 88:247; Newman R, Chrenko R (1959) Phys Rev 114:1507; Propach V, Reinen D, Drenkhaln H, Muller Buschbaum H (1978) Z Naturforsch 33b:619; Cox PA, Williams AA (1985) Surf Sci 152:791; Freitag A, Staemmler V, Cappus D, Ventrice CA, Al Shamery K, Kuhlenbeck H, Freund H-J (1993) Chem Phys Lett 210:10; Fromme B, Schmitt M, Kisker E, Gorschluter A, Merz H (1994) Phys Rev B 50:1874
135. Shukla A, Rueff J-P, Badro J, Vanko G, Mattila A, de Groot FMF, Sette F (2003) Phys Rev B 67:081101
136. Sugano S, Tanabe Y, Kamimura H (1970) Multiplets of transition-metal ions in crystals. Academic Press, New York
137. Mackrodt WC, Noguera C (2000) Surf Sci Lett 457:L386
138. Schirmer OF (1971) J Phys Chem Solids 32:499
139. Rius G, Cox R, Picard R, Santier C (1970) C R Acad Sci Paris 271:824
140. Abraham MM, Unruh WP, Chen Y (1974) Phys Rev B 10:3540; Chen Y, Abraham MM (1990) J Phys Chem Solids 51:747
141. Henderson B (1976) J Phys C 9:579
142. Rius G, Hervé A (1974) Solid State Commun 15:399

Author Index Volumes 101–113

Author Index Vols. 1–100 see Vol. 100

The volume numbers are printed in italics

Alajarin M, see Turner DR (2004) *108*: 97–168
Aldinger F, see Seifert HJ (2002) *101*: 1–58
Alfredsson M, see Corà F (2004) *113*: 171–232
Aliev AE, Harris KDM (2004) Probing Hydrogen Bonding in Solids Using State NMR Spectroscopy *108*: 1–54
Alloul H, see Brouet V (2004) *109*: 165–199
Amstutz N, see Hauser A (2003) *106*: 81–96
Anitha S, Rao KSJ (2003) The Cemplexity of Aluminium-DANN Interactions: Relevance to Alheimer's and Other Neurological Diseases *104*: 79–98
Aramburu JA, see Moreno M (2003) *106*: 127–152
Arcon D, Blinc R (2004) Jahn Teller Effect and Fullerene Ferromagnets *109*: 231–276
Atanasov M, Daul CA, Rauzy C (2003) A DFT Based Ligand Field Theory *106*: 97–125
Atwood DA, see Conley B (2003) *104*: 181–193
Atwood DA, Hutchison AR, Zhang Y (2003) Compounds Containing Five-Coordinate Group 13 Elements. *105*: 167–201
Autschbach J (2004) The Calculation of NMR Parameters in Transition Metal Complexes *112*: 1–48

Baerends EJ, see Rosa A (2004) *112*: 49–116
Barriuso MT, see Moreno M (2003) *106*: 127–152
Bellandi F, see Contreras RR (2003) *106*: 71–79
Berend K, van der Voet GB, de Wolff FA (2003) Acute Aluminium Intoxication. *104*: 1–58
Blinc R, see Arcon D (2004) *109*: 231–276
Bohrer D, see Schetinger MRC (2003) *104*: 99–138
Boulon G (2004) Optical Transitions of Trivalent Neodymium and Chromium Centers in $LiNbO_3$ Crystal Host Material *107*: 1–25
Bowlby BE, Di Bartolo B (2003) Spectroscopy of Trivalent Praseodymium in Barium Yttrium Fluoride *106*: 191–208
Braga D, Maini L, Polito M, Grepioni F (2004) Hydrogen Bonding Interactions Between Ions: A Powerful Tool in Molecular Crystal Engineering *111*: 1–32
Brouet V, Alloul H, Gàràj S, Forrò L (2004) NMR Studies of Insulating, Metallic, and Superconducting Fullerides: Importance of Correlations and Jahn-Teller Distortions *109*: 165–199
Budzelaar PHM, Talarico G (2003) Insertion and β-Hydrogen Transfer at Aluminium *105*: 141–165
Burrows AD (2004) Crystal Engineering Using Multiple Hydrogen Bonds *108*: 55–96

Canadell E, see Sánchez-Portal D (2004) *113*: 103–170
Cancines P, see Contreras RR (2003) *106*: 71–79
Cartwright HM (2004) An Introduction to Evolutionary Computation and Evolutionary Algorithms *110*: 1–32
Clot E, Eisenstein O (2004) Agostic Interactions from a Computational Perspective: One Name, many Interpretations *113*: 1–36

Conley B, Atwood DA (2003) Fluoroaluminate Chemistry *104*: 181–193
Contreras RR, Suárez T, Reyes M, Bellandi F, Cancines P, Moreno J, Shahgholi M, Di Bilio AJ, Gray HB, Fontal B (2003) Electronic Structures and Reduction Potentials of Cu(II) Complexes of [N,N′-alkyl-bis(ethyl-2-amino-1-cyclopentenecarbothioate)] (alkyl = ethyl, propyl, and butyl) *106*: 71–79
Corà F, Alfredsson M, Mallia G, Middlemiss DS, Mackrodt WC, Dovesi R, Orlando R (2004) The Performance of Hybrid Density Functionals in Solid State Chemistry *113*: 171–232

Daul CA, see Atanasov M (2003) *106*: 97–125
Day P (2003) Whereof Man Cannot Speak: Some Scientific Vocabulary of Michael Faraday and Klixbüll Jørgensen *106*: 7–18
Deeth RJ (2004) Computational Bioinorganic Chemistry *113*: 37–69
Delahaye S, see Hauser A (2003) *106*: 81–96
Di Bartolo B, see Bowlby BE (2003) *106*: 191–208
Di Bilio AJ, see Contreras RR (2003) *106*: 71–79
Dovesi R, see Corà F (2004) *113*: 171–232

Eisenstein O, see Clot E (2004) *113*: 1–36

Fontal B, see Contreras RR (2003) *106*: 71–79
Forrò L, see Brouet V (2004) *109*: 165–199
Frenking G, see Lein M (2003) *106*: 181–191
Frühauf S, see Roewer G (2002) *101*: 59–136
Frunzke J, see Lein M (2003) *106*: 181–191

Gàràj S, see Brouet V (2004) *109*: 165–199
Gillet VJ (2004) Applications of Evolutionary Computation in Drug Design *110*: 133–152
Golden MS, Pichler T, Rudolf P (2004) Charge Transfer and Bonding in Endohedral Fullerenes from High Energy Spectroscopy *109*: 201–229
Gray HB, see Contreras RR (2003) *106*: 71–79
Grepioni F, see Braga D (2004) *111*: 1–32
Gritsenko O, see Rosa A (2004) *112*: 49–116
Güdel HU, see Wenger OS (2003) *106*: 59–70
Gütlich P (2004) Recent Advances in Spin Crossover Research *107*: in preparation

Habershon S, see Harris KDM (2004) *110*: 55–94
Hardie MJ (2004) Hydrogen Bonded Network Structures Constructed From Molecular Hosts *111*: 139–174
Harris KDM, see Aliev (2004) *108*: 1–54
Harris KDM, Johnston RL, Habershon S (2004) Application of Evolutionary Computation in Structure Solution from Diffraction Data *110*: 55–94
Hartke B (2004) Application of Evolutionary Algorithm to Global Cluster Geometry Optimization *110*: 33–53
Harvey JN (2004) DFT Computation of Relative Spin-State Energetics of Transition Metal Compounds *112*: 151–183
Haubner R, Wilhelm M, Weissenbacher R, Lux B (2002) Boron Nitrides – Properties, Synthesis and Applications *102*: 1–46
Hauser A, Amstutz N, Delahaye S, Sadki A, Schenker S, Sieber R, Zerara M (2003) Fine Tuning the Electronic Properties of $[M(bpy)_3]^{2+}$ Complexes by Chemical Pressure (M = Fe^{2+}, Ru^{2+}, Co^{2+}, bpy = 2,2′-bipyridine) *106*: 81–96
Herrmann M, see Petzow G (2002) *102*: 47–166
Herzog U, see Roewer G (2002) *101*: 59–136
Hoggard PE (2003) Angular Overlap Model Parameters 106: 37–57
Höpfl H (2002) Structure and Bonding in Boron Containing Macrocycles and Cages. *103*: 1–56
Hubberstey P, Suksangpanya U, Schröder M (2004) Hydrogen-Bonded Supramolecular Chain and Sheet Formation by Co-Ordinated Guadine Derivatives *111*: 33–83

Hutchison AR, see Atwood DA (2003) *105*: 167–201

Iwasa Y, see Margadonna S (2004) *109*: 127–164

Jansen M, Jäschke B, Jäschke T (2002) Amorphous Multinary Ceramics in the Si-B-N-C System *101*: 137–192
Jäschke B, see Jansen M (2002) *101*: 137–192
Jäschke T, see Jansen M (2002) *101*: 137–192
Jaworska M, Macyk W, Stasicka Z (2003) Structure, Spectroscopy and Photochemistry of the $[M(\eta^5\text{-}C_5H_5)(CO)_2]_2$ Complexes (M = Fe, Ru) *106*: 153–172
Johnston RL, see Harris KDM (2004) *110*: 55–94

Lein M, Frunzke J, Frenking G (2003) Christian Klixbüll Jørgensen and the Nature of the Chemical Bond in $HArF^t$ *106*: 181–191
Lever B (2004) Ruthenium Complexes of Non-Innocent Ligands; Aspects of Charge Transfer Spectroscopy *107*: 77–114
Linton DJ, Wheatley AEH (2003) The Synthesis and Structural Properties of Aluminium Oxide, Hydroxide and Organooxide Compounds *105*: 67–139
Lux B, see Haubner R (2002) *102*: 1–46

Mackrodt WC, see Corà F (2004) *113*: 171–232
Macyk W, see Jaworska M (2003) *106*: 153–172
Mahalakshmi L, Stalke D (2002) The R_2M^+ Group 13 Organometallic Fragment Chelated by P-centered Ligands *103*: 85–116
Maini L, see Braga D (2004) *111*: 1–32
Mallia G, see Corà F (2004) *113*: 171–232
Margadonna S, Iwasa Y, Takenobu T, Prassides K (2004) Structural and Electronic Properties of Selected Fulleride Salts *109*: 127–164
Maseras F, see Ujaque G (2004) *112*: 117–149
Middlemiss DS, see Corà F (2004) *113*: 171–232
Miyake T, see Saito (2004) *109*: 41–57
Moreno J, see Contreras RR (2003) *106*: 71–79
Moreno M, Aramburu JA, Barriuso MT (2003) Electronic Properties and Bonding in Transition Metal Complexes: Influence of Pressure *106*: 127–152
Morita M (2004) Photoluminescence and Excitation Energy Transfer of Rare Earth Ions in Nanoporous Xerogel and Sol-gel SiO_2 Glasses *107*: 115–143
Morsch VM, see Schetinger MRC (2003) *104*: 99–138
Mossin S, Weihe H (2003) Average One-Center Two-Electron Exchange Integrals and Exchange Interactions *106*: 173–180
Müller E, see Roewer G (2002) *101*: 59–136

Nishibori E, see Takata M (2004) *109*: 59–84

Ordejón P, see Sánchez-Portal D (2004) *113*: 103–170
Orlando R, see Corà F (2004) *113*: 171–232
Oshiro S (2003) A New Effect of Aluminium on Iron Metabolism in Mammalian Cells *104*: 59–78

Pastor A, see Turner DR (2004) *108*: 97–168
Patočka J, see Strunecká A (2003) *104*: 139–180
Petzow G, Hermann M (2002) Silicon Nitride Ceramics *102*: 47–166
Pichler T, see Golden MS (2004) 109: 201–229
Polito M, see Braga D (2004) *111*: 1–32
Power P (2002) Multiple Bonding Between Heavier Group 13 Elements. *103*: 57–84
Prassides K, see Margadonna S (2004) *109*: 127–164
Prato M, see Tagmatarchis N (2004) *109*: 1–39

Rao KSJ, see Anitha S (2003) *104*: 79–98
Rauzy C, see Atanasov (2003) *106*: 97–125
Reber C (2004) Allowed and Forbidden d-d Bands in Octahedral Coordination Compounds: Intensity Borrowing and Interference Dips in Absorption Spectra *107*: 145–158
Reinen D (2004) The Angular Overlap Model and Vibronic Coupling in Treating s-p and d-s Mixing – a DFT Study *107*: 159–178
Reisfeld R (2003) Rare Earth Ions, Their Spectroscopy of Cryptates and Related Complexes in Glasses *106*: 209–237
Reyes M, see Contreras RR (2003) *106*: 71–79
Ricciardi G, see Rosa A (2004) *112*: 49–116
Riesen H (2004) Progress in Hole-Burning Spectroscopy of Coordination Compounds *107*: 179–205
Roewer G, Herzog U, Trommer K, Müller E, Frühauf S (2002) Silicon Carbide – A Survey of Synthetic Approaches, Properties and Applications *101*: 59–136
Rosa A, Ricciardi G, Gritsenko O, Baerends EJ (2004) Excitation Energies of Metal Complexes with Time-dependent Density Functional Theory *112*: 49–116
Rudolf P, see Golden MS (2004) *109*: 201–229
Ruiz E (2004) Theoretical Study of the Exchange Coupling in Large Polynuclear Transition Metal Complexes Using DFT Methods *113*: 71–102

Sadki A, see Hauser A (2003) *106*: 81–96
Saito S, Umemoto K, Miyake T (2004) Electronic Structure and Energetics of Fullerites, Fullerides, and Fullerene Polymers *109*: 41–57
Sakata M, see Takata M (2004) *109*: 59–84
Sánchez-Portal D, Ordejón P, Canadell E (2004) Computing the Properties of Materials from First Principles with SIESTA *113*: 103–170
Schäffer CE (2003) Axel Christian Klixbüll Jørgensen (1931–2001) *106*: 1–5
Schäffer CE (2004) Ligand-Field Theory, Reformulated and Revived by Density Functional Theory *107*: 207–301
Schenker S, see Hauser A (2003) *106*: 81–96
Schetinger MRC, Morsch VM, Bohrer D (2003) Aluminium: Interaction with Nucleotides and Nucleotidases and Analytical Aspects of Determination *104*: 99–138
Schmidtke HH (2003) The Variation of Slater-Condon Parameters F^k and Racah Parameters B and C with Chemical Bonding in Transition Group Complexes *106*: 19–35
Schröder M, see Hubberstey (2004) *111*: 33–83
Schubert DM (2003) Borates in Industrial Use *105*: 1–40
Schulz S (2002) Synthesis, Structure and Reactivity of Group 13/15 Compounds Containing the Heavier Elements of Group 15, Sb and Bi *103*: 117–166
Seifert HJ, Aldinger F (2002) Phase Equilibria in the Si-B-C-N System *101*: 1–58
Shahgholi M, see Contreras RR (2003) *106*: 71–79
Shinohara H, see Takata M (2004) *109*: 59–84
Sieber R, see Hauser A (2003) *106*: 81–96
Stalke D, see Mahalakshmi L (2002) *103*: 85–116
Stasicka Z, see Jaworska M (2003) *106*: 153–172
Steed JW, see Turner DR (2004) *108*: 97–168
Strunecká A, Patočka J (2003) Aluminofluoride Complexes in the Etiology of Alzheimer's Disease *104*: 139–180
Suárez T, see Contreras RR (2003) *106*: 71–79
Suksangpanya U, see Hubberstey (2004) *111*: 33–83
Sundqvist B (2004) Polymeric Fullerene Phases Formed Under Pressure *109*: 85–126

Tagmatarchis N, Prato M (2004) Organofullerene Materials *109*: 1–39
Takata M, Nishibori E, Sakata M, Shinohara H (2004) Charge Density Level Structures of Endohedral Metallofullerenes by MEM/Rietveld Method *109*: 59–84
Takenobu T, see Margadonna S (2004) *109*: 127–164
Talarico G, see Budzelaar PHM (2003) *105*: 141–165

Trommer K, see Roewer G (2002) *101*: 59–136
Turner DR, Pastor A, Alajarin M, Steed JW (2004) Molecular Containers: Design Approaches and Applications *108*: 97–168

Uhl W (2003) Aluminium and Gallium Hydrazides *105*: 41–66
Ujaque G, Maseras F (2004) Applications of Hybrid DFT/Molecular Mechanics to Homogeneous Catalysis *112*: 117–149
Umemoto K, see Saito S (2004) *109*: 41–57
Unger R (2004) The Genetic Algorithm Approach to Protein Structure Prediction *110*: 153–175

van der Voet GB, see Berend K (2003) *104*: 1–58
Vilar R (2004) Hydrogen-Bonding Templated Assemblies *111*: 85–137

Weihe H, see Mossin S (2003) *106*: 173–180
Weissenbacher R, see Haubner R (2002) *102*: 1–46
Wenger OS, Güdel HU (2003) Influence of Crystal Field Parameters on Near-Infrared to Visible Photon Upconversion in Ti^{2+} and Ni^{2+} Doped Halide Lattices *106*: 59–70
Wheatley AEH, see Linton DJ (2003) *105*: 67–139
Wilhelm M, see Haubner R (2002) *102*: 1–46
de Wolff FA, see Berend K (2003) *104*: 1–58
Woodley SM (2004) Prediction of Crystal Structures Using Evolutionary Algorithms and Related Techniques *110*: 95–132

Zerara M, see Hauser A (2003) *106*: 81–96
Zhang Y, see Atwood DA (2003) *105*: 167–201

Subject Index

Active site 37, 42
Addition, oxidative 4
Ag(111) 141
$AgGaSe_2$ 111
Agostic interaction 1
AIM analysis 30
AIM theory 12
Aldehyde oxidoreductase 44
Alkaline earth cations 13
Alkaline earth oxides 179
Alkylidene 6
Alkyl-lithium complexes 22
Alumina 150
Aluminum hydroxides 135
Anisotropy energy barrier 73
Antiferromagnetism 190
Antiferromagnetic phase 210
AOs, frontier 184, 186

B3LYP 21, 41, 48, 50, 79, 81, 177, 188, 216
$Ba_{14}MnBi_{11}$ 125
Band gaps 176, 179, 199, 205, 219
Band structure 199
Bandwidths 199
Bases, localized 104
Basis sets 108, 138
$BaTiO_3$ 118, 119, 207
Bayerite polymorphs 136
β-$(BEDT\text{-}TTF)_2IBr_2$ 153
Bioinorganic chemistry, computational 37
Biomolecules 107, 158
Bloch functions 185
Blue bronze 151
Bond activation 1
Bond critical point (BCP) 12
Bond path 12
Bonds, agostic C-H 13
–, agostic Si-H 16
Born-Oppenheimer surface 107
Broken symmetry 76
Bulk moduli 178, 196, 220

C_{60} fullerides 141, 146
$Ca_{14}MnBi_{11}$ 125
Ca_2AuN 156
Ca_2GeN_2 156
$CaF_2(111)$ surface 148
Capacitor, ferroelectric 120
Carbon nanotaubes 115
Car-Parrinello 106
CASPT2 80
CASSCF 80
Catechol dioxygenase 43
C-C agostic interaction 20
CDW 151
Chalcogenides, glassy 117
Charge transfer, insulating character 215
Charge transfer excitations 223
Clathrates 134
Clusters 128
CO 143
Cobalt valence tautomers 133
Coenzyme B_{12}-dependent enzymes 52
Cohesion energy 179, 180
Conductors, molecular 153
Continuum, dielectric 45, 49
Copper center, type II 55
Correlated materials, highly 175
Correlation functionals 173
Coupling constants 213, 220
– –, hyperfine 227
Covalence 186
$Cr(CH(SiMe_3)_2)_3$ 21
Crystal field (Coulomb field) 186
Crystal field excitations 223
CRYSTAL98 175

Cu(II), polynuclear oxalato-bridged 81
Cu(II) polysiloxanolates 94
Cu_2Zn_4 96
Cu_4O_4 87
Cu_6 96
Cubane 84
Cytochrome c peroxidase 56

Defects 112
–, intrinsic 176
–, open-shell 182
Dehydration process 136
Delocalisation 22, 30
Densities of state 218
DFT 1, 14, 17, 21, 38, 48, 71, 104, 171, 172
Dielectric continuum 45, 49
Digital ferromagnetic heterostructures 127
Dipole moment 180
Direct coupling 220
Distortion, ferroelectric-like (FE) 203
–, rhombohedral 222
–, structural 203
Distortion profile 206
DMSO reductase 64
DNA 159
Donors, 2e/4e 3
Dopants 114
Double layer 142
DZP bases 108

Effective (Born) charges 190, 202
Effective interaction parameters 183
Effective size 205
EHT 5, 7
Eigenvalue spectrum 223
Elastic constants 177, 222
Electron density 199
Electron hole 225
Electron transfer 53
Electronic polarisability 201
Energy profile 205
Entatic state 42, 47
Enzymes, iron-containing 56
Ethyl cation 13
$EtTiCl_3$ 11
Exact exchange functionals (EXX) 174
EXAFS 43, 59
Exchange and correlation 107
Exchange coupling 71
Exchange functionals 173
Extended defects 115
Extended Hückel theory 5
Extended X-ray absorption fine structure 43

Fe clusters 128
Fe monolayers 129
Fe/*c*-SiFe/Fe sandwiches/multilayers 132
$Fe_4S_4(SCH_3)_4]^{2-}$ 76
$Fe_4S_4(SCH_3)_4]^{n-}$ 84
$[Fe_6S_6Cl_6]^-$ 85
Fe_8 72
Fe_{62} 130
Fe_n aggregates 129
Fermi energy 218
Fermi surface 150
Ferredoxine 84
Ferroelectric distortion 189
Ferroelectric film/capacitor 120
Ferroelectric polarisation 180
Ferroelectrics 104, 117
–, H-bonded 121
Ferromagnetic ordering 190
Ferromagnetic phase 210
Ferromagnetism 131
FeSi(CsCl) 140
Field effect transistors 144
Frontier AOs 184, 186
Fullerenes 157

(Ga,Mn)As 126
GaAs 127
Galactose oxidase 55
Gallophoshates 138
GaN 115
GaSe 109
Gas-phase electron diffraction 11
GaTe 109
Generalized gradient 173
Gibbsite 136
Gmelinite 137
GW techniques 176

Hamiltonian 73, 198
–, Ising 75, 210, 213, 222
–, Ising spin 191, 192
–, phenomenological 73
–, spin 183

–, tight-binding 183, 198
Hartree-Fock 5, 75, 174
Heisenberg model 63
Heme peroxidases 56
HF-DFT 171
Hidden nesting 151
Hole localisation 226
HOMO 2, 6
Hybrid density functionals 171
Hybrid functionals 205, 207
Hydrogen atom transfer 53
Hydrogen bonding 3, 180
Hydrogen molybdenum bronzes 152
Hydrogenase 64
Hypervalent silicon 20

$I_8@Si_{46}$ 134
IMOMM 55
Impurities, semiconductors 113
$In(CH(SiMe_3)_2)_3$ 21
InSe 109
Interdimer coupling 88
Interfaces 128, 139
Interstitials 127
Intradimer coupling 88
Ionicity 188, 202, 211
$IrH_2L(PR_2Ph)_3^+$ 26
$IrH_2L_2^+$ 26
Iron molybdenum cofactor 44
Iron-sulfur clusters 61
Ising Hamiltonian 75, 210, 213, 222
Ising spin Hamiltonian 191, 192

Jellium 173

K_5Bi_4 123
$K_6[V_{15}(As_6O_{42}(H_2O)]\cdot 8H_2O$ 90
Kanamori Hamiltonian 192, 224
KDP 121
$KMnF_3$, perovskite-structured 210
$KNbO_3$ 118, 207
–, cubic 198
Kohn-Sham DFT 107

$La(CH(SiMe_3)_2)_3$ 21
$La(N(SiMe_3)_2)_3$ 17
Lattice instabilities 115
Lattice parameters 178, 203, 211
LCAO 107
LDA 39
– /LSDA 107
LDA+U 174
Lewis base 24
$Li\text{-}CH_2\text{-}SiH_2Me$ 14
Linear response theory 112
Linear-scaling mathods 107
Local density approximation 39
Local spin density 40
Localized bases 104
LUMO 2, 4, 6

Madelung field 187, 202
Magic numbers 129
Magnetic anisotropy effects 93
Magnetic coupling 181
– – constants 176
Magnetic moments 195, 213
Magnetic multilayer device (MMD) 132
Magnets, single-molecule 71, 90
Marcus theory 54
MD 106
Mean field approximation 192
Metal monolayer 143
Metals, low dimensional 150
Metal-semiconductor interface 145
Methane monooxygenase 56, 58
Minerals 134
Mn(III)Cu(II) 82
Mn_{12} 72, 92
Mn_4 dimer 92
MnO 214, 220
Model Hamiltonians 183
$MoFe_7S_9$ 86
Molecular conductors 153
Molecular dynamics 106
Molecular metal, neutral 154
Molybdenum oxides/bronzes 151
Molybdoenzymes 63
Monophosphate tungsten bronzes 151
Monte Carlo, quantum 176
MOSFETs 119
Mott insulators 175
Mott-Hubbard insulator 215
MP2 15, 19
Mulliken population analyses 194
Multiple scattering Xα 38, 76
Multiple-ζ bases 108

$Na_8@Si_{46}$ 134
Nanoscale materials 107

Nanoscience 157
Nanotubes 107, 157
Nanowires 158
NBO 22
Néel temperature 191, 222
Net atomic charges 195
Neutron diffractions 5
Ni(111) 143
Ni(II) polysiloxanolates 94
$Ni(tmdt)_2$ 154
Ni_2Zn_4Cl 96
Ni_6Cl 96
NiO 214, 220
Nitrogenase 44, 60
NMR measurements 5

O(N) 107
Open-shell systems 194, 225
Open-shell transition metal ions 181
Order-N 107
Oxygen atom transfer 64
Oxygen vacancies 115

$PbTiO_3$ 118
Perovskites 182, 184
–, cubic 185, 196
–, ferroelectric (FE) 196, 207
Peroxidases 56
Phonon spectra 178
Plane-wave calculations 118
Plastocyanin 42, 46
Polysiloxanolates 94
Porphyrin 46
Prostaglandin H synthase 49
Pseudopotentials 107

QM/MM 1, 21, 26, 28, 46
QMC 176
Quantum Monte Carlo 176

Rack mechanism 47
Reaction energies 179
Reciprocal space 185
Redox enzyme 37
Relativistic effects 46
Reorganisation energy 47
Rhombohedral distortion 222
Ring critical point (RCP) 12
Rocksalt 192
Rocksalt-structured oxides 182

$RuH_2(H_2)L_2(SiHX_3)$ 18
$Ru(PH_3)_2)(X)(H)(C_3H_5)^{q+}$ 25
Rusticyanin 49

SDW 151
Self-interaction 173
– energy 48
Self-interstitials 112
Semiconductors 104, 109
–, amorphous 116
–, defects 112
–, diluted magnetic 126
–, layered III-IV 109
–, ternary 111
Si/SiO_2 interface 113
Si-SHA 18
Si surfaces, adsorption 144
– –, liquid 139
Si(001) 140, 144-146
Si(557)-Au 147
SiC 114
SiO_2/Si, interfaces 149
SIESTA 103, 105, 159
Sigma complex 4
Silicides, transition metal 140
Silicon 113
–, amorphous 116
–, hypervalent 20
–, impurities/defects 112
Silicon carbide 114
Simple-ζ 108
Single-particle excitation 224
Site-directed mutagenesis 44
Solar cells 111
Spin Hamiltonian 183
Spin moments 213, 226
Spin polarisation 61
Spin-lattice effect 220
Spin-orbit coupling effect 73
Spin-spin interaction 190
Spin-unrestricted procedure 194
$SrTiO_3$ 121
STM 146
Structural constraints 227
Structural distortion 203
Structural parameters 177
Structural relaxation 226, 227
Sulfite oxidase 64
Supercell expansion 194
Superdegeneracy 187, 189

Superexchange 191, 213, 220
Surface adsorption 177
Surface structure 178
Surfaces 128, 139
Surface-tip interactions 148

$TaH_4CH_2^{3-}$ 6
TB Hamiltonian 183, 198
$TeMo_5O_{16}$ 156
Tetragonal phase 203, 207
$Ti(dmpe)Cl_3(CH_3)$ 7
$Ti(dmpe)Cl_3(C_2H_5)$ 9
$TiCl_3(CH_3)$ 7
Tight-binding Hamiltonian 183, 198
TiO_2 115
Titanates 117
TranSIESTA 158
Transition aluminas 135
Transition metal complexes, polynuclear 71
Transition metal oxides 175, 178
Transition metals 37
Trapped electron 225
TTF-TCNQ 150, 156
Tungsten oxides/bronzes 151
Two-particle excitation 224
Tyrosyl radical 50, 53

UB3LYP 80
Underpotential deposition 143
Uniform electron gas 40

V(001) surface 131
Vacancies 114, 127
Vacancy diffusion 115
Valence tautomers 133

$W(CO)_3$ 24
$W(CO)_3(PCy_3)_2$ 24
Water-metal interface 142
Wavefunction, broken symmetry 63
Wavefunction techniques 172
Weak interaction 1
Weakening 6

Xanthine oxidase 44, 64
$Xe_8@Si_{46}$ 134
X-ray diffraction 5
Xα multiple scattering 38, 76

Zeolites 104, 134
Zero-field parameters 93
ZILSH 79
ZINDO 79
Zintl phases 122, 125
Zn(II), diamagnetic 81
Zwitterbewegung 46

The New Springer Global Website

Be the first to know

- Benefit from new practice-driven features.
- Search all books and journals – now faster and easier than ever before.
- Enjoy big savings through online sales.

springeronline.com – the innovative website with you in focus.

The interactive website for all Springer books and journals

Springer

01098Hx